ADVANCEMENTS AND PRACTICAL APPLICATIONS OF MOLECULAR TAGGING VELOCIMETRY IN HYPERSONIC FLOWS

by

Jordan M. Fisher

A Dissertation

Submitted to the Faculty of Purdue University

In Partial Fulfillment of the Requirements for the degree of

Doctor of Philosophy

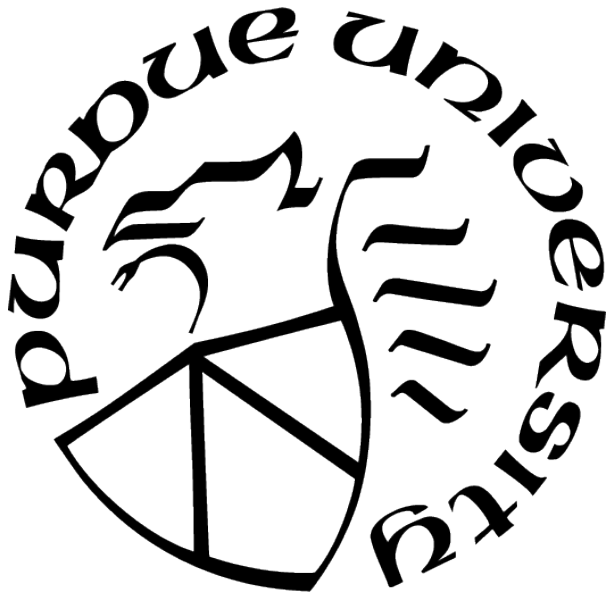

School of Aeronautics and Astronautics

West Lafayette, Indiana

December 2020

THE PURDUE UNIVERSITY GRADUATE SCHOOL
STATEMENT OF COMMITTEE APPROVAL

Dr. Terrence Meyer, Co-Chair

School of Mechanical Engineering

Dr. Guillermo Paniagua, Co-Chair

School of Mechanical Engineering

Dr. Mikhail Slipchenko

School of Mechanical Engineering

Dr. Sally Bane

School of Aeronautics and Astronautics

Dr. Joseph Jewell

School of Aeronautics and Astronautics

Approved by:

Dr. Gregory Blaisdell

ACKNOWLEDGMENTS

There is an old proverb that says 'It takes a whole village to raise a child'. In the same vein it could be argued it takes a whole research lab to make a Ph.D. candidate. All of this work would never have been possible of my own accord without the resources and mentorship I have been given throughout my research path.

I would like to first recognize my main advisors, Terrence Meyer and Guillermo Paniagua, for creating and supervising exciting programs and laboratories where I had the capability of growing and innovating. While they provided the tools for success in terms of funding and equipment, their willingness and support to let me propose and conduct my own projects gave me the ability to grow my research enthusiasm and capabilities, and truly allowed this thesis to manifest and come to fruition. Along with the ability to collaborate with my other committee members, Mikhail Slipchenko, Joseph Jewell, and Sally Bane, with their world-class research facilities and research insight, I have truly been blessed with all of the great resources and opportunities presented to me throughout my doctoral path.

Along with my advising committee, I have had the pleasure of spending many a late night with some of the best coworkers I could ever ask for. While there are too many to name, I would like to personally thank my fellow students such as Michael Smyser, Alex Brown, Austin Webb, James Braun, among many others for always being willing to go the extra mile so that I could pursue my many exciting and sometimes overly difficult and complex research projects. We now know all too well that no matter how many factors and problems we troubleshoot upfront before a testing campaign, something totally unexpected like a bad BNC, a faulty regulator, or dust in the regen cavity of the laser will throw a complete wrench into the hours and days of hard work we've put in to conducting quality experiments. A special thank you to everyone in the Meyer and Paniagua research groups for being there for the bad and the good of all the experiments I've been involved with in my time at Zucrow Laboratories.

From a personal side, I would like to thank my wife Jaclyn, for taking the giant leap of moving to Indiana and supporting me through grad school. From the pain of research related bureaucracy, long nights of failing experiments and long distance internships through

the pleasure of finally finding success and publishing papers, and coming into my own as my career develops, she has been right here with me the whole time.

TABLE OF CONTENTS

LIST OF TABLES 10

LIST OF FIGURES 11

NOMENCLATURE 17

ABSTRACT 19

1 INTRODUCTION AND METHODOLOGY 21

1.1 Hypersonic Flows and the Need for Diagnostics 21

1.1.1 Flow Environment and Applications 21

1.1.2 Need for Velocimetry 21

1.1.3 Hypersonic Wind Tunnels and Available Measurement Methods . . . 26

1.2 Molecular Tagging Velocimetry 28

1.2.1 Fundamentals and Basic Applications 28

1.2.2 Femtosecond Laser Electronic Excitation Tagging and Literature Review 29

Initial Demonstrations 30

Technique Characterization 31

Capability Demonstration 32

Wind Tunnel Implementation 33

1.3 Scientific Objectives 33

1.4 Research Methodology 35

1.4.1 High Spatial Extent Measurement Challenges 35

1.4.2 Extension of Molecular Tagging Capabilities 35

1.4.3 Aerodynamic Application in Test Facilities 36

2 ADVANCES IN THE SPATIAL EXTENT OF FLEET 38

2.1 Motivation 38

2.2 Microlens Array Systems 42

2.2.1 Optical Arrangement 42

2.2.2 Benchmarking Experiment . . . 42
2.2.3 Data Processing and Results . . . 45
2.2.4 Shortcomings of Microlens Method . . . 48
2.3 Diffractive Optical Element Beamsplitters . . . 51
2.3.1 Motivation . . . 51
2.3.2 *Grid-FLEET for instantaneous spatially-resolved and single-ended velocity measurements* . . . 53
Abstract . . . 53
Introduction . . . 53
Background and Experimental Setup . . . 54
Data Processing . . . 57
Results . . . 60
Conclusion . . . 64
2.4 Further Advances in Processing for Gridded Data . . . 65
2.4.1 Centroid-based Outlier Detection . . . 65
2.4.2 Adaptive Velocity Calculation . . . 69
2.4.3 Spatial Binning for Precision Enhancement . . . 73
2.4.4 Flow Parameter Calculation . . . 78

3 EXTENSION OF MOLECULAR TAGGING CAPABILITIES . . . 84
3.1 Improvement of Frequency Resolution . . . 84
3.1.1 Motivation . . . 84
3.1.2 Benchmarking . . . 84
3.1.3 *Burst-mode femtosecond laser electronic excitation tagging for kHz–MHz seedless velocimetry* . . . 89
Abstract . . . 89
Introduction . . . 89
Experiment . . . 91
Results . . . 94
Conclusion . . . 99

3.1.4 Combining High Frequency and High Spatial Extent Measurements . 101
3.1.5 Recommendations . . . 103
3.2 Adaptation to Reacting Flows . . . 104
3.2.1 Motivation . . . 104
3.2.2 Hydroxyl Tagging Velocimetry . . . 105
3.2.3 Proof-of-Concept . . . 106
3.2.4 *Femtosecond laser activation and sensing of hydroxyl (FLASH) for velocimetry in high speed reacting flows* . . . 107
Abstract . . . 108
Introduction . . . 109
Background . . . 110
Evaluation of Technique . . . 112
Experimental Arrangement . . . 112
OH Transition Wavelength Tuning . . . 114
OH tracer lifetimes . . . 115
Read and Write Laser Energy Scaling . . . 118
Velocity Measurement . . . 121
Experimental Arrangement . . . 121
Data Processing . . . 121
Conclusions and Future Work . . . 125
3.2.5 Advanced Write-Read Schemes for FLASH Velocimetry . . . 126
3.2.6 Application to RDE Exhaust Measurements . . . 127
Experimental Arrangement . . . 128
Timing Logic . . . 129
10 Hz Results and Shortcomings . . . 131
1 MHz Results . . . 133

4 APPLIED MEASUREMENTS IN HIGH SPEED FACILITIES . . . 138
4.1 Motivation . . . 138
4.2 Bladeless Turbine . . . 140

4.2.1 Proof-of-Concept in Air . . . 141
4.2.2 *Application of femtosecond laser electronic excitation tagging (FLEET) velocimetry in a bladeless turbine* . . . 143
Abstract . . . 143
Introduction . . . 143
Experimental Facilities . . . 147
Wind tunnel facility . . . 147
Test Section and Operating Conditions . . . 147
Optical Equipment . . . 148
Data Processing . . . 150
Data organization . . . 152
Centroid Analysis . . . 152
Velocity Calculation . . . 154
Measurement Precision and Accuracy . . . 155
Results . . . 157
Evaluation of the Mean Flow Physics and Validation for Computational Tools for High Speed Flows . . . 157
Mean and Fluctuating Flow Field . . . 158
Flow Field Comparison to CFD . . . 159
Measurement of Unsteady Flow Fluctuations . . . 162
Unsteady Flow Shear Stress Measurement . . . 164
Measurement of Highly Transient Spatial Occurrences: Unstarting of the Test Section . . . 166
Conclusions . . . 168
4.3 Boeing/AFOSR Mach 6 Quiet Tunnel . . . 170
4.3.1 Benchmarking at Low Pressure . . . 170
4.3.2 *Femtosecond laser tagging for boundary layer velocity measurements in the Boeing/AFOSR Mach-6 Quiet Tunnel* . . . 175
Introduction . . . 176
Experiment and Data Processing . . . 178

Optical Arrangement . . . 178
Data Processing . . . 179
Results . . . 181
Precision and Accuracy . . . 181
Boundary Layer Traverse . . . 182
Instantaneous Boundary Layer Profile . . . 183
Flow Unsteadiness . . . 184
Conclusions and Future Work . . . 185
4.3.3 Optimization of Measurement Technique for Quiet Hypersonic Flow . 186
Enhanced Precision . . . 186
Improved Spatial Resolution . . . 187
Reduction in Spatial Uncertainty . . . 190
4.3.4 Investigation of Third-Harmonic Excitation and Argon Enhancement 191
4.3.5 Implementation of Fundamental Molecular Tagging Advancements . 196
Multiple Spot Tracking for Extreme Precision . . . 198
High Frequency Measurements . . . 199

5 SUMMARY OF ADVANCEMENTS AND CONCLUSION . . . 200
5.1 Demonstrated Advancements . . . 200
5.1.1 Advances in the spatial extent of FLEET . . . 200
5.1.2 Extension of molecular tagging capabilities . . . 201
Increased Repetition Rate . . . 201
Extension to Reacting Environments . . . 202
5.1.3 Aerodynamic application in ground test facilities . . . 203
Bladeless Turbine . . . 203
Boeing-AFOSR Mach 6 Quiet Tunnel . . . 204
5.2 Conclusion . . . 205

REFERENCES . . . 206

LIST OF TABLES

3.1 Double exponential fit coefficients for all experimental conditions 119

LIST OF FIGURES

1.1 Post shock temperature of a re-entry vehicle [1]. 22

1.2 Real gas processes related to a vehicle re-entering the atmosphere[2]. 23

1.3 Diagram of velocity measurement with FLEET 30

2.1 Composite of line-FLEET images allowing for for semi-spatially resolved velocity measurements 39

2.2 Time series of PIV measurements showing the ability to track multiple spatial flow features with vorticity [77]. 39

2.3 Crossed line grid used to make spatially resolved instantaneous molecular tagging velocimetry measurements [78]. 41

2.4 (A) Diagram of the implementation of a microlens to perform FLEET. (B) Initially tagged results in quiescent air showing possibility of a 6x6 grid of tagged points. 43

2.5 Demonstration experiment of spatially resolved measurements using microlens excitation 44

2.6 Raw composite images of multi-dimensional FLEET measurements at 10, 17.5 and 25 bar. Spatial differences in the signal levels and velocity magnitudes can be seen. This effect becomes more pronounced as pressure increases. 45

2.7 (A) Isolation of individual spots in grid FLEET image. (B) Centroid finding on spot group. 46

2.8 (A) Adaptive displacement evaluation with curve-fitting. (B) Displacement mapping back into original measurement position. 47

2.9 (A) Instantaneous and time-averaged velocity contours after spatial calibration and interpolation. (B) Spatial map of shear stress calculation 48

2.10 SNR of all grid spots as a function of delay. Peripheral spots decrease to the noise level earlier than middle spots. 50

2.11 Diagram of implementation of holographic beamsplitter to produce a grid of focused points. 52

2.12 (a) Operating principles and relevant parameters for 4x4 diffractive optical element (DOE), (b) ensemble-averaged image of Grid-FLEET signal in quiescent air, 6.3 mJ, 10 mm input beam, 200 mm focusing lens.. (c) Experimental verification of grid spacing against focusing length standoff distance, (d) binned intensity profiles of Grid-FLEET rows from image in (b). 56

2.13 Experimental setup for conducting grid-based FLEET velocity measurements. DOE: Diffractive optical element, f1: f = +250 mm lens. 58

2.14 Single-shot raw signal at (a) T_0 , (b) T_0 +60μs,. Spot isolation regions shown as dotted rectangles. 59

2.15 W_c: intensity weighted centroid Location, SF_c: surface fit centroid location overlaid on (a) valid raw data: δ_c=0.11 pix, R^2=0.96, (b) outlier raw data: : δ_c=.08 pix, R^2=0.77, x and Y- binned intensity profiles for raw image and Gaussian surface fits shown in red and yellow, respectively. 60

2.16 (a) Composite of single-shot FLEET images taken at T_0 (red), T_0+40μs (green) and T_0+80μs (blue), and (b) T_0 +10μs (red), T_0+50μs (green) and T_0+90μs (blue) and (c) 4x4 velocity vector fields constructed from image pairs at T_0+0/+10μs (red), T_0+40/+50μs (green), T_0+80/+90μs (blue). (c) Random error in velocity for all measurement locations shown in (b). 61

2.17 Flow around the sharp corner. (a) Composite of single-shot FLEET images taken at. T_0 (Red), T_0+60μs, (Cyan), and T_0+120μs (Magenta). (b) Pseudo-vector field created from burst-mode images of single-shot grid excitation (total acquisition time 150 μs). The position of the plate with 90 corner is shown by the red dotted line. 62

2.18 Instantaneous 3x3 gradient vector sets of U (a) and V (b). Calculated from image pairs at T_0+0/+10μs (yellow) and T_0+120/+130μs (red). 63

2.19 Outlier percentage as a function of desired precision for various grid-FLEET points. 68

2.20 Constant-acceleration curvefits for x and y grid-FLEET velocities 70

2.21 a) Displacement trend with finite difference and constant-acceleration curve fit. b) Velocity time trace result from finite difference and curve-fit methods applied to single-shot data. 71

2.22 Precision improvement of curvefit based velocities over single point finite differencing for Vx and Vy velocity components. 73

2.23 Trend of precision vs. sample size for multi-point FLEET measurements. 74

2.24 Locations and number of measurements for spatial binning levels L=0-3 (n=1,4,9,16). 76

2.25 Precision vs. number of binning points for steady flow Grid FLEET data. Theoretical prediction plotted as dashed line. 76

2.26 Precision improvement over baseline, and number of independent velocity measurements plotted against number of interpolated samples (n). 77

2.27 Effective Spatial Resolution (E.S.R.) as a function of binning level. Data reported in mm with respect to the current measurement as well as percent full grid extent for future experiment planning. 78

2.28 Locations of original and orthogonally interpolated velocity measurements for undisplaced and displaced FLEET grids. 79

2.29 Example vorticity result created from 16 point instantaneous FLEET grid. Original measurement points shown as white circles. 80

2.30 Example shear stress result created from 16 point instantaneous FLEET grid. Original measurement points shown as white circles. 81

3.1 Diagram of experimental setup for benchmarking burst-mode FLEET measurements. (A) Overhead view, (B) front view 85

3.2 Image of FLEET demonstrator nozzle and location of optics and camera system 86

3.3 Images of FLEET signal at decreasing excitation energy 87

3.4 (A) Signal peak intensity vs excitation energy, (B) Signal-to-Noise Ratio vs excitation energy 88

3.5 Parameters of fs laser, including (a) frequency domain bandwidth, (b) temporal domain pulse width, (c) beam quality divergence profiles after temporal compression with M2 = 2.97 and 3.33 in x and y directions, respectively, and (d) burst profiles for 200 kHz and 1 MHz repetition rates. 93

3.6 (a) Top view of FLEET experiment showing laser delivery to probe location through 30 mm focusing lens and (b) front view showing top-down placement of high-speed intensified camera. 93

3.7 (a) Representative spot finding with area centroid (cyan dot), intensity weighted centroid (black dot), and bounding box (white box) with centroid (red dot); and (b) associated trend of uncertainty in velocity measurements for different pressures with pure N2 and air. 95

3.8 Correlation maps for displacement in (a) 34.5 bar nitrogen, (b) 48.3 bar nitrogen, (c) 68.9 bar Nitrogen, and (d) 68.9 bar air. 97

3.9 Velocity time history for 68.9 and 48.3 bar supply pressures with nitrogen. (b) Average velocities and uncertainties for all tested conditions with nitrogen and air. The uncertainty of the air measurement is much larger as compared to the nitrogen measurements. To improve the accuracy of this technique for use in air, a more sensitive imaging system or higher laser energy is required. 98

3.10 (a) Raw data collected with 1 MHz laser excitation. (b) Five velocities measured simultaneously along a streamline with 1 MHz laser excitation (grid spacing is 1 mm). 100

3.11 Eulerian vs Lagrangian flow property tracking [97]. 101

3.12 SImulated data showing combination of high-frequency and spatial extent measurements. 102

3.13 Time-decay of FLEET signal at various equivalence ratios in a Methane-Air Flame [75]. 106

3.14 Spectrum results of femtosecond laser excitation in nitrogen, ambient air and humid air. 108

3.15 Experimental setup for demonstration of FLASH velocimetry in an H2-air Hencken Burner. 113

3.16 Wavelength tuning of the read laser sheet over the OH $Q_1(9)/Q_2(8)$ transition pair. 114

3.17 FLASH raw data at select read laser delays at $\Phi = 1$. All images are 50-data point ensemble averages. 115

3.18 Peak FLASH signal intensity as a function of tag delay for various flame equivalence ratios. Data collected in the reaction zone of an H_2-Air Hencken burner. . 116

3.19 Peak FLASH signal intensity as a function of tag delay for a) stoichiometric and rich equivalence ratios, and b) lean equivalence ratios. Data collected in the post flame region of an H_2-Air Hencken burner. 117

3.20 Signal lifetimes vs equivalence ratio in reaction zone and post flame regions. . . 118

3.21 a) FLASH peak signal intensity vs write laser energy at read laser delays of 2, 10 and 20 μs. b) Peak FLASH signal vs read laser energy at 5 μs read laser delay, with write laser energy 5 mJ/pulse. All data sets taken at $\Phi = 1$ in an H_2-Air Hencken burner. 120

3.22 Setup for measuring velocity in an H_2-Air diffusion flame using FLASH. 121

3.23 Single-Shot FLASH signal in an H_2 diffusion flame with a) no background subtraction, b) background isolation based on linear trend, c) FLASH image with background subtracted. Intensity profiles along dashed lines in (a-c) shown to the right of the images. 122

3.24 (a) Non-displaced and instantaneous images of FLASH signal at select read delays in an H_2-Air diffusion flame. (b) Horizontally-binned intensity profiles of images shown in (a). 124

3.25 Measured flame velocity as a function of read laser delay (left axis). Uncertainty bars represent standard deviation of 100 instantaneous measurements. Percentage of outlier measurements as a function of read delay, determined by $R^2 < 0.8$ (right axis). 125

3.26 Absorption spectrum of water 128

3.27 Optical Arrangement for Demonstrating FLASH in the THOR RDE 130

3.28 A) Timing logic for 10 Hz FLASH measurements. B) Timing logic for 1 MHz FLASH measurements 131

3.29 Raw composite of T_0 reference image (green) and single-shot FLASH image at with 2μs tag delay (magenta). Centroid locations shown as black triangles. . . . 132

3.30 Scatter chart of measured velocity vs flow angle for select RDE operating conditions and read laser delay. Write-read delay of 5 μs shown with red circles. . . . 134

3.31 a) Raw image data. B) Background intensity found by top hat filtering. C) Isolated signal after background subtraction 135

3.32 Scatter plot of velocity and flow angle for RDE exhaust plume 137

4.1 Raw FLEET data from proof-of-concept experiment in air. 142

4.2 Transient results during unstarting for two moving-averaged FLEET measurement points. 142

4.3 Three-dimensional view of a bladeless turbine. 145

4.4 Schematic of generic FLEET experiment. 146

4.5 (a) Schematic of PETAL linear wind tunnel showing nitrogen storage, vacuum tank, and flow conditioning. (b) Image of wind tunnel with test article and optical window installed. 148

4.6 Laser and camera experimental setup. 151

4.7 Time series of raw data with spot isolation regions. Spurious intensifier noise is highlighted in red, which was subtracted during image processing. 153

4.8 Flow field description via Schlieren visualization. 158

4.9 (a) Average velocity vectors obtained from all FLEET measurements. (b) Fluctuation level (standard deviation) vectors for all measurements. 160

4.10 (a) Overlay of CFD predicted axial velocity and FLEET measurements, (b) Percent difference between FLEET and CFD at each measurement point. 161

4.11 (a) CFD predicted transverse velocity, (b) interpolated transverse velocity from FLEET measurements, (c) percent difference between CFD and FLEET velocities. 163

4.12 Probability density functions at (a) select points in the flow of (b) velocity and (c) fluctuation intensity from FLEET measurements. 165

4.13 a) Velocity of two measurement points tagged simultaneously. (b) Shear stress between points as a function of time. 166

4.14 (a-e) instantaneous shadowgraph images during unstarting of the test section. (f) Velocity trace of color-coded points in the unstarting flow field from FLEET measurements. 169

4.15 Schematic of the proof-of-concept experiment showing the vacuum cell, wind tunnel wind and focusing lens, and the integrated imaging system. 172

4.16 Instantaneous FLEET signal at all time delays from laser pulse T_0 174

4.17 Signal Intensity vs. Time for all pressures and time delays 175

4.18 Gaussian Correlation Coefficient vs Time for all pressures and time delays . . . 176

4.19 Signal to Noise Ratio vs Time for all pressures and time delays 177

4.20 Optical arrangement for FLEET velocimetry in the Boeing/AFOSR Mach 6 Quiet Tunnel from (a) end and (b) top views. TA: test article, BAM6QT: Boeing/AFOSR Mach-6 Quiet Tunnel, BE: beam expander, VT: vertical traverse, L1: f = -100 mm achromat lens, L2: f = +300 mm achromat lens, L3: f = +300 mm achromatlens, PE: periscope. 179

4.21 (a) Raw multi-exposure image of FLEET signal acquired in the perpendicular camera view. (b) Vertically-binned intensity profile with peaks highlighted by red triangles. (c) Snapshot of local quadratic interpolation of peaks for sub-pixel resolution. (d) Linear curve fit of sequential displacements with R^2>0.999 showing negligible velocity change over the interrogation length. 180

4.22 Comparison of freestream FLEET velocity measurement and predicted velocity from tunnel instrumentation. 182

4.23 Boundary layer traverse measurements overlaid on CFD prediction. 183

4.24 (a) Raw data image with velocity vectors showing changing magnitude over the length of the tagged line. (b) Trend of velocity against distance from test article overlaid on a CFD prediction. 184

4.25 (a) Simultaneous time-traces of FLEET velocity measurements at y/δ=0.8 (50 sample moving mean filter) and tunnel stagnation pressure measurement. (b) Overlay of power spectra for both signals showing correlation of velocity to periodic drops in tunnel stagnation pressure. 185

4.26 A) Lifetime vs pressure for 800 nm and 267 nm FLEET excitation. B) Spot size vs pressure for 800 nm an 267 nm excitation. 193

4.27 FLEET signal intensity vs percent argon at different pressures with 800 nm and 267 nm excitation. Data normalized by zero argon percent signal intensity . . . 195

4.28 FLEET signal decay lifetime vs percent argon at different pressures with 800 nm and 267 nm excitation 197

NOMENCLATURE

APART	Air Photolysis and Recombination Tagging
ArF	Argon Fluoride
BAM6QT	Boeing-AFOSR Mach 6 Quiet Tunnel
CFD	Computational Fluid Dynamics
DMD	Dynamic Mode Decomposition
DOE	Diffractive Optical Elecment
FLEET	Femtosecond Laser Electronic Excitation Tagging
FLASH	Femtosecond Laser Activation and Sensing of Hydroxyl
fs	Femtosecond
γ	Isentropic Expansion Coefficient
H_2O	water
HTV	Hydroxyl Tagging Velocimetry
LEAF	Linear Experimental Aerodynamic Facility
μ	micro (10^{-6})
MTV	Molecular Tagging Velocimetry
Nd:YAG	Neodymium-doped Yttrium Aluminum Garnet
NO	Nitric Oxide
N_2	Nitrogen
NTF	National Transonic Facility
OH	Hydroxyl
OPO	Optical Parametric Oscillator
POD	Principle Orthogonal Decomposition
Φ	Equivalence Ratio
PIV	Particle Image Velocimetry
PLIF	Planar Laser-Induced Fluorescence
RANS	Reynolds-Averaged Navier Stokes
RDE	Rotating Detonation Engine
R^2	Correlation Coefficient

RELIEF	Raman Excitation and Laser Induced Electronic Fluorescence
SNR	Signal-to-noise Ratio
UV	Ultraviolet
VENOM	Vibrationally-excited Nitric Oxide Monitoring

ABSTRACT

Hypersonic flows consist of harsh environments where chemistry effects are relevant and low speed assumptions such as the ideal gas law and the continuum hypothesis begin to break down. Because of these processes, computer models do a poor job of predicting behavior of vehicles in hypersonic flight. High fidelity ground test measurements are necessary to anchor and extrapolate CFD simulations so that flight vehicle designs can continue to improve. Due to the harsh conditions and complexities of test facilities, implementing experimental measurements can prove challenging.

Molecular tagging methods such as Femtosecond Laser Electronic Excitation Tagging (FLEET) are attractive for use in hypersonic ground test facilities for many reasons. They are generally considered non-intrusive, since they require no physical probes or seed particles to be placed in the flow. This both keeps the facility safe from damage and minimizes the disturbance imparted on the flow field by the measurement. Since the tracer is comprised of molecules already present in the flow, the measurement is reliable and can track velocities over a wide dynamic range. The optical arrangement for FLEET is rather simple, requiring only a focused laser beam and a camera to capture the signal. The method can even be applied as a one-sided measurement requiring only one direction of optical access. The current state-of-the-art for the FLEET method is point-wise measurements made at 1 kHz with a commercially available laser system.

The basis for this thesis is to identify and address current limitations in the implementation of FLEET to relevant flow facilities in terms of the useful aerodynamic information that can be extracted. Fundamental advances to the spatial extent and temporal resolution of FLEET are investigated, and novel applied measurements in high speed flow facilities are presented. Considerations of the precision, spatial resolution and ability to implement fundamental advances to harsh and more complex environments are discussed. A custom-built burst-mode femtosecond laser system is used to enable FLEET measurements at 1 MHz, an improvement of three orders of magnitude in measurement rate. New optical arrangements including microlens arrays and holographic beamsplitters are developed to allow multi-dimensional grids to be tracked to instantaneously measure velocity gradients. Shock

wave and shear measurements in a supersonic bladeless turbine and boundary layer measurements on a Mach 6 cone-cylinder-flare are demonstrated. Additionally, an adapted method, Femtosecond Laser Activation and Sensing of Hydroxyl (FLASH) is developed and applied to measure velocity in reacting environments such as a Rotating Detonation Engine (RDE). These innovations provide a path forward for improving the spatiotemproal fidelity of velocity measurements and extending the capability for investigation high-speed reacting and non-reacting flows in hypersonic ground test facilities.

1. INTRODUCTION AND METHODOLOGY

1.1 Hypersonic Flows and the Need for Diagnostics

1.1.1 Flow Environment and Applications

Hypersonic flow is generally considered to begin at velocities exceeding Mach 5, when flow chemistry effects begin to play a role. This flight regime applies to space launch vehicles, re-entry vehicles, ballistic missiles, and proposed hypersonic interceptors and civilian transport vehicles. For orbital launch and re-entry, this high-speed is a necessity of the flight envelope. There is no way to achieve the mission without excessive velocity. For atmospheric flight, achievement of hypersonic speed is not a must, but a highly desired goal. For national defense and transport, increasing technology levels have continued to push the desire and availability of high-speed vehicles.

For low-speed flows, the general assumption that a fluid behaves as an ideal gas is accurate. As Mach number increases, this assumption becomes less valid. For hypersonic flight, real gas effects become dominant and must be considered to model the flow field accurately. At such high-speeds, energy storage modes such as vibrational excitation and molecular dissociation influence the behavior of shock waves, boundary layers and other flow features. Chemical non-equilibrium influences the flow and causes species to catalitically react with the vehicle surface. Figure 1.1 from [1] shows the temperature behind a shock for a calorically perfect gas and for an equilibrium reacting gas. The reacting gas shows a considerably lower temperature than the perfect gas. This is because flow energy transfers into chemical reactions and dissociation. These reactions in turn influence the interaction of the boundary layer with the vehicle surface and can make fluid dynamic simulation more difficult.

1.1.2 Need for Velocimetry

Current aircraft design relies on Computational Fluid Dynamics (CFD). High-fidelity CFD offers lower time to market, while developing safer vehicles. A rich understanding of a flight vehicle design can be obtained before any hardware is ever built or tested. For subsonic

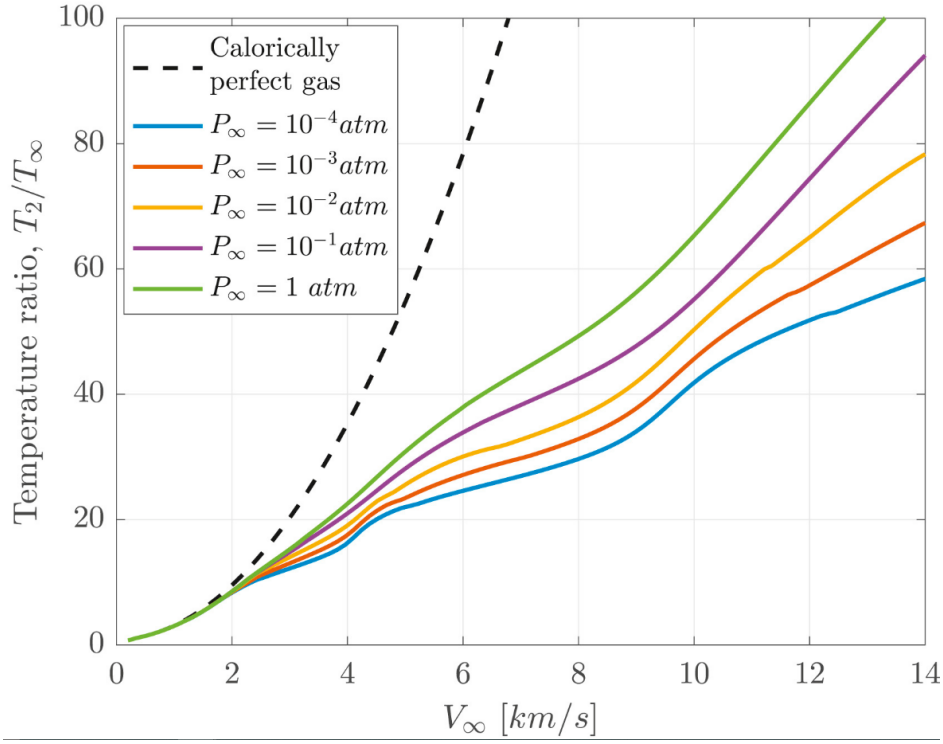

Figure 1.1. Post shock temperature of a re-entry vehicle [1].

flight, properly performed CFD can accurately predict to the conditions that a flight vehicle sees when it is prototyped and evaluated in the real world. As flow complexity increases, such as in subsonic flows when separation in considered, modeling becomes difficult. This problem is exacerbated as Mach number increases. With Mach number approaching supersonic, shock waves and higher levels of flow interaction become pronounced. These flow features tend to make the simulation more complex and pose difficulties in obtaining high spatiotemporal resolution and accuracy. Shock-boundary layer interaction and supersonic flow separation pose a challenge for all but the most complex CFD simulation methods, which are time consuming and computationally expensive. As Mach number increases even further toward the supersonic and hypersonic regimes, flow physics become even more complex. As velocity goes higher, more heating is present which has an effect on isentropic expansion coefficient, $\gamma = \frac{C_p}{C_v}$, which plays a large role in the behavior of the fluid. Molecular energy modes such as vibrationally excited states and chemical dissociation become more pronounced as well. This can be seen in Figure 1.2[3]. Many CFD solver methods do not account for these processes

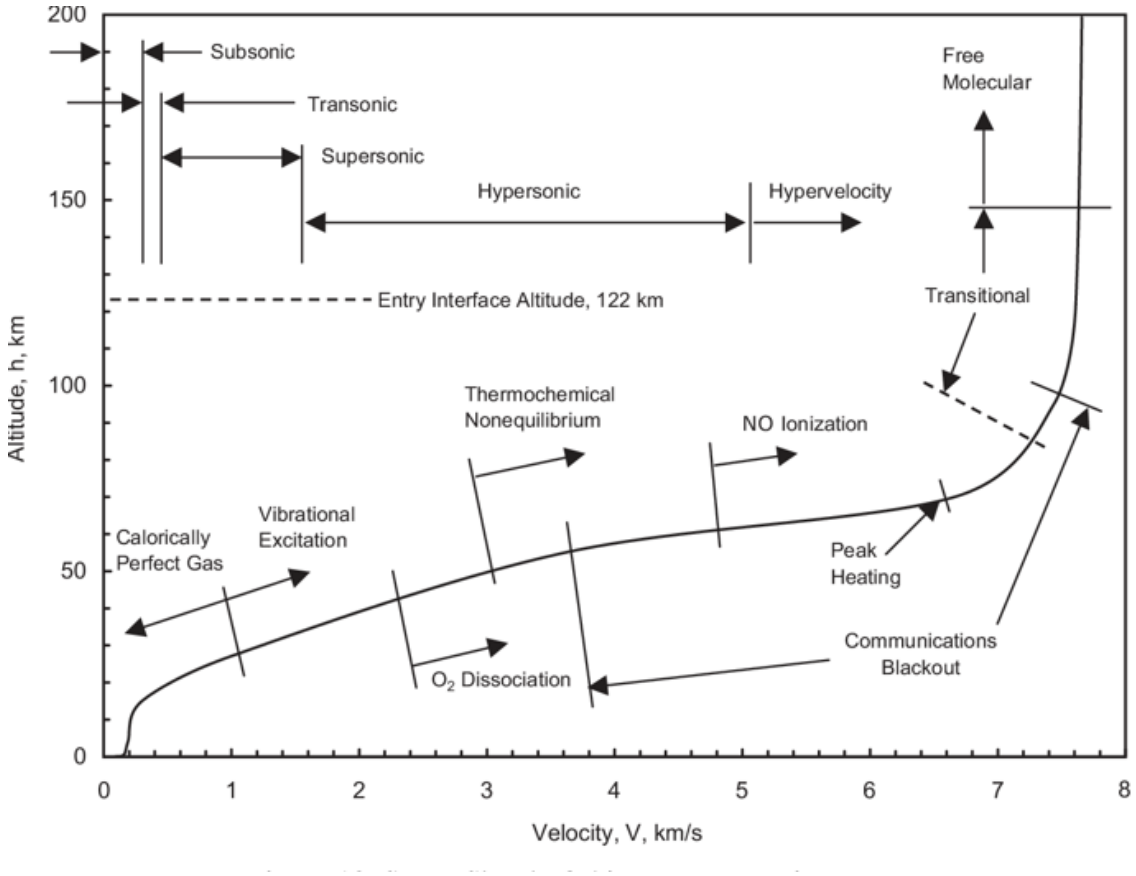

Figure 1.2. Real gas processes related to a vehicle re-entering the atmosphere[2].

and thus cannot be used to simulate such high-speed flow regimes. The simulations that can account for these become increasingly complex and limited in their applications. The desire for 'reduced order models', or simulations that model complex phenomena in a simplified way drives extensive development of advanced flow diagnostic applications. Instead of modeling each complex reaction, reduced order tuning parameters can be created to mimic the real-gas effects. With these reduced order models, simulations can be performed with decreased computational cost; however as their name suggests, tuning parameters must be calibrated and anchored based on real experimental data.

There are three main reasons, although many more can be listed, to focus on implementing velocimetry in ground test facilities.These are: (i) evaluation and characterization of ground test facility parameters such as inlet velocity profiles and startup transients, (ii) collecting reference data to anchor CFD simulations to complex flow fields, (iii) collecting

data on non-simulated design conditions such as changing velocities, flight conditions, and geometries for test articles.

In many CFD studies specifically tailored toward wind tunnel applications, or even more complex fluid-dynamic systems, true boundary conditions may not be known. Nominal design conditions for mass flow, pressure, and temperature can be assumed for initial design and simulation phases, but ultimate evaluation of the system performance necessitates a fuller picture that can account for spatiotemporal variations in the flow. From simple verification of inlet Mach number and velocity, to flow angle and turbulence statistics, velocimetry plays a key role in facility characterization [4]–[7], which in turn is used to support higher fidelity models. Without an accurate characterization of inlet/outlet boundary flow conditions of a facility, CFD models do not have a strong chance of producing system-accurate simulations that represent the overall performance. Even the highest fidelity and most accurate computational codes cannot achieve high accuracy if they are not initialized with the correct boundary conditions [8]–[12]. In some of the most challenging experimental facilities, such as the National Transonic Facility (NTF) at NASA Langely [13] and the Boeing-AFOSR Mach 6 Quiet Tunnel (BAM6QT) at Purdue University [14], parameters such as the inlet velocity magnitude, spatial profile, and state variables have never been fully characterized. For more complex and pioneering designs such as the Turbine-integrated High-pressure Optical RDE (THOR) [15], designed to interface with a supersonic turbine, the outlet condition of the combustion chamber is of great importance because it represents the inlet condition to the turbine. If this flow state is not understood fully through experimental verification, the design of the turbine airfoils cannot be optimized because there is a lack of full design constraints. The analysis and development of proper measurement techniques for the characterization of complex flow facilities such as these has been the focus for many researchers [16]–[23] and the work is continued through the bulk of this thesis.

On the other hand, for situations where boundary conditions are mostly known, there can still remain uncertainty in the fidelity of the model and whether it can accurately capture the accurate flow state. In this vein, we are concerned with model verification and tuning [24]. In many cases, the highest-level CFD that delivers the most accurate results can be prohibitively expensive to perform. When this occurs, researchers must make use of reduced-

order and reduced-fidelity models [25]. For many of these solution methods, reduced-order models do not make use of the full flow equations, but rather simplified equations that are less computationally expensive to assess. With tuning parameters, these models can often produce results that are accurate up to the necessary degree of the research intent. Unless previously validated with a higher-accuracy solution method or previously acquired measurements, these reduced-order models cannot be considered accurate until proven with some form of anchoring data. This is where velocimetry methods come into consideration again [26]. Whether it is to directly verify a CFD solution, or to assist in the adjustment of the model, velocimetry can play a large role in model verification. Specific flow features, such as velocity at a point, boundary layer thickness, shock angle, and boundary layer separation/transition points are all quantitative parameters that can be compared between model and experiment. If the velocity measurement has been performed properly, it can be regarded as the true flow field value, and any discrepancies in the CFD are treated as inaccuracies in the model. By gaining the experimental evidence of the flow field behavior, lower order models can be improved. This avenue was considered during the experiments of this thesis, especially in [27] to show that there was a discrepancy in the shock angle predicted by Reynolds-Averaged Navier Stokes (RANS) simulations of a supersonic turbine in the Purdue Linear Experimental Aerodynamic Facility (LEAF).

The last reason for invoking velocimetry methods occurs when gathering experimental data is considerably less expensive than running simulations. If experimental data is extensive enough to deliver performance metrics of a design, then ground test facilities can be used for full characterization of aerodynamic systems. Velocimetry can be used to evaluate test article performance such as lift [28], drag [29], boundary layer transition [30], [31], surface heating [32], and shock/boundary layer interactions [33]. Often times when a test campaign is conducted, the velocimetry set up takes a long time, but switching between test conditions is rather simple. For this reason, once a velocity measurement is fully developed for a facility, it becomes straightfoward to use it to evaluate a larger design space of a test article. By doing this, performance data across a larger operating space can be gathered, leading to a fuller understanding of the system to guide further advancement of the design before more CFD is conducted. This reasoning supports the work of this thesis to further the

spatial extent and frequency resolution of molecular tagging velocimetry methods in order to extend the usable data output of these experimental techniques with respect to performance characterization of experimental articles.

1.1.3 Hypersonic Wind Tunnels and Available Measurement Methods

As in any flight regime, it is always easier to evaluate a model in a ground test facility than to develop a full-scale vehicle for in-flight evaluation. There are many types of hypersonic wind tunnels in operation around the world today. Many of these wind tunnels are transient flow facilities, comprised of a high pressure plenum, a converging diverging nozzle, and a low pressure tank downstream. The pressure ratio and geometry of the nozzle fix the operational Mach number and the size of the downstream vacuum set the operating time of the facility, typically a few seconds to a few minutes in length. The hypersonic wind tunnel at Sandia National Laboratories (Mach 5, 8, and 14), Hypervelocity Wind Tunnel 9 at Arnold Engineering Development Center (Mach 7, 8, 10 and 14) and the Boeing-Air Force Mach 6 Quiet Tunnel at Purdue University (Mach 6) operate in this transient mode. Continuous-flow hypersonic wind tunnels such as the 31 inch Mach 10 facility at NASA Langley do exist, but they are generally adaptations of the transient blow-down architecture with improvements to the high-pressure upstream supply and vacuum capability downstream. Sustaining long test times in a hypersonic facility can become increasingly difficult and expensive. It can be rather simple to achieve hypersonic Mach number alone in ground test facilities, but matching flight parameters such as pressure, temperature, and freestream turbulence levels can be more difficult. Since ground test facilities involve accelerating the flow to high velocity rather than the vehicle, isentropic gas relations dictate that the static temperatures and pressures experienced in a test facility will generally be much lower than in hypersonic flight. To counteract this, hypersonic facilities employ high pressures into the 10's of atmospheres and temperatures above 2000 K in the supply plenum to the wind tunnel, but even with this the static temperature and pressures achieved in the wind tunnel are lower than in-flight values. Atmospheric hypersonic flight also consists of low-levels of freestream turbulence. In a hypersonic facility, flow conditioning is very difficult, and for this reason studying laminar-to-turbulent transition can be exceptionally difficult. The Boeing-Air Force Mach 6 Quiet

Tunnel (BAM6QT) employs special tunnel construction and flow conditioning to allow for low amounts of flow disturbances to mimic the turbulence level of atmospheric flight. To allow for testing of high-enthalpy environments associated with hypersonic flight, tunnels such as the ONERA F4 and the Aerodynamic Heating Facility (AHF) at NASA Ames are arc-jet facilities that use powerful heaters to achieve high-speed and temperatures to model surface heating similar to flight environments. Unfortunately, no one hypersonic ground test facility can match all of the parameters associated with this flight regime, so multiple facilities must carry the partial burden of simulating different aspects of hypersonic flight.

Because the physical phenomena of hypersonic flight can be difficult to predict a-priori, relevant measurements in these facilities need to be made to confirm designs. Physical-probe flow-field measurements, which are widely used in subsonic test facilities, are generally limited in the hypersonic regime. The harsh nature of hypersonic wind tunnels can easily break a physical velocity or pressure sensor, and the delicate nature of the flow field is heavily influenced by the physical presence of a sensor inserted into the flow. For these reasons, physical sensor measurements are generally limited to those that are mounted in the test article surface. Pressure scanners are extensively used to evaluate flow surface behavior and separation [34], [35]. Other surface sensors include heat transfer and skin friction sensors [36]. These physical probe measurements are also applied in high-enthalpy facilities [37]. Due to the short operational time of most facilities, sensors must be able to capture data at a high rate to make the most out of each test run.

The complex spatiotemporal variations inherent to hypersonic aerodynamics makes the use of optical diagnostics highly desirable. While ground test facilities present many barriers to the full implementation of optical diagnostics, much progress has been made in the past two decades in the way of meaningful measurements. One of the simplest diagnostic methods for flow visualization is Schlieren imaging [38]. This technique only requires pass-through optical access to the test section and can reveal density gradients to view shock waves and boundary layer instabilities. This is a very useful semi-quantitative measurement technique for visualizing the underlying flow-field physics. Particle-based velocity methods such as Particle Image Velocimetry (PIV) and Filtered Rayleigh Scattering (FRS) have also been applied for hypersonic measurements in a limited fashion [39]–[42]. These methods come with

considerable experimental complexity. First, appropriately sized particles must be delivered into the test section. If the particles are too large, they will not follow the flow properly. If they are too small, they will not scatter enough light intensity to be observed by the camera. This trade-off becomes increasingly difficult as flow velocity increases, requiring smaller and smaller particles and higher and higher laser energy. Getting these particles delivered at an acceptable density to the region of interest in the flow field can prove challenging as well. Additionally, many high complexity facilities completely preclude the introduction of tracer particles to protect sensitive equipment, making such methods impossible. Even in facilities where seeding may be allowed, considerable engineering effort, cost, and schedule risk can be involved with implementing particle delivery to the measurement region. Oftentimes, months or even years can be spent on the implementation of particle-based velocimetry techniques, just for measurements with limited applicability and accuracy. To avoid the complexity necessitated by particle-based methods, molecular fluorescence-based have been implemented. These measurements include NO Planar Laser Induced Fluorescence (PLIF) [43], [44]. This method requires the seeding of nitric oxide, which is allowed in many facilities, but can prove challenging and expensive since it usually requires modifications to the wind tunnel and/or test article. Jiang et al.[43] demonstrated this measurement technique in a spatially resolved manner at 1 MHz, although the measurement is semi-quantitative since it only determines flow structures, and not any tangible parameter such as velocity, temperature or pressure.

1.2 Molecular Tagging Velocimetry

1.2.1 Fundamentals and Basic Applications

Due to the aforementioned limitations of particle and PLIF based measurements, new techniques for velocity measurement in hypersonic environments are needed. An alternative type of measurement technique is Molecular Tagging Velocimetry (MTV). Contrary to particle methods, MTV employs molecular tracers to measure velocity, effectively addressing the problems of particle lag due to the inherent inertia. This makes MTV attractive for high-speed flows since the molecular tracers can always follow the rapidly changing flow ac-

curately. These MTV methods are divided into two classes, seeded and unseeded. Naturally, the seeded techniques require a higher concentration of a particular molecule to be doped into the flow as a tracer. Vibrationally-excited nitric oxide monitoring (VENOM) [45] is one of these techniques. This method uses NO_2 seeded into the flow and then dissociated by a laser. A second 'read' laser is used at a time delay to visualize the displacement of the tagged volume of molecules. This is a typical process in molecular tagging - a 'write' laser is used to produce an intermediate species, and then a 'read' laser performs PLIF to measure the displacement. Another seeded technique that is similar is krypton tagging [46].

The second class of molecular tagging techniques uses unseeded measurements. Traditionally, these methods rely on using molecules already present in air as the tracers. Among these methods is Raman excitation and laser-induced fluorescence (RELIEF) and air photolysis and recombination tracking (APART). The RELIEF method uses a dye laser to dissociate oxygen and an excimer laser to track the successive motion. APART uses an excimer laser to create NO in air and then a dye laser to perform PLIF to track the NO. All four of these common methods for molecular tagging require two laser systems to perform, and typically, two directions of optical access. While they have been largely theorized and studied in lab settings, there is limited application of these measurements to hypersonic ground test facilities.

1.2.2 Femtosecond Laser Electronic Excitation Tagging and Literature Review

Femtosecond laser electronic excitation tagging (FLEET) is an MTV method requiring only one laser to perform and can be performed in air or nitrogen. Due to its simplicity and wide range of applications, it has gained popularity in the last decade for hypersonic velocity measurement. The improvement of the temporal and spatial resolution of the method, as well as practical applications of the measurement to hypersonic test sections will be the main focus of this thesis. As an extension of this technique, the use of the same femtosecond laser is investigated for tagging water molecules in femtosecond laser activation and sensing of hydroxyl [FLASH].

FLEET was first theorized and demonstrated by the Miles group of Princeton University [47], [48]. A femtosecond laser is focused into the flow with a peak intensity up to 100

TW/cm^2. The laser focus creates a region of nonlinear optical excitation, in which nitrogen molecules become ionized and eventually dissociated. As recombination begins, B-state nitrogen molecules are created. These excited molecules relax back to the ground state and release photons in the 560 nm to 680 nm range. This optical emission can exist for up to 100 microseconds and is the signal which FLEET tracks. Figure 1.3 shows a diagram of how FLEET is implemented. The femtosecond laser is focused to a high peak-irradiance in a high-speed flow. The long-lived optical emission is tracked with a high-speed gated camera and multiple frames can be captured. With a spatial calibration, the displacement of the excitation point can be used to calculate velocity.

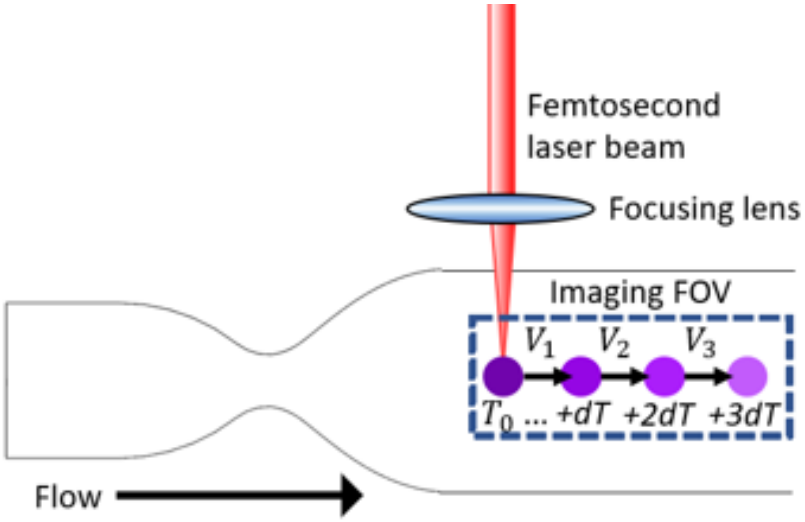

Figure 1.3. Diagram of velocity measurement with FLEET

Initial Demonstrations

The Miles group investigated the fundamental performance of the method across a wide variety of flows. In the first papers [47], [48], initial measurements of the signal lifetime in air and nitrogen environments were performed. The initial mechanisms for signal production were theorized, as well as mechanisms for oxygen quenching of the signal in air. These initial measurements were made with a relatively slow 10 Hz laser and a time-delayed camera, yet showed the potential for FLEET as a highly accurate measurement technique that could be applied very close to surfaces and in a wide range of applications. Immediately, FLEET

became an interesting technique due to its simple implementation of only needing one spatially calibrated camera and one focused laser. Since no seeding is involved, the technique can be applied to many flow facilities without hardware modification. Follow-on research work characterized the effects of pressure, temperature, and gas composition on signal levels, the achievable accuracy and precision, and the potential flow perturbations due to energy deposition, as elaborated in the discussion below.

Technique Characterization

One of the first trends to be predicted and evaluated was the signal dependence on temperature. As with many spectroscopic emission based techniques, it was observed by Edwards et al. [49] that the FLEET emission spectrum varies significantly with temperature. By using a spectrometer, the temperature of a high-speed gas flow could then be measured with up to 10% uncertainty. A limitation on this measurement is that the spectrum also trends with pressure. Calvert et al. [50] studied the effect of changing pressure on the spectrum, and introduced improved fitting methods to account for this. From initial works it was also well known that oxygen significantly decreases signal lifetime and intensity. Halls et al. [51] utilized this knowledge to make measurements of oxygen mixture fraction in flows by calibrating the signal lifetime. On this track, effects of other gas compositions were studied. Calvert et al. [52] evaluated the FLEET signal in the presence of oxygen, carbon dioxide, methane, argon, and helium. It was shown that gases such as oxygen, carbon dioxide, and methane significantly quench the FLEET emission mechanism, while argon and helium act to promote the second positive system of nitrogen and improve signal level and lifetime. Zhang et al.[53] and recommended argon as the best gas for enhancement of FLEET signal, even in small concentrations (<5%).

After understanding of the fundamental signal characteristics, studies of the accuracy and implementation of the technique became necessary. One of the most important parameters to consider is the minimum spatial resolution of the technique. Edwards [54] showed that flow velocity could be measured down to the 100 micron spatial scale. Peters [55] evaluated the precision of the technique with multiple types of cameras, magnifications, and time delays.

Without regard to SNR degradation, the higher magnifications and time delays tended to produce higher precision measurements due to a decreased impact of centroid finding error.

A few works have attempted to characterize the effect of performing FLEET on the overall nature of the flow field. Since FLEET involves energy deposition and molecular dissociation, there is evidence that there can be a small perturbation on small features in the flow field. Limbach et al.[56] performed Rayleigh Scattering to evaluate the temperature and density perturbations present after femtosecond tagging. Even at lower energies (320 μJ), significant acoustic perturbation was seen in quiescent flow. However, it was unknown how much of a real effect that this pertubation would have on the velocity measurement. New-Tolley et al.[57] performed more experiments and modeling to assess this effect. In a fully established boundary layer, there was little effect observed from the FLEET tagging. However, in the shear layer, an effective thickening was observed due to heat input.

Capability Demonstration

Many different demonstrations of FLEET have been conducted to show measurement capability. One of the first experimental arrangements was the cross-tagging method employed in [58], where two focused beams were aligned into a cross. This cross was used to measure a semi-2d velocity profile and vorticity. This was a highly specialized optical setup that was difficult to implement, however it showed the need for tailoring of FLEET to measure instantaneous spatial profiles. In the same vein, Danehy et al. [59] showed the capability of implementing orthogonal camera views to measure three components of velocity in a simplified flow experiment. A number of experiments were conducted to show boundary layer measurements [60], [61], to within 10 μm of a surface, but due to laser delivery constraints, the experiment was only conducted over a curved surface. Signal intensity and lifetime were studied in reacting environments such as Hencken Burner to evaluate the measurement applicability in flames. DeLuca et al. [62] and Zhang et al. [63] both evaluated this environment and found severely limited lifetimes in flame zones. The signal lifetime of less than 1 μs showed that FLEET is not tailored for application to reacting environments. Jiang et al. [64] developed STARFLEET, a method which uses resonant UV excitation to significantly reduce the excitation and deposition energy to minimize the thermal effect of the measure-

ment. Additionally, burst-mode lasers have recently been used to extend measurement rates to 100 kHz [65] and 1 MHz [66]. Very recently, simultaneous multi-line measurements [67] have gained some attention, but the application of this method is still forthcoming.

Wind Tunnel Implementation

The overall goal of FLEET is to make useful aerodynamic measurements in high-speed flow facilities. One of the first aerodynamic demonstrations was the measurement of velocity statistics in a sweeping-jet actuator [68]. This was still a bench-scale measurement, but showed that FLEET was capable of making measurements in a highly unsteady flow field. In recent years a small body of work has been put forth by a few research groups showing the initial application of measurements to select high-speed flow facilities including the NASA Transonic Cryogenic Tunnel (TCT) [69], [70], NASA National Transonic Facility (NTF) [13], the AEDC Tunnel 9 [20], Sandia Hypersonic Wind Tunnel [19], [71], and the Purdue Linear Experimental Aerothermal Facility (LEAF) [27]. For many of these works, the initial difficulty was in integrating the measurement system into the complex construct of the facility. After this was accomplished, aerodynamic measurements were conducted such as evaluating separation over a transonic airfoil [69], the wake behind the common research model wind [13], the wake behind a 7 degree cone model [71], and the flow over a supersonic bladeless turbine [27]. While these research efforts show significant promise, the low number of works still leaves much to be accomplished in terms of fundamental technique understanding and optimization, as well as aerodynamic application in ground test facilities.

1.3 Scientific Objectives

The previous section describes the current state of the art in FLEET measurements. While FLEET has been shown to be useful for accurately measuring velocity over a wide dynamic range and many facilities, there are still many limitations. Current commercial femtosecond laser systems limit the measurement rate of FLEET to 1 kHz, which is insufficient to capture unsteady processes in hypersonic flows. Aside from tagged crosses with limited applicability, FLEET remains a point or line measurement with highly limited spatial extent.

While there have been a few applications to wind tunnels at NASA, Sandia, and AEDC, the body of work still remains limited. Lastly, while FLEET is well poised to measure velocity in inert environments, it is not suited for application to high-speed facilities that involve combustion.

The overall outcome of this thesis is to provide the technical advancements necessary to achieve useful data in relevant aerodynamic environments. This is a multi-faceted problem requiring investigation, demonstration, and characterization of a number of new capabilities. A goal is to improve the spatiotemporal fidelity closer to that of PIV withouth the challenges of particle seeding. With PIV, measurements can be made at repetition rates of 1 MHz [72], with large spatial extents, and precision better than 2% [73]. High-precision and spatiotemporally resolved velocity data can be highly insightful to aerodynamics researchers. CFD simulations can be either validated or adjusted with confidence using such rich information. Direct comparison of test articles across flight conditions and small design iterations can then be obtained. Spatial fields such as turbulent kinetic energy, shear stress, and vorticity can be measured to gain understanding of coherent flow structures. Lastly, modal analysis such as POD and DMD are available which can give a physical representation of the spatial and temporal energy content of the flow field.

Approaching the capabilities listed previously is the goal of this thesis. To achieve this outcome, three sub-goals are laid out here:

1. Advances in spatial extent of the measurements
2. Extension of molecular tagging capabilities to a wider range of flow conditions
3. Application of aerodynamic measurements in ground test facilities

These sub-goals are approached individually and examined at the current available technology level. Each sub-goal has it's own chapter in this thesis. Possibilities for further improvement and combination of these sub-goals is discussed where applicable.

1.4 Research Methodology

A number of technical challenges were addressed for each avenue of advancement and are included in a brief summary as follows:

1.4.1 High Spatial Extent Measurement Challenges

The desire to increase the instantaneous spatial extent to two-dimensions was motivated by the need to measure spatial velocity gradients and capture the dynamic behavior of high speed flows. The measurement of these gradients in an instantaneous fashion can be applied toward understanding of vorticity, shear stress, spatial velocity correlations involving turbulence properties, and flow feature tracking.

To achieve this advanced implementation of FLEET, a number of new optical arrangements including manual beamsplitting, microlenses, and holographic beamsplitting were evaluated. The desired result of the method was to achieve laser excitation in a gridded pattern, which would be adjustable in both size and standoff distance, with a high degree of uniformity in SNR between grid points. In Chapter 2, the microlens and holographic beamsplitting methods are demonstrated for spatially resolved measurements. The microlens system pooved to not be sufficient according to the previous requirements of adjustability and uniformity. The holographic beamsplitting method was devised and evaluated following this attempt as an avenue for two-dimensional FLEET measurement with improved applicability, adjustability, and precision. A demonstrational experiment was conducted to prove the optical arrangement can achieve the requirements of ease-of-implementation, adjustability, and optical access. With higher-dimensional FLEET data, the processing method needed to be improved to provide identification and isolation of individual grid points, velocity vector spatial reconstruction, velocity field interpolation and flow property calculation such as vorticity and shear stress.

1.4.2 Extension of Molecular Tagging Capabilities

Considering that hypersonic flows can be inherently unsteady at high frequencies above 100 kHz, there is a need to increase measurement rates as far as possible. Boundary layer

and shock unsteadiness play a large role in determining the stability of a hypersonic field and the resultant aerodynamic effects such as heating, drag, and vibration on a flight system. The processes warrant work into improving the measurement rate of FLEET to 1 MHz.

Conducting FLEET at high repetition rates up to 1 MHz required a laser system capable of producing sufficiently high energy pulses at the desired measurement rate. This system was already in development for work in MHz-rate CARS thermometry [74], and was leveraged here improve FLEET capabilities. First, an understanding and optimization of the minimum energy required to perform FLEET was studied in a supersonic jet. The lowest energy threshold was used to inform the development of the high-speed laser system. From the original laser architecture, modifications were made to maximize the per pulse energy output. This allowed demonstration of 1 MHz FLEET capabilities.

In addition to increasing the measurement rate of femtosecond laser tagging, there is a need to extend the applicability to other gas compositions other than inert flowfields. FLEET has been previously demonstrated in combusting environments to an extent [75], but the signal levels and lifetimes are not well suited for reliable measurements. An extensive literature search of molecular tagging methods applied to various environments was conducted. Hydroxyl tagging velocimetry [76] was highlighted as a method for unseeded velocimetry in flames. The laser systems to conduct the original version of the technique are not common in most research facilities, including Purdue University. Therefore, planning and demonstration of an extension of the method named Femtosecond Laser Activation and Sensing of Hydroxyl (FLASH) was conducted leveraging laser platforms that are widely available. After this demonstration and initial characterization, the method was applied to measure velocity in the exhaust of a Rotating Detonation Engine (RDE), a flow-field that displays many of the challenging features of hypersonic flows, including high velocities and shock waves.

1.4.3 Aerodynamic Application in Test Facilities

Some pioneering work has been performed to apply FLEET to relevant flow facilities such as in [20], [69], [71] among others, however the body of work still remains somewhat limited. In Chapter 4 the demonstration of aerodynamic measurements of complex flow fields such

as those in a supersonic bladeless turbine passage and in the BAM6QT hypersonic ground test facility are shown.

There are many facility and test article specific concerns while conducting applied FLEET measurements in supersonic wind tunnels. Often times the facility cannot be modified to facilitate the measurement, and therefore optimization and careful planning of the optical arrangement must be considered. Specific issues that must be planned and evaluated in advance are: (i) the facility operating pressure, which impacts the signal levels of the measurement, (ii) optical access level, which determines where beams can be brought in and focused to make measurements, (iii) test article flow physics, which determine what areas to target when making measurements, and (iv) window quality and thickness, which affect how much laser energy can be used in the experiment. Addressing all these issues together presents a significant challenge in planning measurements in a ground test facility. Oftentimes rigorous planning is conducted that includes computer modeling of the optical access to determine if there is enough clearance for lasers and cameras, low-pressure benchmarking to determine if measurements are possible at simulated facility conditions, and experimental mock-ups to mimic the camera and optical settings to verify any problems before large amounts of resources are used in the real experiment. Even when the measurement technique succeeds and produces results, careful planning with respect to diligence in optical alignment, calibration, and data recording is necessary to provide reasonably low uncertanties such that the results provide a useful end product.

2. ADVANCES IN THE SPATIAL EXTENT OF FLEET

2.1 Motivation

The current state-of-the-art of FLEET measurements consists of measurements generally made at one point at a time. With a longer focal length lens, a line can be tagged which gives the ability to measure one-dimensional velocity along a linear profile. As the tagged point or line travels downstream, it can be repetitively imaged to provide continuing measurements at different locations in the flow field. This represents Lagrangian tracking of the same initial packet of molecules in the flow and is in contrast to spatially resolved Eulerian measurements where information about multiple locations in the flow can be measured simultaneously. Figure 2.1 shows a composite image of FLEET data taken along a tagged line. The middle of the line shows a higher velocity than the periphery of the line. This is sufficient to capture a streamwise velocity gradient, but due to the nature of the processing methods necessary, two-dimensional velocity cannot be measured on this line. As the line travels downstream, the velocity profile may change, but since this measurement develops over time, it does not represent an instantaneous spatially resolved measurement. The goal is an unseeded molecular tagging method that can create time histories of flow parameters such as vorticity and shear stress, as well as measure the spatial variations in velocity used to determine flow coherence length scales associated with turbulent fluctuations. Modal analysis methods such as principal orthogonal decomposition allow for the recognition of coherent structures and modes underlying the dominant energetic structures of the flow fluctuations. Figure 2.2 shows an example of time-resolved tracking of coherent wake structures of vorticity that can be obtained using a spatiotemporally resolved technique such as PIV.

For alternate molecular tagging methods, a grid pattern of crossed lines is created in order to develop an instantaneous method for measuring velocity gradients. Reference [78] shows this approach, and Figure 2.3 shows the corresponding result. While this method is promising for its ability to produce spatially resolved measurements, there are a number of limitations to employing this method for FLEET measurements. First, the optical arrangement is

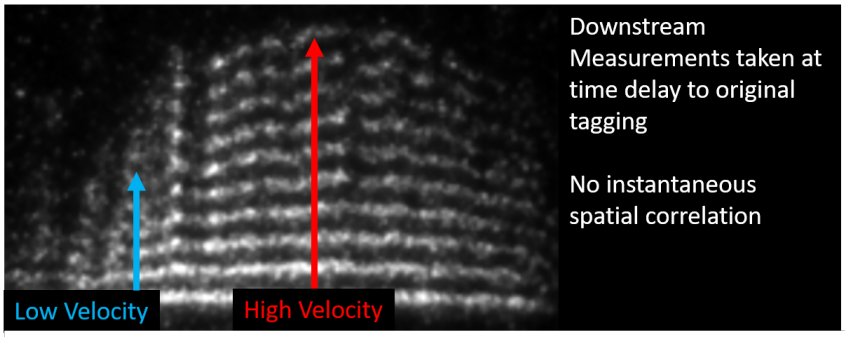

Figure 2.1. Composite of line-FLEET images allowing for for semi-spatially resolved velocity measurements

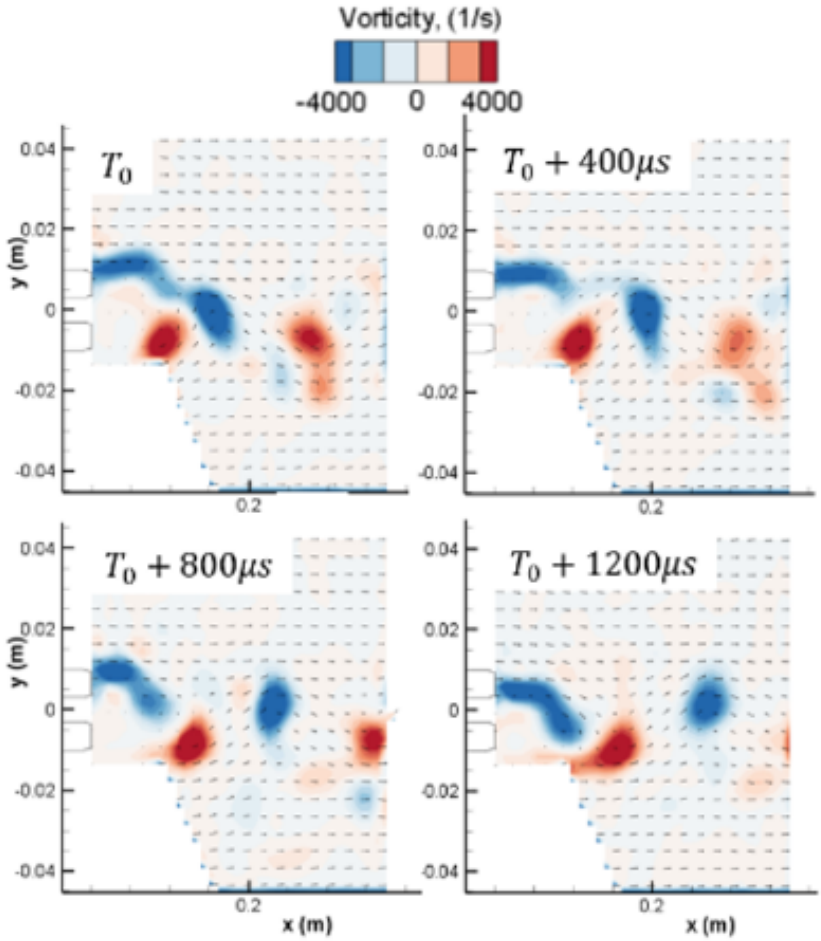

Figure 2.2. Time series of PIV measurements showing the ability to track multiple spatial flow features with vorticity [77].

rather complex. This method requires a multi-step optical beam-splitting process to create the grid, and then two directions of optical access to deliver the grid into the test section. A third direction of optical access is then needed to image the grid. In [78], this was achieved easily because the test section was a low-speed liquid flow with all optically transparent walls. However, in hypersonic test sections, this is generally difficult to achieve. A second limitation to employing this technique for FLEET is the laser energy concern. To perform FLEET, oftentimes a millijoule or more is needed per excitation point. Relatively high power femtosecond laser platforms in use can only produce 2-15 millijoules at 1 kHz which limits the number of lines and/or the measurement rate. Additionally, the longest lines that can be drawn are only on the order of a few centimeters in length. Each of these limitations prevents this method from being effectively applied. Nonetheless, a more simplified method of producing gridded excitation for FLEET measurements is needed.

A few groups have acknowledged the need for, and attempted the development and implementation of multi-point and multi-line FLEET measurements during the course of this thesis work. To the best of the author's knowledge the first published instance of simultaneous multi-point is Fisher et al.[27], which is included in its entirety later in this work. A complex arrangement of beam-splitting optics was necessary to produce 3 simultaneous measurement points to measure instantaneous values of wall-normal shear stress.

Moving forward from this work, researchers at Sandia National Laboratories [67], have produced an initial work describing simultaneous multi-line FLEET measurements of an unsteady supersonic jet. This work utilizes a periodic mask to block portions of the incident laser to create multiple spatially separated excitation lines. In the manuscript, results are shown for spatial correlation of velocity in the downstream direction.

Since the measurement scheme in [67] tracks lines instead of points, only the downstream component of velocity can be measured. Thus, as compared to point-based FLEET measurement, this implementation is inherently unable to measure gradients in two-dimensions and flow parameters such as vorticity. Additionally, the low damage threshold of the custom periodic masks limited the excitation rate to 10 Hz to prevent ablation from the femtosecond laser. The arrangement also requires imaging and excitation to be aligned orthogonally,

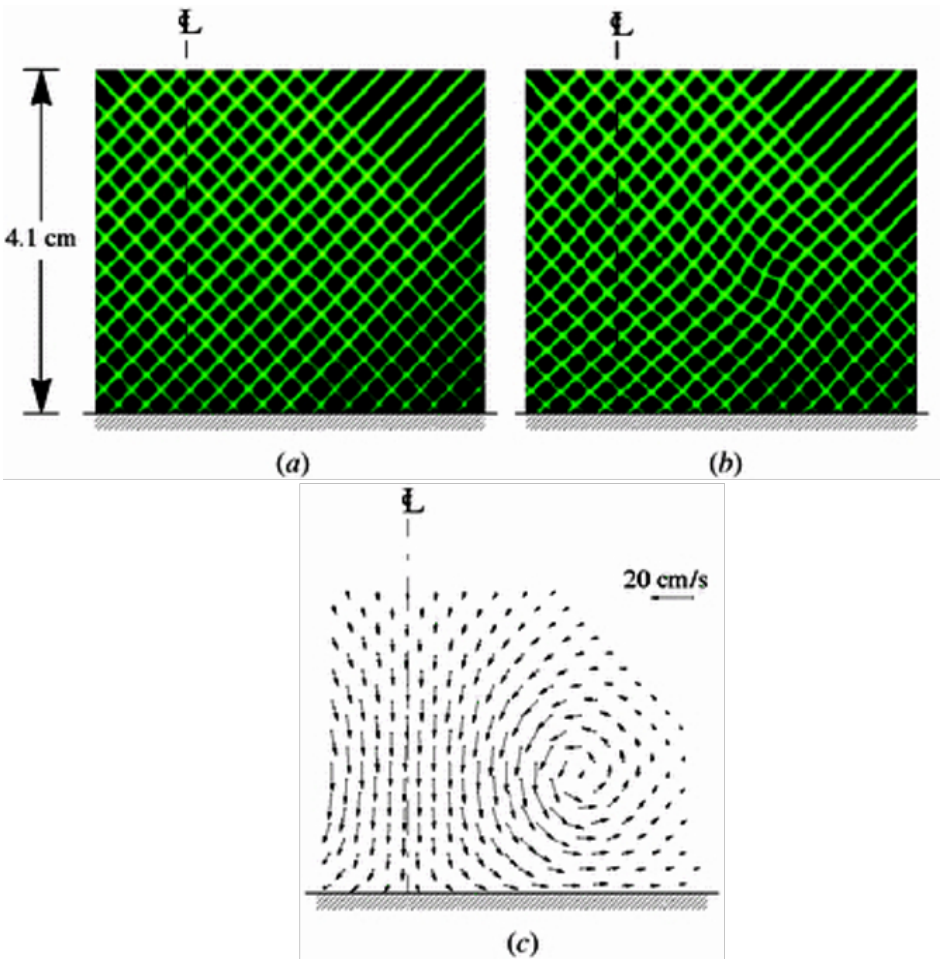

Figure 2.3. Crossed line grid used to make spatially resolved instantaneous molecular tagging velocimetry measurements [78].

meaning that two directions of optical access are necessary. The work in coming sections of this thesis aim to address these concerns using alternative optical arrangements.

2.2 Microlens Array Systems

The first grid-tagging method under investigation is the use of a microlens array system for laser focusing. This section details the development of the optical arrangement necessary to employ this technique. Preliminary results of spatially resolved measurements are shown, along with the steps needed to process the data obtained into velocity values. Lastly, the shortcomings of this method and neccessary improvements are discussed.

2.2.1 Optical Arrangement

The optical arrangement to perform FLEET with a microlens is rather simple. The lens array consists of a rectangular grid of 40 mm focal length lenses separated at a pitch of about 4 mm. To focus through all of these lenses simultaneously, the femtosecond laser is first de-focused through a negative focal length expansion lens to fill the ∼2 inch square microlens optic. Figure 2.4 (a) shows a diagram of this optical arrangement. When this system was first developed, an intensified single-shot PI-Max4 camera was used to image the grid excitation in quiescent air. With the camera running, the optical arrangement and location of the expansion lens were adjusted until the contrast and spot number were optimized. After this, ensemble-averaged data was collected to demonstrate feasibility of the method. Figure 2.4 (b) shows the initial results of this method. Promising results were obtained, as a grid of more than 6x6 points can clearly be seen. This gave justification for further pursuit of the method to make spatially resolved velocity measurements.

2.2.2 Benchmarking Experiment

To demonstrate the capability of measuring instantaneous spatially-resolved FLEET measurements, a demonstration experiment was conducted. The flow field to be investigated was a high-pressure free-jet of N_2. This flow field was chosen for its simplicity of construction and for its inherent high-shear characteristics. Figure 2.5 shows a diagram of

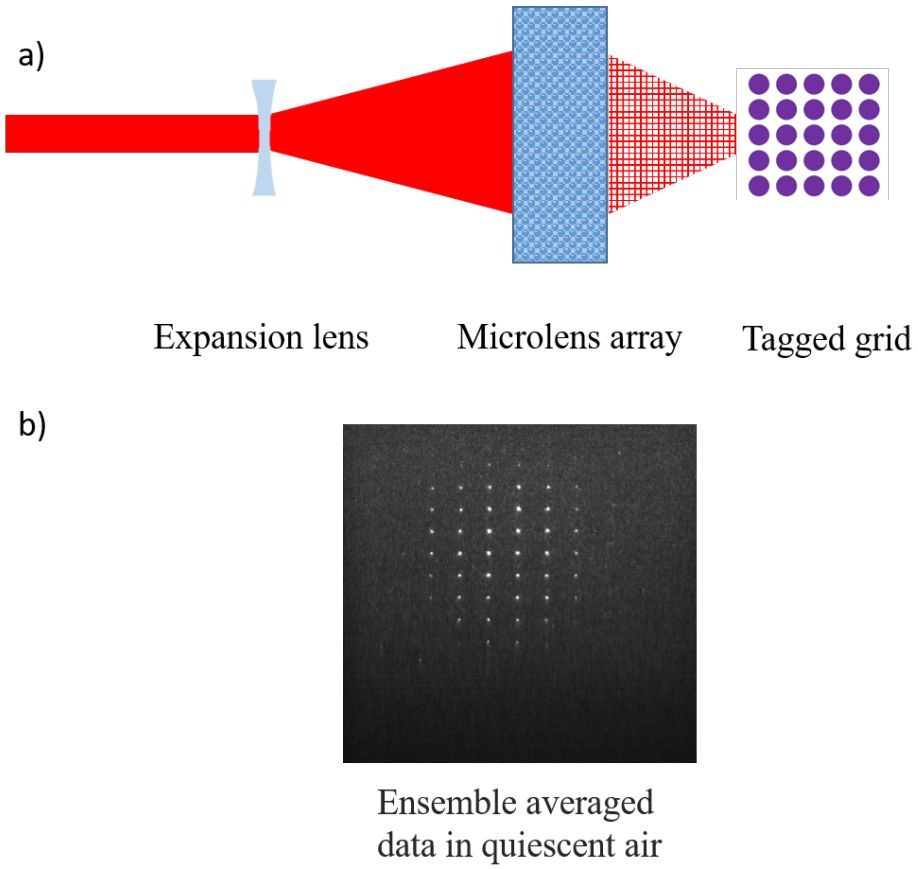

Figure 2.4. (A) Diagram of the implementation of a microlens to perform FLEET. (B) Initially tagged results in quiescent air showing possibility of a 6x6 grid of tagged points.

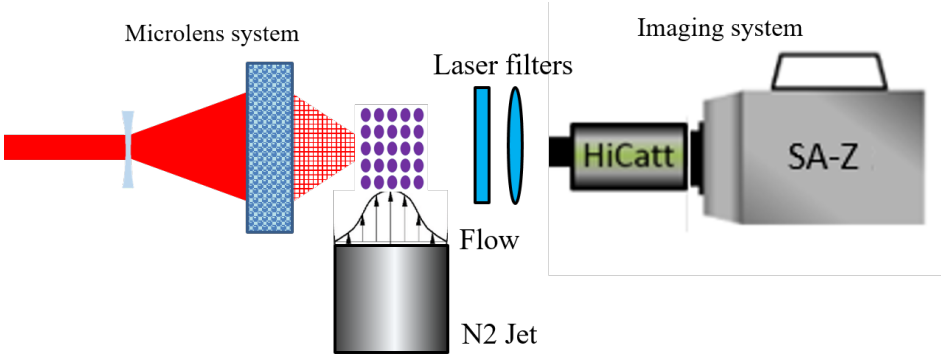

Figure 2.5. Demonstration experiment of spatially resolved measurements using microlens excitation

the setup. The same optical arrangement for gridded excitation is used as previously described. The grid is focused directly above the 25 mm diameter exit of the nitrogen jet. Since the grid appears perpendicular to the direction of laser beam propagation, the optimal location for the imaging system is directly opposite the laser beam path. To avoid directing the laser beam into the camera, the imaging system is skewed at a small angle to the beam path. Additional laser filters are placed in front of the imaging system to give extra protection in the case of stray beams. A Photron Fastcam SA-Z coupled to a Lambert HiCatt intensifier is used to collect signal. The camera is synchronized to the firing of the laser, and is used to take 5-frame bursts every laser pulse with spacing of 5 μs per image. The jet is operated at five supply pressure levels between 10 and 25 bar.

Figure 2.6 shows composite images of the signal taken at supply pressures of 10, 17.5 and 25 bar. A few immediate features can be noted. The first feature is the spatial discrepancy in the signal levels. The middle FLEET spots appear brighter than the spots on the periphery of the image. This is due to two factors. The first is the spatial inconsistency of excitation energy due to sending a Gaussian beam through the microlens. The outer spots receive considerably less excitation energy than the middle spots. The second factor is signal quenching. In the middle of the jet, the flow is pure nitrogen. When the outer parts of the jet are approached, ambient air can be entrained in increasing amounts, which decreases the FLEET signal due to oxygen quenching. A second feature of the raw composite images that

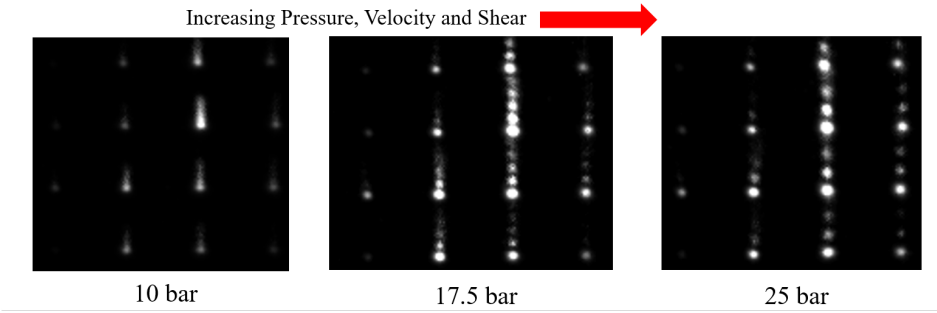

Figure 2.6. Raw composite images of multi-dimensional FLEET measurements at 10, 17.5 and 25 bar. Spatial differences in the signal levels and velocity magnitudes can be seen. This effect becomes more pronounced as pressure increases.

can be noticed is the spatial variation in velocity. The middle bright spots are characterized by higher velocity than the outer spots due to flow shear of the free jet.

2.2.3 Data Processing and Results

Multiple steps were undertaken to transform the raw data into spatially resolved velocity and ultimately shear-stress measurements. The first process was to isolate each individual excitation point. This was done manually by selecting rectangles containing only signal from one excitation point at a time. For future developments of the code, this step can be automated by using an intensity based peak finding routine and cropping the images correspondingly. Each cropped rectangle for each spot now contains five time chronicled images of the spot moving. The centroids for these spots is found iteratively. First, an intensity-weighted centroid approach is used to find a guess for the centroid location. This centroid is used as a guess input into a two-dimensional Gaussian surface fitting routine. The routine calculates centroid location, peak intensity, and goodness of fit characteristics for spot location, lifetime, and outlier analysis. Figure 2.7 details these first two steps.

After centroid locations are determined for each FLEET spot observation, a net displacement calculation is performed adaptively. Since the flow is assumed to vary smoothly, a curve fit is applied through all five of the centroid locations. In this analysis, acceleration is ignored and a linear fit for velocity is used. Higher order curve fits can be employed to ac-

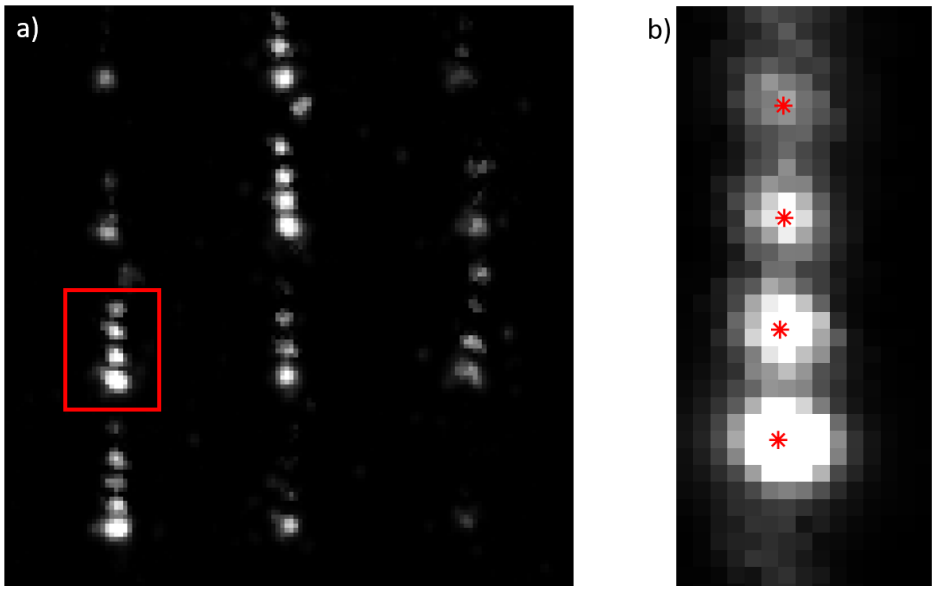

Figure 2.7. (A) Isolation of individual spots in grid FLEET image. (B) Centroid finding on spot group.

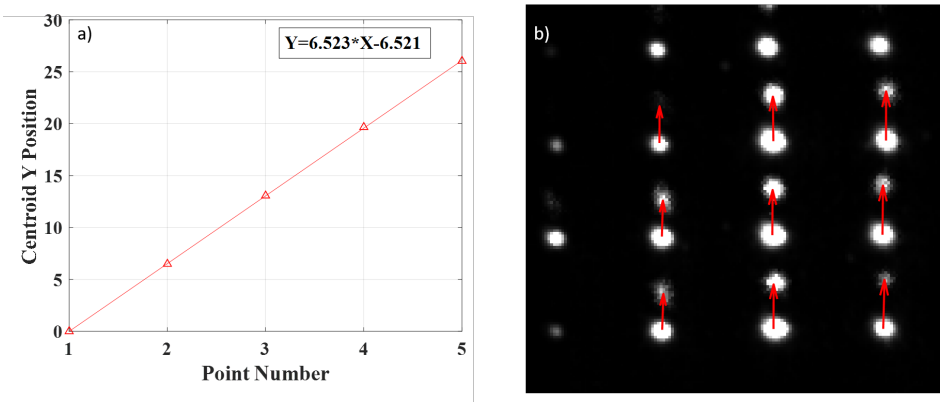

Figure 2.8. (A) Adaptive displacement evaluation with curve-fitting. (B) Displacement mapping back into original measurement position.

count for changing flow velocity. Based on the goodness of fit parameter obtained previously, individual spots can be disregarded from the curve fit if they do not meet certain accuracy criteria. This curve fit is applied in two dimensions to obtain the x and y displacement slopes for the spot motion. An example curve fit is shown in Figure 2.8 (a), which displays strong agreement to a linear velocity profile. When the displacements are obtained, they are mapped back onto their original locations in the FLEET grid, as shown in Figure 2.8 (b). This scattered grid of velocity measurements can be used to create a spatially resolved interpolation of the velocity field.

By using a MATLAB native interpolation feature for scattered data, the displacements are mapped onto a more refined and two dimensional grid. At the same time, the time and spatial calibrations of the experiment are applied so that the displacement in pixels is transformed into velocity with real-world units of m/s. With this, a clear spatial variation is seen in the resulting data. Figure 2.9 (a) shows three examples of instantaneous velocity fields and the time-averaged field as well. The time-averaged field shows a linearly varying velocity increasing from left to right in the flow. This is also captured in the instantaneous measurements with the magnitude and location of the gradients changing slightly between observations, indicating high levels of flow unsteadiness. Figure 2.9 (b) shows an instantaneous result of calculating the shear stress contour of the flow field. The left side of the image shows a high value of positive shear-stress due to the increasing velocity in this region. The

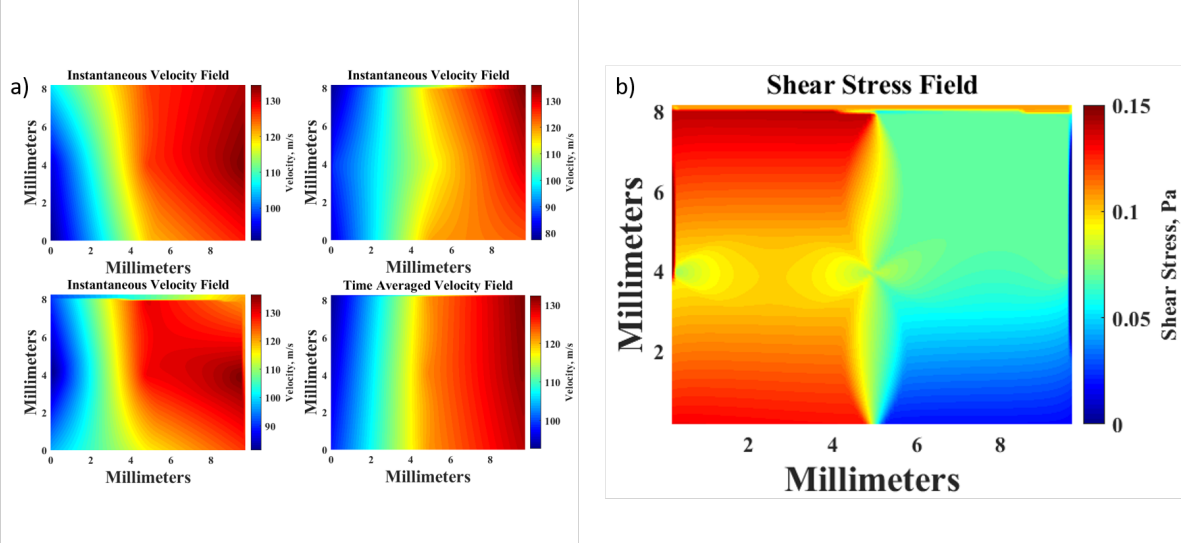

Figure 2.9. (A) Instantaneous and time-averaged velocity contours after spatial calibration and interpolation. (B) Spatial map of shear stress calculation

bottom right portion of the image shows almost no shear due to a mostly constant velocity, but downstream the shear increases slightly, representing a small flow acceleration.

With this experiment, the first demonstration of instantaneously spatially resolved velocity measurements with FLEET has been performed. Using the results, instantaneous shear stress fields can be calculated. There are a number of shortcomings of this excitation method, which are described in the next section, with improvements to gridded FLEET tagging process described later in this chapter. After development of improved excitation methods, uncertainty propagation is discussed along with advanced data processing methods.

2.2.4 Shortcomings of Microlens Method

There are many shortcomings of the microlens method and data processing employed in the previous section, which are the subject of continued improvement work. With regard to the processing code, the analysis function can be improved for higher levels of automation in spot finding. Additionally, the script can be streamlined and parallelized further as it takes a significantly larger amount of computer resources compared to traditional FLEET analysis. Since signal levels and quality can vary extensively between excitation points and

shot-to-shot, more robust outlier handling and adaptive displacement calculation becomes necessary.

With regard to the optical arrangement, the microlens system is a good starting point for demonstration, but its full implementation is limited. The first problem is with the point-to-point signal inconsistency. Due to the nature of focusing a Gaussian profile beam through many adjacent lenses, more laser energy is concentrated in the middle of the grid, meaning that signal is much higher from these spots. While the lower energy spots are still sufficiently luminous to be tracked, their contrast with respect to the bright spots is too low to be observed. The result is that the camera can only be set to capture the brightest spots, and if the gain is increased to capture the dim spots, significant saturation occurs in the bright spots which will damage the imaging system. Figure 2.10 shows this phenomena in a graphical sense. In the initial image, a grid of 12 points can be observed, although the middle spots are much brighter. After 5 microseconds, a few of the corner spots have disappeared completely because they are too dim. As the delay continues to increase, more peripheral spots disappear at different rates. This nuance to the microlens poses a large challenge to the proper implementation of gridded data. Although the laser possesses enough energy to produce more than 36 points, distributing this energy evenly between points is challenging with this method.

There are a few other challenges with the implementation of the microlens for applied measurements. Among these are the focal length of the lens. For each microlens system, there is a fixed focal length. In the demonstration experiment the focal length is 40 mm because this is a practical distance for small scale experiments and because it was the easiest microlens to procure from an off-the-shelf supplier. To make measurements in wind tunnels, focal lengths up to 300 mm or larger are generally required. Microlenses in these distances are not easily available and might need to be custom ordered. Additionally, the separation of the lenses in the optic determines the separation of the interrogation points. To refine the grid spacing, completely new optics need to be used. As the microlens optics get smaller in order to produce smaller spot separations, the quality of the lenses and thus the quality of the FLEET focusing will necessarily decrease. For a highly optimized experiment, the microlens works well to perform grid measurements, but the outlook for applied wind tunnel

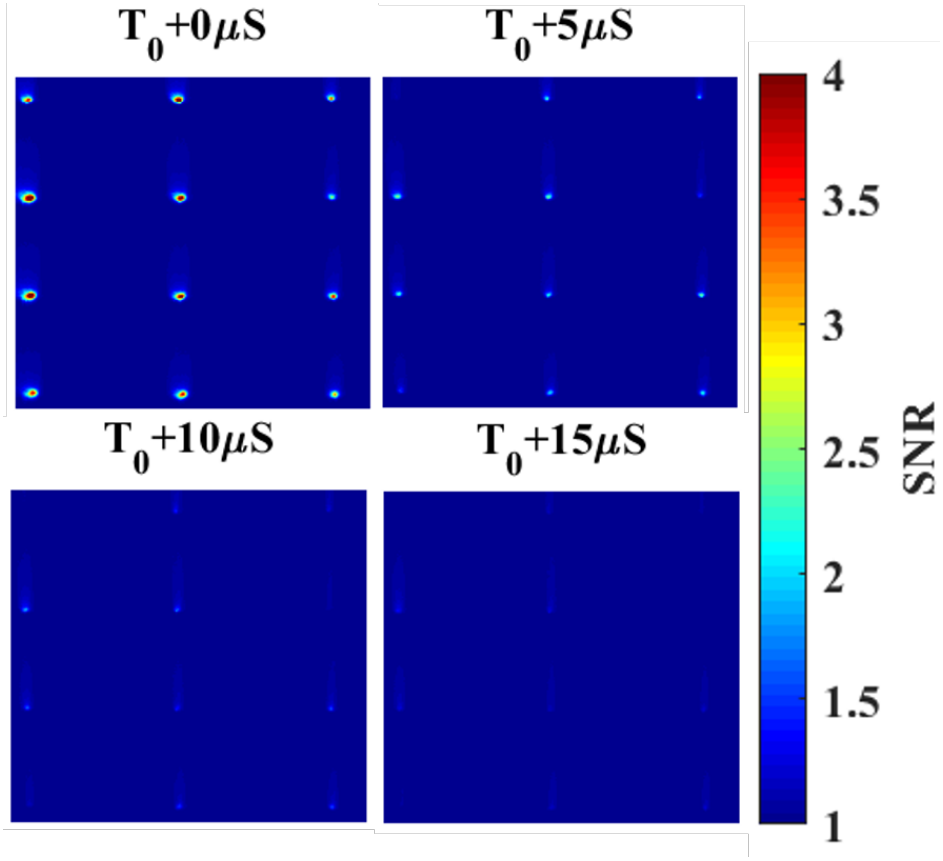

Figure 2.10. SNR of all grid spots as a function of delay. Peripheral spots decrease to the noise level earlier than middle spots.

measurements is not promising. A new optical arrangement is proposed and explained in the next sections.

2.3 Diffractive Optical Element Beamsplitters

2.3.1 Motivation

The three main shortcomings of the microlens method are spot intensity consistency, adjustable focal length, and adjustable spot separation. To counter these problems, the new proposed approach for multi-dimensional FLEET tagging involves using a holographic beamsplitter to produce a grid of laser beams and a separate focusing optic to focus each beam to a point. The holographic beamsplitter is a type of diffractive optical element that takes an input beam and divides it into an NxN grid of diverging beams. Diffractive optical elements are constructed of thin micro-patterns which control the phases of light propagation. Almost any structured light pattern can be created using a diffractive optical element with high efficiency and energy. For a holographic beamsplitter, output beams are exact copies of the input beam aside from their energy and direction of travel. By using special design methods, the number and propagation direction of the output beams can be chosen. Figure 2.11 shows the typical implementation of a holographic beamsplitter to produce a focused grid. For our application, the beamsplitter produces a 4x4 grid of beam copies with a small divergence angle. By placing a focusing lens in front of this beam array, a focused grid is produced at the focal point of the lens. To control the focusing distance the focal length of the lens can be changed, which is straightforward to modify since many variations of focusing optics are widely commercially available. The grid resolution can be controlled by altering the distance between the beamsplitter and the focusing lens. This optical arrangement gives full control over the grid parameters making it attractive for research and application to a wide variety of test sections.

The results for this section are summarized in a journal article for submission to Applied Optics entitled '*Grid-FLEET for instantaneous spatially-resolved and single-ended velocity measurements*', which is adapted into the thesis in the following section:

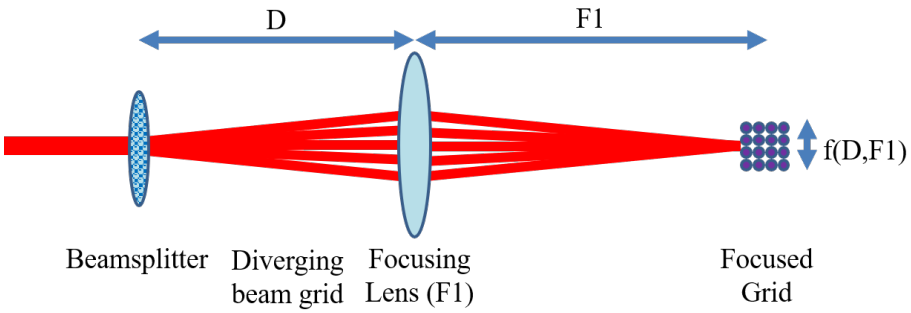

Figure 2.11. Diagram of implementation of holographic beamsplitter to produce a grid of focused points.

2.3.2 *Grid-FLEET for instantaneous spatially-resolved and single-ended velocity measurements*

Abstract

A novel optical arrangement for performing single-shot FLEET across a 4x4 grid (Grid-FLEET) is described. The optical arrangement includes a diffractive optical element beam splitter to produce a grid of laser beams in a simplified and efficient manner. Verification of the optical element with respect to beam forming is described. Grid-FLEET measurements achieve a similar precision to previously described single-point FLEET measurements, with an improved spatial extent. Velocity results in a laminar flow, and around a sharp corner are shown. With gridded measurements, instantaneous vector fields and spatial velocity gradients can be analyzed to gain deeper understanding of flow physics.

Introduction

Femtosecond Laser Electronic Excitation Tagging (FLEET) [47] is a molecular tagging velocimetry method used in unseeded gaseous air and nitrogen flows. FLEET employs a focused femtosecond (fs) laser to dissociate nitrogen molecules to create a tracer packet. As the nitrogen molecules recombine, broadband visible emission from the packet can be imaged by a high-speed time-gated camera. Velocity is measured by calculating the relative displacement of the packet between two or more time-delayed frames. FLEET is commonly performed at 10 Hz or 1 kHz [47], [48], [79] in a single-point or line measurement arrangement although cross-based measurements [71], [80] have been made as well. Recent advancements have made use of interference masks to characterize single-component velocity over the axial extent of an overexpanded supersonic jet.

FLEET is attractive for use in velocity measurement due to its simple implementation, without seeding and needing only one laser. However, the frequency content and spatial extent of measurements possible with FLEET are currently limited in comparison to other measurement techniques. To combat frequency limitations, burst-mode femtosecond laser technology [74] has recently been used to demonstrate FLEET at MHz rates [66]. Methods such as Particle Image Velocimetry (PIV) [72], Krypton Tagging Velocimetry (KTV) [46],

Hydroxyl Tagging Velocimetry (HTV) [81] allow for instantaneous measurement of velocity across two or even three spatial dimensions, while FLEET currently can only measure across zero-dimensional (point) and one-dimensional (line) extents. Repeated imaging of the same FLEET excitation can extend the streamwise extent of measurements [27], however these measurements lack instantaneous correlation because of the time-delay between images. Attempts to use traditional beam-splitting methods [27] to make instantaneous multi-point measurements has been limited due to complexity of alignment, spatial constraints, and propagation losses through the large number of optical components.

This work presents a novel optical arrangement to perform simultaneous FLEET measurements over a 4x4 grid (Grid-FLEET) to instantaneously resolve two-dimensional velocity gradients. The arrangement consists of a diffractive optical element beam splitter to allow for in-line creation of laser grids with low complexity and limited propagation losses. In addition to the improvement in spatial extent, the arrangement allows for the measurement to be conducted in a single-ended manner with only one direction of optical access. By selecting an alternate diffractive optical element or focusing lens, the number of spots, grid spacing, and stand-off distance can be adjusted according to experimental needs.

Background and Experimental Setup

The successful implementation of measurements in this work relies on proper operation and understanding of the diffractive optical element (DOE) beamsplitter. The basic operating principle for the DOE is an element which takes a collimated input beam, and outputs a set of beams with pre-designed separation angles and intensity distribution. Aside from propagation angles and intensity, characteristics such as beam size, shape, divergence, and polarization remain the same compared to the input beam. The individual beams are the result of diffraction orders created by stacking layers of periodic gratings to form the optical element. By changing the properties of these layers, a large variety in output beam combinations can be created. Figure 2.12a shows an overview of the DOE operational principle. In this work, a 1" diameter 4x4 DOE (Holo/Or MS-696-800-Y-A) with a separation angle of 0.33and an overall efficiency of 76% is utilized. Overall efficiency in a DOE refers to the

percentage of laser energy present in the desired diffractive orders rather than undesired or parasitic orders. The energy uniformity between individual beams is quoted at <3%.

In order to characterize the DOE in terms of laser grid spacing, multiple combinations of single and dual-lens systems with effective focal lengths between f = + 100 mm and f = + 300 mm were used to create Grid-FLEET excitation in quiescent air. The separation of individual grid points can be predicted by the formula: D=f*tan(α), where D is the spot spacing in mm, f is the effective focal length in mm, and α is the separation angle of the DOE. Figure 2.12b shows an example of an ensemble-averaged Grid-FLEET image in air used to assess grid uniformity and spacing. All 16 excitation points are well resolved and suitable for velocimetry. Through spatial calibration of the camera and centroid finding, the grid separation can be measured. Figure 2.12c shows this result as a function of the system effective focal length. For each data point, 100 images from FLEET in quiescent air are averaged. The analytic formula prediction is shown with a dashed line, and the individual data points are shown as red triangles. The data shows convincing agreement to the predicted value. This gives conclusive evidence that the DOE functions as designed, and if alternate grid spacing or number of spots is desired, the necessary optic can be ordered from the supplier. Figure 2.12d shows binned intensity profiles of each row of the FLEET grid from ensemble-averaged data. From this, it is clear that the middle two points in rows 2 and 3 have the highest overall intensities. In the periphery of the grid, the intensity begins to decrease. The least intense Grid-FLEET points exist at the corners of the grid. The reason for this discrepancy in intensity is spherical aberration. Since the outer beams pass through the focusing lens further away from the centerline, they do not focus as well and thus create dimmer FLEET emission.

After confidence was gained in the general operation of Grid-FLEET with the DOE, a velocimetry demonstration experiment was conducted. Figure 2.13 shows the configuration used in this experiment. To produce the high-energy laser pulses, a 6.3 mJ, 800 nm, 80 fs Ti:sapphire laser (Spectra Physics Solstice:Ace) was used. With an f = + 300 mm focusing lens, FLEET has been performed with energies as low as 320 μJ in an individual beam [82]. With the full available energy of the femtosecond laser divided across 16 beams, per-beam energy is estimated to be 390 μJ, which is above the lower threshold for performing the

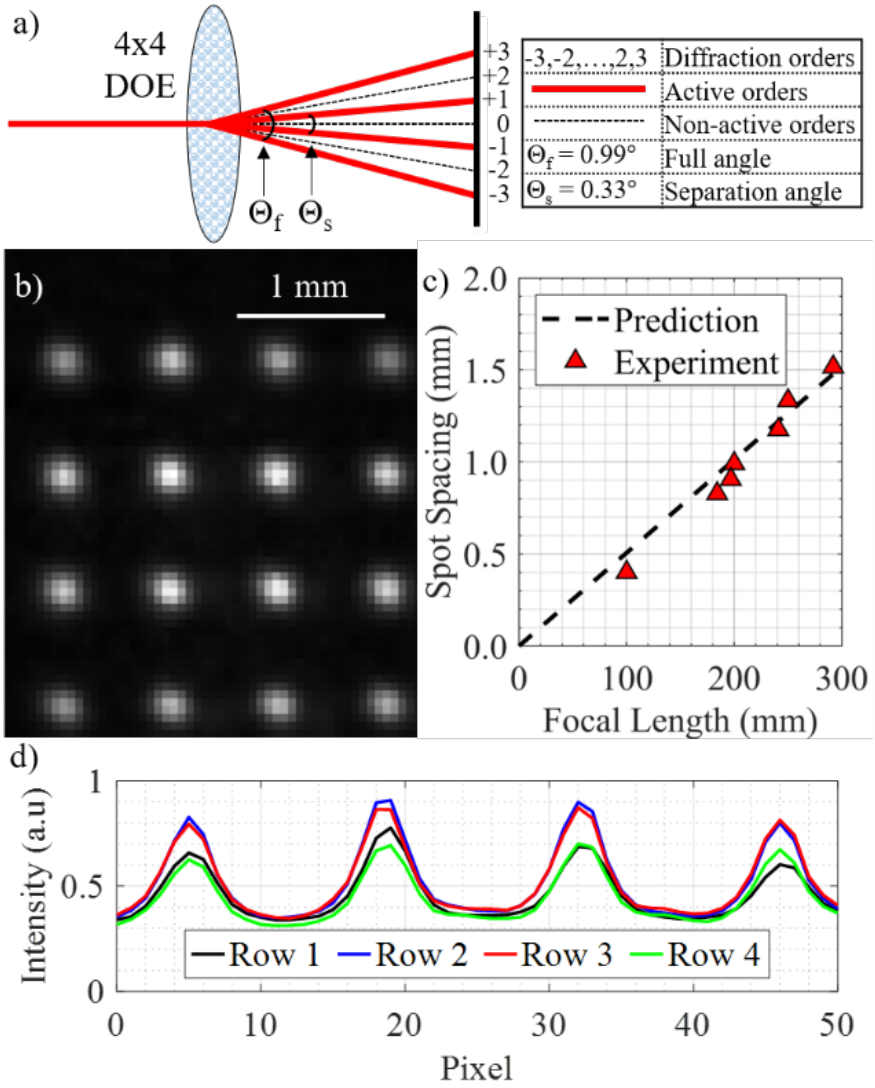

Figure 2.12. (a) Operating principles and relevant parameters for 4x4 diffractive optical element (DOE), (b) ensemble-averaged image of Grid-FLEET signal in quiescent air, 6.3 mJ, 10 mm input beam, 200 mm focusing lens.. (c) Experimental verification of grid spacing against focusing length standoff distance, (d) binned intensity profiles of Grid-FLEET rows from image in (b).

FLEET diagnostic. The repetition rate for the laser system is 1 kHz. Infrared-reflective mirrors (Thorlabs BB1-E03) guide the beam to the experiment. The beam travels through the DOE and forms into a 4x4 grid of beams with divergence angle of 0.33. After the beam-splitting element, all beams in the group travel through the same 2" (50.4 mm) diameter f = +250 mm plano-convex focusing lens to resemble stand-off distances required for high-speed flow facilities at Purdue University [66]. A short-pass mirror (Thorlabs DMBP740B) with a cut-on wavelength of 740 nm reflects the beam such that the focal plane lies at the centerline of a 2" (50.4 mm) exit diameter nitrogen-fed laminar flow facility. The supply pressure of the facility can be adjusted from 0-17 bar to create freestream velocities of 0-61 m/s. A simple test article mount allows for positioning of obstacles such as a 90 corner in the flow to create spatially varying velocity fields. The 4x4 grid of points is imaged by a CMOS camera (Photron Fastcam SA-Z) coupled to a high-speed intensifier (Lambert HiCatt, GaAsP Enhanced Red Phosphor). The 740 nm cut-on of the short-pass mirror transmits most of the broadband FLEET signal so the camera can image the movement of the grid. This mirror allows the measurement to be taken on a single-ended form factor requiring only one direction of optical access. A short-pass filter with a 775 nm cut-on further isolates the imaging system from possible exposure to the laser beam. An 85 mm lens with an 8 mm extension ring and an f-number of 2 gives the imaging system a magnification of 20.2 pixels per millimeter, with an image size of 384x384 pixels (19x19 mm). For every laser pulse, the imaging system takes 15 frames of the Grid-FLEET signal motion at 100 kHz, with an exposure time of 1 μs, and an intensifier gain of 65%.

Data Processing

To measure velocity, the centroid locations of each individual FLEET spot must be found reliably. For conventional FLEET, centroid finding can be performed on the whole image in one step since there is only one spot present. In the gridded images, centroids for all 16 spots must be found separately. To perform this step, the spots are isolated from one another. A two-dimensional peak finding algorithm is used on the ensemble-averaged images to find the most likely position of each Grid-FLEET spot. An isolation region of 10x10 pixels around each nominal spot location is created. To perform the centroid finding steps for all the spots

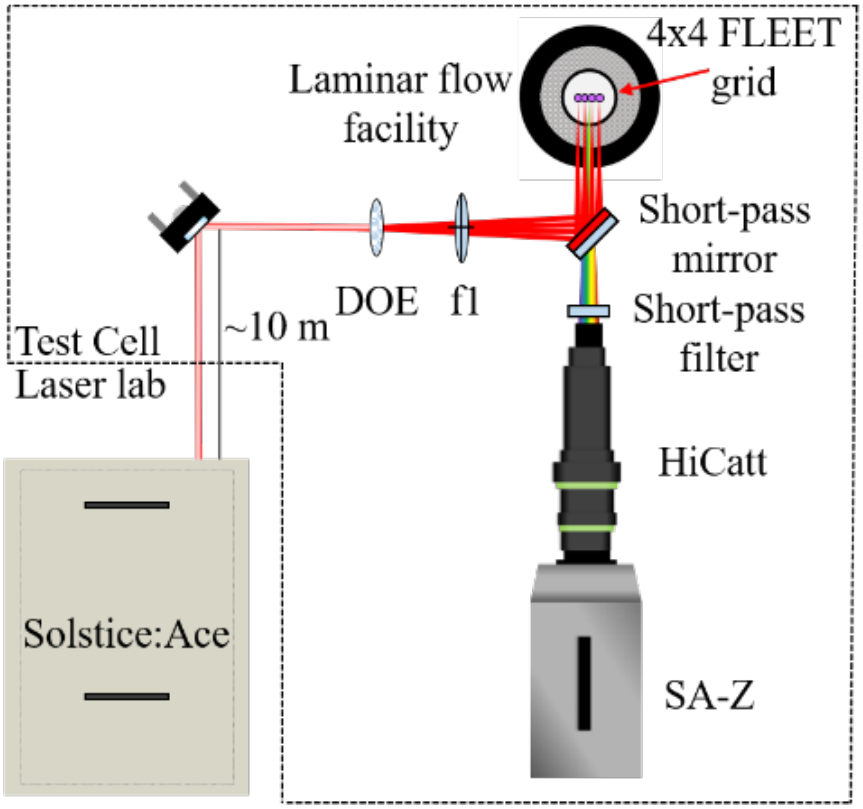

Figure 2.13. Experimental setup for conducting grid-based FLEET velocity measurements. DOE: Diffractive optical element, f1: f = +250 mm lens.

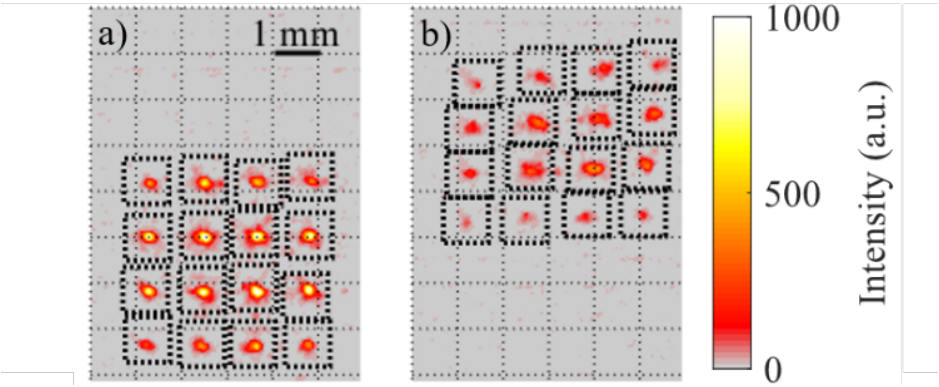

Figure 2.14. Single-shot raw signal at (a) T_0 , (b) T_0 +60μs,. Spot isolation regions shown as dotted rectangles.

in the instantaneous images, only pixel intensity inside these isolation regions is considered. Figure 2.14a shows an instantaneous image of the non-displaced grid, and Fig. 2.14b shows the same grid after a 60 μs time-delay. The dotted rectangles in these images represent the isolation regions that are used for centroid finding. Between the images in the pair the grid can be seen to skew due to the non-uniform velocity field. Due to aberration in the outer beams as previously mentioned, the SNR is considerably decreased in the corners of the FLEET grid.

For each isolation region, a two-step centroid finding process is invoked. The first step is an intensity weighted centroid approach as described in [27]. This step serves as the input guess to a least-squares Gaussian surface fitting algorithm. The fitting algorithm is capable of returning x and y centroid locations, predicted peak intensity, spot size, and goodness of fit parameters. To identify and discard outliers, two parameters, δ_c, the difference in predicted centroid location between the two methods, and R^2 , the correlation coefficient from the surface fit are used. If the either threshold δ_c >0.75 pixels, or R^2 <0.8 are met, the individual spot is discarded as an outlier. A valid FLEET point and outlier FLEET point are shown in Fig 2.15a and b, respectively. While the centroid agreement in Fig 2.15b is strong, the spurious intensity in the lower right corner of the image causes a larger disagreement between the raw data and the Gaussian fit. Therefore, this data point is discarded.

This centroid finding is performed for all individual spots for each image. After this step, a dot-target camera calibration is used to transform the pixel locations into real-world

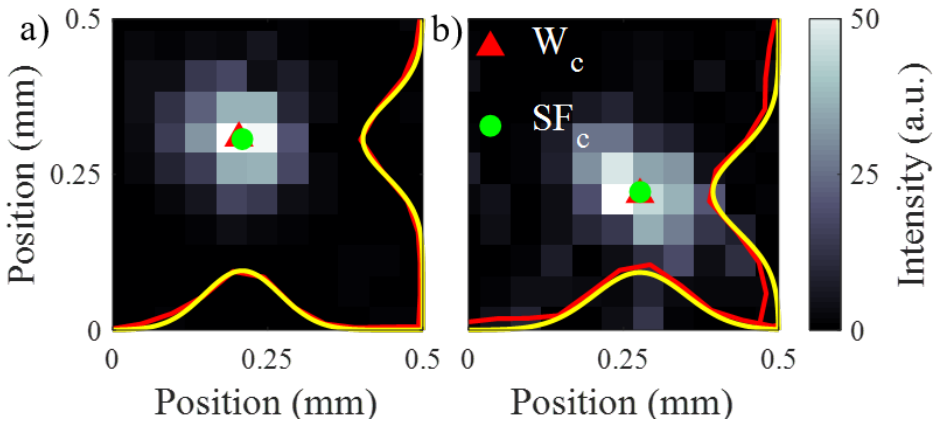

Figure 2.15. W_c: intensity weighted centroid Location, SF_c: surface fit centroid location overlaid on (a) valid raw data: δ_c=0.11 pix, R^2=0.96, (b) outlier raw data: : δ_c=.08 pix, R^2=0.77, x and Y- binned intensity profiles for raw image and Gaussian surface fits shown in red and yellow, respectively.

coordinates. With the known time-delay of 10μs between successive frames, a simple finite differencing scheme is used to calculate velocity. For each image pair, a total of 16 velocity vectors can be measured in a 4x4 grid.

Results

With centroid finding and velocity calculation as previously described, 4x4 velocity vector sets can be obtained over a period of 150 μs in 10 μs increments for every laser pulse. Figure 5a shows a composite of selected single-shot Grid-FLEET images taken at T_0 (red), T_0+40μs (green) and T_0+80μs (blue). In Fig. 2.16b, the corresponding 10μs time-delayed images used to calculate velocity are shown. T0 represents the start time of the first camera frame, which is approximately 100 ns after the laser pulse. The motion of the grid over time appears straight and uniform, reinforcing the assumption that the flow is laminar.

Figure 2.16b shows velocity vector grids created from the image pairs taken at times of T_0+0/+10μs (red), T_0+40/+50μs (green), and $T_0$0+80/+90μs (blue). The mean flow velocity for the measurement set is 61.1 m/s, and the mean flow angle is 3.72, owing to slight rotational misalignment of the grid with respect to the outlet of the flow facility. In the single-shot vector field, the vector magnitude and direction is considerably uniform.

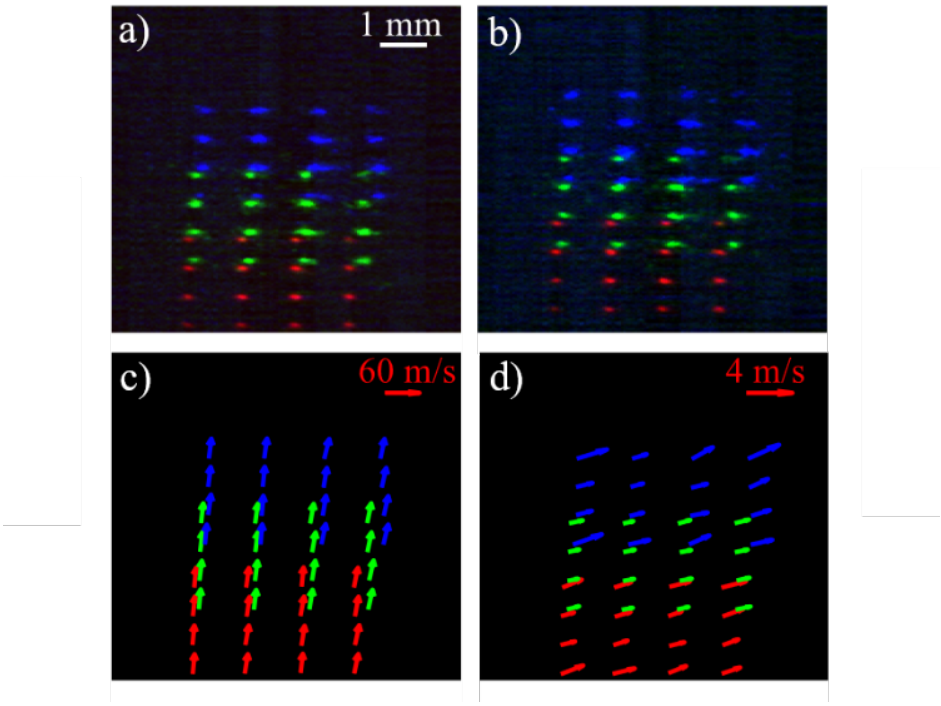

Figure 2.16. (a) Composite of single-shot FLEET images taken at T_0 (red), T_0+40μs (green) and T_0+80μs (blue), and (b) T_0 +10μs (red), T_0+50μs (green) and T_0+90μs (blue) and (c) 4x4 velocity vector fields constructed from image pairs at T_0+0/+10μs (red), T_0+40/+50μs (green), T_0+80/+90μs (blue). (c) Random error in velocity for all measurement locations shown in (b).

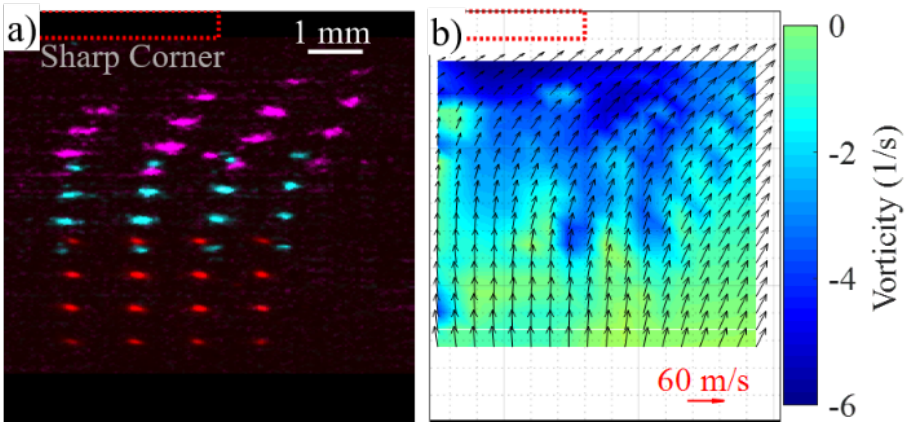

Figure 2.17. Flow around the sharp corner. (a) Composite of single-shot FLEET images taken at. T_0 (Red), T_0+60μs, (Cyan), and T_0+120μs (Magenta). (b) Pseudo-vector field created from burst-mode images of single-shot grid excitation (total acquisition time 150 μs). The position of the plate with 90 corner is shown by the red dotted line.

Under the steady flow assumption, the standard deviation of the measurement set at each grid point can be used to judge precision. Figure 2.16c displays this result for the measurement points shown in Fig. 2.16b. The results are shown as vectors with length representing the magnitude of precision and directionality determining individual contribution from the x and y components of velocity. In all cases, the standard deviation in the x direction is larger than the y direction. Peters [55] describes precision improvement for increased displacement of FLEET spots, which holds true for the larger y component of velocity in this case. For the majority of the grid points, the precision is between 0.25-0.75 m/s. In the points that are toward the edges and corners of the grid, the standard deviation of measurements grows, which decreases the precision. This is due to lower SNR in these excitation points as stated earlier. Further evaluation of the optical arrangement is necessary to improve the uniformity of SNR across the extent of the tagged grid. Overall, the mean precision of measurements is 0.83 m/s, which amounts to 1.37% of the bulk flow velocity. This precision is comparable to traditional single-point and line FLEET measurements [83].

A rectangular plate with a 90 corner is placed in the flow to create a field with strong spatial velocity gradients. For this case, a composite of single-shot frames is shown in Fig. 2.17a for imaging times of T_0 (yellow), T_0+60μs (cyan), and T_0+120μs (magenta). The

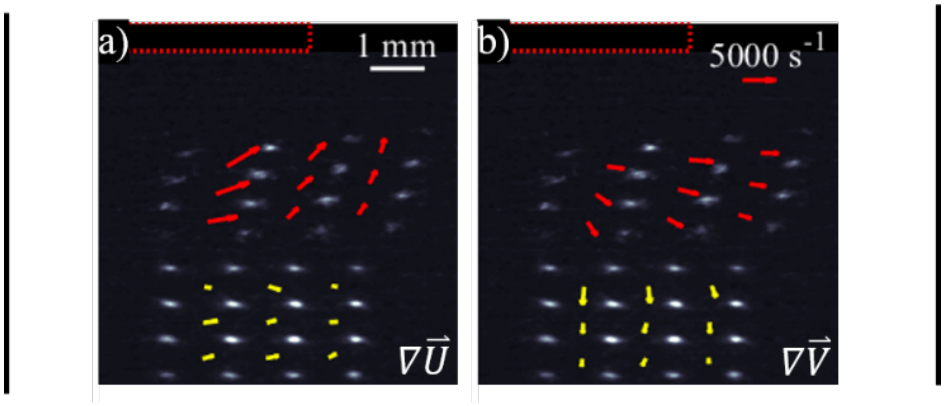

Figure 2.18. Instantaneous 3x3 gradient vector sets of U (a) and V (b). Calculated from image pairs at T_0+0/+10μs (yellow) and T_0+120/+130μs (red).

location of the 90 deg sharp corner plate is marked with a red dotted rectangle. Originally, in the T_0 measurement, the x component of velocity is near zero, and the flow is vertical. As the grid moves closer to the obstacle, the flow must turn and accelerate so the grid can travel around the obstacle. There is a strong spatial gradient in velocity due to the obstruction caused by the sharp corner.

By taking each 16 vector group acquired from image pairs between T_0 and T_0+150μs, a pseudovector field can be created. By using the location and velocity vectors from each of these measurements, the results can be interpolated with a nearest neighbor approach onto a rectangular and evenly spaced grid which represents the motion of the tagged grid over its fluorescence lifetime of 150 μs. The vector result is shown in Fig. 2.17b with background of vorticity. The initial vectors are straight, with zero magnitude in the x direction. As proximity to the sharp corner increases, the vectors turn so the flow can travel around the obstacle. The turning of the flow is shown well in the map of vorticity, with the magnitude increasing considerably in the near vicinity of the geometry.

With instantaneous velocity measurement over a two-dimensional grid, spatial gradients that relate to vorticity and shear can be calculated. As the flow approaches the sharp corner, the velocity field must change drastically to travel around the obstacle. To calculate velocity gradients, the 4x4 grid of velocity measurements is used to construct a 3x3 arrangement of quadrilaterals. With discrete velocity measurements at the vertices of these quadrilaterals,

spatial finite differencing can be applied to calculate the velocity gradient. Figure 2.18 shows this result from the T_0+0/+10μs (yellow vectors) and T_0 +120/+130μs (red vectors) image pairs as vectors representing gradient magnitude in the x and y direction. As a result of the numerical scheme, the measurements are spatially averaged across the extent of each quadrilateral, and the vectors are plotted at the quadrilateral centroids for clarity.

In Fig 2.18a, the gradient of horizontal velocity is shown. In the T_0 +0/+10μs set of values, the gradients are small due to the limited effect of the geometry on the velocity in this region. From left to right in the grid, there is a small amount of increase in the horizontal velocity, due to the flow starting to turn slightly. In the T_0+120/+130μs the velocity gradient is more pronounced. The arrows point toward the largest increase in velocity at each point, and the length of the arrow represents the magnitude of the gradient. The most pronounced gradient exists in the points toward the upper left corner of the grid. In this region, the flow must accelerate sharply to travel around the sharp corner obstacle. Toward the right of the grid in this case, the flow acceleration decreases, since the flow has does not need to turn as much.

Similar influence of the geometry on the gradient of vertical velocity can be seen in Fig 2.18b. In the T_0+0/+10μs set of values, the gradients are strictly vertical. There is a gradual deceleration of the flow which increases in magnitude with the grid approaching the sharp corner. For the T_0+120/+130μs set of measurements, the gradient becomes pronounced in the horizontal direction. Here, the points that are not directly underneath the physical geometry do not have a vertical component of acceleration. From left to right in the grid, the vertical component of velocity increases because there is decreasing blockage effect due to the corner.

Conclusion

Initial setup, characterization, data processing, and results have been described for single-shot FLEET across a two-dimensional grid (Grid-FLEET). A diffractive optical element was used as a beam splitter to produce a grid of laser beams with a simplified, space- and energy efficient, and single-ended layout. Precision for the majority of the 4x4 grid measurements is similar to previously described in single-point FLEET works. Further optical analysis is

necessary to optimize the SNR uniformity across the grid extent. With single-shot Grid-FLEET measurements, instantaneous vector fields and spatial velocity gradients can be measured to describe the overall response of the flow to physical geometry and infer properties such as shear stress and vorticity.

2.4 Further Advances in Processing for Gridded Data

This section details advances in the processing methods necessary to accommodate grid-FLEET data and improve the quality of results that are achievable. Analysis presented in this section includes: improved outlier detection based on centroid finding schemes, adaptive velocity calculation based on streamlines, multi-point precision enhancement, and higher-order flow parameter calculation.

2.4.1 Centroid-based Outlier Detection

To invoke a FLEET measurement, some form of Equation 2.1 is assumed. The t in the denominator refers to the time between acquisitions and may consist of one or multiple time intervals. The D represents the displacement that the FLEET spot travels during image acquisition.

$$V = \frac{D}{t} \tag{2.1}$$

From the simplest single-point finite differencing schemes to curve or path fit multiple observations of FLEET spots, one aspect of data processing is always necessary: centroid finding. For any single image of a FLEET spot, the centroid location of the signal must be found. Once the images have been transformed into centroid locations, any number of displacement calculation methods may be invoked.

In Fisher et al. [66] and Chapter 3, simple and unreliable centroid-finding methods are originally described. Many of these methods are biased due to their tendency to require intelligent pre-processing or to skew toward noise in the image. Later in the work, surface fitting is invoked as the method-of-choice for centroid finding. For surface fitting, the FLEET spot is assumed to fit perfectly to a theoretical surface such as Gaussian [66] or pseudo-Voight

profiles [20]. These profiles are theorized as a result of the Gaussian nature of the input laser beam, in combination with the motion of the signal as it travels and expands in the flow. Surface fits are desirable because they give an analytic representation of the signal which can be interrogated for parameters such as centroid location, signal shape, peak intensity, and quality.

For much of this work, a two-dimensional Gaussian fitting function is used to analyze FLEET data. This function gives outputs of x- and y- centroid location for calculation of displacement, peak intensity for calculation of SNR and signal lifetime, x- and y- spot width for calculation of spatial resolution and R^2 for calculation of spot quality. This function is implemented in MATLAB and uses an iterative least-squares approach. To ensure convergence of the iteration, initial guesses for the fit parameters are necessary. The initial guesses are obtained from a preliminary intensity-weighted centroid function. The equations for the intensity weighted centroid and Gaussian fit are shown in Equations 2.2, 2.3, and 2.4.

$$X_{cg} = \frac{\sum_{\mathrm{i}=1}^{columns} \sum_{\mathrm{j}=1}^{rows} Intensity(\mathrm{i},\mathrm{j}) * \mathrm{i}}{\sum_{\mathrm{i}=1}^{columns} \sum_{\mathrm{j}=1}^{rows} Intensity(\mathrm{i},\mathrm{j})} \tag{2.2}$$

$$Y_{cg} = \frac{\sum_{\mathrm{i}=1}^{columns} \sum_{\mathrm{j}=1}^{rows} Intensity(\mathrm{i},\mathrm{j}) * \mathrm{j}}{\sum_{\mathrm{i}=1}^{columns} \sum_{\mathrm{j}=1}^{rows} Intensity(\mathrm{i},\mathrm{j})} \tag{2.3}$$

$$I(x,y) = I_0 \mathrm{e}^{-\frac{x-x_c}{\sigma_x}} \mathrm{e}^{-\frac{y-y_c}{\sigma_y}} \tag{2.4}$$

In the first two equations, X_{cg} and Y_{cg} are the locations of the centroid guess based on direct calculation of the intensity weighted centroids. These values, along with the peak intensity in the image, become inputs into the least-squares Gaussian surface fitting function. In Equation 2.4, I_0 is the analytic peak intensity, x_c and y_c are the analytic centroid locations, and σ_x and σ_y are the x and y spot widths. The goodness of fit parameter R^2 is calculated from the SSE (sum-squares-error) between the analytic curve fit and the original input image.

For a perfect Gaussian surface, the analytic centroids, x_c and y_c, will agree perfectly with the weighted-centroids, x_{cg} and y_{cg}. This is self-evident as a perfect Gaussian will be symmetric in intensity about its major and minor axes. In a real-world example of a FLEET spot, the centroids will not agree perfectly. The parameter δ_c is used to represent

the disagreement in centroid guess and analytic centroid, in pixels. For FLEET spots that approach Gaussian nature, δ_c will be minimal, but for images of poor quality, this value will increase. By using this parameter, an idea of the precision of any individual measurement can be obtained due to the 'disagreement' of centroid location between the two methods. Thus, a threshold on this value can be used to discard datapoints that do not fit an acceptable quality. An optimization can be invoked to achieve the greatest reasonable precision in the measurement without discarding too much data. An example of a valid and outlier measurement were shown previously in Figure 2.15.

The optimization process in selecting a threshold for δ_c involves running a portion of the datapoints through both algorithms and plotting the percentage of outliers vs. the precision of the measurement. The value δ_c can be converted nominally to precision by applying the spatial calibration, time between images, and the expected mean velocity of the flow. This analysis has been performed on a select dataset to show the trade-off between desired precision and percentage of data that must be discarded. The result is shown in Figure 2.19, for various spots in a FLEET grid. At the periphery of the grid, as explained in previous sections, the SNR is lower which reduces the quality of the data. As a result, for a given precision, points 1, 3, 13, and 15 have a considerably higher percentage of outlier measurements. Inner grid points that experience higher SNR's have lower outlier fractions at the same precision. For grid-FLEET measurements, either a single precision can be desired, or this threshold can be varied across the extent of the grid. Either way, using the two-step approach to centroid finding gives the user the ability to tune the precision based on the quality of the data.

Due to the low energy and low magnification used in the grid-FLEET measurement, the overall precision of the technique suffers in this case. Points 1 and 11 are the lowest performance, with 40% outliers at 5% precision level. Neither of these percentages are ideal for a reliable measurement. With elevated numbers of outliers, more data is required to be collected and processed for an accurate statistical representation of the flow. For the bulk of the measurements in this figure, the outlier percentage is <20% for a precision of 5%. This is still relatively low-precision, but the number of outliers is more acceptable. In the range

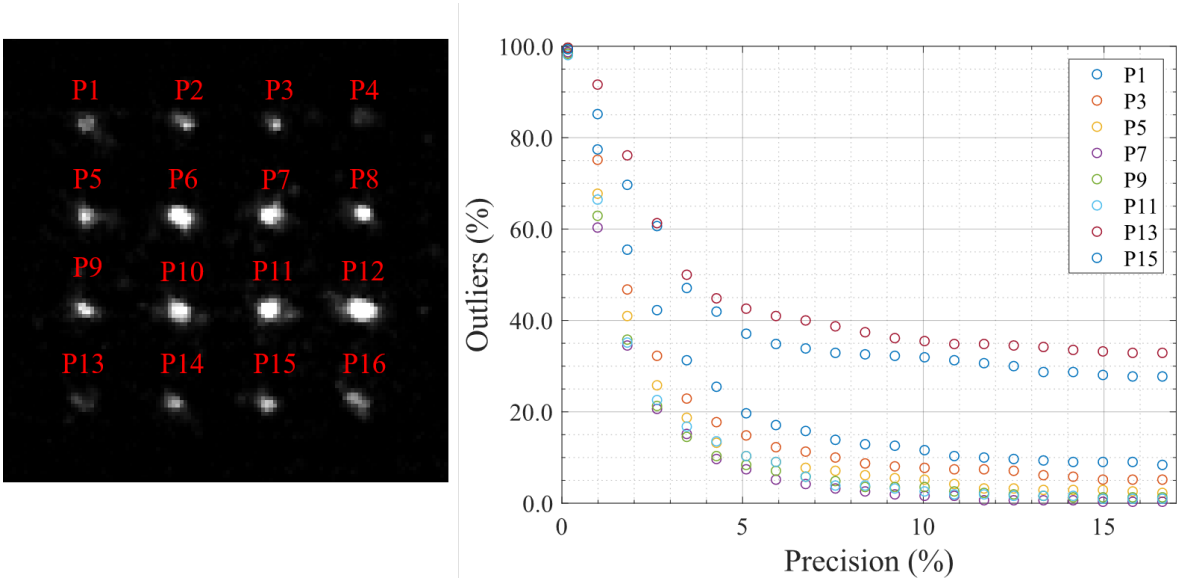

Figure 2.19. Outlier percentage as a function of desired precision for various grid-FLEET points.

of 2-3% precision which is desirable, the outliers range from 20-40%. This is the optimal result in this case, where the measurement can be rather precise.

2.4.2 Adaptive Velocity Calculation

Once FLEET centroid locations are calculated, there are many numerical schemes for estimating velocity. The simplest of these is a finite difference [27], where two locations and one time delay are used to make a velocity measurement. Precision methods [21] utilize the locations of multiple FLEET observations over the emission lifetime. Since multiple images of the same motion are used, experimental noise is averaged out. This enhances the precision of the method, because it makes use of more datapoints to achieve a single measurement. The last group of methods is adaptive curve fitting. This type of method is invoked in Chapter 4 for the BAM6QT processing, as well as in [21]. In the tagged molecules are assumed to follow a streamline in the flow. The acceleration along the streamline in x and y directions is assumed to be either negligible, constant, or time varying depending on the flow field. In the case of Chapter 4 in this thesis, the acceleration is assumed to be negligible, and this assumption is validated. Using this method, a precision of 0.33% is achieved. For the work conducted by Burns et al. [21], a time-constant acceleration is assumed. In this case the measurement was shown to be inferior in precision to the 'Precision' method because the number of points used in the curve fit was too small, and the actual acceleration in the flow was minimal. As was noticed in the processing of the quiet tunnel data, in Chapter 4, assuming constant acceleration can actually over-fit the data and reduce precision if this is not the best assumption.

Grid-FLEET is designed to measure spatially-varying flowfields, and thus as a result will be utilized in regions with relatively large accelerations. For this reason, making assumptions such as constant or even time-varying acceleration in the flow may improve velocity results considerably as it can represent the natural behavior of the flow-field.

As the first step of all FLEET processing, all centroid locations of each FLEET spot are found as previously described. For a single FLEET spot in the grid, the time-history of centroids in x and y can be plotted. Looking at the behavior of the motion, the researcher can decide which type of acceleration assumption to make. From there, the proper curve-fit

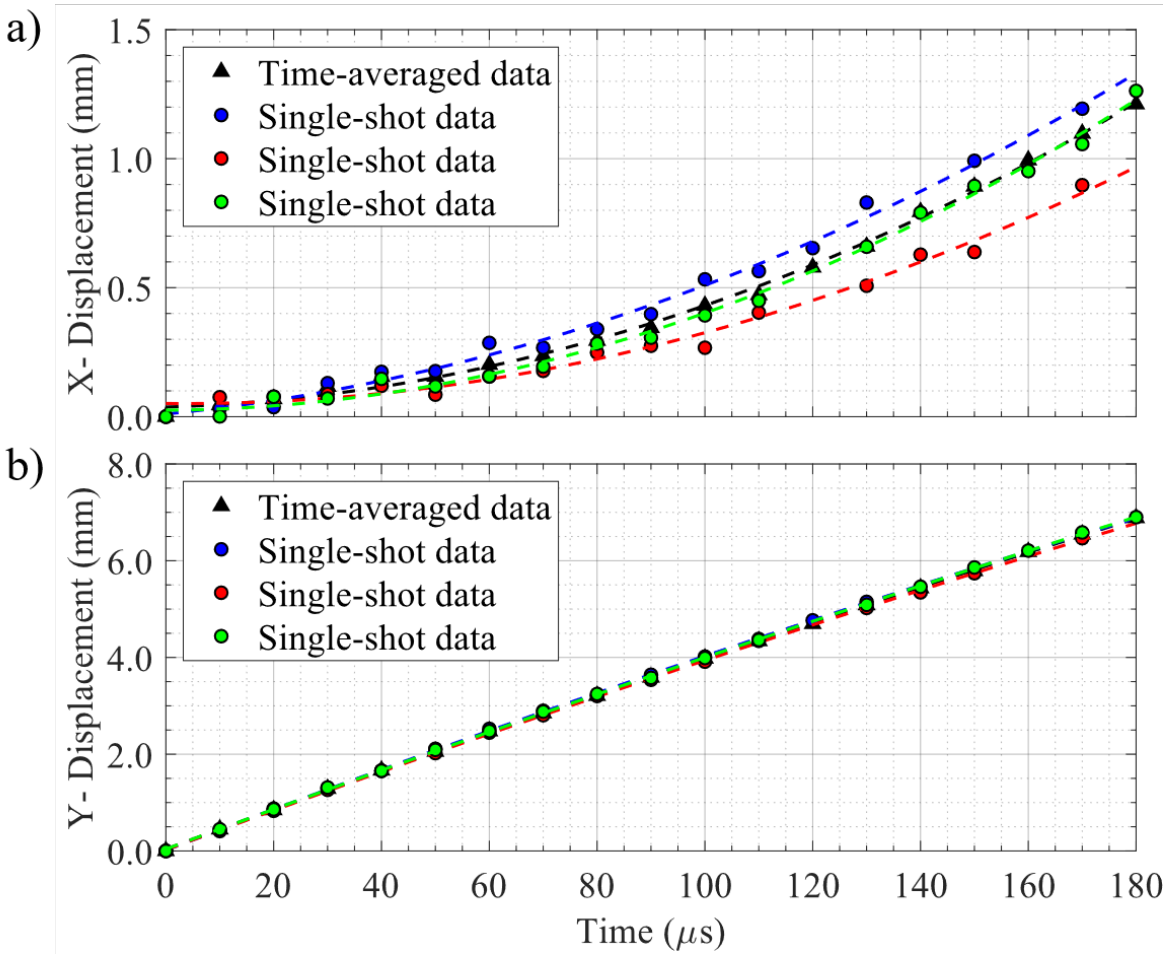

Figure 2.20. Constant-acceleration curvefits for x and y grid-FLEET velocities

can be applied to the data. Figure 2.20 shows this result for curve-fits of x and y centroid locations of the grid-FLEET data from the experiment described previously with sharp-corner flow.

In the x-direction, there is strong acceleration as the flow needs to travel around the obstacle. In the y-direction, there is minimal deceleration. Multiple single-shot measurements and the time-averaged measurement are shown for both cases. For the y-direction data, the deviation from the curve fit is minimum and random fluctuation via noise is almost non-existent. For velocity in this direction, simple finite differencing could be invoked with acceptable precision, but the curve fit enhances the measurement. For the x-direction the trend in the data is more unique. Since the flow velocity is predominantly in the y-direction,

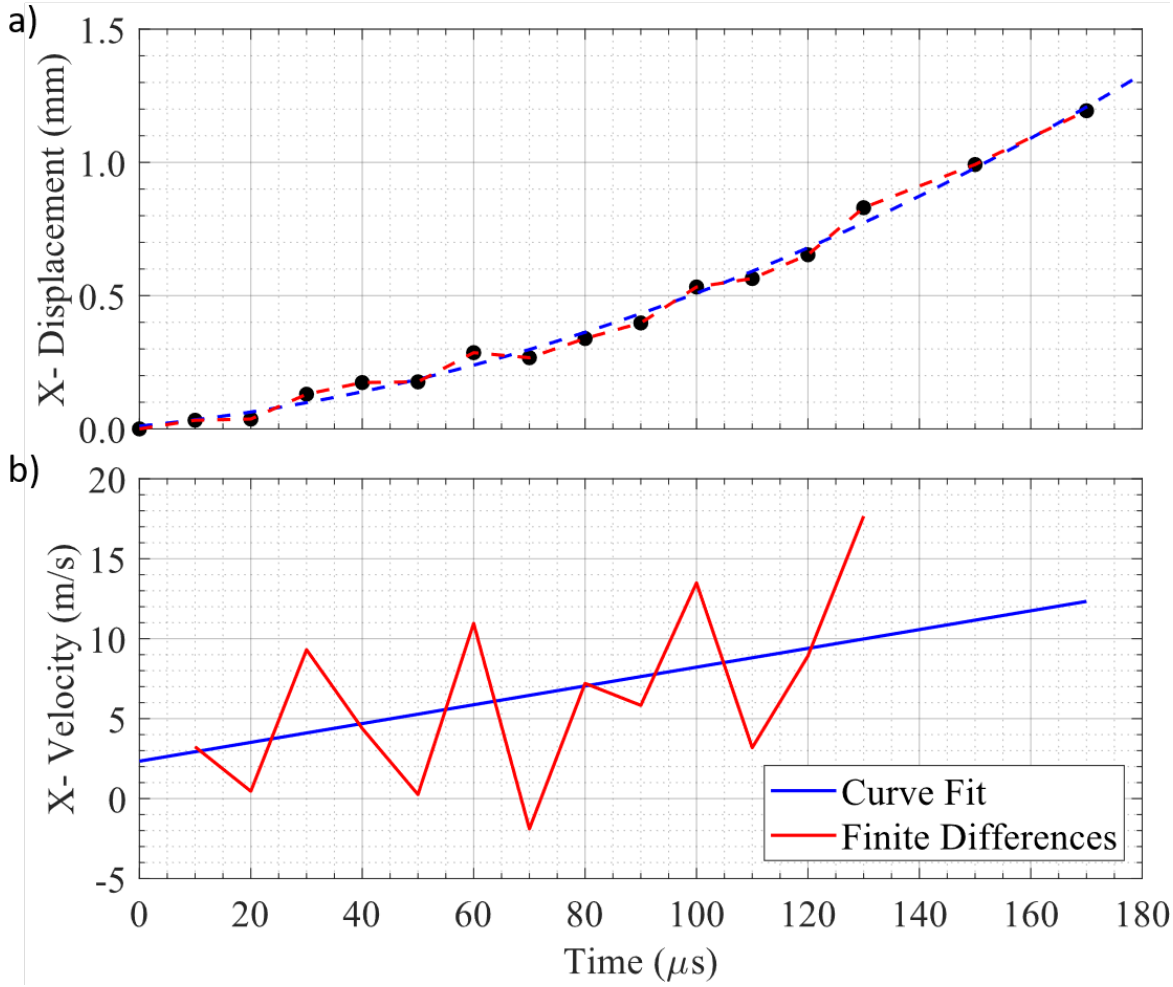

Figure 2.21. a) Displacement trend with finite difference and constant-acceleration curve fit. b) Velocity time trace result from finite difference and curve-fit methods applied to single-shot data.

the magnitudes of displacement in the x-direction are minimal and the random noise has a larger effect. In the graph this manifests as large deviations from the curvefit. If a simple finite differencing scheme were applied here, these measurements would drastically reduce the precision of the results. Thus, the curve fit is necessary to get reliable velocity measurements here.

Figure 2.21 shows this conundrum in more detail. In Figure 2.21 a) a successive series of spot observations are plotted over time of a single FLEET excitation. Again, a general trend in increasing velocity is clear. Two paths are shown: in red, the path assuming direction connection of each observation assumes the simple finite differences methods. The path in

blue applies the assumption of constant acceleration in the form of a curve fit. While the blue path does not pass through each observation, it uses a least-squares curve fit to apply the best-fit path to the spot motion. As a result, it is much smoother than the red path. This difference becomes more apparent in Figure 2.21 b). Here, the path of displacement over time is numerically differentiated to achieve the velocity measurement. The finite differences measurement is clearly jagged, and the range is >200% of the data mean value. This is non-physical as the flow will not accelerate by this large magnitude on this short of a timescale. The blue velocity curve is linear, by definition of the curve fit. This is a more accurate representation of the flow, and smooths out any individual uncertainty in centroid finding from the end result.

This procedure of curvefitting centroids is evaluated for measurements taken in steady flow with the Grid-FLEET arrangement. With the assumption that the flow is not varying in time or space, the standard deviation of the set of measurements can be taken as the precision. The precision of the curve-fit based measurements is directly compared to the precision of the baseline finite differencing method. The results are shown in Figure 2.22. Here, the results are plotted in terms of percent improvement against measurement time delay. The time delay is the time which has passed since the original laser excitation. As measurement time delay increases the emission signal captured by the camera decreases, making data acquisition more difficult. Precision improvement is calculated by comparing the percent difference in precision between the curve-fit and finite differencing schemes. This improvement value is positive always, meaning that in all cases the curve-fit method provides a net improvement in the achievable measurement precision. There are only four instances out of the ensemble for both V_x and V_y where the precision improvement is less than 100%. This means that in most cases, the precision for the curve-fit method is generally twice as precise as the simplified method.

While this analysis directly contradicts the findings in [84], the measurement situation is much different. In the case of Burns, the number of total acquisition points to construct a curve fit is much lower, which can cause data to be generally over-fitted. Additionally, a larger difference is the magnitude of total velocity. In the case of the Grid-FLEET data, the magnitude of velocity (especially V_x) is very low. This means that the relative magnitude of

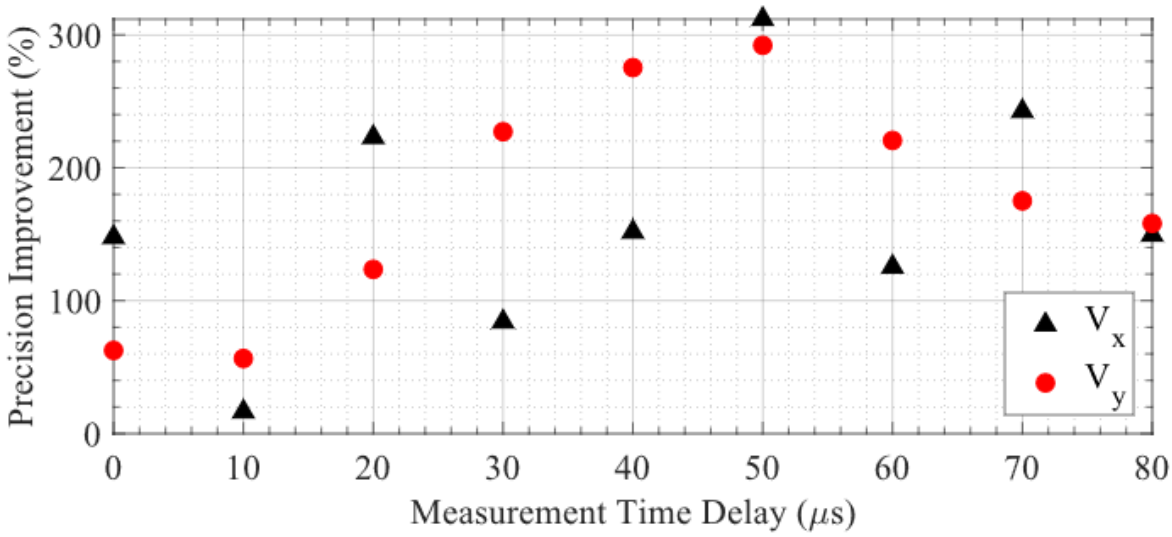

Figure 2.22. Precision improvement of curvefit based velocities over single point finite differencing for Vx and Vy velocity components.

uncertainty in any one measurement will be large with respect to value of the measurement. In this case, being able to fit a curve through multiple observation points greatly smooths out any otherwise-large uncertainties in individual spot position. Depending on the velocity measurement situation, curve-fitting may result in an overall improvement in measurement precision, although this must be considered on a case-by-case basis.

2.4.3 Spatial Binning for Precision Enhancement

In certain arrangements of FLEET [21], a precision of 1% or better can be achieved. While this is rather precise, it may not be sufficient for certain applications such as low levels of turbulence. An alternate method, PIV, achieves higher precision by tracking groups of particles rather than single objects. In this way, spatial resolution is sacrificed in exchange for reduction in noise from the measurement of single particles. While the PIV cross-correlation algorithm is not always ideal for FLEET, the idea of tracking multiple tag locations simultaneously can be invoked.

To employ this principle, the freestream Grid-FLEET data are considered. In this situation, there is a 4x4 grid of individual measurements. The velocity across the extent of the grid is assumed to be constant, and the fluctuation level is expected to be minimal

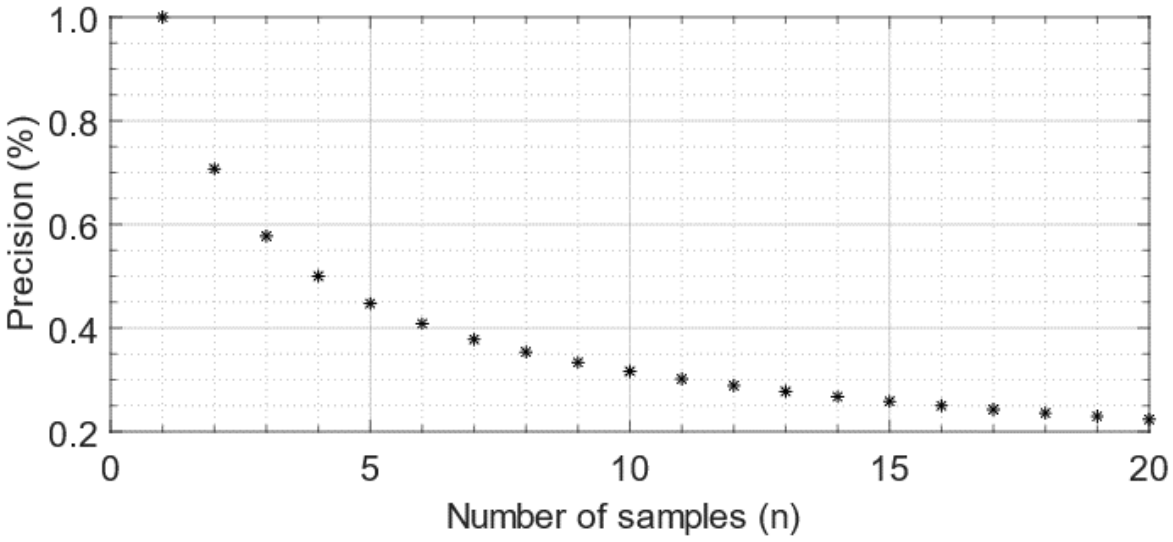

Figure 2.23. Trend of precision vs. sample size for multi-point FLEET measurements.

($u << \delta_y$) such that any unsteadiness of the measurement can be attributed to the precision of the method. In order to increase the precision of the free-stream measurement, multiple velocity measurements are averaged together. Assuming the standard deviation of all measurement points is the same, the standard error (standard deviation of precision-enhanced velocity measurements) can be modeled by Equation 2.5.

$$SE = \sigma/\sqrt{n} \tag{2.5}$$

where SE is the standard error, σ is the standard deviation of the individual velocity measurements, and n is the number of points used in the sample. It is self-evident that increasing the number of measurements in the sample will decrease the error and increase the precision of the measurement. Figure 2.23 shows this theoretical trend, where single-point measurement precision is 1%. By binning 4 simultaneous measurements, there is a 50% predicted improvement in the measurement precision. This continues scaling, and at 8 measurement points there is a 75% improvement in precision. This trend has diminishing returns as the successive improvement in precision decreases with increasing sample number.

An obvious solution to maximizing the precision of FLEET measurements is to average across all measurement points in a grid. With 16 points, this will theoretically give an

order of magnitude improvement in the precision. There are multiple downsides to this idea however; this will decrease the number of independent instantaneous measurements and the spatial resolution. In the arbitrary sense, one could choose any number of randomly scattered datapoints to average across to increase the precision. The result would be a higher accuracy measurement, but the result would be spatially averaged across the extent of the individual measurement points. To optimize and understand the trade-off in spatial resolution and precision of measurements through spatial binning in the 4x4 grid, four progressive levels of binning are defined (L=0-3). Level 0 refers to the baseline measurement, where there is no degree of spatial binning and each measurement is located at the original FLEET centroid location. Progressing from here, at each level, L, a set of $(4-L)^2$ rectangles are defined. The vertices of the rectangles are the locations of measurements from the L−1 binning level. To conduct the spatial binning, the velocity values at the vertices of the rectangles are averaged, and the location of the measurement is considered to be the center of the rectangle. The recursive algorithm to perform this binning is conducted sequentially for the binning levels L=1−3. The number of points, n, to make each average can be calculated as $(L+1)^2$. Thus, for each level, the number of points used to make a measurement is increased, but the number of resulting measurements and spatial resolution are decreased. Locations and number of individual velocity measurement for each level are shown in Figure 2.24.

This binning scheme is applied to the laminar flow Grid-FLEET data to evaluate the precision gain for real FLEET data. The results are shown in Figure 2.25. The results are plotted against the number of individual velocity measurements used to make an averaged reading, and the theoretical prediction is shown with a dashed line. With no spatial binning, the precision is ∼2.25%. By binning to the L=1 level, precision is instantly improved to better than 1%. Proceeding further, the maximum precision is achieved at L=3, at 0.65%. By fully binning the measurement points, a 70% improvement in precision can be achieved. The experimental data points follow the predicted trend within reason. However, by comparing the real results to the theoretical prediction directly, the improvement of precision is underestimated at L=1, and overestimated at L=3. This shows that in actuality, there are diminishing returns in over-binning the data, especially considering that there will be a significant trade-off in spatial resolution and number of discrete measurements.

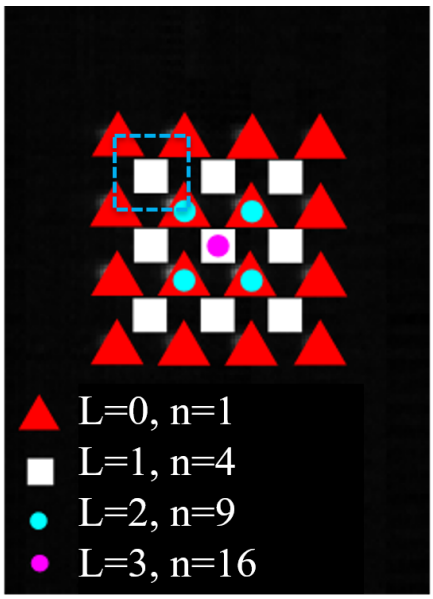

Figure 2.24. Locations and number of measurements for spatial binning levels L=0-3 (n=1,4,9,16).

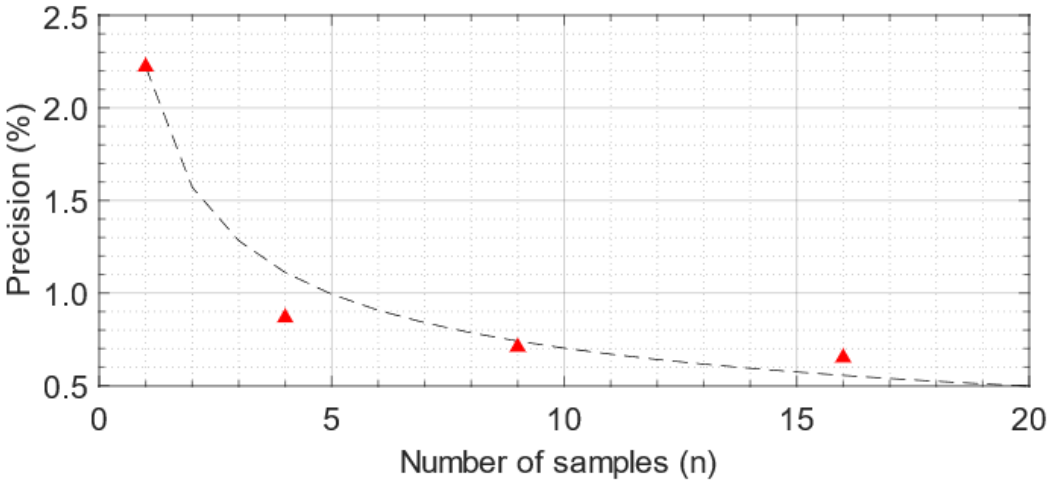

Figure 2.25. Precision vs. number of binning points for steady flow Grid FLEET data. Theoretical prediction plotted as dashed line.

f

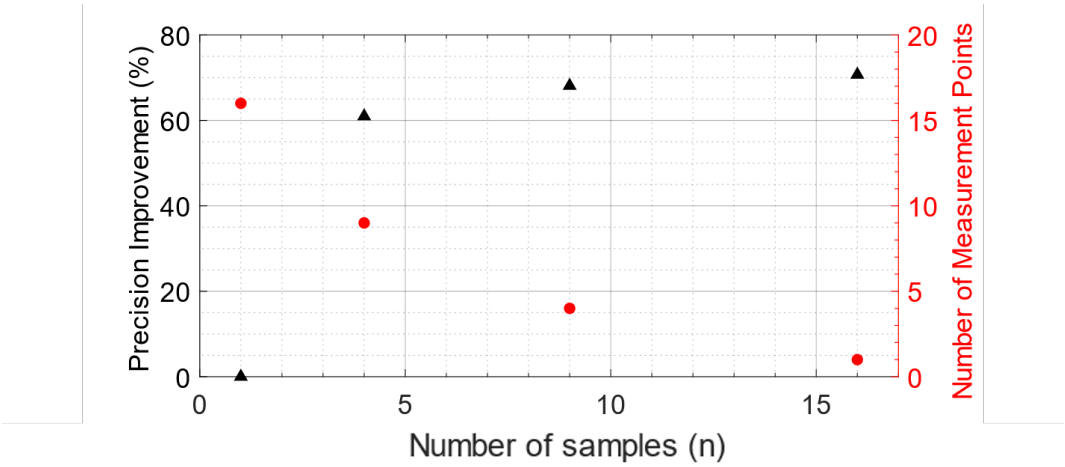

Figure 2.26. Precision improvement over baseline, and number of independent velocity measurements plotted against number of interpolated samples (n).

To begin evaluating the trade-off in precision against spatial binning level, the results need to be generalized. Figure 2.26 shows the precision improvement over the baseline for each successive binning level. On the right y-axis the number of independent measurements available at each level is also plotted. Here the user is enlightened more to the diminishing returns of higher-level spatial binning. At levels 2 and 3, the number of independent measurement points, and thus the capability to measure spatial velocity gradients, becomes greatly reduced. Unless the desired outcome is purely an increase in precision at the expense of spatial resolution and number of measurements, the optimal binning level seems to be L=1. Here, the precision improvement is greater than 60%, and there are still 9 independently located spatial measurements over which spatial velocity gradients and other flow parameters can be evaluated.

The final concern to address in the spatial binning process is the reduction in effective spatial resolution. At the baseline, L=0, the effective spatial resolution of the measurement is a factor of the size of the FLEET excitation spot and the total travel distance of the spot during the image acquisition time. At levels L= 1, 2, and 3 the spatial resolution becomes the total spatial extent of the points utilized in the binning process. This trend is linear, and is shown in Figure 2.27. The ideal trade-off level, L=1, has an effective spatial resolution (ESR) of 1.5 mm in this measurement. This is due to the measurements being

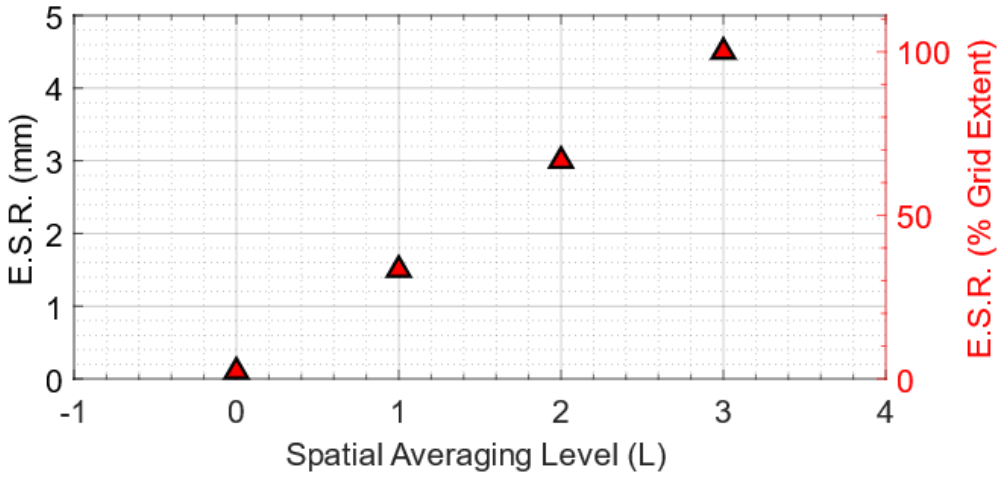

Figure 2.27. Effective Spatial Resolution (E.S.R.) as a function of binning level. Data reported in mm with respect to the current measurement as well as percent full grid extent for future experiment planning.

spatially averaged over 2 adjacent rows and columns of the 4x4 grid of FLEET points, which are separated by 1.5 mm. At the highest binning level, L=4, the spatial resolution extends to 4.5 mm. This is again far from ideal, as any measurement is averaged over this large region. On the right y-axis of Figure 2.27, the ESR is shown in percent of the full grid resolution. As mentioned previously, by selecting an alternate DOE beamsplitter, the grid spacing can be increased or decreased. If a researcher desires an experiment to optimize both spatial resolution and precision, one can select a DOE that produces minimum grid spacing, and perform the maximum level of spatial binning during data processing. With this theoretical arrangement, precision could be maximized while keeping the spatial resolution of measurements to a reasonable value.

2.4.4 Flow Parameter Calculation

With instantaneous data across a two-dimensional spatial extent, first-order velocity gradients can be calculated. These gradients can be used to measure flow parameters such as vorticity and shear stress. The first step of this process is to interpolate the velocity measurements onto an orthogonal grid. With an orthogonal grid, gradients in two directions can readily be computed. For the initial experiment, the velocity is assumed to have smooth

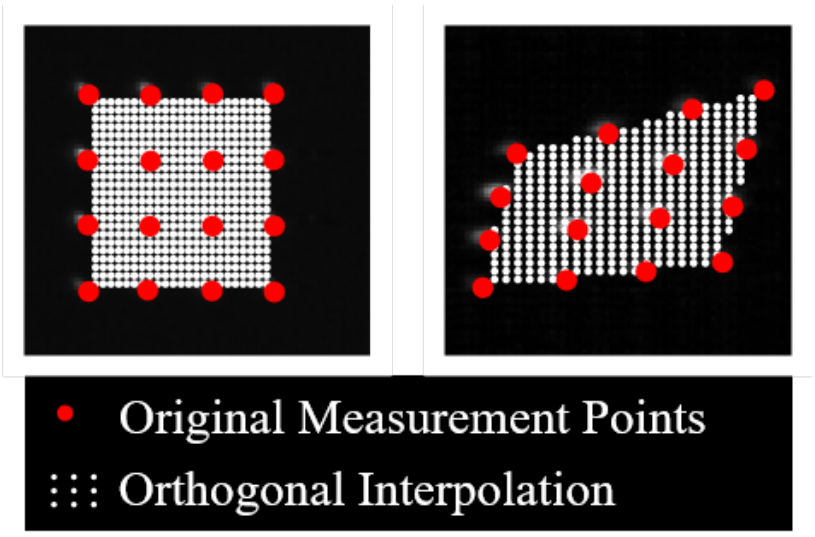

Figure 2.28. Locations of original and orthogonally interpolated velocity measurements for undisplaced and displaced FLEET grids.

and continuous variation on the order of the grid extent. This assumption will not hold true when grid separation is large, or the measurement passes through features such as shear layers or shocks in a supersonic flow. Invoking this assumption, the measurement grid is upscaled to a 25x25 grid from a 4x4 grid. Any grid-points that fall outside of the outer bounds of the original grid are not considered. Using bilinear interpolation, the velocities are calculated at these new grid points. Figure 2.28 shows this process for two examples of Grid-FLEET measurements. The first is a minimally-displaced grid in a near-freestream environment, and the second example is a grid in the vicinity of a sharp corner. For the near-freestream case the original grid is closely orthogonal. In the near-obstacle grid, the measurement points are highly-skewed from orthogonal.

By locating the velocity measurements on an orthogonal grid, four spatial velocity gradients: du/dx, du/dy, dv/dy and dv/dx can readily be calculated by invoking finite differences. The three-dimensional formula for vorticity is represented as $\vec{w} = \nabla x \vec{u}$, which evaluates to $\vec{w} = (\frac{\delta u}{\delta x} - \frac{\delta v}{\delta y})\vec{z}$ when only in-plane velocities are considered. An example of employing this process is shown in Figure 2.29. The original measurement points are shown as white circles. The vorticity in this case forms as the flow curves around a sharp corner obstacle. As proximity to the obstacle increases, the vorticty increases as well due to turning of the flow.

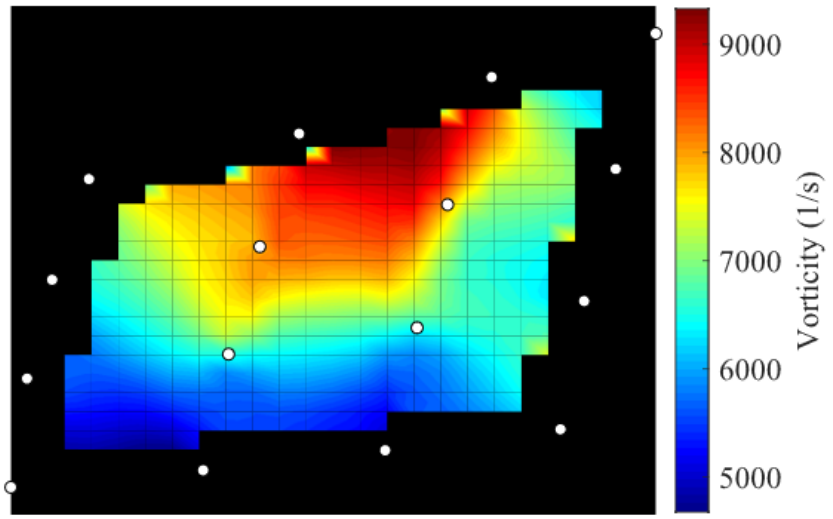

Figure 2.29. Example vorticity result created from 16 point instantaneous FLEET grid. Original measurement points shown as white circles.

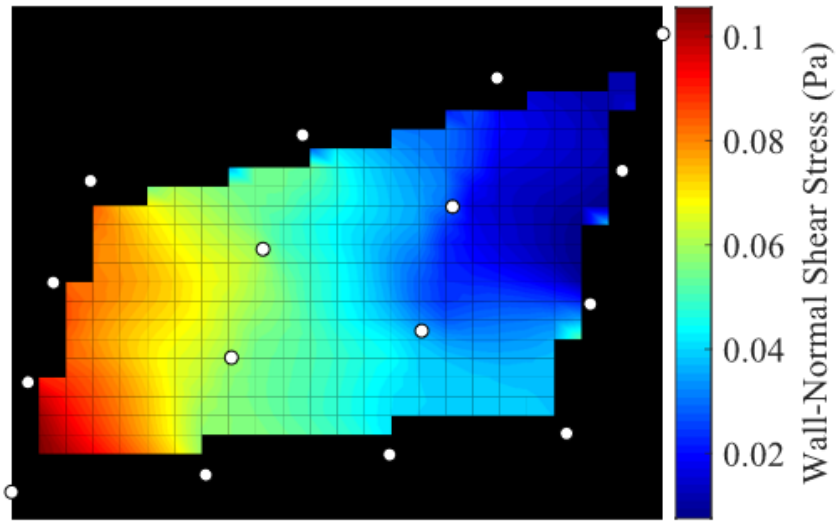

Figure 2.30. Example shear stress result created from 16 point instantaneous FLEET grid. Original measurement points shown as white circles.

In the same manner that vorticty is calculated, wall-normal shear stress, $\tau = \mu du/dy$ can be estimated as well. An example result for this is shown in Figure 2.30. Due to the low speed of the flow, viscosity is assumed to be constant. In higher velocity scenarios, the Sutherland relation is invoked. In Figure 2.30 there is shear stress present due to the deceleration of the fluid as it approaches a stagnation near the sharp corner obstacle.

While the 4x4 Grid-FLEET measurements allow preliminary demonstration of measuring vorticity and shear stress, the results must be taken with some caution. In order to prove reliable, the error propagation through the results must be carefully evaluated. The error in mapping irregularly spaced data onto a rectangular grid is discussed in [85]. To minimize error, grid density must be increased. In fixed-time interval velocity measurement techniques, the true location of the velocity measurement resides at half the distance between the initial and final spot observation points. This is true even in PIV. In PIV however, the vector fields are generally so dense this error is almost always discarded. Cohn and Koochesfahani [85] recommend keeping the value R/δ, the ratio of interpolated grid spacing to original grid

spacing small to minimize bias errors from relocating velocity values. To achieve this in practicality for Grid-FLEET, the number of measurement points would have to be significantly increased. This is a matter of improving the optical arrangement to foster optimized sizing of the measurement grid with respect to the flow in study.

If R/δ can be minimized, the bias error in relocating the velocity measurements to an orthogonal grid becomes negligible with respect to the random error propagated through uncertainty in the original velocity measurement. The original formulation for error in velocity for FLEET is Equation 2.6:

$$\frac{dV}{V} = \sqrt{(\frac{dX}{X})^2 + (\frac{dt}{t})^2} \tag{2.6}$$

The timing jitter is 10 ns, which when compared to the integration time of 5 μs, can be neglected. Therefore, the error can be simply represented by $\frac{dV}{V} = \frac{dX}{X}$. Any error in velocity measurement is directly the result of the error introduced in centroid location of the FLEET spot. The formula for vorticity is mentioned earlier in this section, and the representation for error is Equation 2.7:

$$\frac{dw}{w} = \sqrt{(\frac{dU}{U})^2 + (\frac{dX}{X})^2} + \sqrt{(\frac{dV}{V})^2 + (\frac{dY}{Y})^2} \tag{2.7}$$

where U and V are orthogonal velocity components and X and Y are orthogonal spatial dimensions. From the velocity error relation we know that $\frac{dV}{V} = \frac{dX}{X}$, so all terms can be combined. The result is that the error in vorticity is: Equation 2.8:

$$\frac{dw}{w} = 2\sqrt{2}\frac{dX}{X} = 2.828\frac{dX}{X} \tag{2.8}$$

Thus by propagating the velocity measurement through to vorticity measurements, the total random error is magnified by almost a factor of 3. This shows that in order to utilize Grid-FLEET reliably for spatial gradient measurements, the overall uncertainty and centroid finding error must be minimized. Combining the other advancements in centroid finding, outlier detection, and velocity curve-fitting may improve this error, but these processes must be considered on a case-by-case basis with respect to the operating parameters of the flow

being studied. To gain reliable measurements for any flow in question, the magnification of the imaging system, characteristic velocity and flow feature scale, and required accuracy in velocity and velocity gradients must be carefully considered.

3. EXTENSION OF MOLECULAR TAGGING CAPABILITIES

3.1 Improvement of Frequency Resolution

3.1.1 Motivation

Current commercially available femtosecond laser systems limit the measurement rate of FLEET to 1 kHz. While this represents a high data rate for accruing statistical measurements, it is not fast enough to capture time-resolved processes in high speed flows. Namely, the second-mode instability wave [86]–[88] is a transient process present in hypersonic boundary layers that plays a large role in laminar to turbulent transition. This instability can have characteristic frequencies on the order of 50−500 kHz. In order to study this phenomenon, a laser system capable of performing FLEET at repetition rates of 100 kHz−1 MHz is necessary. With the laser development expertise present at Purdue University, a burst-mode femtosecond laser platform has been created to deliver high energy pulses at 1 MHz[74]. During the creation of this system, benchmarking experiments were performed using the FLEET method to inform the energy requirements of the system for extended repetition rate measurements.

3.1.2 Benchmarking

A pressure-fed converging diverging supersonic nozzle with a 1" wide slot outlet was constructed to provide high speed flow to evaluate FLEET measurement techniques. The supersonic jet has a design Mach number of 3.6 allowing for exit flow up to 650 m/s. The fluid supply system delivers high pressure air or nitrogen at up to 82.7 bar before a relief valve opens to prevent damage to the system. The ability to switch between air and nitrogen is included to study the behavior of FLEET in changing oxygen concentrations. The nozzle is mounted horizontally on an optical bench so that cameras and optics can be mounted around it. A camera tower is constructed and integrated vertically looking down on the exit of the nozzle. The vertical integration of the camera and intensifying system allows for easy adjustment in three dimensions of the focus and interrogation plane of the imaging system

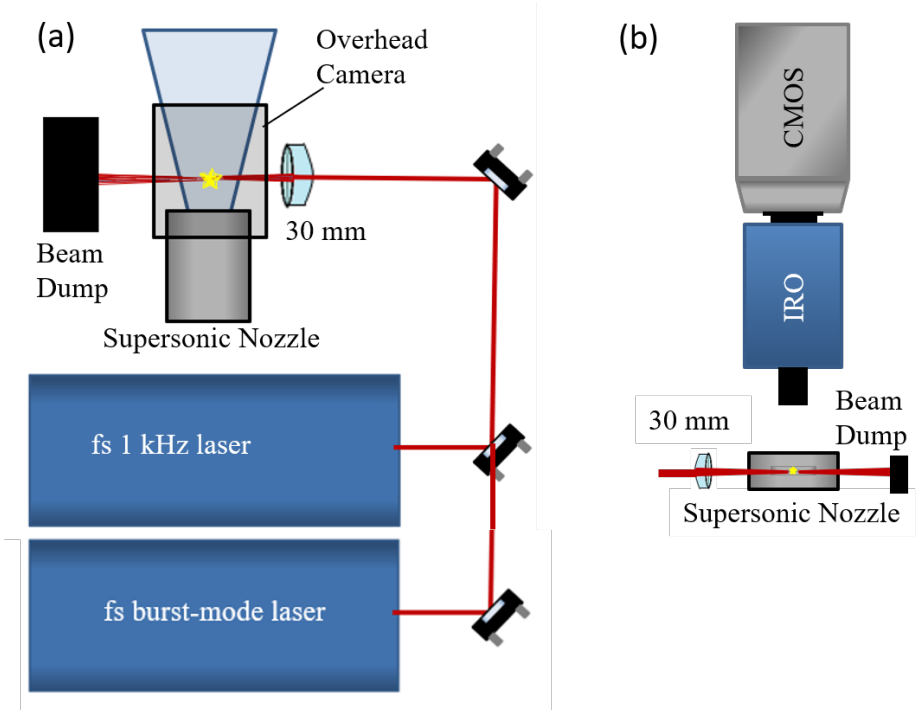

Figure 3.1. Diagram of experimental setup for benchmarking burst-mode FLEET measurements. (A) Overhead view, (B) front view

to capture the FLEET signal with high magnification. A +30 mm achromat is located adjacent to the supersonic nozzle so that the laser can focus tightly to the center of the exit plume. Delivery optics for a Spectra Physics Solstice laser (wavelength 800 nm, energy 2.5 mJ/pulse) and the burst mode femtosecond laser in development are placed with magnetic mounts so the systems can be easily swapped and compared. Figure 3.1 shows a diagram of the experimental arrangement and Figure 3.2 displays a picture of the optics and camera lens installed next to the nozzle during the experiment.

By using neutral density filters between the output of the Solstice laser and the focus location, discrete energy steps were used between 1.8 mJ and 0.13 mJ per pulse to produce FLEET excitation. The supersonic nozzle was operated near its maximum pressure at 70 bar to deliver a constant stream of nitrogen for excitation. The imaging system captured the FLEET signal at a 1 μs delay with a 1 μs gate and a gain of 85%. The imaging and experimental conditions were held constant as laser energy was decreased to enable direct comparison of the signal behavior. Figure 3.3 shows the signal as energy is decreased. The

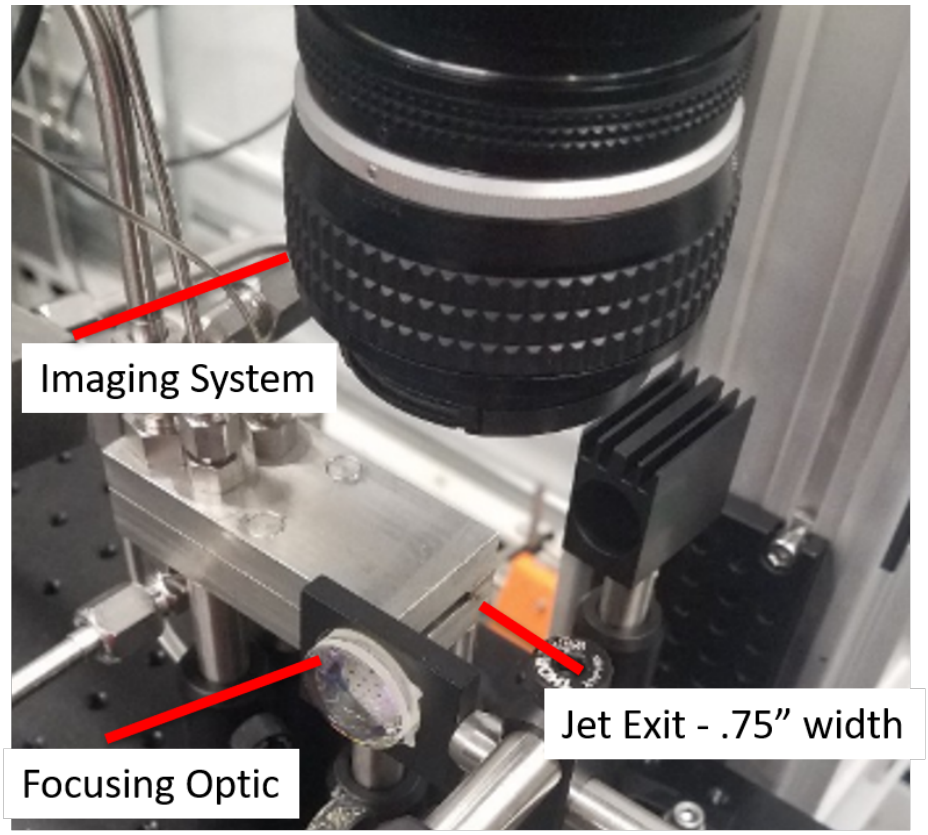

Figure 3.2. Image of FLEET demonstrator nozzle and location of optics and camera system

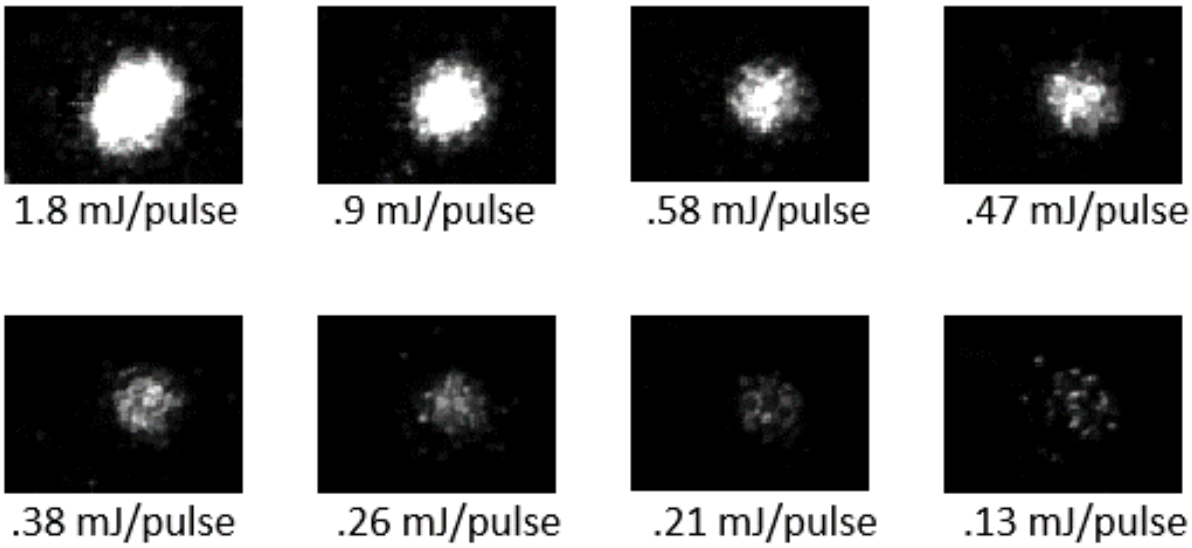

Figure 3.3. Images of FLEET signal at decreasing excitation energy

images are plotted on the same color scale, so the higher energy images display as saturated so the low energy images can be resolved. The results show that signal can be seen all the way down to the lowest energy attempted, at 0.13 mJ. All the way down to 0.26 mJ/pulse, the signal is fairly continuous and well defined. This result is promising, as FLEET can be performed with SNR as low as 3-4 as long as the shape is well-defined [89]. The signal in the two lowest energies can still be seen, however the quality of the signal begins to decrease significantly, and what was once a continuous region begins to split into multiple regions of intensity. The results are quantified in Figure 3.4. The trend of signal maximum intensity and SNR is plotted in (a) and (b) respectively. These graphs show that even at the lowest energy, SNR is still above 200 which means that this method can be utilized at very low energies.

With the results of the low energy study completed, a baseline for the threshold needed to make FLEET measurements was obtained. This experiment was not all-inclusive, since the wavelengths and pulse durations of the two lasers is different, but it provided a guide for the energy values necessary from the burst mode laser system to make high repetition rate measurements.

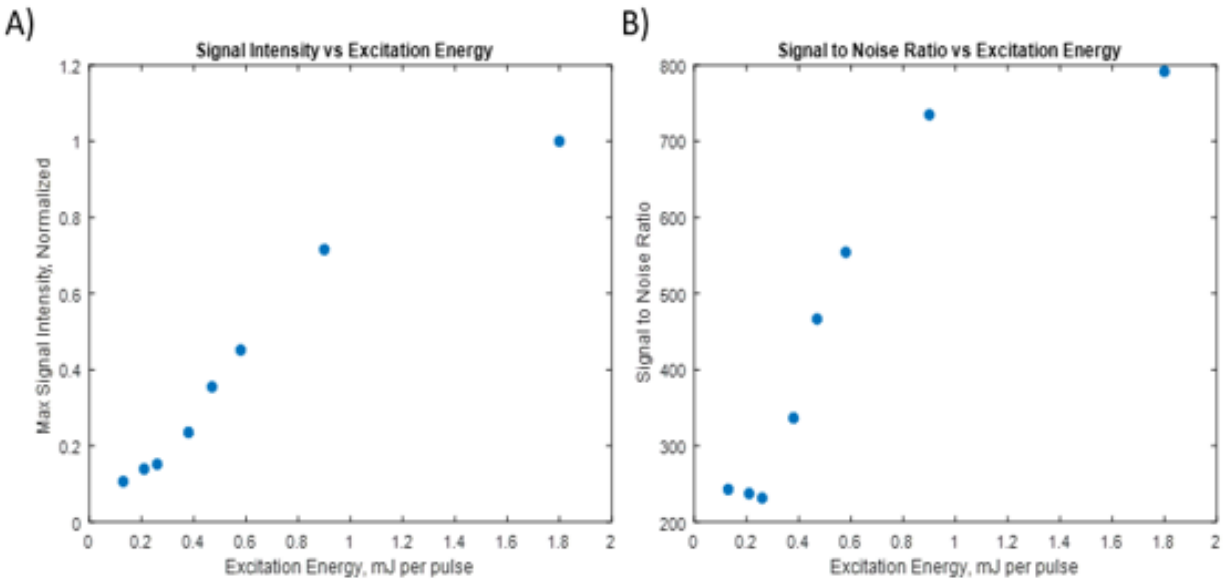

Figure 3.4. (A) Signal peak intensity vs excitation energy, (B) Signal-to-Noise Ratio vs excitation energy

3.1.3 *Burst-mode femtosecond laser electronic excitation tagging for kHz–MHz seedless velocimetry*

This section details advances in the measurement rate of FLEET from 1 kHz to 1 MHz leveraging advancements in burst-mode femtosecond laser technology. To achieve the increase in measurement rate, a supersonic jet test section was designed and constructed for demonstration of measurements. First, using a commercial femtosecond laser, a low-energy threshold study was performed to find the SNR limit of FLEET measurements matching the capability of the burst-mode laser. Then, demonstration FLEET measurements were made at increasing excitation rates with the burst-mode laser. The results of this work were formulated into a journal publication entitled '*Burst-mode femtosecond laser electronic excitation tagging for kHz–MHz seedless velocimetry*'[66], published in Optics Letters, and adapted into this thesis as follows:

Abstract

Burst-mode femtosecond laser electronic excitation tagging (FLEET) of nitrogen is introduced for tracking the velocity field in high-speed flows at kHz–MHz repetition rates without the use of added tracers. A custom-built Nd:glass femtosecond laser is used to produce 500 pulses per burst with pulses having a temporal separation as short as 1 μs, an energy of 120 μJ, and a duration of 274 fs. This enables two orders of magnitude higher measurement bandwidth over conventional kHz-rate FLEET velocimetry. Characteristics of the optical system are described, along with a demonstration of time-resolved velocity measurements with $\sim$0.5% precision in a supersonic slot jet.

Introduction

Accurate measurements of flow velocity in supersonic and hypersonic test facilities are important for the design and validation of performance models for high-speed flight vehicles. Probe based measurements traditionally used in subsonic facilities are not only limited in spatial and temporal resolution but can also significantly perturb the flow field around high-speed test articles. Optical techniques such as particle image velocimetry (PIV) have

been demonstrated at high repetition rates in supersonic flows [90]; however, the accuracy is limited by particle lag in regions with high velocity gradients (e.g., within the boundary layer or across shock fronts). Additional challenges such as limited optical access, particle seeding density issues, and desire to avoid hardware contamination discourages the application of PIV in many supersonic and hypersonic test facilities. Molecular-tagging-based velocimetry techniques have been developed to address the challenges of optical measurements in wind tunnel environments. Introducing a gas-phase tracer, such as nitric-oxide into the flow, allows for velocity measurements that are not subject to particle lag [45], [91]. However, flow mixing and diffusion limit the ability of tracers to get into the desired measurement region, and tracer injection can perturb the flow being analyzed. Recent progress in the Krypton tagging method has shown promise for reliable supersonic velocity measurements [46] as it is chemically inert and less prone to alter flow physics. Unseeded molecular tagging techniques take advantage of the fluorescence properties of molecules already present in flow and represent a promising approach for non-intrusive velocimetry in ground test facilities. Raman excitation and laser-induced electronic fluorescence (RELIEF) [92], Rayleigh scattering [93], and air photolysis and recombination tracking (APART) [94] have been demonstrated but are subject to their own limitations, such as complex setup requiring multiple lasers to be spatially overlapped. Femtosecond (fs) laser electronic excitation tagging (FLEET) [47], [62], [95] is a technique that has been developed and demonstrated for velocimetry measurements based on the dissociation and tracking of the fluorescence that occurs during the subsequent recombination of nitrogen molecules. FLEET can be performed in a line-of-sight configuration with a single focused laser beam and camera, requiring only one small window for optical access [69], [84], [95]. While this approach has been shown to be applicable over a wide range of flow conditions and test facilities, data acquisition has generally been limited to a repetition rate of 1 kHz. This is not sufficient to track the evolution of dynamical features in high-speed flows, such as turbulence and shock-flow interactions [43]. This limitation was overcome recently by using a custom-built burst-mode laser that could operate at 100 kHz with 100 ps pulse durations in a 10 ms long burst [96]. Time-resolved flow measurements have been made using this technique, referred to as PLEET [65], but due to the longer pulse duration and lower peak power, the minimum energy threshold is around two orders of mag-

nitude higher than FLEET and is not feasible at MHz rates with available laser energies. This work aims to increase the repetition rate of FLEET measurements by up to three orders of magnitude by employing a burst-mode fs laser capable of generating signals at rates of 200 kHz to 1 MHz. This laser is modified from a previous design that is described in detail in Ref. [74]. The current design enables a more compact laser architecture with fewer amplification stages and is described in further detail within the Supplementary Materials. Figures 3.5a and b show the time-bandwidth beam characteristics of the laser source, with a Gaussian transform limited pulse width of 274 fs at a central wavelength of 1063.6 nm. This differs from prior FLEET measurements using Ti:Sapphire lasers near 800 or 400 nm [47], [59], [62], [84], which show an improvement in signal intensity at shorter wavelengths [62]. It is of interest, therefore, to evaluate FLEET measurements using the current laser because of differences in laser wavelength, beam quality, and pulse width. The quality of the compressed transform-limited beam was measured using a D4σ technique. The 4-mm-diameter beam was shown to diverge slightly astigmatically, resulting in an average M^2 of 3.15, as shown in Fig. 3.5. Burst profiles for 200 kHz and 1 MHz repetition rates can be seen in Fig. 3.5d, with 200 $\pm$ 19.2 μJ/pulse and 120 $\pm$ 11.3 μJ/pulse, respectively. The burst duration of the laser is about 0.8 ms, however the pulse energy of the laser during the beginning of the burst is too low to achieve sufficient signal. Therefore, FLEET measurements are only acquired for .5 ms. A +30 mm focal length achromatic lens doublet was used to produce a tightly focused spot, resulting in a calculated peak irradiance of 77.2 $\pm$ 7.4 TW/cm^2 and 46.3 $\pm$ 4.4 TW/cm^2, respectively, at the probe volume. The optical path of the laser was enclosed in lens tubes to mitigate environmental variations in the refractive index along the beam path. Optics were also placed on translating mounts to provide higher precision for focusing the laser spot to the desired measurement region of interest.

Experiment

FLEET velocimetry was performed in a pressure-fed converging-diverging slot jet capable of delivering a steady supersonic flow, as shown in Fig. 3.6. The design mach number of the nozzle is 3.6 and perfect expansion to atmospheric pressure occurred at 89 bar. Due to pressure losses in the system, supply pressures could be varied from 0 to 82.7 bar to attain

range from subsonic to supersonic velocities. FLEET has been shown to be quenched in intensity and lifetime in the presence of oxygen [47]. This is due to a tendency of dissociated nitrogen to recombine into nitric oxide rather than nitrogen molecules, which bypasses the FLEET emission mechanism. Hence, a gas mixing system allowed testing with either air or nitrogen to evaluate applicability for different wind tunnel conditions. The FLEET probe laser was aligned precisely across the exit of the supersonic nozzle to 2.8 mm from from the exit plane.

A high-speed CMOS camera (Photron, SA-Z Fastcam) was used to capture images of the FLEET signal as it propagated downstream in the flow. An image intensifier (LaVision, HS-IRO) with an S20 photocathode and P46 phosphor was used in series with the high-speed camera to provide precise time gating and increase in signal level. Sequences of tagged nitrogen spots were generated at both 200 kHz and 1 MHz rates. Images were captured at 200 kHz for all datasets. A pixel resolution of 384×160 was achieved with a Nikon 50 mm lens set to an f-stop of f / 1.2 and coupled with a 14 mm extension ring. The intensified camera was positioned above the nozzle to look downward onto the flow. The magnification of the imaging system was 32 μm/pixel. With a zoom lens and/or longer extension rings, the resolution can be improved. However, there is a trade-off between resolution and frame size since the signal can move significant distances in the high-speed flows being studied.

Originally, a 600 $\pm$ 25 nm bandpass filter was used to isolate the FLEET signal, but the reduction in signal posed a challenge in cases with lower excitation energy. Instead of using a spectral filter to eliminate laser scattering, the gate of the camera was delayed to 70 ns after the laser pulses to to ensure only the FLEET fluorescence was captured. This approach provided a significant improvement in signal level.

Datasets were collected at upstream supply pressures between about 30 and 70 bar to gain an understanding of the measurement technique performance over a range of flow velocities (see Fig. 3.7). For all of these operating conditions, the exit flow of the nozzle was slightly overexpanded. For the 68.9 bar condition, an intensifier gate of 800 ns was used with a gain of 65%, and for the 34.5 bar case the gate was 900 ns with a gain of 73%. A noticeable decrease in signal intensity was observed in the lower supply pressures. The authors theorize that since there is no nitrogen co-flow for the nozzle, the exit flow can entrain quiescent air

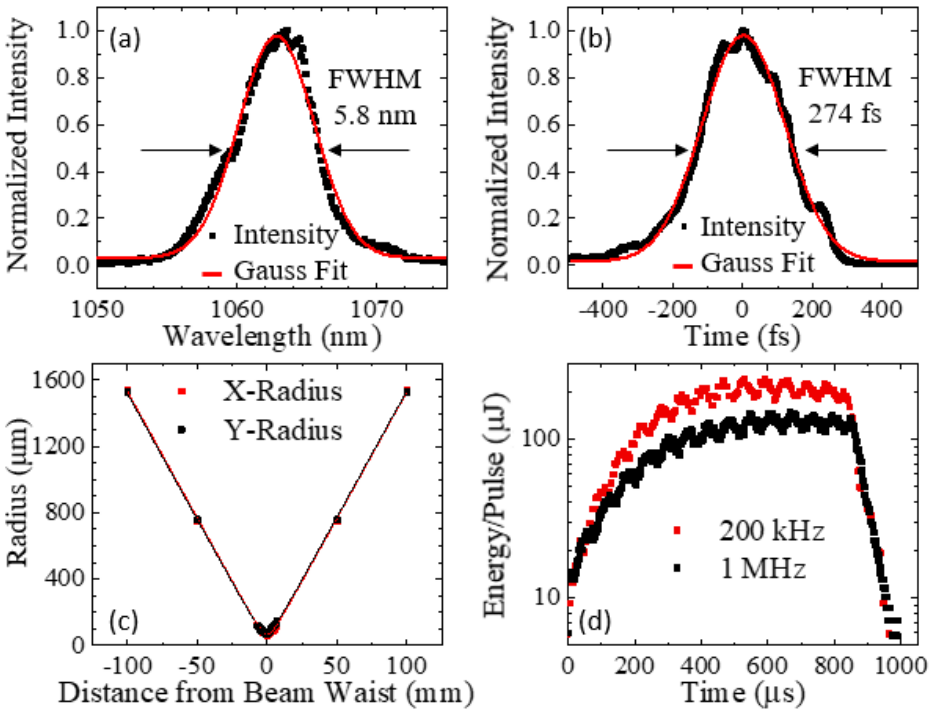

Figure 3.5. Parameters of fs laser, including (a) frequency domain bandwidth, (b) temporal domain pulse width, (c) beam quality divergence profiles after temporal compression with M2 = 2.97 and 3.33 in x and y directions, respectively, and (d) burst profiles for 200 kHz and 1 MHz repetition rates.

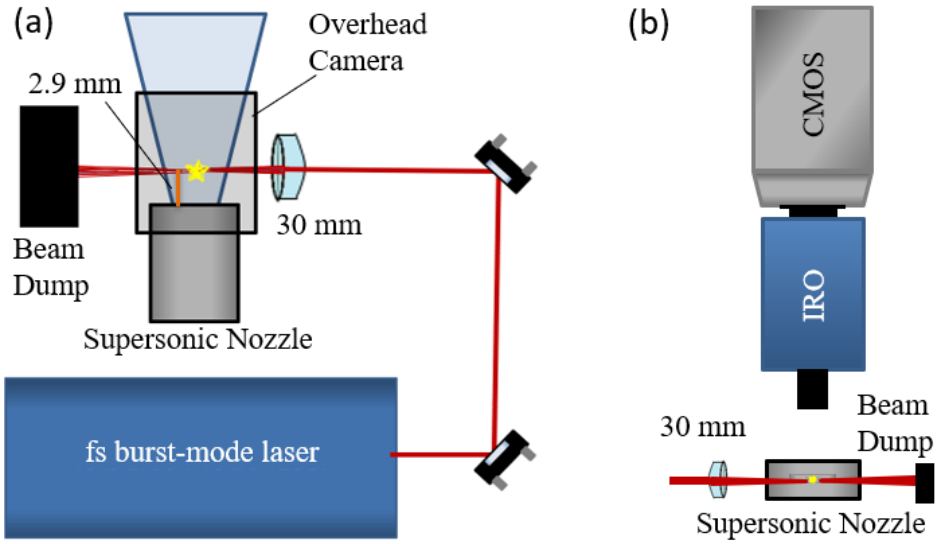

Figure 3.6. (a) Top view of FLEET experiment showing laser delivery to probe location through 30 mm focusing lens and (b) front view showing top-down placement of high-speed intensified camera.

and cause FLEET signal quenching. For this reason, the gain on the intensifier needed to be increased, leading to a lower signal to noise ratio. To evaluate the applicability of high-speed FLEET measurements to a wider range of facilities, the experiment was replicated with air as the supply fluid at 68.9 bar. Due to much higher signal quenching, the intensifer gate was set to 1500 ns with a gain of 85% to enable imaging of the less intense FLEET signals.

The tagged nitrogen molecules formed a spot at the focal point of the beam. With framing at 200 kHz, images of each spot could be taken every 5 μs. and the velocity obtained from the displacement of the spot between two successive frames. First the images were cropped to local regions around each spot with user input. A noise threshold for the image was found from the background values and any pixel below this threshold was set to zero. In FLEET velocimetry, a Gaussian intensity distribution can be fit across the spot to find the centroid location. Two dimensional Gaussian surface fitting was applied to the data collected in this experiment; however, this algorithm produced a large proportion of outlier velocity measurements due to poor fitting.

Three methods of centroid finding were then applied to the FLEET images, including a simple centroid, a bounding box centroid, and a weighted centroid. For each measurement, the largest discrepancy between centroid finding algorithms was taken to be the uncertainty in the velocity measurement. Figure 3.7a shows a trend of decreasing spot quality with decreasing supply pressure. Representative signals are shown for each supply pressure with associated results from the area centroid, bounding box centroid, and weighted centroid shown in cyan, red, and black, respectively. This leads to a correlated increase in the measurement uncertainty at lower pressures. Additionally, the uncertainty with the experiment in air was significantly higher due to poorer relative spot quality causing more relative error in centroid finding. As shown in Fig. 3.7b, the uncertainties vary from 14.3 m/s at 34.5 bar (2.6%) to 7.3 m/s at 68.9 bar (1.14%), with the uncertainty for the air measurement being 53.2 m/s (8.3%).

Results

Due to strong dependency on the binarization threshold and spot shapes associated with the area and bounding box centroid methods, an image correlation based velocity mea-

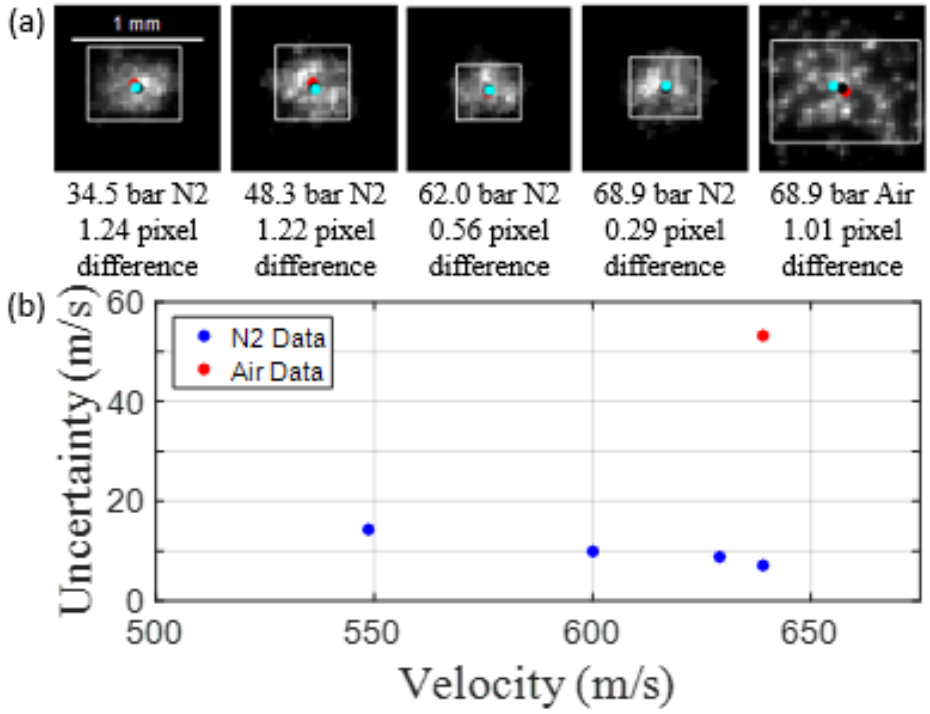

Figure 3.7. (a) Representative spot finding with area centroid (cyan dot), intensity weighted centroid (black dot), and bounding box (white box) with centroid (red dot); and (b) associated trend of uncertainty in velocity measurements for different pressures with pure N2 and air.

surement method was implemented instead to further reduce uncertainty. The correlation method does not require thresholding, therefore it is insensitive to low signal levels. Between successive images of the same spot, a cross-correlation map of all possible displacements was created. The peak of this map was treated as the most likely displacement for the spot. A two pixel wide median filter was applied to each image before correlation was processed to eliminate small amounts of spatial non-uniformity. Bicubic interpolation near the correlation peak was applied to achieve sub-pixel accuracy on the displacement measurements. Figure 3.8 shows representative correlation maps for velocity measurements over the range of conditions tested. For the nitrogen cases, the correlation map is generally a Gaussian distribution about a clear peak, and the pixel shift is well defined. For the air case, the correlation map quality is lower, but a clear peak is still present.

In general, there was good agreement between the weighted centroid and correlation-based approaches. Ultimately, velocity is reported as the mean value of both methods, and the uncertainty is considered to be the absolute difference between both results at a given data point. Figure 3.9a shows the time history of measured velocity in nitrogen at 68.9 and 48.3 bar at the exit of the nozzle. The mean values for these measurements are 639 and 600 m/s with standard deviations of 9.1 and 8.7 m/s, respectively. The uncertainties for these pressures using this method are 2.75 m/s (0.43%) and 3.32 m/s (0.55%), which is a marked improvement over using a centroid-only approach. Since the deviation of the measured flow velocity is larger than the uncertainty, it is concluded that this measurement method is sensitive enough to capture the unsteady flow fluctuations. Figure 3.9b shows the average trend of velocity with uncertainty bands. The uncertainty grows with decreasing pressure due to poorer spot quality. The expected velocity for a perfect expansion case for this nozzle at 89 bar is 651 m/s. While this condition could not be achieved with the experimental setup, the results trend toward this value as pressure increases showing good agreement between theory and measurements.

Due to limitations in the framing rate of the imaging system, time-resolved data could not be taken above 200 kHz, but the laser was operated at 1 MHz to test the image quality that could be obtained for the pulse energies available at the highest possible repetition rate of the custom burst-mode fs laser. The gate and gain of the intensifier were set to 400 ns and

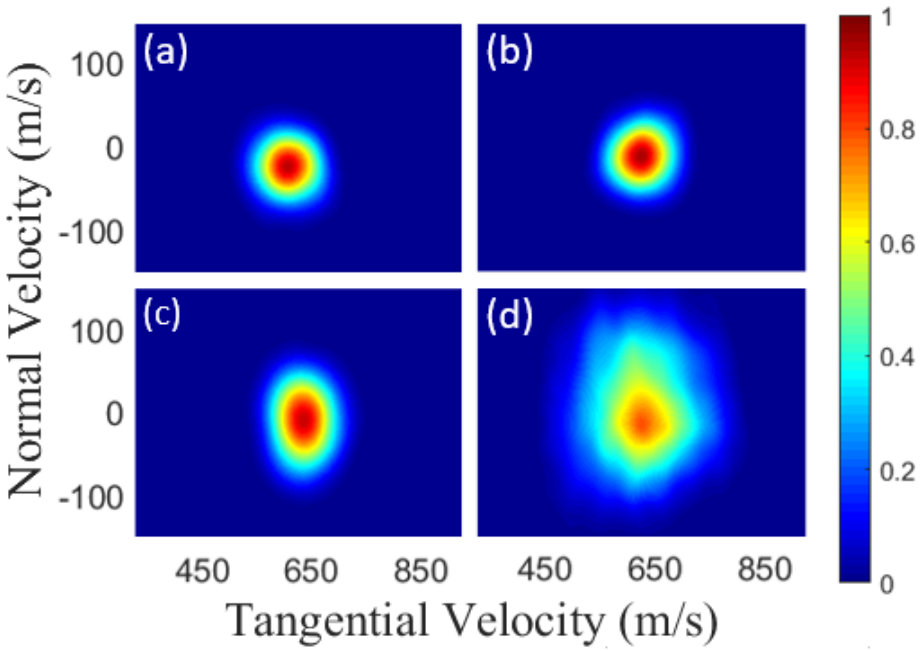

Figure 3.8. Correlation maps for displacement in (a) 34.5 bar nitrogen, (b) 48.3 bar nitrogen, (c) 68.9 bar Nitrogen, and (d) 68.9 bar air.

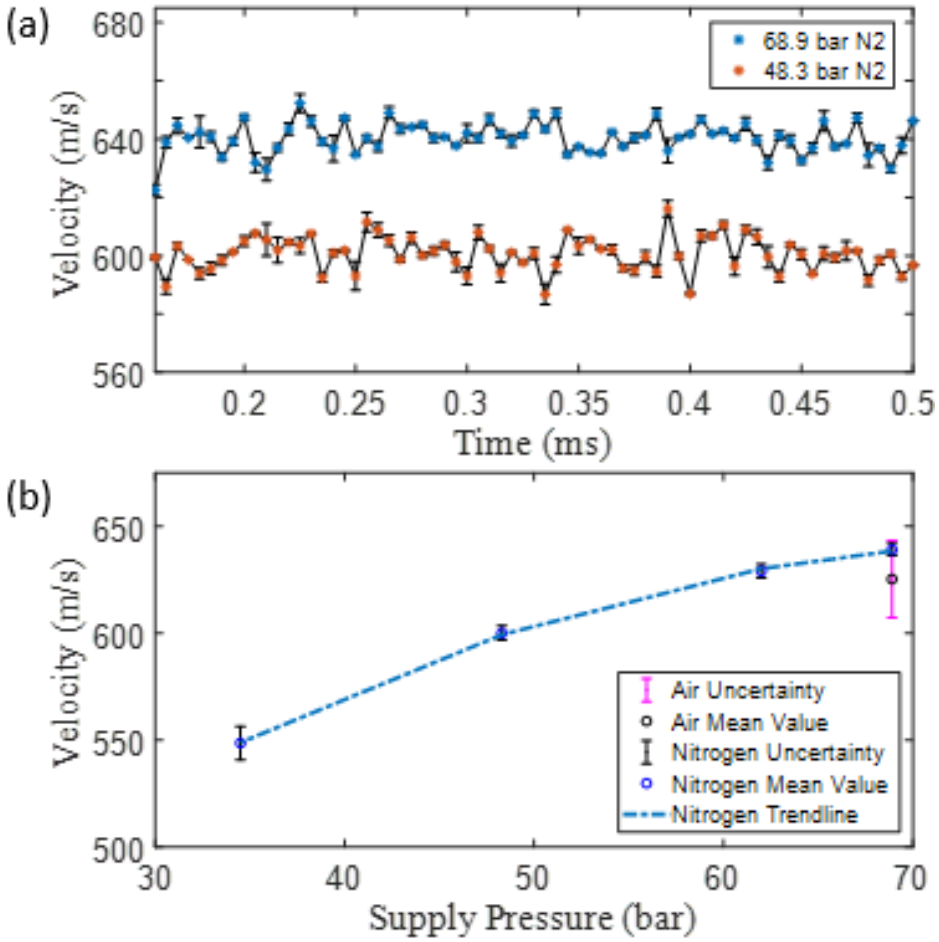

Figure 3.9. Velocity time history for 68.9 and 48.3 bar supply pressures with nitrogen. (b) Average velocities and uncertainties for all tested conditions with nitrogen and air. The uncertainty of the air measurement is much larger as compared to the nitrogen measurements. To improve the accuracy of this technique for use in air, a more sensitive imaging system or higher laser energy is required.

72%, respectively. Figure 3.10 shows results of two successive frames taken 5 μs apart with 1 MHz laser excitation. Each of the two frames captures all of the spots generated by the 1 MHz laser that have convected downstream and which display sufficient fluorescence to be detected on the intensified camera. An example of five individual FLEET spots and their shift during the 5 s time delay between images is marked in Fig. 3.10a. Centroid finding is then performed as previously described to calculate all velocities, as shown in Fig. 3.10b.

Unlike prior work with 1 kHz or even 100 kHz excitation, 1 MHz excitation allows for simultaneous measurement of velocity at multiple streamwise locations in supersonic flows without the use of beam-splitting optics. In addition, the measurement rate at each location is limited only by the framing rate of the imaging system. The rate of 200 kHz is higher than that demonstrated in prior work and is accomplished with two orders of magnitude lower excitation energy than prior 100 kHz PLEET measurements [65]. Moreover, with the current signal levels, available commercial MHz-rate image intensifiers and cameras will make it feasible to collect multi-point data at rates up to 1 MHz. Note that the signal-to-noise ratio for the images captured in this experiment is ~120, but the laser energy at the 1 MHz rate fluctuates above and below the lower signal threshold for FLEET, so only some acquisitions provide useful data at this repetition rate. As such further improvement in the laser energy amplitude and consistency would increase the data rate in these experiments.

Conclusion

In conclusion, custom burst-mode laser development has allowed the creation of a compact laser platform capable of producing high-energy femtosecond pulses for excitation of FLEET signals at rates up to 1 MHz. A supersonic nozzle was used as a test case for proof-of-concept velocity measurements in supersonic flows with uncertainties of ~0.5%. Time-resolved velocimetry was conducted in unseeded nitrogen and air flows using the FLEET technique with laser excitation rates of 200 kHz to 1 MHz. The image collection rate of 200 kHz represents a significant improvement over prior FLEET measurements. However, single-shot measurements were achieved with 1 MHz laser excitation and demonstrate the feasibility for MHz-rate seedless velocimetry using intensified camera systems that are currently commercially available. With 1 MHz excitation and 200 kHz detection in the current work, five

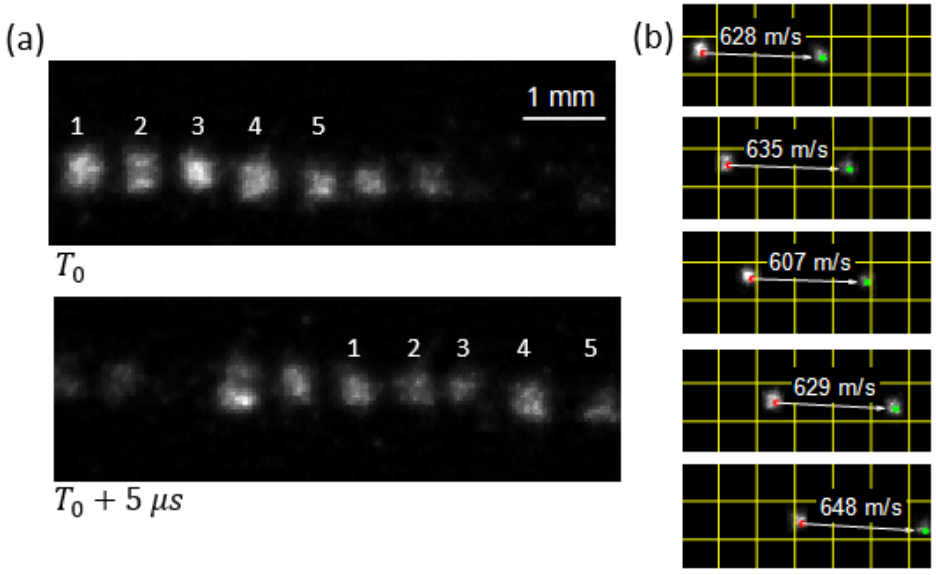

Figure 3.10. (a) Raw data collected with 1 MHz laser excitation. (b) Five velocities measured simultaneously along a streamline with 1 MHz laser excitation (grid spacing is 1 mm).

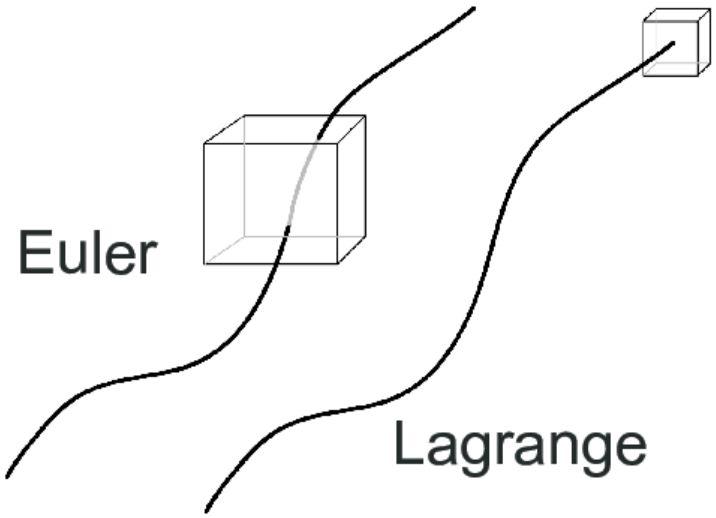

Figure 3.11. Eulerian vs Lagrangian flow property tracking [97].

or more downstream locations could be tracked simultaneously for high-speed multi-point velocimetry. This work demonstrates an approach to increasing the spatio-temporal resolution of FLEET measurements, with the potential for further improvements in laser excitation energy, image collection efficiency, and framing rate of the intensified camera system in future work .

3.1.4 Combining High Frequency and High Spatial Extent Measurements

The ultimate goal of the fundamental advancements in FLEET is to enable combination of high-frequency measurements with measurements of high spatial extent. It is well known that FLEET signal is long-lived, up to and exceeding 200 μs of emission lifetime in certain environments. With repeated imaging of the FLEET excitation, this allows multiple velocity measurements to be taken along the streamline that the tagged molecules follow. With a single excitation this allows Lagrangian tracking of the velocity over time. With this form of tracking, the researcher gains information of velocity over time, however the location of the measurement travels with the motion of the tagged molecules. This is in contrast to Eulerian tracking where time-dependent information on velocity is measured for a static location in space, as shown in Figure 3.11.

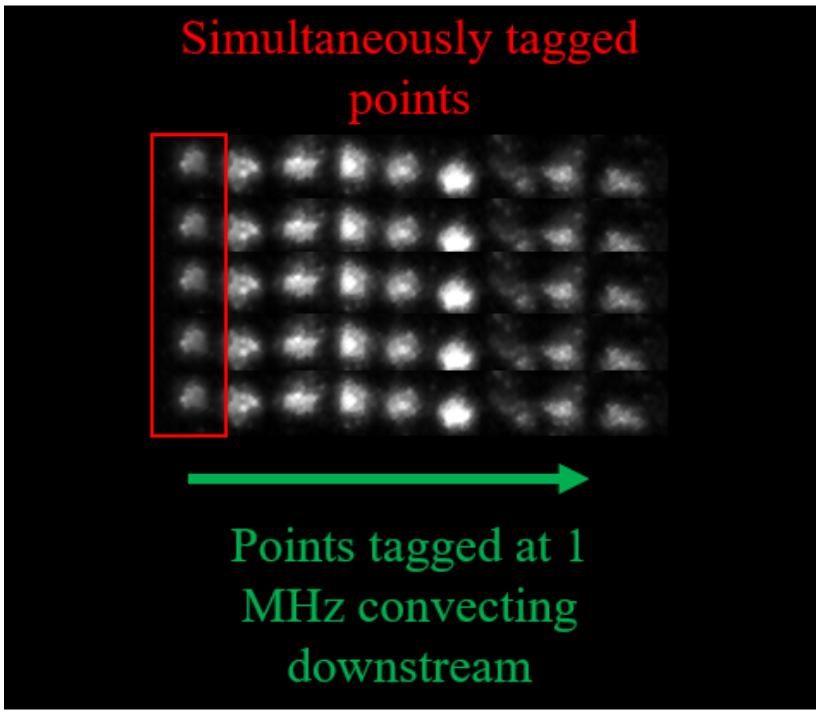

Figure 3.12. SImulated data showing combination of high-frequency and spatial extent measurements.

As shown with MHz-rate velocity measurements, the Lagrangian measurement capability in the streamwise component of measurement can be transformed into Eulerian measurement by the addition of high-frequency flow excitation. Additionally as shown in Chapter 2, spatially-resolved Eulerian measurement can be gained by tagging multiple points simultaneously. In essence, these two advanced methods can be combined to gain additional information about the flow. With repeated flow excitation at 200 kHz or 1 MHz, previously-tagged FLEET molecules will continue to fluoresce as they propagate through the fluid, and enable Eulerian velocity measurement in the streamwise direction. In the transverse direction of the flow, diffractive optical elements can create multiple simultaneous excitations to create the second dimension of instantaneous Eulerian measurements. Figure 3.12 shows the data that would be capable by performing this combination. In the previous implementation of Grid-FLEET, 6 mJ of energy was needed to produce 16 simulataneous points. By combining high-frequency excitation, only the first row of points in the grid needs to be drawn, reducing the amount of energy required to create gridded measurement.

While the laser technology to allow multi-point measurements at 1 MHz is still being created, this process is well on the way. At a minimum pulse energy of 300 μJ/pulse/point, improvement of the laser up to 3 mJ/pulse will be able to provide up to 10 simultaneous tag points. By continuing to follow these points as they convect through the flow, grids of up to 10x10 can be created, which will greatly extend the flow measurement capabilities of the technique.

3.1.5 Recommendations

This section details advances in understanding low-excitation energy FLEET and how advances in burst-mode laser technology can be leveraged to make high frequency measurements. In this work, accurate measurements at 1 MHz were made in an atmospheric pressure supersonic jet utilizing only 120 μJ/pulse. The laser that was utilized was adapted from a previous project in which higher levels of energy were not ultimately necessary. The test section was optimized to allow for simple implementation of FLEET in terms of optical access and high working pressure, to maximize possible signal. With more practical test sections such as high-speed wind tunnels, the working pressure will be lower, and the necessary stand-off distance for focusing optics will be larger.

In order to adapt the technique to high-frequency measurements in larger, lower pressure facilities, the minimum excitation energy will increase. At the least ideal conditions presented in this thesis, the minimum excitation energy per point is around 500-700 μJ/pulse. At 1 MHz repetition rate, this is well above the upper limit of energy capability of the currently operational quadruple pass femtosecond burst mode laser. Decreasing the repetition rate to 100-200 kHz, this figure comes closer into reach, but is still slightly above the maximum capability of the system.

While the work in this thesis does not involve development of advanced laser systems, it directly informs the desired outcomes of this technology path. During the course of this work, proper constraints on the energy requirements for burst-mode femtosecond lasers have materialized. It will become necessary to switch from multi-pass amplification to a regeneratively-amplified laser system in order to extract the maximum pulse energy for FLEET. This work is underway at Purdue University, and the theoretical maximum energy

output of the system in on the order of several mJ/pulse at 1 MHz. With all of the benchmarking and diagnostic development to evaluate measurement capabilities, this system will be capable of implementation directly into hypersonic test facilities when it comes online. This will allow the immediate measurement of highly-transient phenomena in high-speed ground test facilities.

3.2 Adaptation to Reacting Flows

3.2.1 Motivation

FLEET has been shown to work well in relatively low temperature air and nitrogen environments for aerodynamic characterization of flow fields. The previous sections have described in detail the work put forth to further increase the data output and application capability of the FLEET method to more complex aerodynamic environments. One large problem still remaining is the application to non-air/N_2 and reacting environments. While inert flow wind tunnels provide a large fraction of the hypersonic ground testing capability, there are a number of ground test facilities that consist of reacting environments. Among these are high temperature combustion assisted facilities such as the NASA Langley 8 ft High Temperature Tunnel (HTT) [98] and arc jet facilities such as the Aerodynamic Heating Facility (AHF) at NASA Ames Research Center [99].

The architecture of combustion assisted facilities resembles that of traditional blowdown hypersonic tunnels with a few differences. Upstream of the test section, instead of a pressurized inert plenum, a high pressure combustor is present. Here, propellants are injected and burned to produce a flow with high stagnation temperature. These test facilities can be used to evaluate the performance of hypersonic propulsion system models. Arc jet facilities utilize electrodes to produce high levels of enthalpy in the flow to provide environments similar to re-entry conditions for spacecraft materials testing. These facilities created a flow consisting of highly ionized plasma. In addition to these types of hypersonic flow facilities, velocity measurements are desired in experimental hypersonic propulsion devices such as optical scramjets [100] and optical RDEs [15]. In all of these environments, the flow can consist

of air, nitrogen, unburned oxidizers and fuels, and combustion products such as water vapor and hydrocarbon compounds.

Previous research has been conducted to evaluate the performance of FLEET in nitrogen-containing combustion environments such as Methane-Air flames [75]. The thought behind applying FLEET to air flames is that the nitrogen will stay inert in the reaction and still remain free to be tagged as a tracer. Figure 3.13 shows the results from Deluca et al[75]. Compared to FLEET in inert environments, the lifetime of the signal is much lower, with a maximum lifetime of 631 nanoseconds. With this result, the longest a FLEET signal can be tracked in a flame is slightly longer than 1 microsecond. This is two orders of magnitude shorter than the >100 microsecond tracking possible in pure nitrogen. This result does not completely exclude FLEET from being used in this environment, but it does require measurement by single frame acquisition, or a camera with frame rate greater than 1 MHz to accurately capture the signal motion. Even with this, the SNR of the measurement will be rather low. For these reasons, an alternate molecular tagging technique for application to reacting environments is desired. In the proceeding sections, adaptation of a previously utilized molecular tagging technique involving dissociation and tracking of H_20 molecules is described.

3.2.2 Hydroxyl Tagging Velocimetry

Hydroxyl tagging velocimetry (HTV) is a molecular tagging technique that has been applied to inert air, humid air and flame environments [76], [101], [102]. This method is similar to the two-step MTV techniques described in the introduction to this thesis. First, a 'write' laser is used to photodissociate H_20 molecules into radicals of OH and H. The second 'read' laser performs PLIF on the tagged volume of OH radicals at a time delay. While OH-PLIF signal can be observed from the background of humid air, and even more in flames, the photodissociation laser produces a locally much higher concentration of OH which stands out in intensity above the background level. In typical HTV experiments, a 193 nm ArF excimer laser is used to dissociate the water molecules. This laser has a typical pulse energy of 10 mJ and a pulse duration of 10 ns[102]. For many applications the write laser is split into a crossed grid of beams to improve spatial resolution of measurements. The

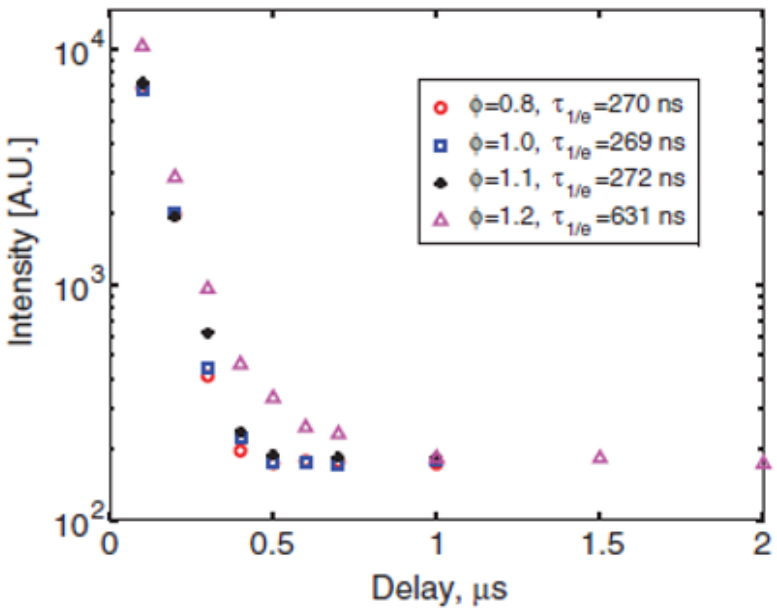

Figure 3.13. Time-decay of FLEET signal at various equivalence ratios in a Methane-Air Flame [75].

ArF excimer laser has a wavelength that is highly absorbed by water molecules, but is not tuned to any specific absorption peak. This implies that the technique, similar to FLEET, can be performed across a wider range of excitation wavelengths. For the read laser, either a 248 nm, or 283 nm wavelength laser is used. This can be either an excimer laser system or a dyed Nd:YAG system. This laser is used to induce laser fluorescence in the OH radicals. For this laser, the wavelength must be finely tuned to the correct wavelength to induce OH fluorescence for maximum signal. The read laser is pulsed at a time delay, often a one or several microseconds after the write laser to allow movement of the tagged volume. To perform more accurate measurements, the read laser can be multi-pulsed to provide multiple observations of the tracer radical motion. This requires a doublet-based [103] or burst-mode dye laser system [104].

3.2.3 Proof-of-Concept

While ArF excimer lasers have generally fallen out of favor in the research industry due to their poor beam quality, large size, operating costs and maintenance needs. Some of these

aspects of poor reputation are undeserved, and excimer lasers can produce high pulse energies in the ultraviolet spectrum which is desirable for many laser diagnostics. Another drawback of using excimer lasers to perform laser diagnostics is the repetition rate limit. Many excimer lasers have been limited to operation at 10 Hz, although some commercial systems can reach 500 Hz − several kHz. A few decades ago, this was sufficient for laser diagnostics applied to statistical measurements as high speed cameras were difficult to acquire and high speed lasers were not largely available. Now, with the advent of burst mode lasers and high-speed CMOS cameras, laser diagnostics have improved to rates up to and exceeding 1 MHz.

Femtosecond lasers have become increasingly more desirable for laser based diagnostics in recent years. Although the dominant repetition rate of 1 kHz is not exceedingly high, it can produce data at a much higher rate than a 10 Hz system. Additionally, the high peak power available from a femtosecond system allows non-linear diagnostics to be performed with lower pulse energies. As these laser systems become more popular, the commercial development and improvement of the platforms will continue. For this reason, the use of a 1 kHz femtosecond laser to perform the H_2O photodissociation of H_2O for hydroxyl tagging velocimetry is investigated with a proof-of-concept experiment. The method is entitled Femtosecond Laser Activation and Sensing of Hydroxyl (FLASH), and is theorized, analyzed, and applied as a portion of this thesis.

The first proof-of-concept to validate this method was a spectral analysis of the femtosecond laser interaction with an H_20 containing environment. This result is shown in Figure 3.14 for dry and humid air, as well as nitrogen. The OH emission manifold is clearly seen in the air cases, and absent in the nitrogen result. The nitrogen spectrum is collected from a pressurized source, so the overall intensity is higher. The individual peaks of OH improve in intensity when the air is humid. With this result, convincing proof was obtained that FLASH was a feasible molecular tagging technique.

3.2.4 *Femtosecond laser activation and sensing of hydroxyl (FLASH) for velocimetry in high speed reacting flows*

After proof of concept was performed, a set of evaluation experiments to understand this technique were conducted, and the results arranged into a publication entitled '*Femtosecond*

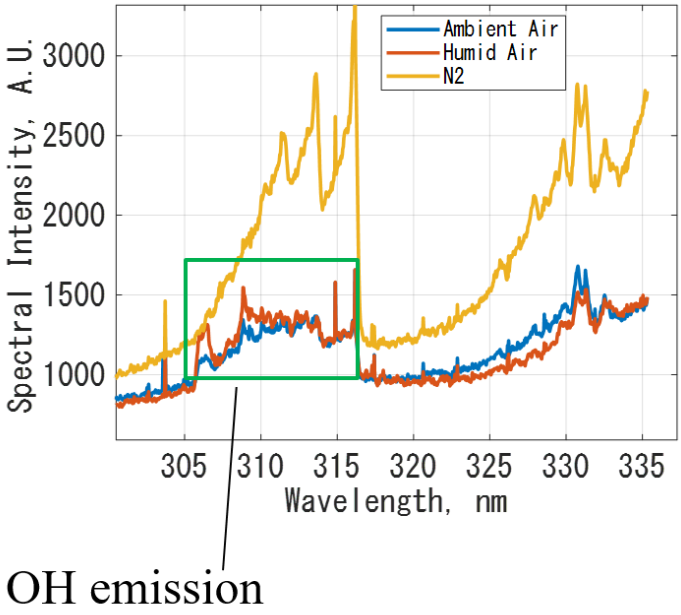

Figure 3.14. Spectrum results of femtosecond laser excitation in nitrogen, ambient air and humid air.

laser activation and sensing of hydroxyl (FLASH) for velocimetry in high speed reacting flows' which has been accepted for publication in Applied Optics, pending minor revision. The following sections are an adaption of this manuscript.

Abstract

A molecular tagging method for velocity measurements in high-speed reacting environments such as propulsion devices and high-temperature combustion-assisted wind tunnels is described. The method employs a femtosecond (write) laser to photodissociate H_2O, a common combustion product, into a locally high concentration of OH radicals. These radicals are tracked by fluorescence from the $A^2\ \Sigma$ - $X^2\ \Pi$ (1-0) vibrational band excited by a time-delayed 284 nm (read) laser sheet. Signal lifetime is studied in a hydrogen-air Hencken burner operating at Φ=0.5-1.8 to demonstrate tracking capability for velocimetry in a varied range of conditions. Effects of changing read laser wavelength, excitation energy and influence of background flame emission are also studied. Processing methodology and results are described for velocimetry in a hydrogen diffusion flame. This method provides an

avenue for improvements in the repetition rate (up to 1 kHz), precision, and applicability over previously demonstrated hydroxyl tagging schemes.

Introduction

Experimental characterization of the flow present in high speed propulsion systems relies on accurate *in situ* velocity measurements. The complex construction and operation of gas turbines, scramjets, rockets and rotating detonation engines creates harsh environments where many conventional measurement techniques may experience difficulty. In subsonic and non-reacting environments, physical sensors such as hot wires and pitot probes can be introduced into the flow to make measurements. In high speed regimes, these methods may become unreliable because of their large size and intrusiveness into the flow field. When the flow field is non-inert, the high temperature and flame products can pose harm to the physical sensor. Thus, implementation of physical probes is generally limited for measurements in propulsion test devices.

To combat these problems, a number of optical velocimetry methods have been investigated for implementation in high speed reacting environments. Among these techniques are Particle Image Velocimetry (PIV) [105], Tunable Diode Laser Absorption Spectroscopy (TD-LAS) [106] and Molecular Tagging Velocimetry (MTV) [85]. While both PIV and TD-LAS have their advantages in many applications the ability of MTV to acquire velocity vectors using molecules instead of seeding particles and at precise location benefits its application in high-speed flows.

MTV describes a multitude of techniques in which lasers are used to excite fluorescence from packets of molecules as tracers. These can be imaged and used for velocity measurement in a time-of-flight arrangement. Since the molecules being tracked have the same inertia as the flow under study, the packet being tracked will respond instantaneously to strong spatial velocity gradients, thus mitigating the lag effect present in particle based techniques. This makes MTV methods attractive in high speed flow environments. For inert flows, there are a large number of MTV techniques that are either seeded [45], [46], [91], requiring introduction of a tracer species, or unseeded [27], [47], [92], [94], utilizing a species that is native to the flow. The general method of molecular tagging that has been applied in

reacting environments is known as Hydroxyl Tagging Velocimetry (HTV), which involves photodissociating water into OH radicals for tracking. HTV was first demonstrated by Boedeker [76] to show capability of velocimetry in the exhaust of the Space Shuttle Main Engine. The method was continued and extended by Wehrmeyer and the Pitz group [102] at Vanderbilt University. Previous applications of the technique include measurement in the exhaust of a J85 turbine **Perkins2009Dual-PulseExhausts**, [107], a combustion-driven shock tube [108], a scramjet combustor [109] and the exhaust of a peroxide monopropellant thruster [110]. These previous works have all been applied at 5-10 Hz repetition rate with deep-UV excimer lasers producing the tracer photofragment. In this work we demonstrate Femtosecond Laser Activation and Sensing of Hydroxyl (FLASH), an adapted version of the general HTV technique promising advances in the repetition rate up to 1 kHz, precision of measurements, and ease of implementation over the previously described methods by leveraging recent advances in femtosecond laser and burst-mode optical parametric oscillator (OPO) technologies.

Background

In a review of the previous literature, it becomes clear that there are a number of ways to perform HTV measurements. Common to each method are two necessary steps: the write step, and the read step. In the write step, a focused laser is used to dissociate molecules into a photofragment consisting of a locally high concentration of OH radicals. After a sufficient amount of time, the photofragment will travel a perceptible distance that can be tracked with a spatially calibrated camera. The read step is necessary to induce fluorescence of the OH radicals so they can be imaged. The read laser is tuned to one of the many OH transitions in the ultraviolet spectrum. The planar laser-induced fluorescence (PLIF) signal induced by the read laser occurs in the 306-325 nm range. Through surface fitting, velocity is calculated by measuring the displacement of the photofragment over delay time between the write and read steps.

In the first HTV work by Boedeker in 1989 [76], the write step was performed with a 248 nm KrF nanosecond excimer laser with a pulse energy of 150 mJ. The read step was performed with a dye laser pumped at 10 Hz with an Nd:YAG laser to excite the $Q_1(3)$

transition of OH at 308.154 nm. Images of the OH motion were captured on a vidicon with 40x40 channel resolution. While these experiments proved the concept of HTV, the technology available at the time limited the accuracy, precision and applicability of the technique. Further research on HTV was conducted by Wehrmeyer [102] and Pitz [101] beginning about ten years later. In this case the write laser step was performed with a 193 nm ArF laser system. At this shorter wavelength, water molecules are more susceptible to laser absorption leading to an increased dissociation efficiency. This allows the method to be performed with 8 mJ per pulse or lower. Ribarov [111] investigated using read lasers centered at 248, 284 and 308 nm to access and compare multiple OH transitions. It was determined that the 308 nm transitions yield the highest level of signal, but is subject to light scattering interference since this overlaps the OH-PLIF emission wavelength band. For this reason many experiments now utilize 284 nm excitation for the read laser. Additional improvements to the method included implementation of grid-based tagging with multiple beams [112], [113], dual-read laser configurations to mitigate uncertainty from facility vibrations **Perkins2009Dual-PulseExhausts** and vibrational OH formation [114] to increase signal-to-noise ratio. Each of these measurements were conducted at 5-10 Hz repetition rate due to limitations laser and/or camera capabilities.

The main difference between FLASH and the previous HTV experiments is the write laser which is used. Each of the former works utilized nanosecond UV excimer lasers to dissociate water molecules. In FLASH, an infrared femtosecond laser at 800 nm is used to create OH photofragments. While is less susceptible to laser absorption at 800 nm, the increased peak power available in the shortened femtosecond laser pulse allows FLASH to be performed with write laser energies as low as 1.4 mJ. Higher harmonics of the fundamental wavelength at 400, 267 and 200 nm may produce higher signal at decreased laser energies, but this is not investigated in this work. The femtosecond laser has a repetition rate of 1 kHz as opposed to the previously used 10 Hz rate in HTV measurements. While excimer lasers are available which can achieve this repetition rate, recent increases in the implementation of ultrafast non-linear diagnostics drive the continual increase in femtosecond laser technology with respect to repetition rate and pulse energy [74] making this an attractive avenue for further study. The 800 nm beam produced by the femtosecond laser is also better suited

for use in practical test sections because it can be propagated with more efficient mirrors, focusing optics, and transmissive glass materials; whereas deep-UV optics for 193 nm can deplete energy significantly over the beam path.

Evaluation of Technique

To determine feasibility of the FLASH measurement technique, a demonstration experiment was conducted across a wide range of flame conditions to evaluate signal intensity and tracer lifetimes. An H_2-Air Hencken burner is used as the basis for the demonstration to provide a controlled environment. In order to prove valid in applied reacting environments, the signal must be present with sufficient intensity and signal-to-noise ratio (SNR) at extended read laser delays in a large range of equivalence ratios. Signal intensity is obtained from fitting the images to a two-dimensional curve-fit, which also gives outputs of spot length and width, signal centroid location, and R^2 to analyze signal quality. SNR in all data sets is defined as the ratio of the maximum signal intensity from the analytic curve fit, to the standard deviation of intensity over a 50x50 pixel region around the signal. A lower SNR threshold of 5 is imposed from Rose [89] to determine when signal is insufficient for reliable tracking. This criterion similar to what is used in previous HTV measurements [111], [115]. For optimization of the method, an accurate understanding of the minimum laser energies for the write and read steps must be obtained.

Experimental Arrangement

The experimental arrangement can be viewed in Fig. 3.15. The hydrogen, air and nitrogen co-flow are supplied to the burner by OMEGA mass flow controllers giving control over the flow rate and equivalence ratio of the flame. Dissociation of H_2O is performed by a Ti:sapphire femtosecond laser (Spectra Physics Solstice:Ace). The laser wavelength is 800 nm, pulse duration is 80 fs, maximum pulse energy is 7 mJ per pulse, and the maximum repetition rate is 1 kHz. For this demonstration the laser is pulsed at 10 Hz with an energy from 1.0 - 5.3 mJ per pulse. An f = +300 mm lens focused the write laser to a theoretical waist diameter of 33.6 μm and a theoretical irradiance range of 1200-6500 TW/cm^2. This is

5-6 orders of magnitude more irradiance as estimated from previous works [102] owing to the reduced photodissociation efficiency at 800 nm. A frequency-doubled 10 Hz Nd:YAG laser pumps a dye laser (Continuum ND 6000) to produce 568 nm yellow laser light. The dye laser output is frequency-doubled to 284 nm in a 5 mm long Type I BBO crystal to induce OH-PLIF from the dissociated H_2O. The energy of the UV output is 0.01-2.0 mJ per pulse. An f = +200 mm spherical and f = -50 mm cylindrical lens combination forms the beam into a thin sheet (about 35.6 μm by 1.075 cm) at the probe location. A Berkeley Nucleonics delay generator synchronizes an input pulse from the femtosecond laser to trigger the dye laser and imaging system at a programmable time delay. A Photron Fastcam SA-Z CMOS high speed camera is coupled to a LaVision UV-IRO to create the imaging system. The camera lens is a Cerco 45 mm UV lens with a 14 mm extension ring to provide increased magnification of the signal. To isolate the PLIF emission wavelengths, a Semrock filter with a 40 nm FWHM and a 320 nm center wavelength is used. A constant-illumination calibration is performed across the imaging system operating space so that signal intensities can be directly compared even when camera settings are changed between data points.

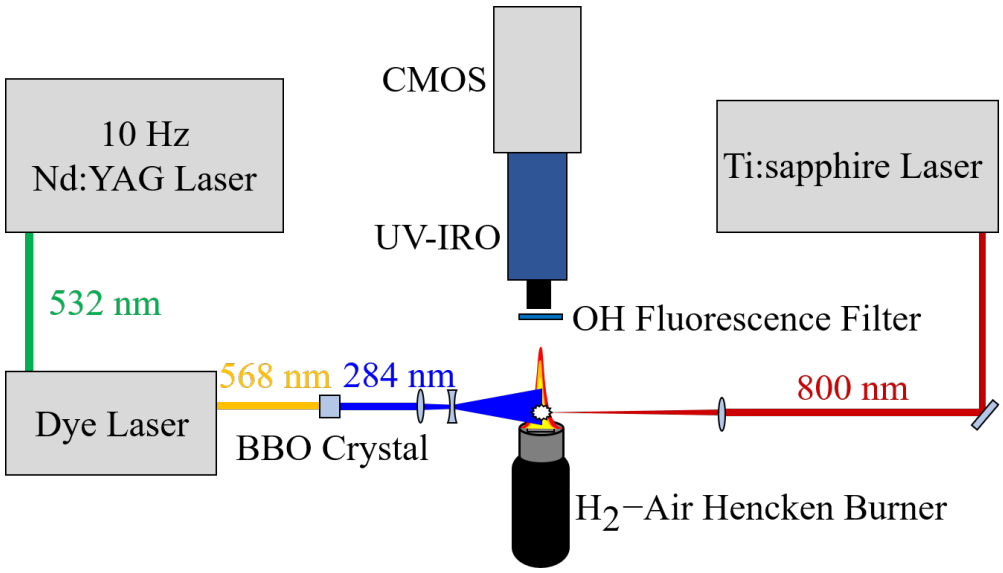

Figure 3.15. Experimental setup for demonstration of FLASH velocimetry in an H2-air Hencken Burner.

OH Transition Wavelength Tuning

The read laser is initially tuned to target the $Q_1(9)$ absorption line of the OH $A^2\Sigma$ - $X^2\Pi$ (1-0) vibrational band. This peak is centered at a frequency of 35210.64 cm^{-1} (284.005 nm) and slightly overlaps the $Q_2(8)$ absorption line at 35210.15 cm^{-1}. To maximize the OH-PLIF signal, and to ensure that fluorescence is not coming from any unknown sources, a wavelength scan over the transition was conducted. A high precision wavelength meter (HighFinesse, WS7-60) captures the the 568 nm output from the dye laser, and the excitation wavelength is calculated by halving the measured value. The results are shown in Fig. 3.16, where peak signal intensity is plotted against read laser frequency. To estimate the signal variation with wavelength, the data points are fit to a Gaussian profile. The peak of this fit occurs at 35210.44 cm^{-1}, with a FWHM of about 0.8 cm^{-1} and an R^2 >0.99. Due to the laser linewidth of 0.18 cm^{-1}, the thickenes of the signal peak is due to the convolution of the $Q_1(9)$ and $Q_2(8)$ transitions. Far from the wavelength of the transition pair, the signal falls near zero showing there is no luminescence from non-OH sources interfering with the measurement. Following this result, the read laser frequency is set at 35210.44 cm^{-1} for the duration of the experiment and closely monitored for drift.

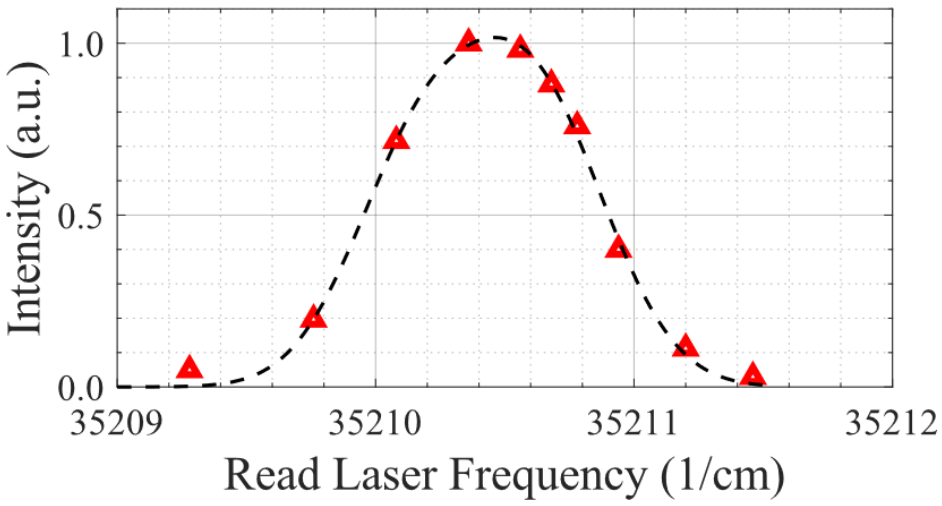

Figure 3.16. Wavelength tuning of the read laser sheet over the OH $Q_1(9)/Q_2(8)$ transition pair.

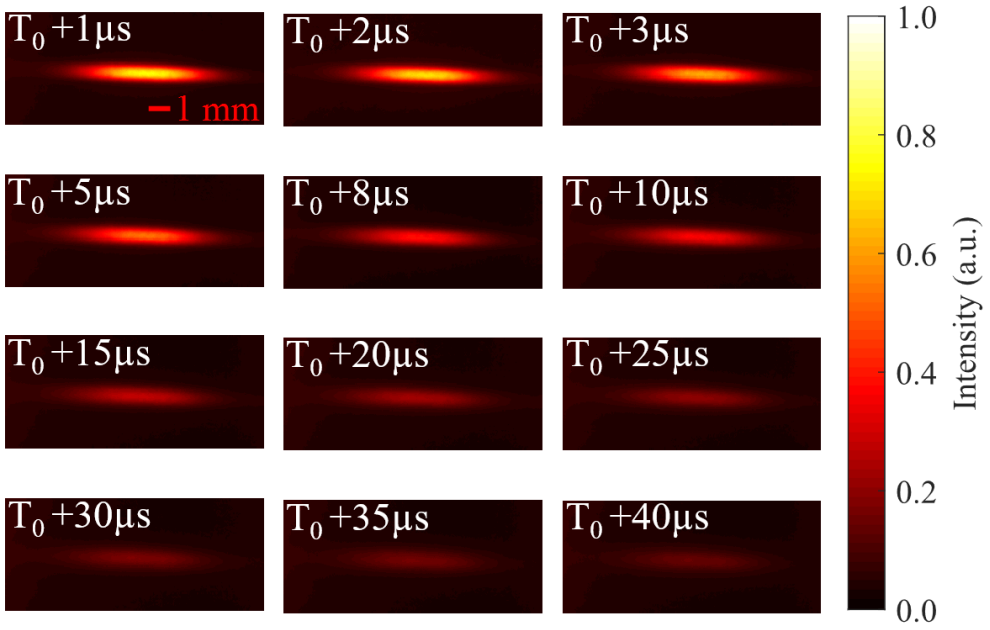

Figure 3.17. FLASH raw data at select read laser delays at $\Phi = 1$. All images are 50-data point ensemble averages.

OH tracer lifetimes

After the wavelength tuning, the raw data images are evaluated to gain an understanding of the general signal quality. Figure 3.17 shows images of the FLASH signal across read laser time delays from 1-40 μs. These data are collected at stoichiometric conditions in the Hencken burner, with write and read laser energies of 5.0 mJ/pulse and 2.0 mJ/pulse, respectively. The images shown are 50-image averages to reduce the impact of laser timing jitter, however the instantaneous data show minimal shot-to-shot variation. The intensity is normalized to the maximum intensity of the $T_0 + 1$ μs image to show the full dynamic range of the data.

The FLASH signal intensity shows a gradual decay with increasing read delays which is to be expected. Sufficient intensity is observed at the largest time delays meaning that the OH tracer is long-lived and well suited velocimetry. The shape of the signal does not degrade significantly over the long delay time. For high speed molecular tagging measurements, signal lifetimes in the range of 5-40 μs are generally sufficient [13], [27], [116].

To ensure that FLASH is viable across a sufficient range of flame conditions, the equivalence ratio of the Hencken burner is varied from 0.6-1.4. First, FLASH is performed in the reaction zone about 3 mm from the burner surface. Images of the signal are taken with read laser time delays from 1-150 μs. The energy for the write laser is held constant at 5.0 mJ per pulse, and the read laser energy remains at 2.0 mJ per pulse. The results of this study can be seen in Fig. 3.18. Long-lived tracer signal is observed across all equivalence ratios in this test. It is clear that the tracer decay rate increases with increasing Φ.

This same experiment against equivalence ratio was repeated in the post-flame region at a distance of 30 mm above the burner plate, where the temperature is lower and more flame products have formed. Fig. 3.19 shows these results for (a) rich and (b) lean conditions. The rich equivalence ratio signal decays appear similar in trend to the results from the reaction zone of the flame. Peak intensity and signal lifetime decrease as equivalence ratio increases. In Fig. 3.19 (b) the results are more surprising. At the most lean conditions of Φ=0.5-0.7, the signal increases after an initial short decay. The intensity reaches a maximum between 20-40 μs before decreasing again. In both cases, the improvement of signal at lower equivalence ratios is described by Wehrmeyer et al. [117]. In lean flames, there is an excess

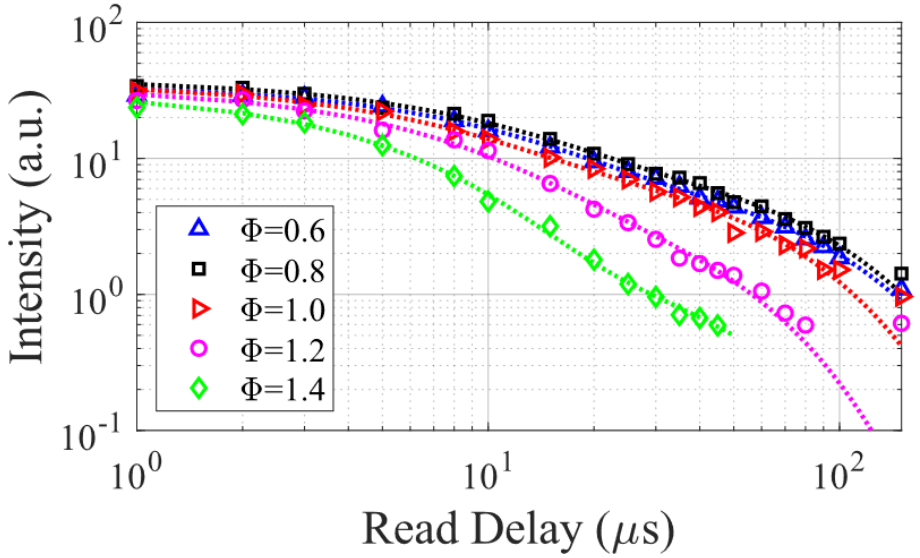

Figure 3.18. Peak FLASH signal intensity as a function of tag delay for various flame equivalence ratios. Data collected in the reaction zone of an H_2-Air Hencken burner.

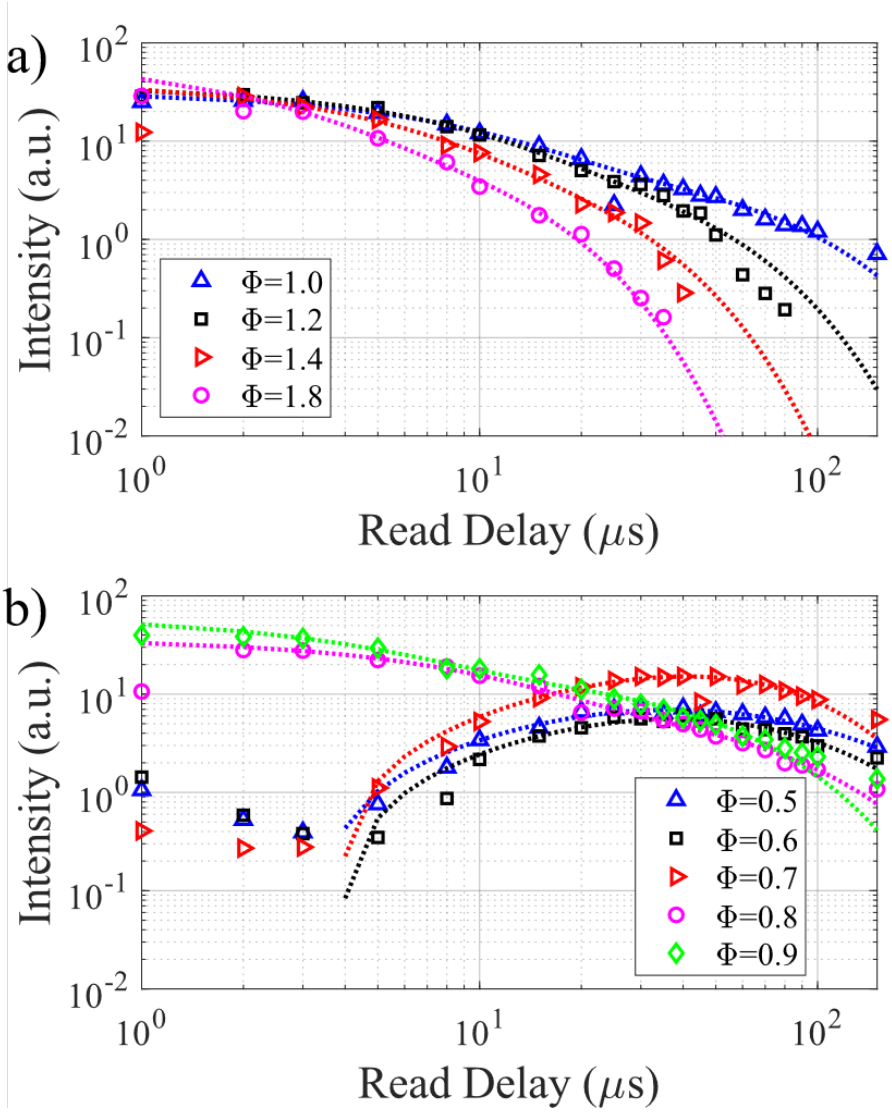

Figure 3.19. Peak FLASH signal intensity as a function of tag delay for a) stoichiometric and rich equivalence ratios, and b) lean equivalence ratios. Data collected in the post flame region of an H_2-Air Hencken burner.

of O_2 which reacts with the atomic H produced by photodissociation, in turn producing OH. In rich flames, the excess of H_2 tends to destruct OH by producing H and H_2O, thus reducing signal.

To quantify the decays, the peak signal intensities are analytically fit to double-exponential decay profiles. By evaluating these curve-fits the signal lifetime, $\tau_{SNR=5}$, can be defined as the time it takes for the signal to degrade to the lower SNR threshold of 5. This lifetime is shown for all conditions in Fig. 3.20, and the curve fit coefficients are listed in Table 3.1.

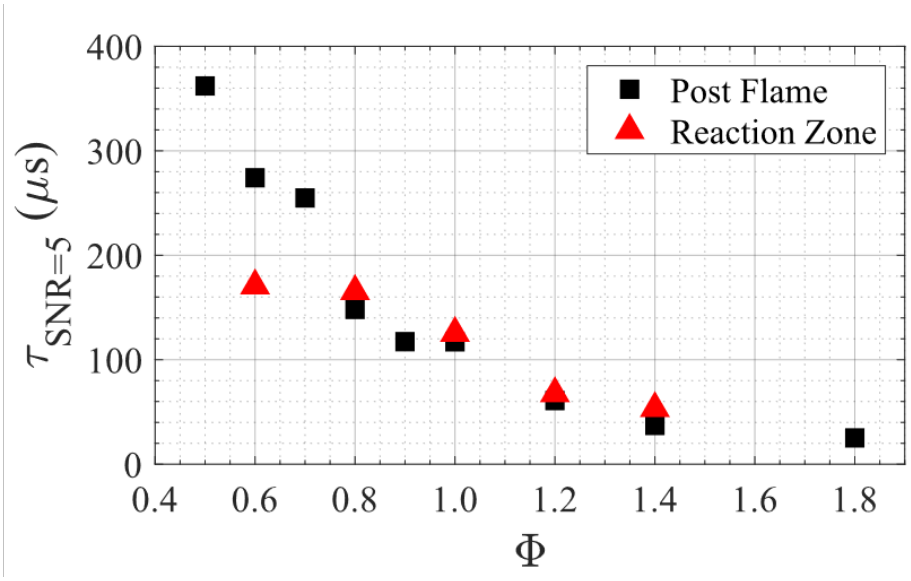

Figure 3.20. Signal lifetimes vs equivalence ratio in reaction zone and post flame regions.

In the reaction zone, the signal lifetime decreases from 170 μs as Φ=0.6 to 53 μs at Φ =1.4. In the post-flame region the decrease in lifetime is even more pronounced, from 360 μs at Φ=0.5 to 25 μs at Φ=1.8. From Φ=0.8-1.4, the signal lifetime remains relatively unchanged between the reaction zone and the post-flame region. In the very lean case of Φ=0.6, the signal lifetime is largely extended due to the initially increasing signal levels.

Read and Write Laser Energy Scaling

An important parameter for scaling the implementation of FLASH is the behavior of the signal over a range of write and read laser energies. At stoichiometric conditions in the reaction zone of the Hencken burner the write laser energy was varied while holding the read laser energy constant at 2.0 mJ per pulse. These results are displayed in Fig. 3.21 (a), alongside the lower SNR threshold of 5. The peak signal levels from Gaussian surface fitting are shown for real delays of 2, 10 and 20 μs. At energies above 2 mJ, the trend is linear, as shown in Fig 3.21 (a) as dotted lines, but the intensity trend deviates from linear below 2 mJ. At a write laser energy of 1.8 mJ, the SNR reaches the lower threshold at a read delay of 20 μs. For focusing with an f = +300mm lens, this is the lower write energy limit for the measurement technique. With shorter focal length lenses, the energy limit could be decreased

Table 3.1. Double exponential fit coefficients for all experimental conditions

Exponential Coefficients: $Ae^{\tau_1 t} + Be^{\tau_2 t}$				
Equivalence Ratio	A	τ_1 (μs)	B	τ_2 (μs)
Reaction Zone				
0.6	25.81	8.96	9.41	63.49
0.8	26.65	8.65	11.52	61.63
1.0	25.51	6.36	10.66	46.32
1.2	26.98	6.28	6.88	29.11
1.4	29.34	4.88	2.21	33.50
Post Flame Region				
0.5	11.12	109.75	-13.61	14.31
0.6	11.60	78.94	-13.73	17.62
0.7	80.96	49.66	-85.69	28.51
0.8	8.45	62.27	27.91	8.29
0.9	17.82	39.86	43.43	4.04
1.0	25.36	7.92	6.33	55.68
1.2	28.57	6.50	8.36	26.62
1.4	30.51	4.00	10.35	13.66
1.8	51.47	1.84	14.94	7.18

by providing increased laser irradiance at the focal point. Burst-mode femtosecond lasers are currently in development [74] for demonstration of MHz rate molecular tagging [66], but the current maximum energy is around an order of magnitude lower (100-200 μJ) than what is required for FLASH. However, it is feasible that these technologies may advanced to usable energies for this method at increased repetition rates of 100 kHz-1 MHz in the near future.

Fig. 3.21 (b) shows how the peak intensity trends with a varying read laser energy. In this case, a constant read laser delay of 5 μs is used while read laser energy is varied. The Hencken burner is operated at Φ=1.0 and the write laser energy is 5 mJ. The trend between signal level and read laser energy here is linear. The SNR greater than 5 threshold for each data point is plotted as well. At lower read energies, the noise level decreases because there is less laser induced fluorescence from OH in the background flame. The lower energy data points deviate from the trend because there is a larger uncertainty in the measurement of energy in this range. The result of this study shows that FLASH can be performed with less than 50 μJ per pulse of UV read laser energy, which is an important observation for eventual

implementation of high-speed OPOs or dye lasers as the read laser where available energy is limited.

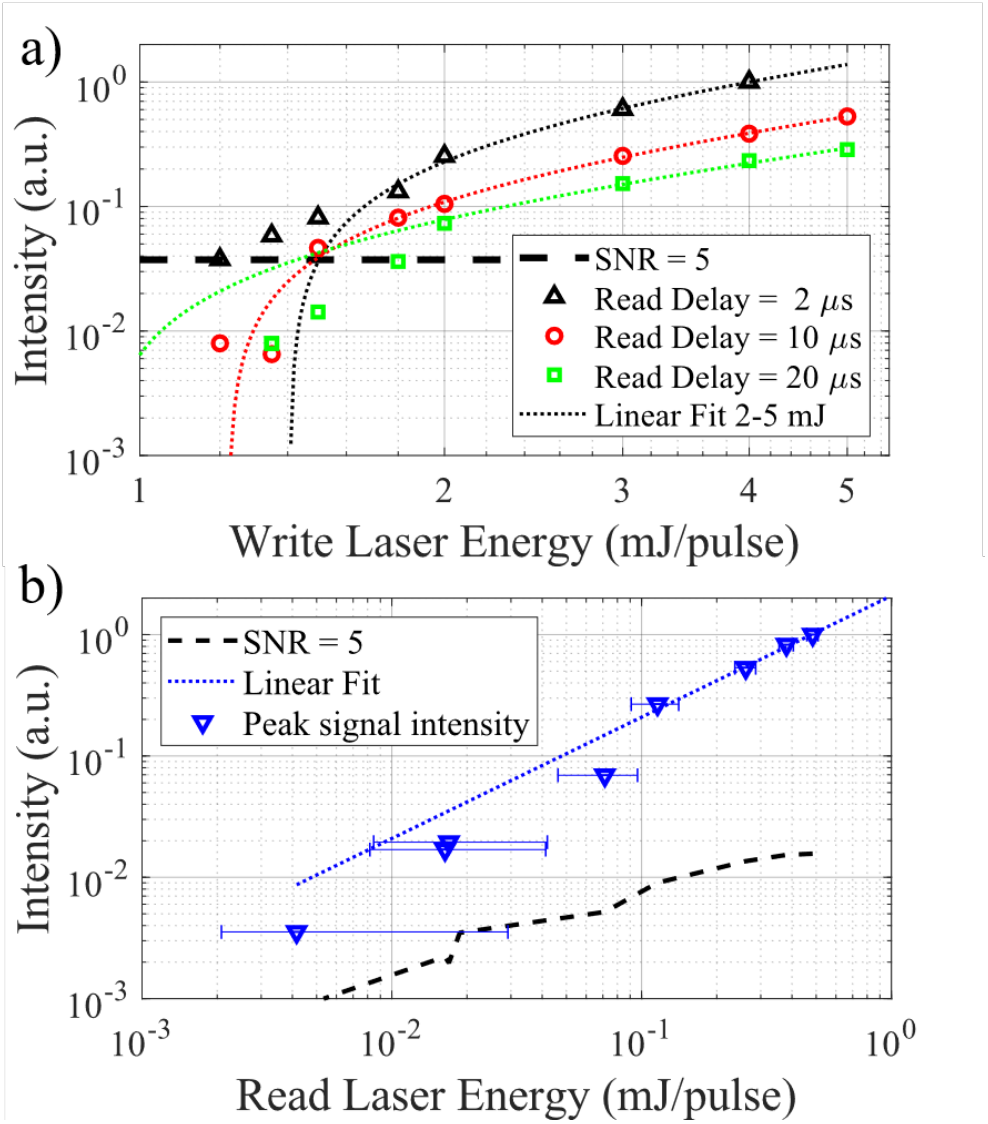

Figure 3.21. a) FLASH peak signal intensity vs write laser energy at read laser delays of 2, 10 and 20 μs. b) Peak FLASH signal vs read laser energy at 5 μs read laser delay, with write laser energy 5 mJ/pulse. All data sets taken at $\Phi = 1$ in an H_2-Air Hencken burner.

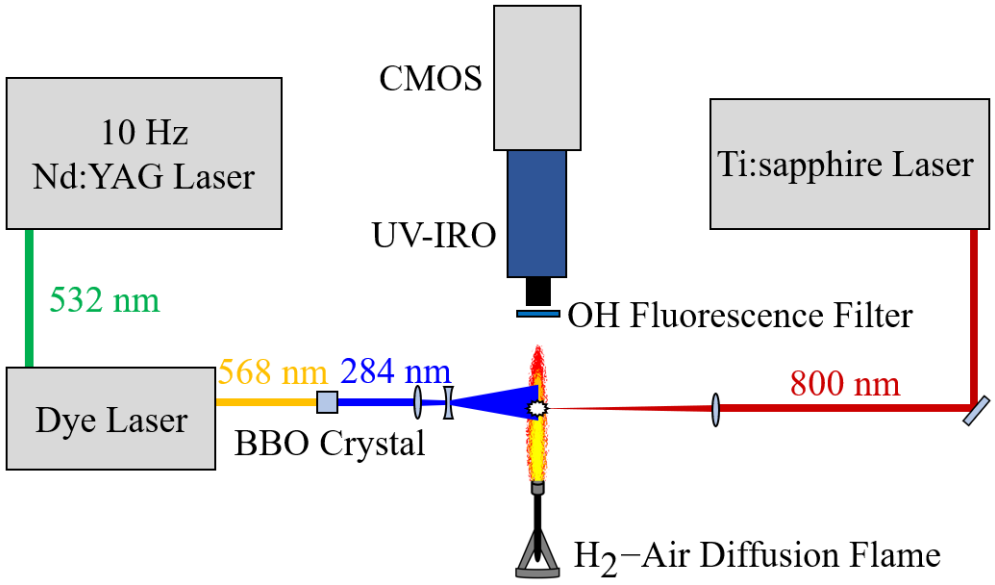

Figure 3.22. Setup for measuring velocity in an H_2-Air diffusion flame using FLASH.

Velocity Measurement

Experimental Arrangement

The experimental arrangement used in the technique evaluation section was modified to replace the Hencken burner with an H_2-Air diffusion flame, which is shown in Fig. 3.22. Hydrogen is supplied at 8 SLPM by an OMEGA mass flow controller. The exit diameter of the jet is 10 mm, giving an estimated exit velocity of 6.8 m/s with a Reynolds number of 350. The flame operates in the laminar regime, and the measurement location is 30 mm above the exit of the flame, where the velocity is estimated to be in the range 2-6 m/s. No-flow images capturing the FLEET emission present with the flame turned off are used to measure the location of the non-displaced line. With the flame running, FLASH data sets of 100 images were taken with read laser delays of 5, 15 and 30 μs. The write and read laser energies for this portion of the experiment are 5.0 mJ/pulse and 2.0 mJ/pulse respectively.

Data Processing

The read laser used in FLASH is able to excite fluorescence of the natural OH present in the flames being measured. This interference competes with the FLASH signal and can

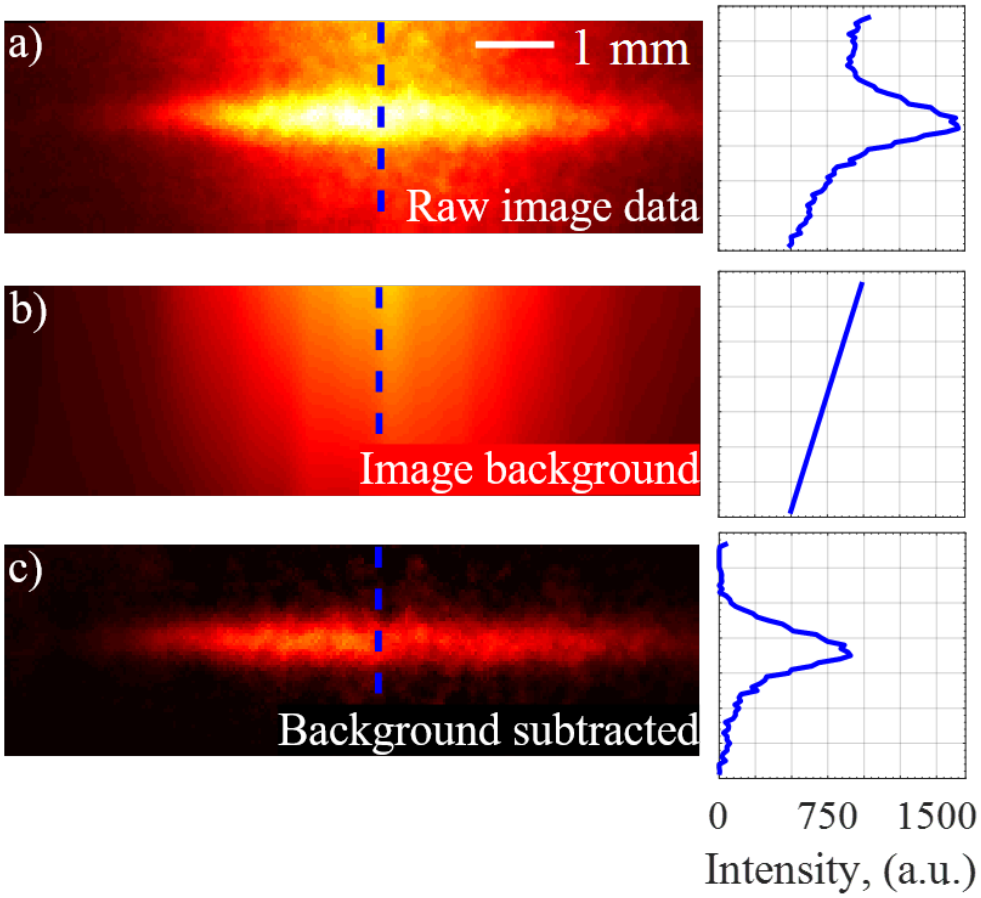

Figure 3.23. Single-Shot FLASH signal in an H_2 diffusion flame with a) no background subtraction, b) background isolation based on linear trend, c) FLASH image with background subtracted. Intensity profiles along dashed lines in (a-c) shown to the right of the images.

lead to unreliable measurements. In environments such as the Hencken burner, the equivalence ratio is controlled and the flame is rather steady with time. Thus, the acquisition parameters can be tuned to maximize SNR, and the background can be removed easily using time-averaged images. In comparison, the diffusion flame is less predictable. There are large shot-to-shot fluctuations in the flame-front location and equivalence ratio which have a large impact on SNR. Even with acceptable signal levels and SNR greater than 5, variable background intensity profiles can skew velocity results in unpredictable ways.

The first portion of the data analysis procedure is dedicated to robust removal of this background PLIF signal with spatial filtering. Figure 3.23 shows intermediate results of the background removal process, with the intensity profile of the centerline pixel row plotted to

the right of each image. Figure 3.23 (a) shows an instantaneous image of the FLASH signal in the diffusion flame environment. In this image, the FLASH tag line can be discerned, but the background PLIF signal intensity is half the magnitude of the peak FLASH intensity. To create a background image, the raw data is first filtered with a 5 pixel moving mean in the column-wise direction to lower the effect of random noise. For each column in the image, the background is assumed to vary linearly. A de-trending operation in MATLAB is used to separate the linear trend from the signal. The result of this operation is shown in Fig. 3.23 (b). Figure 3.23 (b) shows the result of subtracting the computed background image from the raw image. Through these filtering operations, the spurious intensity around the FLASH signal is eliminated and the peak intensity location of the signal can be reliably found.

After background removal is completed, the FLASH images are prepared for velocity processing. The images are first cropped to a small region around the signal to decrease computational cost of the displacement finding algorithms. The images are then rotated to align the signal with the horizontal axis (about 1.75 degrees). Figure 3.24 (a) shows an example of a pre-processed image for each read laser delay. There is slight vertical displacement of the signal as the read laser delay increases. In the low-density environment of the flame, the signal grows in diameter over time due to molecular diffusion, which can also be observed in Fig. 3.24 (a). The line appears the thinnest in the T_0 no-flow image because the density is higher with the flame turned off. The noise level is also higher because the intensifier gain must be increased to capture the lower level of fluorescence. To increase SNR, the images are horizontally binned to create one-dimensional intensity profiles representing the signal. These intensity profiles are fit with a Gaussian function which gives the peak intensity, signal width, and peak intensity location as outputs with sub-integer resolution. All pixels with intensities less than 50% of the maximum value of the profile are not considered for this fit. The binned intensity profiles of the images in Fig. 3.24 (a) are shown in (b), with the dotted lines showing the analytic curve fits, and markers showing discrete pixel intensity values. The location of peak intensity is also marked for each profile. The x-axis is converted to displacement in millimeters via a dot-target calibration image taken during the experiment. A displacement of zero millimeters corresponds to the location of the signal intensity peak for the flame-off image taken at T_0. The velocity is calculated by dividing the

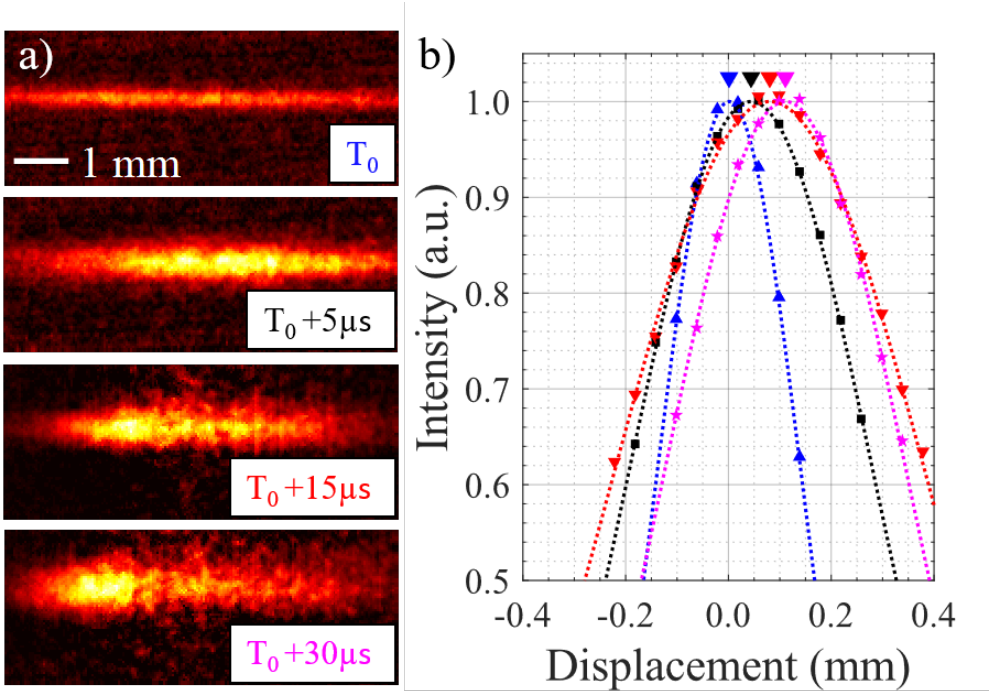

Figure 3.24. (a) Non-displaced and instantaneous images of FLASH signal at select read delays in an H_2-Air diffusion flame. (b) Horizontally-binned intensity profiles of images shown in (a).

displacement of the profile by the read laser delay of the image. An R^2 threshold of 0.8 is used to identify and discard outlier data points.

Figure 3.25 shows the measured velocity plotted against each read laser delay. The results are in the range of expected velocities for the diffusion flame, although no precise velocity comparison is available. As read laser delay increases from 5 μs to 30 μs, the mean velocity decreases from 4.3 m/s to 3.2 m/s. The error bars show the standard deviation over 100 samples for each time delay. Assuming the flame is steady, the standard deviation represents the precision of the measurement, which improves from 1.6 m/s at 5 μs read delay to 1.2 m/s at a read delay of 30 μs. For molecular tagging measurements, the precision is expected to improve with increased read delays, as described in [55]. The precision of these measurements amounts to about 37% of the mean flow velocity, which is relatively imprecise. This is due to the low magnitude of the flow in study, with respect to the error in Gaussian fitting of the signal. For molecular tagging techniques, as the magnitude of velocity increases, absolute uncertainty in centroid finding generally remains the same, which has the effect of improving

precision when measuring higher speed flows [27]. Typical precision of molecular tagging methods can be better than 1% in high-subsonic [21] and supersonic [66] regimes.

In the diffusion flame, the intensity of the FLASH signal decreases and the shape degrades as read delay increases. The right axis of Fig. 3.25 shows the percentage of outlier measurements for each read laser delay. It is more likely that images from longer time delays will not be sufficiently high in quality to achieve the R^2 threshold of 0.8 applied during Gaussian fitting. Between read delays of 5 μs and 30 μs the percent of outlier measurements increases from 1% to 10%. When designing experiments, it becomes necessary to consider the expected velocity, desired precision, and tolerable percentage of outliers to choose a read laser delay that yields the optimal result.

Conclusions and Future Work

This work describes an adapted method of molecular tagging to perform velocity measurements in reacting environments. A tracer packet of high OH radical concentration is written in the flow through dissociation with a femtosecond laser. Proof-of-concept experiments for behavior across different flame conditions and laser energies in an were shown

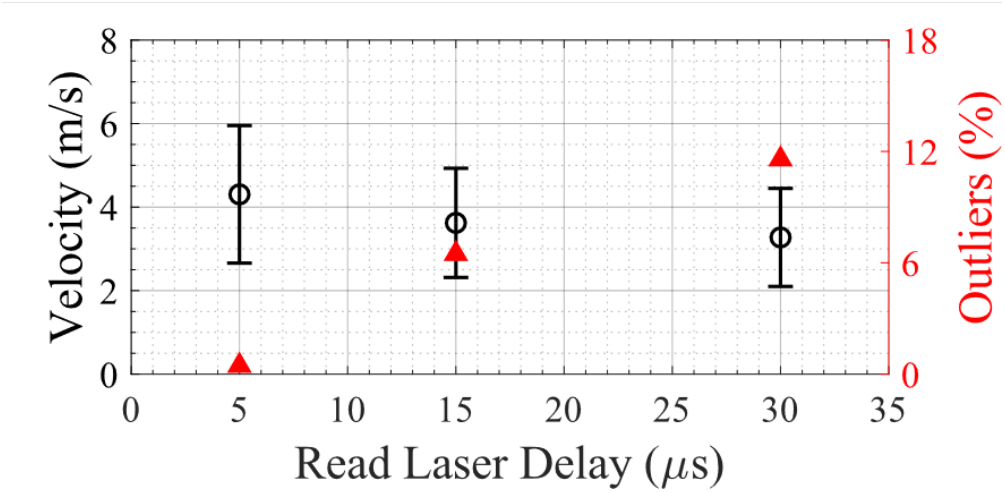

Figure 3.25. Measured flame velocity as a function of read laser delay (left axis). Uncertainty bars represent standard deviation of 100 instantaneous measurements. Percentage of outlier measurements as a function of read delay, determined by R^2 <0.8 (right axis).

using a 10 Hz dye laser for the read step. Using the same setup, velocity measurements are capable in a low-speed hydrogen diffusion flame. The femtosecond laser operates at 800 nm at up to 1 kHz repetition rates, which provides improvement of the measurement rate and applicability of the technique to complex test sections as compared to previous Hydroxyl Tagging schemes.

While the read step in this work was performed with a 10 Hz dye laser system, the wavelength and energy were controlled to represent the performance of an improved burst-mode optical parametric oscillator (OPO) similar to what is described in [104]. By extending the repetition rate of the read laser to the range of 100 kHz-1 MHz, multiple images of the motion of each photofragment can be achieved. In previous FLEET measurements [55], [118], it was shown that higher degree finite differencing between multiple signal observations can yield higher precision measurements. Additionally, in [27], it was shown that sequential observations of the same molecular tag can be used to make multiple streamwise velocity measurements. Thus, by utilizing a burst-mode OPO as the read laser, the precision and spatial resolution of FLASH measurements can be improved as well.

3.2.5 Advanced Write-Read Schemes for FLASH Velocimetry

FLASH has been proven as a possible alternative to FLEET for velocity measurements in humid and combusting environments. The method was demonstrated with a 10 Hz read laser and statistical analysis of the signal decay across the operating regime of a hydrogen-air Hencken burner. The results show the possibility of more than an order of magnitude improvement in tracer lifetime compared to FLEET measurements in flames.

In order to use this technique to produce meaningful velocity measurements, alternate write-read schemes must be employed. At a minimum, two separate location measurements of the spatial location of the FLASH-tagged OH packet must conducted with a known time delay in order to calculate velocity. The simplest option for conducting this with the technology currently employed is to perform the write and read steps at 10 Hz, with a fixed time delay (several microseconds) between. Fortunately, as shown in previous literature [75], there is short-lived FLEET emission on the order of 200-600 ns after the write step. This emission can be directly imaged by the camera without requiring the read laser. The short-

lived FLEET emission image can be used as a reference 'undisplaced' image of the tagged molecules. After a few microseconds, the read laser sheet can be used to illuminate the tagged molecules and produce a second 'displaced' image. This way, 10 Hz velocimetry can be conducted with FLASH.

A higher-complexity write-read scheme to be investigated requires the use of a burst-mode OPO to produce the read laser sheets. This system is currently in use at Purdue University, and capable of delivering sufficiently high pulse energies to perform OH-PLIF at repetition rates from 100 kHz-1 MHz. With this system, excitation can be performed at 1 kHz with the femotosecond laser, and the read laser can be fired at 1 μs intervals to follow the tagged molecules as they travel further downstream. This arrangement would allow for visualizing the changing of velocity as the tracer packet continues to travel along its streamline.

The last write-read scheme is the most complex, and mainly a theoretical assumption for future research. At 800 nm, the wavelength currently used for dissociation, water is not highly susceptible to laser absorption. This means the method is far from optimal in energy. Looking at the absorption spectrum in Figure 3.26 gives insight into possible alternate excitation wavelengths for water dissociation. Several orders of magnitude absorption are gained above 1000 nm and around/below 200 nm. While a 1 kHz femtosecond laser is capable of performing FLASH at 800 nm, burst mode short-pulsed lasers at alternate wavelengths such as 1064 nm and 266 nm [74] may be more efficient. With a wavelength-dependant signal study, if either of these excitation wavelengths prove more efficient, the possibility of conducting FLASH at write laser repetition rates of 100 kHz$-$1 MHz may be possible. This would open the door to greatly improving the measurement rate of the technique.

3.2.6 Application to RDE Exhaust Measurements

After the initial proof-of-concept and characterization experiments, enough evidence was observed to warrant an attempt at velocimetry in the Turbine-integrated High-pressure Optical RDE (THOR). With the complex coupled, and high frequency fluid dynamics occurring during the operation of THOR, CFD models struggle to estimate the flow state both in the combustion chamber and the exhaust plume. Accurate measurements in either of these are-

Figure 3.26. Absorption spectrum of water

nas will help to anchor and calibrate these models so that researchers are able to get better predictions of the RDE flow-state. The overall goal of the THOR RDE is to enable interfacing of a supersonic stator row that is capable of handling the high-temperature, high-speed inlet flow and extracting power. This makes the exit boundary condition of the RDE especially attractive for in-depth velocity measurement. Using two write-read schemes at 10 Hz and 1 MHz as described previously, the implementation of FLASH was investigated in the exhaust plume of the THOR RDE.

Experimental Arrangement

Delivering two laser beams to the correct measurement location with respect to the RDE becomes a significant concern. In order to measure axial velocity, the read laser sheet must be aligned in-plane with the flow direction. The desired measurement plane is the mid-section of the combustion chamber, oriented vertically, and intersecting the horizontal mid-line of the test article. With this measurement plane, both the axial and vertical components of velocity can be measured.

Figure 3.28 shows a labeled image of the experimental arrangement for this measurement campaign. The main difference between the 10 Hz and 1 MHz portions of this measurement setup is the camera that is used. For the 10 Hz experiment, a Photron Fastcam SA-z is utilized. For the MHz framing variant, a Shimadzu HPV-X is used. In each case, the camera is interfaced with a MHz framing capable UV-sensitive intensifier (Lambert HiCatt). A 320/40 bandpass filter blocks out background signal from sources other than the PLIF that is excited by the laser.

Both write and read lasers are stationed in an isolated laser laboratory to separate the equipment from the harsh vibration induced from the operation of the RDE. The write laser, as described previously, is a Spectra Physics Solstice:Ace operated at 100 fs pulse duration, 800 nm wavelength, and 6 mJ pulse energy. The beam is brought to to the test section horizontally, and focused with an f = +150 mm spherical lens. The read laser beam is produced by sending a pump laser through a custom-built OPO similar to what is described in [104]. In the 10 Hz arrangement, the OPO is pumped with a 10 Hz Quanta-Ray ND:Yag laser, and for the 1 MHz measurement, the OPO is pumped with a Spectral Energies Quasimodo burst mode laser. The beam is delivered to a breadboard at the horizontal level adjacent to the RDE, and then reflected to an optical rail that travels above the test section. A mirror is located directly above the measurement location which reflects the read laser directly downward. Lastly, an f = +200 mm spherical and f = -50 mm cylindrical lens focus the laser into a thin sheet across the measurement plane.

Timing Logic

The 10 Hz method of operation involves acquiring a single image of FLASH signal after a set time delay from the initial H_2O dissociation. This time delay is precisely controlled by an external delay generator as previously described, and is shown in Figure 3.27 a). The nominal time-delay used is either 2 or 5 μs. When only taking a single frame of displaced signal, a second non-displaced reference image is necessary to calculate the velocity. This reference image is obtained by taking a statistical average of the FLASH signal without the RDE running. There are three main advantages to taking data with the 10 Hz arrangement. In this setup, the camera resolution is 1024 x 1024 pixels, allowing maximum magnification

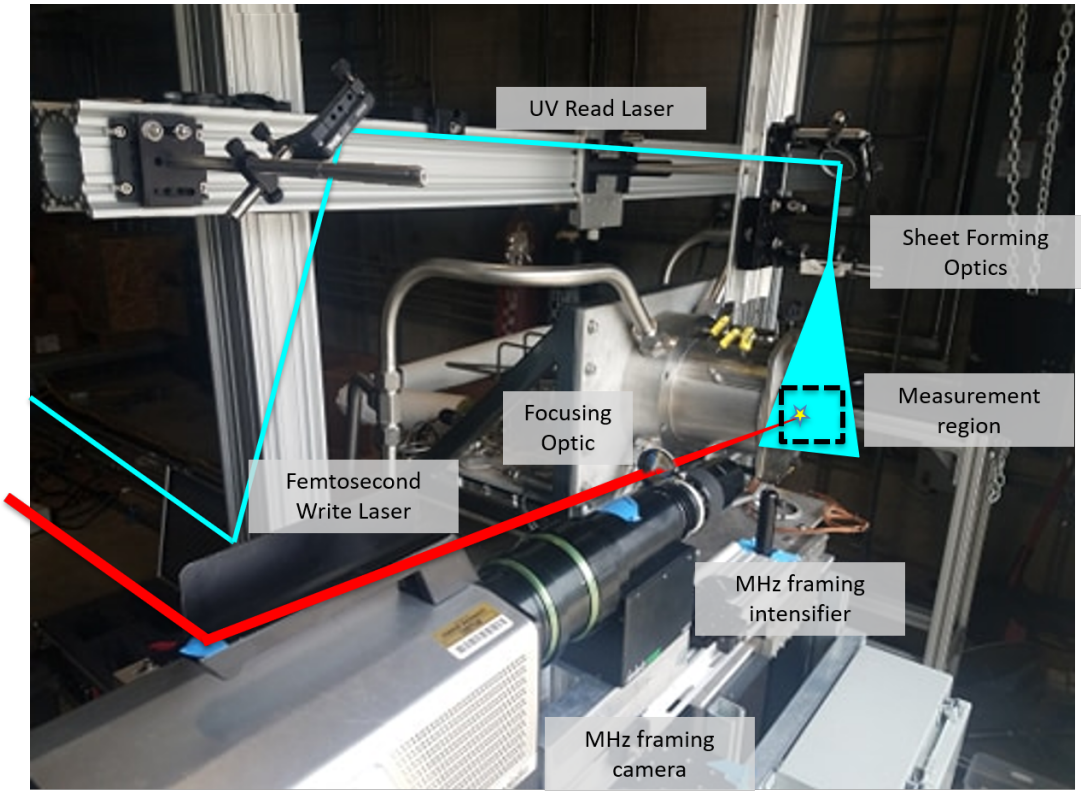

Figure 3.27. Optical Arrangement for Demonstrating FLASH in the THOR RDE

of the measurement region. The 10 Hz laser generally has 300-400 μJ of energy per pulse, which is twice as much as the burst-mode laser is capable of. The 10 Hz pump laser and OPO combination is more stable than the burst-mode system, making the experiment more reliable to setup and perform. Lastly, the continuous 10 Hz pulsing allows 10 measurements per test which significantly improves the rate of independent observations available for statistical interpretation of the system, since the RDE can only run for 1 second at a time.

The 1 MHz FLASH experiment timing logic is shown in Figure 3.27b). In this arrangement, the burst mode laser allows for capturing 5 sequential images of the FLASH signal with 1 μs spacing after the initial H_2O dissociation. Here, the measurement relies on the initial FLASH image in the burst as a reference for non-displaced location, and the rest of the frames as successive displacement observations. The benefit in this arrangement is that there is no independent reference image necessary for calculation of velocity. Additionally, the multiple displacement observations, acceleration in response to the detonation wave

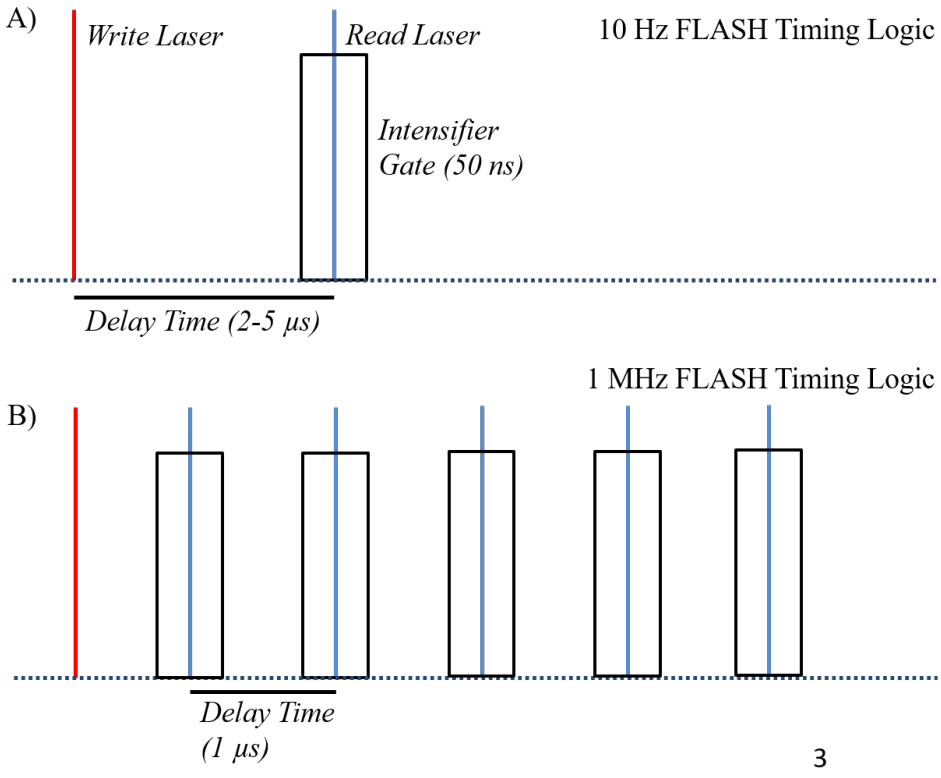

Figure 3.28. A) Timing logic for 10 Hz FLASH measurements. B) Timing logic for 1 MHz FLASH measurements

can be measured. The large downfall of the MHz implementation is that the burst mode laser only allows for 1 set of measurements per RDE test, which results in a much lower data-acquisition rate for statistical studies.

10 Hz Results and Shortcomings

For the 10 Hz portion of the experiment, two different mass flow conditions, $G_{ox} = 750 kg/ms^2$ and $G_{ox} = 350 kg/ms^2$ were evaluated. The write-read delay used to measure both of these conditions was 2 μs. Centroid locations are calculated using Gaussian surface fitting as previously described, for the reference image and each single-shot FLASH signal image. Displacement is calculated between the centroid of the reference image and the centroid of the signal image. This measurement is converted into velocity with the use of a spatial calibration image and the known time-spacing between the write and read lasers.

Figure 3.29 shows a two-color overlay of the reference image and a time-delayed FLASH image. Here, a large displacement can be seen, as well as a significant non-axial velocity component due to the swirl induced by the rotating detonation wave.

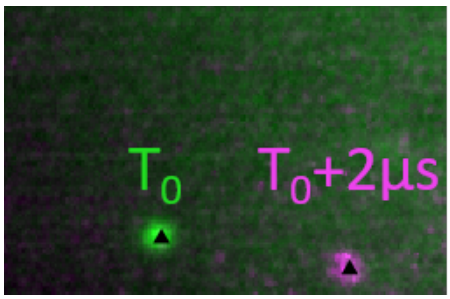

Figure 3.29. Raw composite of T_0 reference image (green) and single-shot FLASH image at with 2μs tag delay (magenta). Centroid locations shown as black triangles.

For each RDE operating condition, 10 total tests were run. In each test, 10 individual velocity measurements can be made. Figure 3.30 shows the initial statistical results in the form of a scatter plot between velocity magnitude and flow angle. The two mass flux conditions are plotted as well as a comparison of the higher mass flow at a write-read delay of 5 μs. For both 2 μs delay cases, the results trend similarly. There is a tight grouping of flow angle and velocity magnitude between 90-105 and 1400-1800 m/s. For the lower mass flux value, the spread of flow conditions is smaller, due to less disturbances in the flow. For each flow condition, there is a separate tail of smaller velocities and higher flow angles is present. This tail of flow conditions is due to the measurement being in the vicinity of the detonation wave. When the wave is near the measurement location, it tends to turn the flow significantly and cause swirl which reduces velocity magnitude.

As an evaluation of the reliability of the single-displaced framing technique with no-flow reference images, the $G_{ox} = 750 kg/ms^s$ was repeated with a write-read delay of 5 μs. With the assumption of minimal acceleration, the measured velocity magnitude and flow angle should be independent of write-read laser delay. As can be seen in Figure 3.30, the results from the extended read delay have significantly lower velocities than the short read laser delay. The reason for this is drift in the location of write laser over time. After the reference image is taken, a considerable amount of time passes before the data are collected. Due to

drift in the laser position over time, and RDE-induced vibrations in the focusing optics, the write-laser location ends up changing with respect to where the reference image is taken. This is a major source of error in velocity measurement, as a drift of only 1 mm in write laser location can cause an error of 500 m/s in the velocity calculation.

Overall, the implementation of the 10 Hz measurement shows great promise, because it demonstrates that adequate signal level and high enough data quality for processing is possible in the exhaust of the THOR RDE. Additionally, even without accurate quantitative results the measurement is able to qualitatively describe the statistics of the flow field and identify that there is considerable deceleration and flow turning in the vicinity of the detonation wave. In order to reduce the error in velocity magnitude, the write location of the laser must be well categorized. In practice this is very difficult to accomplish. Over the large distance the laser travels to the test section, any small mis-alignment over time will result in a large relative motion of the tag location. Additionally, the high amount of facility vibration during testing results in random fluctuations in the tag location which cannot be predicted. With both of these factors considered, it is unlikely that this framing strategy can result in accurate measurements in this facility. However, the implementation of this version of the technique represents a valuable proof-of-concept showing that sufficiently high-quality FLASH images can be captured before the more in-depth and technically-challenging 1 MHz framing strategy is attempted.

1 MHz Results

After validation of adequate signal was obtained from the 10 Hz framing implementation, the 1 MHz rate FLASH experiment was conducted. The main benefit of the MHz measurement is that it does not rely on a no-flow reference image to calculate velocity. Instead, after the initial write step, 5 sequential FLASH images of the tagged OH packet are collected. With this, 4 independent time-sequenced displacement measurements can be made, allowing for high accuracy tracking of velocity as well as fluid acceleration.

With instantaneous FLASH images, there is a large amount of spurious background illumination. This illumination is caused by naturally occurring in the flame products of the RDE. During the read step, the read laser tags the FLASH OH packet as well as the natural

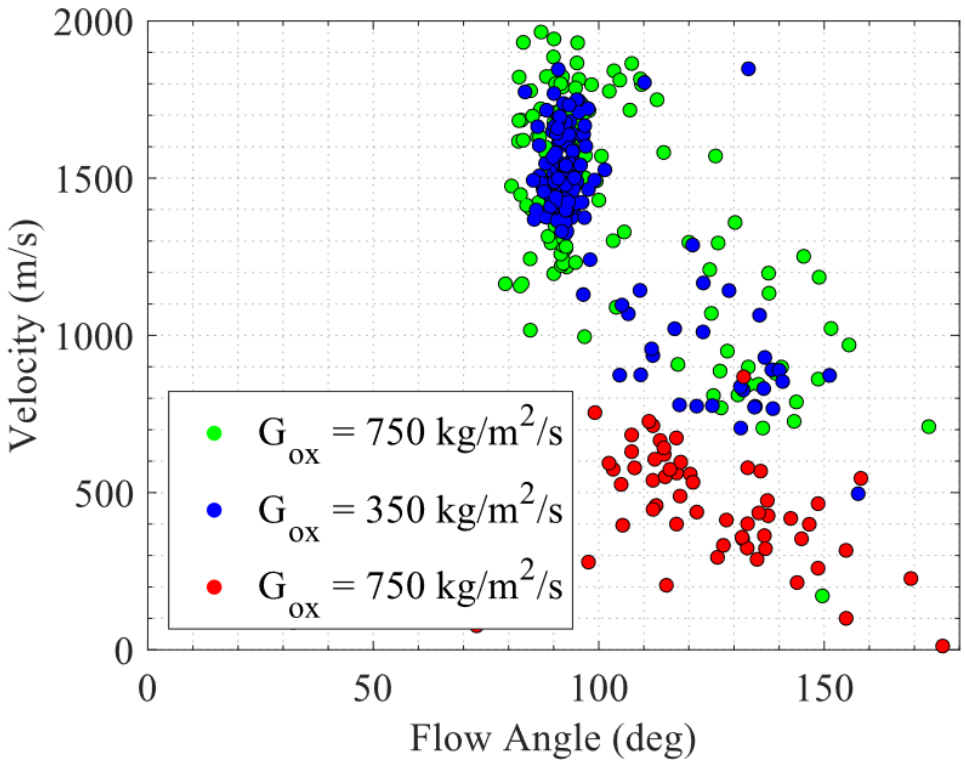

Figure 3.30. Scatter chart of measured velocity vs flow angle for select RDE operating conditions and read laser delay. Write-read delay of 5 μs shown with red circles.

OH of the reaction. This background illumination is stochastic and cannot be removed with the use of a statistical background image.

For each FLASH image, the background must be removed independently. This is achieved by invoking a top hat filter. A top hat filter is designed specially to isolate objects of a known shape from a varying-illumination background. For the FLASH experiment, the object is a 5-pixel diameter disk. Figure 3.31 shows the raw data, background, and isolated signal results. In Fig. 3.31 a), the signal is clearly seen however there is significant background illumination. If centroid finding algorithms were invoked on this image, the results would be skewed away from the signal peak due to the non-zero background intensity. In Figure 3.31 b), this background intensity is isolated away from the FLASH signal peak. The background intensity profile is subtracted from the original image to give Fig. 3.31 c), the isolated signal image. From this result, centroids can be found, leading to accurate velocity measurements.

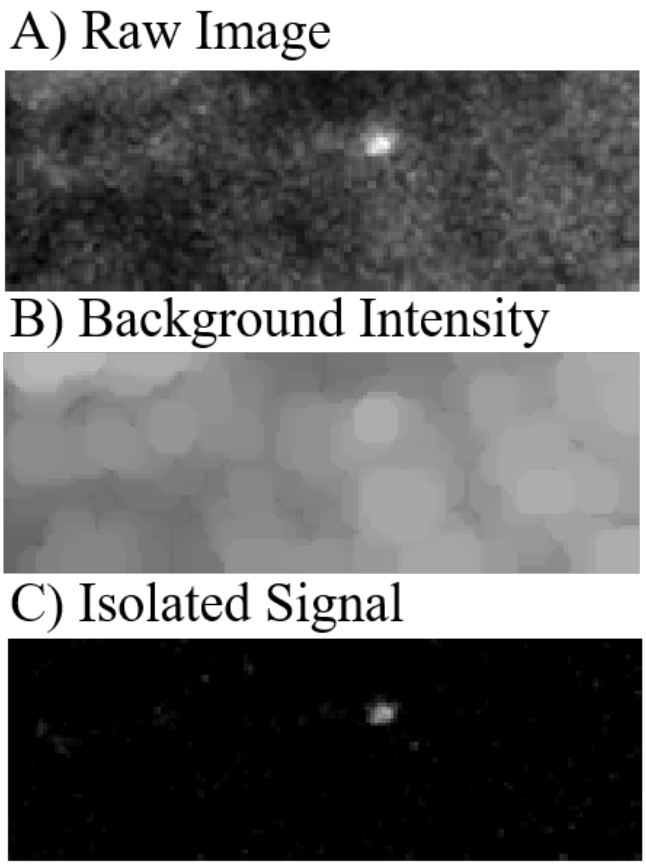

Figure 3.31. a) Raw image data. B) Background intensity found by top hat filtering. C) Isolated signal after background subtraction

Figure 3.32 shows the results of velocity plotted against flow angle for multiple RDE operating conditions. Across all operating conditions, the mean flow velocity is 299 m/s, and the mean flow angle is -6.9. The variance in the data, however is very large. There is a significant dependence of the flow velocity and angle on the position of the detonation wave with respect to the measurement volume. The largest velocities correspond to the the lower flow angles. When the detonation wave is in the vicinity of the measurement volume, it significantly turns the flow, and decreasing the velocity magnitude as a result. The overall magnitude of velocity is similar between the $G_{ox} = 750 kg/ms^2$ cases, but markedly decreased for the $G_{ox} = 350 kg/ms^2$ case due to lower mass flow rate.

With respect to downstream components such as a turbine, the variance in velocity magnitude and flow angle poses a major difficulty. Traditional turbo-machinery is designed

for a nominal flow velocity and inlet angle. While current design tools allow a very high isentropic efficiency at the design point, a deviation of only a few percent in velocity or flow angle causes large losses. With a system such as the THOR RDE the fluctuation in flow angle spans a full 180 degrees. Making a turbine that can accept this large variation in flow state while still extracting work at a high efficiency is a significant engineering challenge that stands in the way of making practical propulsion devices to harness the heat release benefit gained by utilizing detonative combustion. Using FLASH as velocimetry method for characterizing the exit flow of this device allows for the evaluation of alternate geometries. In Figure 3.32, the High Loss Injector data set shows a significantly lower amount of spread in flow angle and velocity. By achieving this measurement, evidence is shown that this variation in the design will allow for a more controlled inlet condition to the theoretical turbine to be coupled to the RDE.

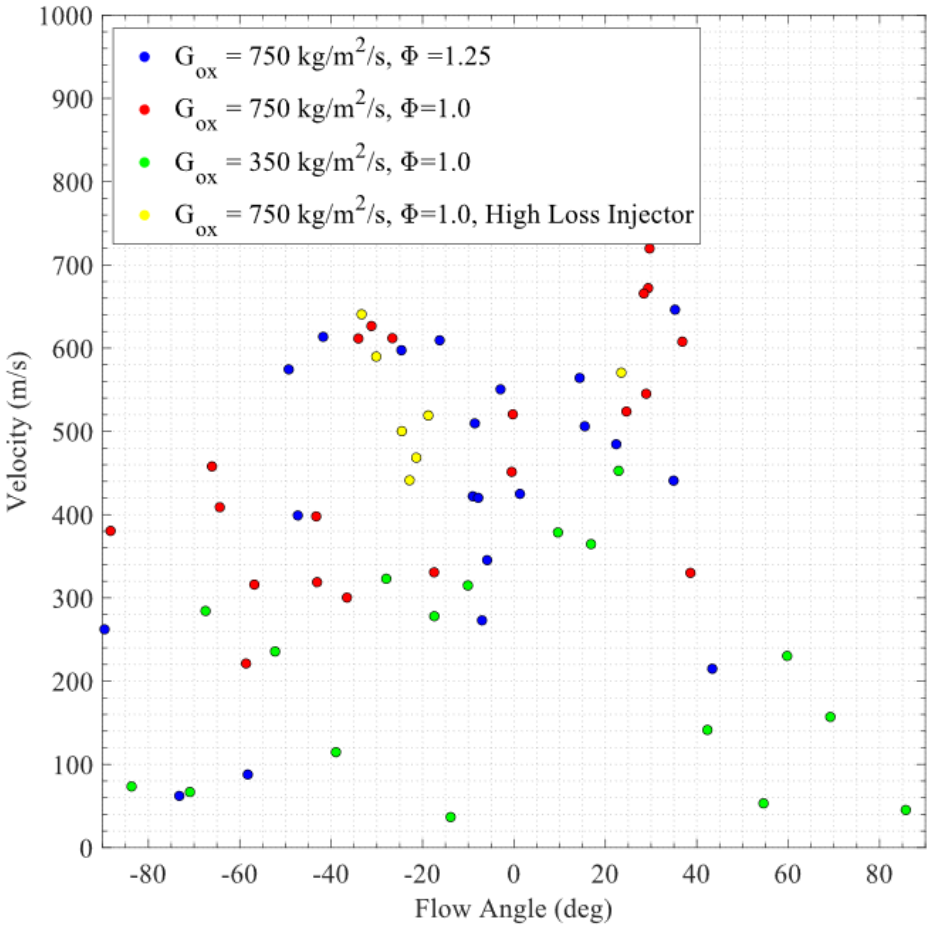

Figure 3.32. Scatter plot of velocity and flow angle for RDE exhaust plume

4. APPLIED MEASUREMENTS IN HIGH SPEED FACILITIES

4.1 Motivation

At the time the laser was invented, it was commonly deemed a 'solution in search of a problem'. In essence, this means that the development of the technology came about as a demonstration of capability, but not necessarily a specific need or use for this capability. As the technology grew and matured, continual improvements opened the door for application in many areas, including manufacturing, communication, and especially scientific research.

With rapidly increasing capability in lasers, cameras and scientific sensors, the use of laser-based diagnostics for scientific measurement soon became a possibility. While practical wind tunnel measurements were soon being made, a significant portion of the advancements being made in the laser diagnostics field were informed by the technology available, rather than the measurement needs of the community. As research continued for decades to its current state, many pioneering pieces of research [66], [104], [119] have been presented in which measurement techniques push the envelope of capability in terms of measurement rate, or other new capabilities. However, these measurements are somewhat out of context, as the work that went into them focused only on advancement of the technique with no aerodynamic application readily available. Specifically in terms of FLEET [49], [120], flow parameter measurements such as mixture fraction and temperature can be made in highly controlled experiments, but involve assumptions about the flow that could not be readily applied to any high-speed ground test facility.

While advancement in technology, and standalone demonstration of measurement capabilities can pave the way for significant advances in applied measurements, the approach needs to be more two-sided, with insight into the specific test article in question. Attention needs to be paid to the logistics of how FLEET can be made useful in practical aerodynamic test environments and the useful information which can be extracted as compared to alternate measurement techniques. Additionally, instead of taking one measurement technique and applying it to any facility, a researcher should consider all the options for diagnostics in a

test campaign and select the most applicable solution. For FLEET, it was only recently that progress been made on this front specifically in the various works at NASA Langley [13], [55], [69], [84]. Here, the problem is approached by considering the desired results such as airfoil separation and wing wake, and deeming which experimental measurements are necessary to achieve this outcome.

In this chapter, FLEET measurements are performed in two high-speed test facilities. These measurements were not made for the purpose of demonstrating capability, but rather because facility conditions and previous experiments suggested that FLEET was the pragmatic option for making velocity measurements. In the course of implementation, benchmarking of the technique at relevant facility conditions was necessary, and this work continued on to test section-specific method optimization to maximize the aerodynamic output of FLEET. For the bladeless turbine campaign, PIV was considered as a first-choice technique for its extended spatio-temporal resolution. Multiple test entries were attempted with PIV in order to address the various problems encountered with applying this technique. Eventually, this method was abandoned due to difficulties in achieving useful results. It was only then that FLEET was considered an alternative for providing velocity measurements that were not subject to the same downfalls experienced by PIV. With FLEET, the results were able to reconstruct the complex supersonic flow field including measuring unsteady nature of multiple interacting shock waves. In the Boeing-AFOSR Mach 6 Quiet Tunnel, the complex and precise construction of the facility bars any seeded diagnostics from being conducted. For this reason, only probe-based velocity diagnostics had been conducted. FLEET was implemented here because it represented one of the only safe paths forward to achieve velocity measurements in this environment. Here, remarkable agreement to the predicted velocity in the tunnel freestream and test article boundary layer were achieved. A specific path for future advancement of the output of FLEET in this facility is also laid out. As a result of both of these test campaigns, the usefulness of FLEET as a tool for aerodynamic measurement was evaluated.

4.2 Bladeless Turbine

The bladeless turbine test section is a long-running experiment that has taken place in the PETAL Linear Experimental Aerothermal Facility (LEAF). The design, CFD simulation and optimization, and experimental evaluation of the bladeless turbine was the subject of the thesis of James Braun, and is described in [121]. The overall basis of the design is to accept supersonic inlet flow interacting with a wavy-hub surface. The waves in the surface lead to impingement of oblique shock waves which in turn foster shock-boundary layer interaction and separated flow. The result is a highly complex flow regime with many interacting shock waves and a large shear layer. During the extensive testing campaign, the test article has served as a proving ground for implementation and analysis of various laser diagnostics. The first method to be applied for velocimetry was PIV, as this is the one of the most widely implemented velocimetry techniques at Purdue University. Many PIV test entries were conducted, with varying levels of success. Due to the transient nature of the wind tunnel, troubleshooting seeding density seemed to be the largest challenge. Just like many hypersonic tunnels, the facility can only run for a total of 30 seconds before losing sufficient vacuum to remain in supersonic operation mode. After the test, there is a wait time of 8 hours before a flow can be conducted again. This transient operating mode makes it highly difficult to fine-tune the amount of tracer particles delivered into the test section for velocity measurement.

After many attempts, some success was had in seeding the supersonic flow. Upon analyzing the results an unfortunate realization was made. The particles do not respond to the changes in velocity across the shock waves due to their large finite inertia. This is because the particles used were too large to be appropriate for the high speed flow field. For this reason all the PIV data was unreliable for this test section. Instead of spending a great deal more time trying to optimize the measurement technique, FLEET was implemented as a more reliable method of measuring velocity. The implementation of this measurement technique has been described in an article titled "Application of femtosecond laser electronic excitation tagging (FLEET) velocimetry in a bladeless turbine" which has been published in the journal Measurement Science and Technology, special edition on turbomachinery [27].

The proceeding sections are an adaptation of this manuscript. Considerable engineering and technical effort was conducted to provide the test section with the capability of flowing pure nitrogen to increase the quality of measured data after analyzing the results of a proof-of-concept experiment in air.

4.2.1 Proof-of-Concept in Air

To show feasibility of conducting FLEET in this test section, a proof-of-concept measurement campaign was conducted. The original test section was only capable of flowing air, which is well known to cause a degradation of signal quality and lifetime. The low pressure and turbulent nature of the flow hampered the implementation of the technique as well. Nonetheless the purpose of the original campaign was to give a business case for continued pursuit of FLEET for measurements in the bladeless turbine.

The proof-of-concept was successful in acquiring data, although the image quality was significantly reduced. Figure 4.1 shows a time series of single-shot images from one laser excitation. By eye, motion of spots 1 and 2 can be seen as they convect through the flow. However, instead of simply-connected regions, the spots appear as loosely grouped intensity lobes. With the processing described in Chapter 2, these data are not of high enough quality to pass outlier testing. By applying a time-moving average to groups of images, some temporal content of the flow could still be gained. Figure 4.2 shows the capturing of the wind tunnel unstarting. For every instance in time, a forward-moving average of 50 data points was used to calculate the velocity measurement. While this temporally smoothed the data considerably, it still produced meaningful insight into the behavior of the flow, and the performance of the measurement technique.

In Figure 4.2, the difference in velocity between points 1 and 2 is apparent. This was a main concern of the proof-of-concept experiment. In order for the measurement to be practical in this case, FLEET must be capable of resolving sharp gradients over small distances, such as these two points which are located in a strong shear layer. While the instantaneous data here were not of remarkably high quality, enough evidence was shown that FLEET could be beneficial to pursue further. After this proof, the facility was modified to allow testing with pure nitrogen, which allowed for a considerable increase in data quality and

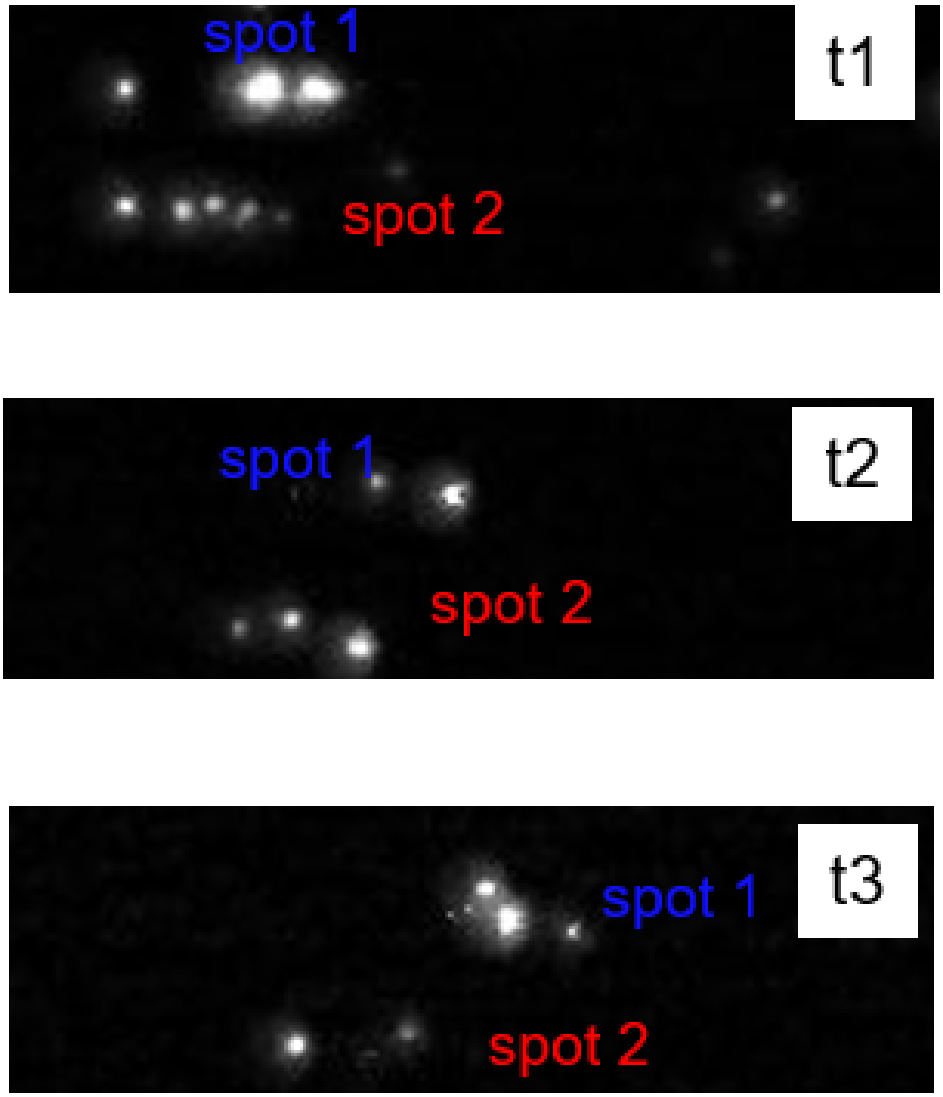

Figure 4.1. Raw FLEET data from proof-of-concept experiment in air.

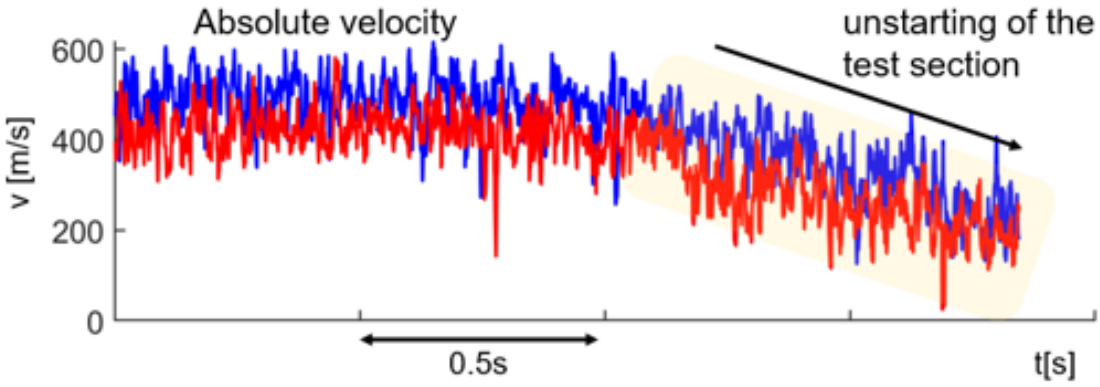

Figure 4.2. Transient results during unstarting for two moving-averaged FLEET measurement points.

signal lifetime. Between the initial and final experiments, the optical arrangement was also optimized to allow for transmission of maximum laser energy to the measurement volume.

4.2.2 *Application of femtosecond laser electronic excitation tagging (FLEET) velocimetry in a bladeless turbine*

Abstract

Shock waves appear in numerous high-speed propulsion applications, including intakes, nozzles, and transonic and supersonic turbomachinery. The aerodynamic performance in bladeless turbines, which is designed for work extraction under such conditions, is dominated by flow separation induced by shock-wave pressure gradients. The large velocity gradients pose limitations on flowfield characterization using particle-based optical diagnostics, such as Particle Image Velocimetry (PIV) and Laser Doppler Anemometry (LDA). These limitations, along with challenges in seeding the flow, can be overcome by tracking the molecules already present in the flow. This paper presents kHz-rate femtosecond laser electronic excitation tagging (FLEET) to excite long-lived fluorescence of nitrogen molecules, acting as in-situ flow tracers. The technique was demonstrated in an optically accessible linear turbine test section, developed to investigate bladeless turbines. The femtosecond laser is coupled with an intensified CMOS camera with a frame rate of 200 kHz. High-speed measurements were made of the steady and unsteady performance in the bladeless turbine, with particular attention to capturing flow structures and the starting and unstarting of the supersonic passages.

Introduction

Bladeless axial turbines with a sinusoidal wavy surface enable power extraction from high-speed harsh environments [121], [122], as sketched in 4.3. Oblique shock waves cause a cyclic pressure differential across the wall geometry, which induces a torque on the rotating drum. To understand the complex flow physics occurring around the wavy hub geometry, which involves compression and separation shocks, experimental assessment of velocity and flow angle are required. A traditional measurement technique for obtaining spatio-temporally resolved velocity measurements is Particle Image Velocimetry (PIV). For the flow field in

question, PIV may be compromised for several reasons. In the region of interest, several shock-boundary layer interaction patterns exist with consequent high spatial gradients in the velocity field. Due to non-negligible inertia, the particles used in PIV experience a finite relaxation time in response to changing velocity; and this can cause a bias in measurement. Without diligent selection of the observation window and particle size, this effect will cause smearing of the flow features being interrogated [123], [124]. In simplified supersonic flows with low numbers of shocks this smearing can be accounted for [125]; however, this becomes impractical in more complex experiments. Another challenge with PIV is obtaining near-wall data. PIV relies on laser light scattering from particles, and a by-product of this is laser scatter from solid boundaries in the test section. Wall scattering signal tends to be much brighter than particle scattering and the result of this is that data acquisition near walls and in boundary layers becomes increasingly difficult. To combat this, fluorescent PIV methods have been used [126]. Seeding fluorescent particles into gas flows can, however, be hazardous to personal health and sensitive equipment. In large flow facilities, acquisition of large amounts of these particles also can become prohibitively expensive.

PIV was initially attempted in bladeless turbine experiments. Consequently, laser scattering, particle density, and particle lag represented major challenges. To acquire velocity data in a simplified and more reliable manner, femtosecond laser electronic excitation tagging (FLEET) [47], [59], [62], a molecular tagging velocimetry (MTV) method which employs a femtosecond laser focused at a point to dissociate nitrogen molecules, was implemented. The recombination process of the excited state nitrogen produces a long-lived fluorescence signal, which can be sequentially imaged to measure velocity. To perform FLEET, a femtosecond laser beam is focused to the point of interest in the flow field. Figure 4.4 sketches the FLEET application in a supersonic flow, and the subsequent imaging process. The focusing distance depends on the size and optical access of the experimental test section. An intensified camera is focused on the interrogation region. Once nitrogen molecules are excited by the laser, they emit visible broadband fluorescence, which can be observed for greater than 100 μs, depending on the flow conditions. With sequential imaging of the motion of the tagged molecules, velocity measurements can be made from the measured displacement and known time spacing between frames. Multiple images of the same excitation can be

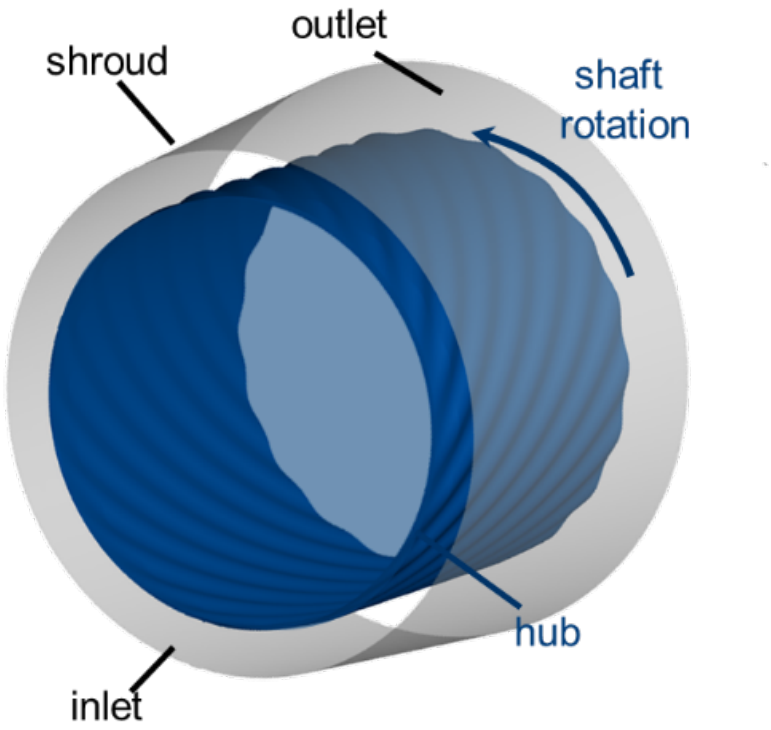

Figure 4.3. Three-dimensional view of a bladeless turbine.

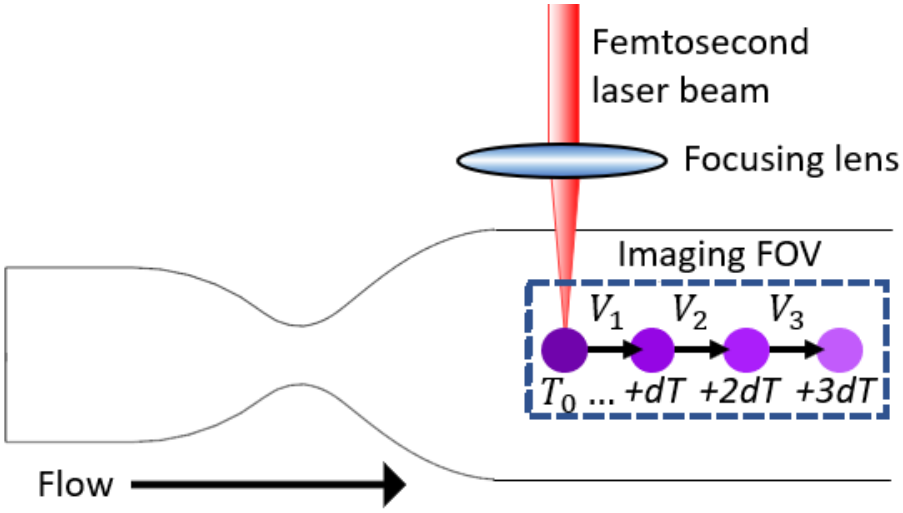

Figure 4.4. Schematic of generic FLEET experiment.

acquired, allowing for multiple streamwise velocity measurements. Adjustment of the camera magnification and time spacing between images can optimize the precision and dynamic range of the measurement technique, which is discussed in detail in [55]. An explanation of how these parameters were selected for this experiment is included in the optical equipment section.

FLEET offers a wide range of applicability, and simplicity in the optical setup. Other molecular tagging techniques generally require molecules to be seeded into the flow [45], [91] and/or careful alignment and overlap of multiple laser beams to produce and excite intermediate species [92], [93]. Alternatively, FLEET only requires one focused laser and one camera to perform measurements, making it attractive for its ease of implementation. Although not always necessary, FLEET can be performed in a line-of-sight configuration only requiring one direction of optical access [84]. Since the molecules being tagged are nitrogen, this method can be used in air or nitrogen flow facilities. Image acquisition for FLEET occurs with a time-delay from the initial excitation, and signals are emitted at a different wavelength. Therefore, laser scattering can be temporally and spectrally filtered, allowing for near-wall measurements to be collected. With proper camera sizing and timing, velocity dynamic range from tens to thousands of meters per second can be captured with uncertainties near one percent [118]. Recent advancements in FLEET have focused on evaluating the reliability

of the measurement technique in more applied environments such as the 0.3-m Transonic Cryogenic Tunnel Facility at NASA Langley [69]. Much promise in gaining useful aerodynamic data such as wake profiles and pseudo-streamlines have been presented in this prior work with high accuracy and precision. Other researchers have presented progress on improving the temporal resolution of FLEET up to the MHz rate to acquire rapid fluctuations in high speed flows [127]. The present work reports on the use of FLEET for characterizing the flow field in supersonic bladeless turbine environments. Specifically, this work utilizes this approach to resolve flow angles, shock structures, steady and unsteady components of velocity, and transient behavior of the supersonic environment as it becomes unstarted.

Experimental Facilities

Wind tunnel facility

All experiments were performed in a linear blowdown wind tunnel at the Purdue Experimental Aero-thermal Laboratory (PETAL) [128]. A 283 cubic meter vacuum tank downstream of the test section to allow for high Mach and low Reynolds number operation. The system is drawn down to 38 millibar before testing to allow the sonic throat to choke at lower total pressures. The facility was specially modified prior to this experiment to allow for supply of pure nitrogen at flow rates up to 6 kg/s. Flowing pure nitrogen has the effect of increasing signal quality and lifetime of FLEET measurements [62]. The linear blowdown tunnel was designed to allow a high amount of access for optical diagnostics. For the tests reported in the current work, the tunnel was constructed with metal blanks on the top and back side, a large optical quartz window on the front, and the sonic throat/test section attached to the bottom. A schematic of the facility architecture is shown in Figure 4.5 (a).

Test Section and Operating Conditions

Figure 4.5 (b) displays the arrangement of the supersonic test section. The wavy turbine shape is mounted in the lower part of the test section, downstream of a converging-diverging nozzle, in a region where the free-stream velocity exceeds Mach number 2. The wavy hub surface mimics a two-dimensional simplification of the three-dimensional bladeless turbine

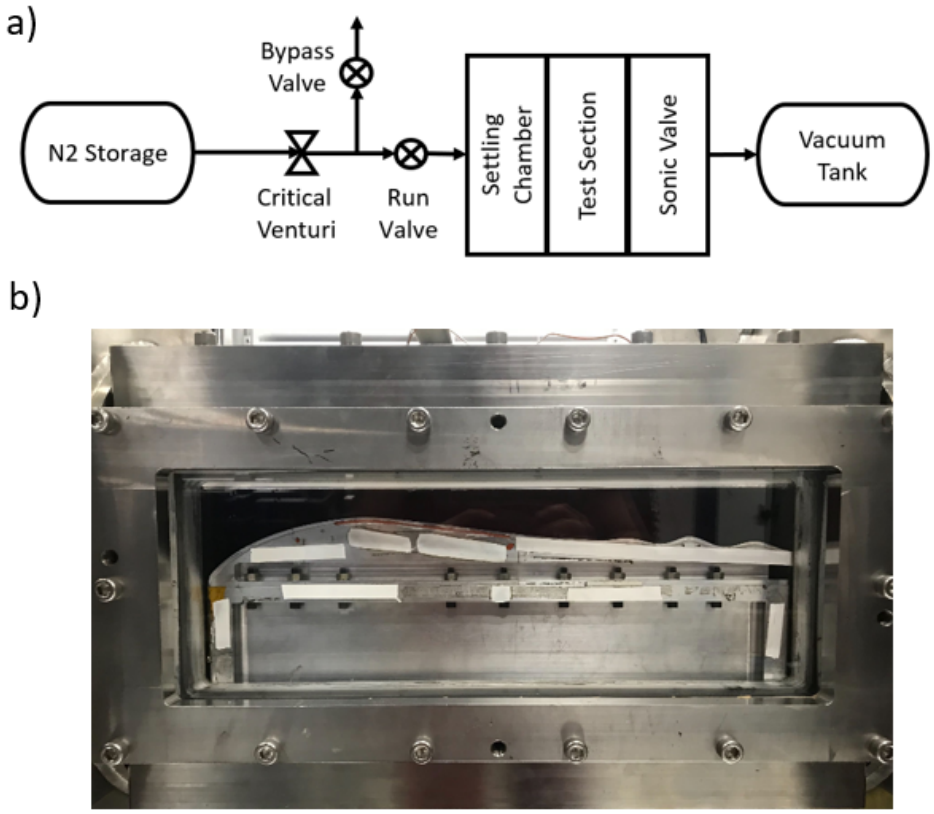

Figure 4.5. (a) Schematic of PETAL linear wind tunnel showing nitrogen storage, vacuum tank, and flow conditioning. (b) Image of wind tunnel with test article and optical window installed.

to enable detailed optical diagnostics with a variety of measurement techniques. For these tests, the mass flow was ∼2 kg/s with a flow total temperature of 270 K. The Reynolds number based on the momentum thickness upstream of the wavy hub geometry was 91,000. The vacuum pressure at the onset of testing was 0.1 bar.

Optical Equipment

A Ti:Sapphire femtosecond laser system (Spectra Physics, Solstice:Ace) was used during this experiment to provide the FLEET excitation for velocity measurements. The laser is regeneratively amplified to produce up to 7 mJ/pulse at a 1 kHz repetition rate with 800 nm center wavelength and 100 fs pulse duration. The femtosecond laser is located outside of the wind tunnel laboratory in a separate humidity and temperature controlled room to reduce

the negative impacts of the harsh test cell environment during tunnel runs. The beam is routed towards the wind tunnel through a series of mirrors to an optical table next to the test section. On the optical table, the beam travels through a $\lambda/4$ waveplate, a periscope, a 1:2 telescope, 30:70 and 50:50 beamsplitters and ultimately three +250 mm focal length plano-convex lenses before entering the test section through the front window. The waveplate is installed to allow optimization of the laser polarization for maximum performance of the beamsplitters and mirrors in the optical system. The periscope allows the beam to be brought to the correct height to enter the test section near the top surface of the experimental article. The 1:2 telescope doubles the beam diameter from 8 cm to 16 cm, which decreases the beam waist by a factor of two, as shown in equation 4.1 below:

$$w_0 = \frac{2\lambda F}{\pi D} \tag{4.1}$$

where w_0 is beam diameter at the waist, λ is laser wavelength, F is focal length of the lens in use, and D is input beam diameter. Reducing the beam waist allows delivery of the same amount of energy into a smaller volume to improve FLEET signal generation. Another benefit of the telescope is that it increases the beam area by a factor of four prior to focusing and lowers the risk of damaging the windows from laser absorption and supercontinuum generation [129], which broadens the laser wavelength and can significantly reduce the laser energy available for tagging. After the telescope, beamsplitters are used to separate the beam into three legs so that each path can be individually focused to an interrogation point. By design, the first beamsplitter reflects 30% of the beam and transmits 70% of the beam, while the second beamsplitter transmits and reflects 50% each. While actual transmission and reflection vary depending on wavelength, polarization, and incident angle, this combination provides the closest to a uniform energy distribution between each beam path. Three +250 mm focal length lenses are placed adjacent to each other with minimal separation and the laser beams were aligned into each lens such that the foci are in close proximity (1–3 mm). With beamsplitters, multiple excitation points were produced to increase the data rate of the measurements, and to evaluate the capability of measuring instantaneous spatial velocity gradients. To the authors' knowledge, there is very little prior work reported on multi-point

FLEET tagging. To tag different points in the flow, the locations of the beamsplitters and lenses were slightly adjusted between test runs. An overview of the laser and camera setup is depicted in Figure 4.6. For image acquisition, a high-speed CMOS camera (Fastcam, SA-Z) was coupled inline to an intensifier (Lambert, HiCatt). An 85 mm lens with an 8 mm extension ring and an aperture of f/1.4 provided the imaging system a magnification of 4.9 pixels per millimeter with a field of view of 384 pixels in the streamwise direction and 160 pixels in the vertical direction. To set the magnification of the imaging system, the spot displacement was estimated a priori based on the expected flow velocity from computational fluid dynamics (CFD) simulations. At a maximum velocity of 650 m/s and a total imaging time of 100 microseconds, a tagged spot will move 65 millimeters in the flow direction, or 318.5 pixels in the camera frame. This provides a near maximization of the relative motion of the excited spots in the camera field of view and ensures the highest precision to measure the velocity. As the predicted flow is mostly axial, there is additional space in the vertical direction of the field of view of the camera so that the imaging system does not need to be moved and re-calibrated to investigate other points in the wall-normal direction. For data collection, the imaging system is framed at 200 kHz, or one image every 5 μs. In [55] it was shown that longer time delays between images can lead to higher precision, although this has the effect of spatially averaging the measured velocities. As the velocity gradients are high for supersonic flows subjected to shock waves, the shortest time delay allowable by the imaging system was selected to capture the smallest spatio-temporal flow features. To save on data collection, the camera is operated in a burst mode where only 20 frames of the FLEET signal are captured per laser pulse. The intensifier gate was set to 1000 ns, and the gain was set between 800-900 volts (85-95% of maximum). To reduce spurious noise in the data at high intensifier gain, special care was taken to eliminate stray light entering the test cell during testing.

Data Processing

Various steps need to be taken to transform the raw image sequences into position and velocity measurements. These include data organization of image sequences, centroid finding, and velocity calculation. These steps are summarized in the proceeding sections.

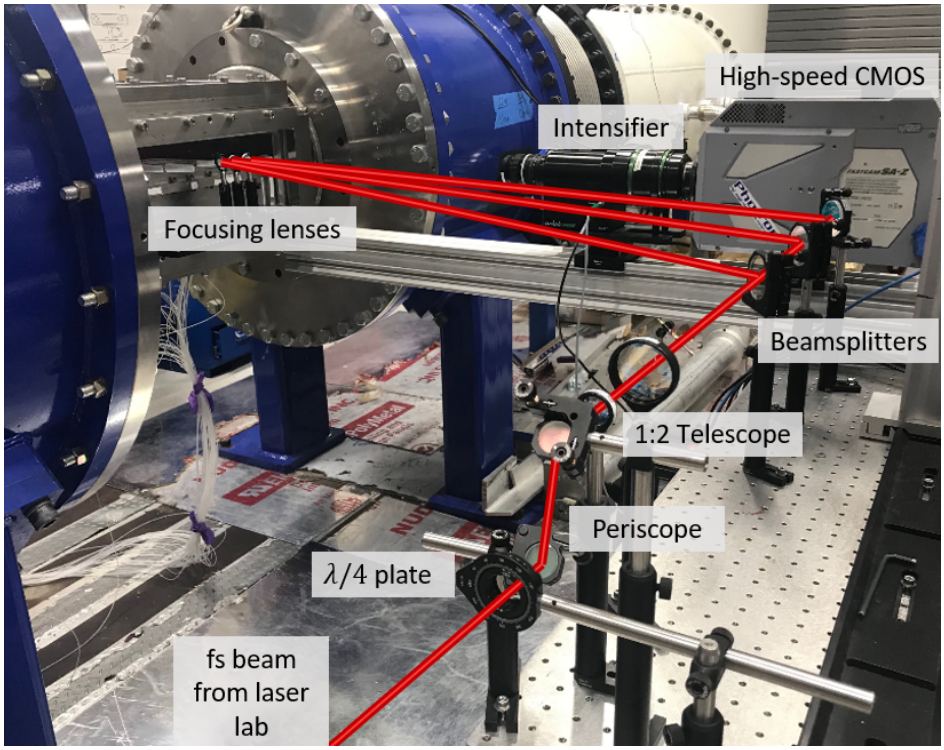

Figure 4.6. Laser and camera experimental setup.

Data organization

During data collection, the images are saved as a sequence whose length is a function of the acquisition period. During processing, these sequences are rearranged into a 4-dimensional array with the last dimension being the index of the image with respect to the laser pulse. This results in a 384-160-N-20 matrix, where the first two indices denote the number of pixels in the images, N is the number of total acquired measurements, and 20 is the number of obtained images per laser excitation. As the excited spots continue to fluoresce as they travel downstream, the 20 successive images allow additional velocity measurements along the path line of the tagged molecule. The upper limit of N, the number of sequential measurements that can be taken during one acquisition is set by the on-board memory of the camera which can hold 74,240 images and corresponds to 3712 individual measurements over a time span of 3.7 seconds. During a typical experiment, this full memory capability was not used, and N value was 500 to foster acquisition of proper statistical measurements. Since multiple excitation spots are drawn in each image, the spots must be isolated with respect to one another. While automated spot finding is possible to an extent, the isolation step is performed manually. The data are collapsed into a 384-160-20 matrix of average images for each frame index. From here, a region around each spot is selected for the algorithm to begin the centroid analysis. A time series of raw data with associated isolation regions is plotted in Figure 4.7.

Centroid Analysis

After spots are individually isolated, their absolute position must be found. Typically, either a Gaussian surface fitting [84], or cross- correlation [69], [127] have been employed to analyze FLEET data. In previous works [127], it was shown that there is a negligible difference in accuracy between the cross-correlation method and the simpler weighted centroid method. In situations where cross-correlation is used for velocity, a separate step for finding the spot position must still be taken [69]. The weighted centroid finding scheme was chosen for its balance between accuracy and lower computational expense. To perform the method, a cut-off intensity for all images was chosen as two times the root-mean-square background

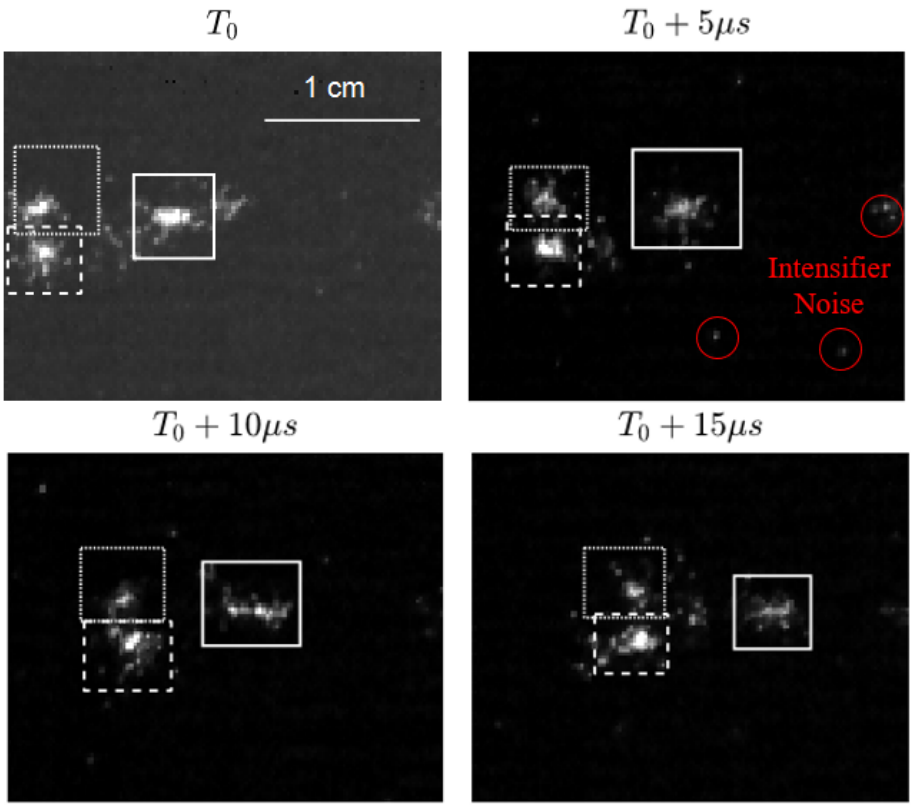

Figure 4.7. Time series of raw data with spot isolation regions. Spurious intensifier noise is highlighted in red, which was subtracted during image processing.

intensity value. In the following step, each pixel with an intensity above the cut-off is multiplied by its location in either the x- or y- direction and all weights are summed. This weight is divided by the total image intensity to obtain the centroid location. Equations 4.2 and 4.3 outline the algorithm for finding the x- and y- centroids of an image with this method.

$$\bar{X} = \frac{\sum_{\mathrm{i}=1}^{columns} \sum_{\mathrm{j}=1}^{rows} Intensity(\mathrm{i},\mathrm{j}) * \mathrm{i}}{\sum_{\mathrm{i}=1}^{columns} \sum_{\mathrm{j}=1}^{rows} Intensity(\mathrm{i},\mathrm{j})} \tag{4.2}$$

$$\bar{Y} = \frac{\sum_{\mathrm{i}=1}^{columns} \sum_{\mathrm{j}=1}^{rows} Intensity(\mathrm{i},\mathrm{j}) * \mathrm{j}}{\sum_{\mathrm{i}=1}^{columns} \sum_{\mathrm{j}=1}^{rows} Intensity(\mathrm{i},\mathrm{j})} \tag{4.3}$$

The cutoff intensity is a critical parameter in the centroid finding algorithm which, if not chosen conservatively, can highly bias the results. Additionally, the background of the image has a non-zero intensity, which can lead to a bias in the location of the centroid if the algorithm does not take this into account. The noise in each image is comprised of two main aspects: camera chip noise and intensifier electrical noise. The camera noise is well predicted and eliminated, as it remains near a constant value across the extent of all frames. The electrical noise from the intensifier is slightly harder to account for since it has a higher random behavior. Small illuminated spots of intensifier noise are circled in red in Figure 4.7. A cutoff intensity to account for these random noise spots is selected by applying a factor of 2 to the mean background intensity level. This centroid finding procedure is performed individually for each isolated spot in its interrogation region, and then the offset of the interrogation region to the base image is added to the centroid location to achieve the absolute position of the spot.

Velocity Calculation

To perform velocity calculations after the spot locations are defined, finite differencing and spatial calibrations are applied. After optical setup and before data acquisition, a calibration image is recorded. A grid target of known size is placed into the camera field of view. At low laser energy and without operating the camera, the calibration grid is moved to the focal point of the laser beams. When in position, the laser is turned off and the camera is focused. With the lens aperture fully opened to decrease the focal depth, the camera is

focused onto the target. Opening the aperture serves to increase the sensitivity of focusing to ensure the best results. Once a calibration image is acquired, the camera focus is locked and the aperture can be set appropriately for data collection. The spatial calibration is adopted to convert the position of all spots in pixels to an absolute location in meters. First order finite differencing is used to determine the spot velocity between the i^{th} and $(i+1)^{th}$ locations. Since the velocity measurement is path averaged between the two spots, the location of the velocity measurement is reported at the midpoint between the two locations. In previous works, higher-order finite differencing [69], [84] as well as smoothing and optimal path definition [69] were demonstrated to improve the accuracy of the measurement. These methods were applied to subsonic flows where velocity was assumed to vary smoothly. From prior characterization of the wavy hub surface via experimental Schlieren and computational fluid dynamics (CFD), the existence of multiple shock interactions was proven, meaning the flow field could not be assumed to vary smoothly or continuously. For this reason, more complex velocity evaluation methods were not investigated for this work as they might smooth out the results spatially. Since FLEET measurements are non-instantaneous, there is a high effect of flow velocity and camera frame rate on the streamwise resolution of velocity measurement. In high supersonic velocity flow fields where FLEET is an attractive tagging method, the signal can move several millimeters in the time between images. Minimization of interframe time is preferred to increase the spatial resolution of measurements for this experiment.

Upon calculation of all the velocities, some data points appear to be anomalous and non-physical. These points need to be reviewed manually and many are a result of the FLEET signal spatially overlapping with background reflections that were not mitigated at the time of the experiment. These outlier datapoints were then manually removed from the results.

Measurement Precision and Accuracy

In previous experiments [69], [84], [118] in subsonic recirculating facilities, measurement accuracy was evaluated with respect to reference velocities set in the wind tunnel. By performing simultaneous FLEET and probe measurements over the operating envelope of the facility, an uncertainty correlation was created. For short-duration supersonic blow down

tunnels, such as the one used in this experiment, performing this comparison was not feasible. To gain an understanding of the measurement in this case, wind-off data was collected. Since there is no flow in the wind tunnel, the theoretical velocity is 0 m/s. 50 datapoints were taken with FLEET and the standard deviation of the velocity measured is taken as the precision of an instantaneous measurement, which is 33 m/s. For this experiment, this correlates to an average bias shift of 0.8 pixels in the centroid location of the FLEET signal at zero flow. This is lower than reported in previous experiments [69], [84], [118], [127] because of the processing method and the flow conditions at which the zero data was taken. Previous works have increased precision by averaging the velocity along several downstream positions. By performing this averaging, a trade-off is invoked between spatial resolution and precision. Since the flow field in this study contained many discrete shocks and other features, this could not be performed. During pre-test, the wind tunnel pressure is below 100 mbar. At sub-atmospheric pressure, low number density and diffusion cause an increase in the size of the apparent FLEET spot [62]. While an increase in spot size does not necessarily cause a decrease in accuracy, the diffusion and mixing of the spot due to the flow causes a changing spot shape, which adds a bias to the individual centroid locations and increases the uncertainty of the measurement. Because of FLEET signal degradation at no-flow test conditions, the actual uncertainty may be improved at flowing conditions. At a mean flow velocity of 500 m/s, the uncertainty on the instantaneous measurement corresponds to 6.6% , which leads to a technique capable of resolving the fluctuations in this flow field. Further improvements to laser focusing, image acquisition and data filtering can improve this uncertainty to approach the levels demonstrated in previous experiments. Comparable uncertainties from PIV experiments in supersonic wind tunnels approach 2% [73]; however, implementation near shock fronts and near-surface measurements are more limited. The mean velocity for the zero-flow data is .3 m/s, however no other comparable data is available at high speed caused by the unsteady nature of the flow field. Additionally, the accuracy can be inferred from two main components that make up the error in the measurement: the uncertainty associated to the time between camera frames, and the uncertainty associated to the spatial calibration of the camera. Thus, the relative velocity accuracy can be computed by Equation 4.4:

$$\frac{dV}{V} = \sqrt{(\frac{dX}{X})^2 + (\frac{dt}{t})^2} \tag{4.4}$$

dV is the velocity uncertainty, and dX and dt are the uncertainties related to the distance and the time. For the camera system, the timing uncertainty is <10ns. By comparing the results of the centroid finding from the previously described weighted centroid method with a two-dimensional Gaussian surface fitting, the average disagreement in centroids is 0.13 pixels. Time spacing is always 5 microseconds between images, but the distance (X) the signal travels is dependent on the velocity, and results in a velocity dependent accuracy. With this uncertainty in time and distance, the accuracies at 200, 400 and 600 m/s are 2.64, 1.34, and 0.901 % respectively. The accuracy increases for increasing velocity, because the uncertainty in the centroid location decreases with increasing total displacement. A similar result is achieved and noted in [55] where an increased time delay leads to higher accuracy because the signal has traveled further.

Results

The most important improvement of the FLEET measurement technique is the increased spatio-temporal resolution. The method has already been shown to work well for categorizing flow fields in a time-averaged manner. By resolving spatially resolved instantaneous velocities, additional data can be extracted from the experiment such as shear, vorticity and turbulence length scales. With beam splitters, multiple focal points could be produced and resulted in the ability to resolve instantaneous velocity gradients. Specifically, 4 features relevant for high-speed internal flows could be addressed with this new non-intrusive measurement technique and are described below.

Evaluation of the Mean Flow Physics and Validation for Computational Tools for High Speed Flows

Schlieren visualization is used to illustrate the dominant flow features, as shown in Figure 4.8. A first compression shock compresses the flow due to the increase in amplitude of the wavy contour of the lower wall (hub). In the aft part of the wavy contour, a separation shock

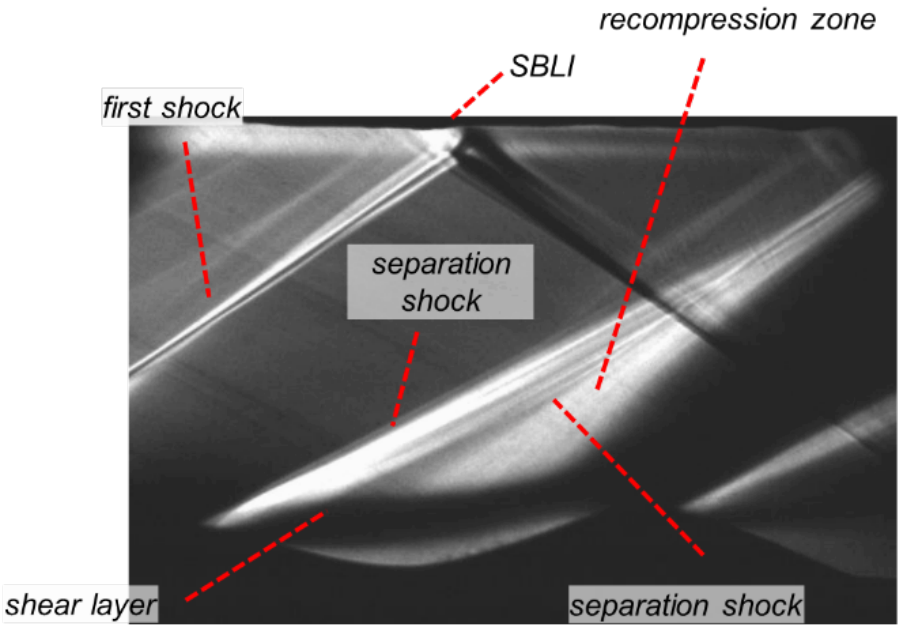

Figure 4.8. Flow field description via Schlieren visualization.

is formed as well as a shear layer and a subsequent recompression zone at the onset of the second wavy contour. An unsteady shock-boundary layer interaction (SBLI) arises due to the interaction of the compression shock and the upper wall (shroud).

Mean and Fluctuating Flow Field

All measurements from the steady-state tests were added together to obtain a statistical view of the flow field of the aft part of the first wavy contour and the onset of the second wave. All statistical mean values were calculated from 500 samples to ensure proper calculation of the mean. Figure 4.9 adds a velocity-oriented context to the flow features of Figure 4.8. In Figure 4.9(a) the average flow field vectors are visualized. The flow experiences a slight upward component as it travels over the first wavy contour due to the presence of the first compression wave (which results in an oblique shock further away from the hub boundary). At the descent of the wavy contour, the flow turns due to expansion fans up to the location of the separation shock, which turns the flow back towards the axial direction. Downstream, at the onset of the second wavy contour, the flow is again compressed with consequent positive flow angles. The overall magnitude of velocity is highest in the acceleration zone, and is

slightly lower upstream and downstream of this flow feature. The level of flow unsteadiness is visualized through the fluctuation level vectors in Figure 4.9(b). This plot displays the standard deviation of velocity over the set of all measurements at each location. The mean axial flow component for all points is generally steady, proven by the rather vertical nature of each vector. Upstream of the separation shock the flow experiences small fluctuation vectors, with standard deviations ∼20 m/s, within the experimental uncertainty. Proceeding into the acceleration zone, the fluctuation magnitude grows due to the presence of the unsteady separation shock. In most downstream measurements, the fluctuation levels decrease again due to the absence of unsteady shock patterns. The highest levels of fluctuation, however, can be observed in the measurements nearest to the surface. At this location, velocity is influenced by the shear layer created by the separation region of the first wavy contour.

Flow Field Comparison to CFD

In between test runs the laser foci were traversed through the measurement region to tag different locations in the flow field. This allowed for a statistical interrogation of the flow structures present above the test article. CFD simulations were performed for benchmark comparison and to obtain insight in the regions with important flow field features that need to be captured with the FLEET measurement technique. For these simulations, The Reynolds Averaged Navier-Stokes (RANS) equations were solved with Metacomp from CFD++, a commercial computational fluid dynamics (CFD) software package [130]. The turbulence closure was provided by the k-omega shear stress transport (SST) model. The non-dimensional wall distance was kept below one to solve the viscous sublayer and the entire converging-diverging nozzle was modelled. Further details about the simulations can be found in [131]. Figure 4.10 shows a comparison of the CFD simulated axial velocity component to the measured velocity in the experiment. The FLEET measurements are overlaid on the CFD contour in (a) and plotted on the same colormap. This gives an initial indication of the agreement between the two values. The percent error between the two is given by the points in (b).

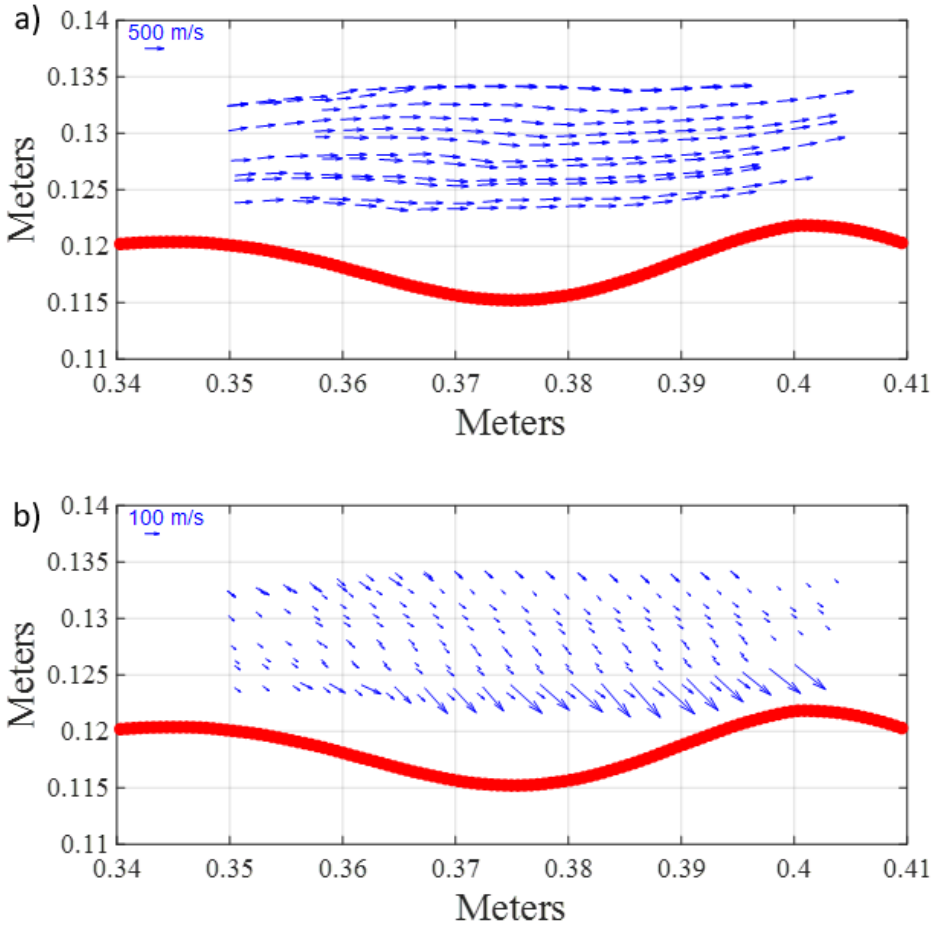

Figure 4.9. (a) Average velocity vectors obtained from all FLEET measurements. (b) Fluctuation level (standard deviation) vectors for all measurements.

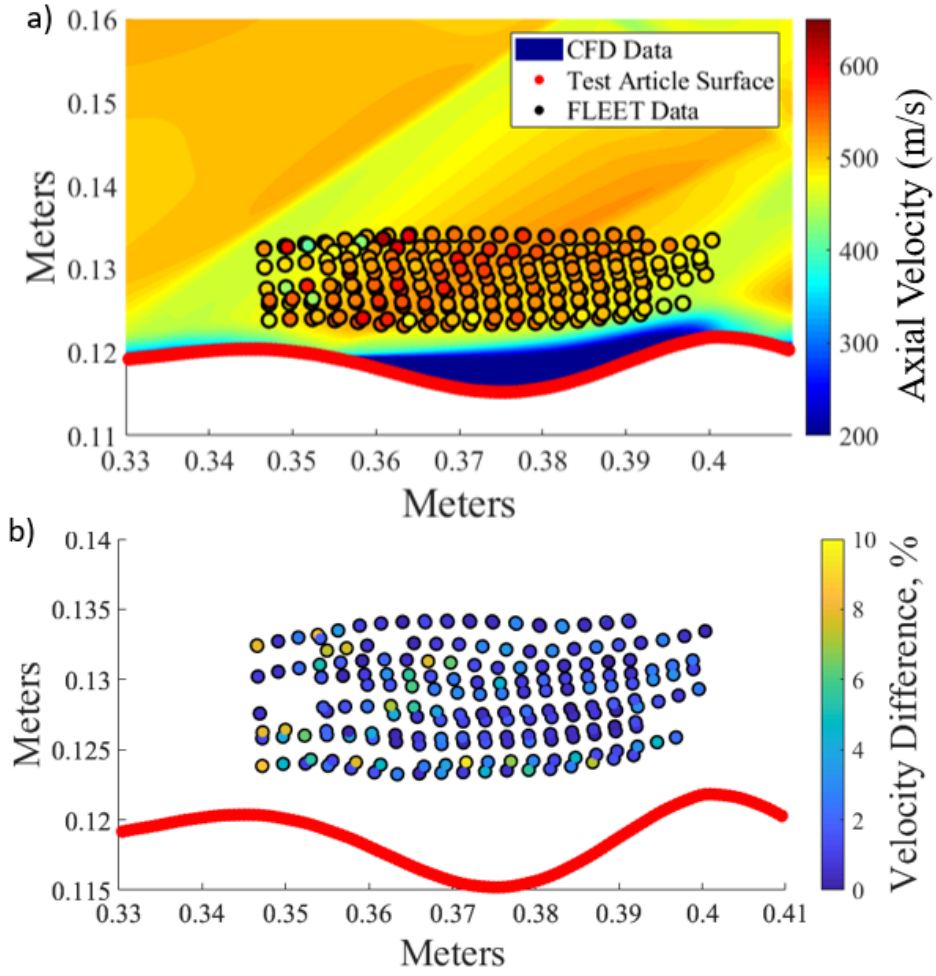

Figure 4.10. (a) Overlay of CFD predicted axial velocity and FLEET measurements, (b) Percent difference between FLEET and CFD at each measurement point.

The mean disagreement between the measurements and CFD is 2.2%. The larger values of disagreement tend to appear near where the separation shock appears above the shear layer and near the bottom of the where the separation region is beginning .

To understand the comparison of CFD and experiment further, the transverse velocity is plotted. Figure 4.11 (a) shows the CFD contour of transverse velocity, and (b) displays the same contour made from the FLEET measurements. To create the contour for (b), the data was interpolated and extrapolated from the discrete datapoint locations shown in Figures 4.9 and 4.10 to create a continuous profile. The bounds for the extrapolation were set to the x- and y- extrema of the datapoint locations. Qualitatively, the simulation agrees well with the measurements. The separation shock is clearly captured by the FLEET measurements as well as the recompression zone downstream, in which the flow turns to positive transverse velocities. In (b) a number of non-uniformities in the contour are observed and is due to the sparsity of FLEET data points used in this experiment. To gain a more uniformly converged flow field contour, more data points with a calibrated traverse system can be implemented.

The difference between the contours in (a) and (c) is depicted in Figure 4.11 (c), and this further displays the disagreement between CFD and FLEET. Many locations in the contour exceed 10% disagreement, and this is more pronounced because the transverse flow component is an order of magnitude smaller than the axial flow component. Again, localized smaller spikes in disagreement can be attributed to sparsity in the data point locations. However, a clear region of up to 40% disagreement is visualized, which reflects the location of the separation shock. Figures 4.10 and 4.11 reveal that the RANS simulations locally mispredict the vicinity of the separation shock and the region of the shear layer compared to FLEET. This is due to the inability of RANS to properly capture the separation point [132], leading to misprediction of the aero-thermal properties at these locations.

Measurement of Unsteady Flow Fluctuations

Shock-boundary layer interactions inherently cause unsteadiness. To evaluate flow unsteadiness, probability density functions (PDFs) are calculated and Figure 4.12 depicts the PDFs of six select points in the flow. The points of interest are shown on the CFD contour

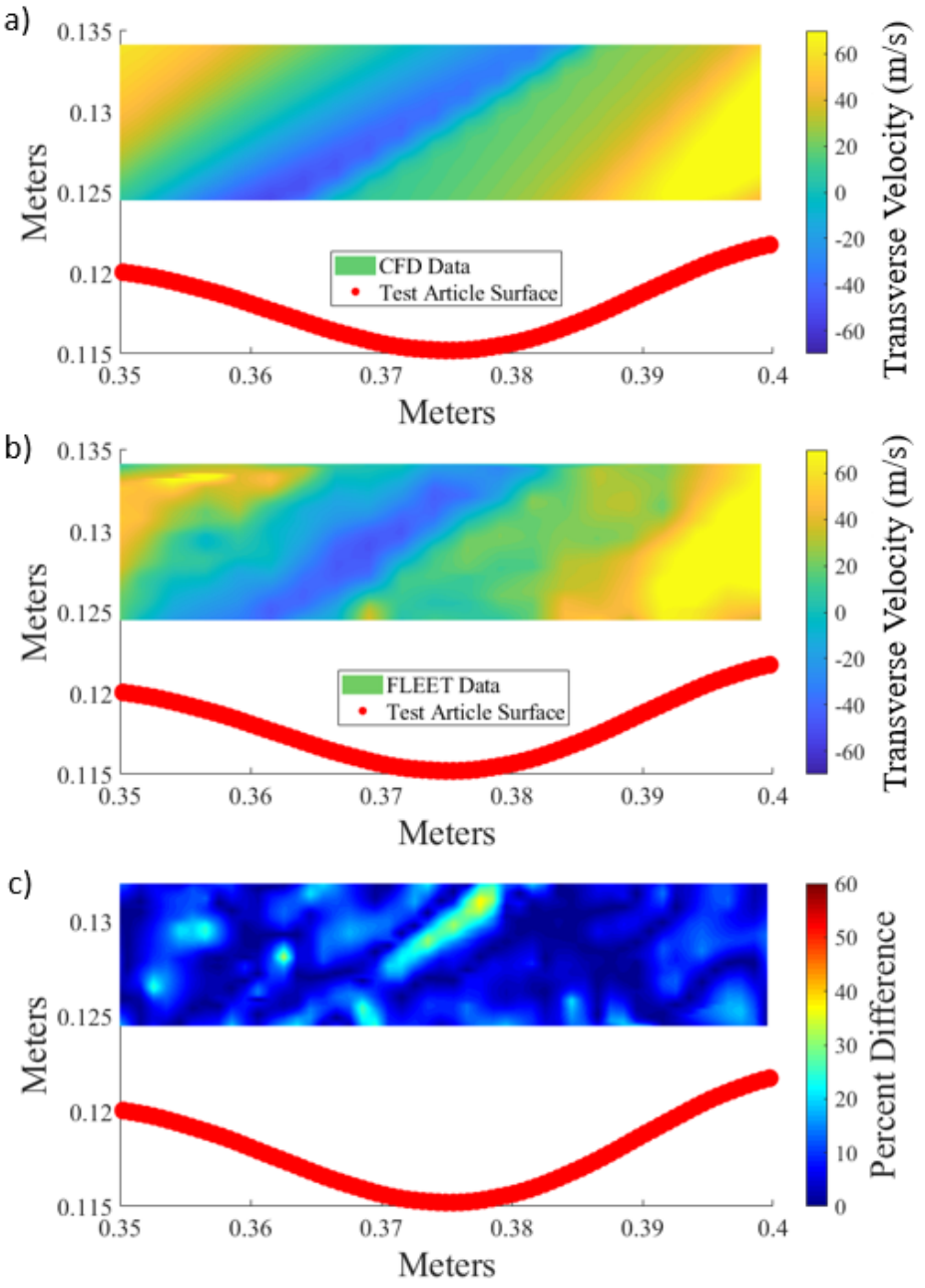

Figure 4.11. (a) CFD predicted transverse velocity, (b) interpolated transverse velocity from FLEET measurements, (c) percent difference between CFD and FLEET velocities.

in (a) and are color-coded to their respective PDF in (b). Normalized PDF's with respect to the mean velocity magnitudes are displayed in (c).

The black (+) point has a concentrated probability density function. This shows that the velocity at this point is relatively steady with velocity fluctuations indicated by a standard deviation of ±15%. The magenta (o) and red (x) points have similar distributions to one another. This part of the flow lies in the region upstream of the strong acceleration region and at the same axial location of the separation shock, which could explain for the high local unsteadiness. The standard deviation of the fluctuations is around ±25% for these points. The cyan () and green (•) points have somewhat broad PDFs featuring less unsteadiness than the previous points and lie in the acceleration region upstream of the separation shock, whereas the blue () point lies just downstream of the separation shock. The unsteadiness in the latter region is additionally influenced by the shear layer downstream of the first wavy contour and the consequent interaction with the recompression wave.

Unsteady Flow Shear Stress Measurement

By aligning two or more FLEET focal volumes in close proximity, instantaneous measurements of shear stress could be extracted. To calculate shear stress, the following equations were solved:

$$\tau = \mu \frac{du}{dy} \tag{4.5}$$

$$T_0/T_s = 1 + \frac{(\gamma - 1)}{2} M^2 \tag{4.6}$$

$$M = \frac{U}{\sqrt{\gamma R T_s}} \tag{4.7}$$

$$\mu = \mu_0 (T_s/T_0)^n \tag{4.8}$$

Parameters $\mu_0 = 1.782 * 10^-6$ Pascal seconds, $\gamma = 1.4$, and $R = 296 \frac{J}{Kg*K}$ are assumed for nitrogen. $T_0 = 298K$ and is known from the facility operating point. U and du/dy are known from the FLEET measurement results. The remaining parameters including the shear stress, , are calculated for each velocity measurement via equations 4.5, 4.6, 4.7, and

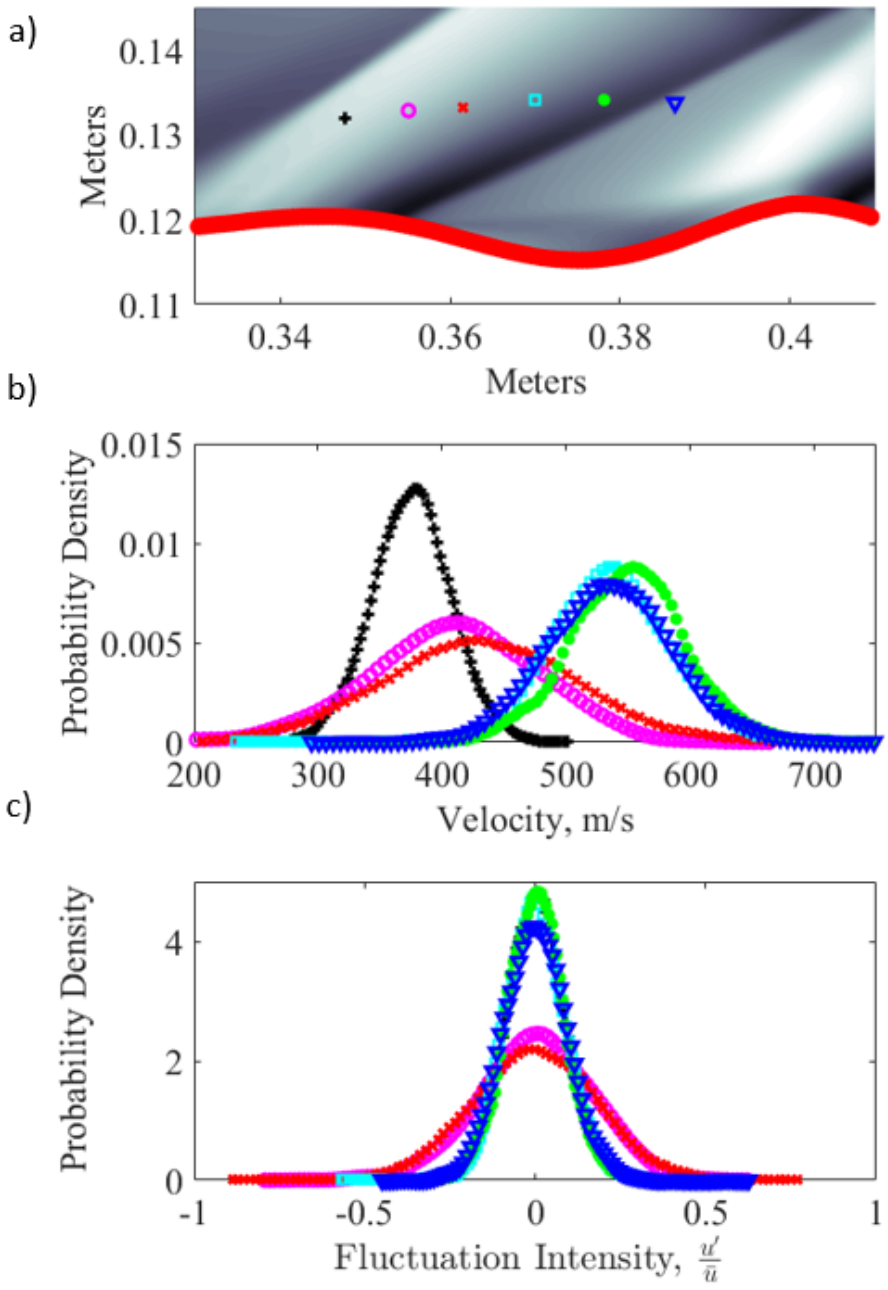

Figure 4.12. Probability density functions at (a) select points in the flow of (b) velocity and (c) fluctuation intensity from FLEET measurements.

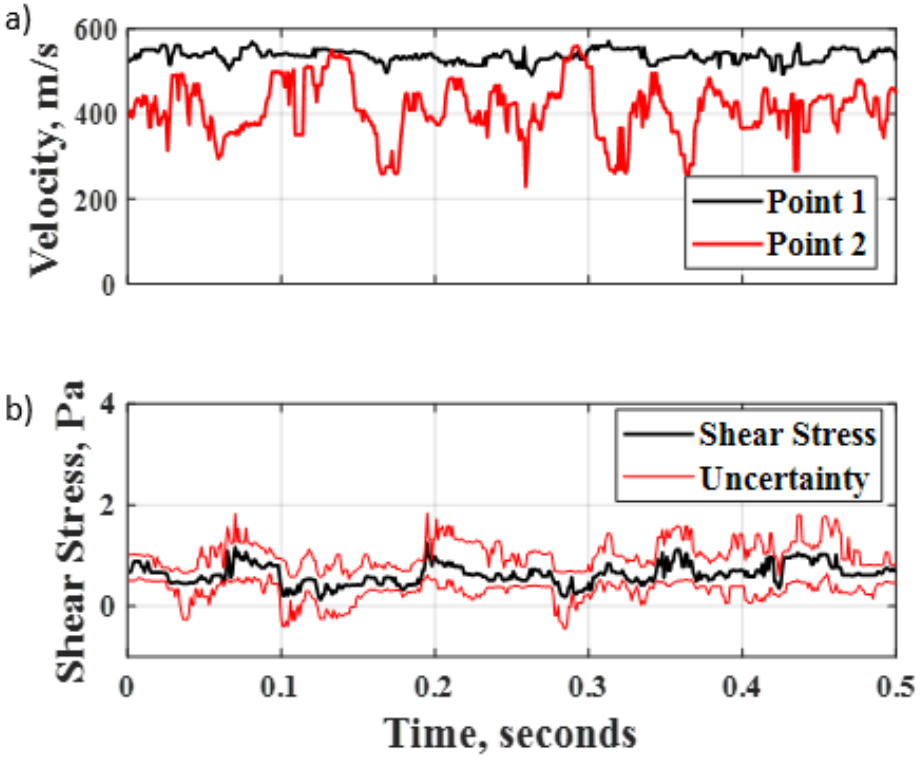

Figure 4.13. a) Velocity of two measurement points tagged simultaneously. (b) Shear stress between points as a function of time.

4.8. The velocity difference between two points had nominal separation of 3 mm and the corresponding shear stress are shown in Figure 4.13.

The measured shear stress fluctuates around .62 Pa, and with and standard deviation of 1.38 Pa due to fluctuations in the velocity at point 2. Uncertainty in the shear stress value is calculated by propagating the velocity uncertainty through the calculation of shear stress to give upper and lower bounds for each value. Multi-point FLEET tagging can thus be used to measure instantaneous flow shear.

Measurement of Highly Transient Spatial Occurrences: Unstarting of the Test Section

During start up and shutdown of the supersonic turbine, a transient shock wave passes through the turbine and might endanger the structural integrity of the geometry due to pressure fluctuations as well as transient heating. As the shock wave travels upstream, the

flow speed decreases to subsonic velocities, and this process is known as unstarting. This phenomenon is common for supersonic internal flows and represents a highly transient process and the accurate quantification of this phenomenon is important for the design of supersonic turbomachinery and to calibrate transient CFD models. Two possible scenarios occur to unstart the bladeless turbine during the experiment: sudden closure due to upstream flow stoppage and gradual closure due to the increase of the back pressure. FLEET was used to capture the first transient event and to track the spatio-temporal evolution on the flow field. A shadowgraph sequence of the shutdown of the turbine passage is displayed in Figure 4.14 (a-e). Due to the elevated back pressure at the end of the test, the rear part of the test section was already 'unstarted' (no separation shock is detected near the second wavy contour). When the valve is closed, a shock wave travels upstream followed by a zone of supersonic/subsonic flow until the flow becomes subsonic and ultimately decreases to zero velocity. Total time to 'unstart' for this experiment is around 250 ms, and the limitation is set by (1) the closing of the upstream valve, which was ∼100 ms, and (2) the pressure ratio. Additionally, during shut down, shock waves seem to be locally moving back and forth on top of the shear layer. Figure 4.14(a-e) illustrates the entire sequence conducive to the unstarting of the supersonic passage. At the onset of unstarting numerous shocks are formed, the elevation of back pressure causes the separation region to enlarge and become more unstable. Several velocity locations are plotted in Figure 4.14 (f). A median filter with a 21 sample wide window is applied to smooth out random fluctuations. An initial deceleration from 0.5–0.6 s is seen in all interrogated points due to the onset of unstarting, as also highlighted in the shadowgraphs of Figure 4.14 a). At time 0.6 s in (Fig 4.14b), the first separation shock already lifts off and moves upstream. Between these two time steps the velocities of all interrogated points have dropped drastically due to altering flow field. Point 3, in blue, shows a small increase in velocity between 0.6 s and 0.65 s, caused by the instantaneous acceleration in the free stream. From (b) and (c) a grouping of reflected oblique shocks anchored on the shear layer in the aft part of the first wavy contour is observed. This pattern persists for a few tens of milliseconds, and the velocities at points 4 and 5 remain steady during this time. Between 0.65 s and 0.75 s in (c–e), the velocity at point 3 drops drastically while points 4 and 5 remain constant. Points 16 and 17 continue

decreasing at a moderate rate due to the increasing back pressure. After the passing of the terminating shock at 0.7 s, lambda-shock structures appear, and the entire flow field becomes subsonic. In (e) one of these waves is seen right at the location of Points 16 and 17. Soon after the moment that the pressure wave passes upstream of these points, their velocities drop significantly. Shortly after, points 4 and 5 experience the same phenomenon. After the upstream propagation of these waves, the pressure is equalized over the entire field and the flow speed in the test section drops to zero. This measurement shows the ability of FLEET to capture the time-evolution of a spatially resolved transient event. Previous works have described the application of FLEET to transient wind tunnel startup [20] measurements, however the results were limited to one point and were taken in the freestream of the wind tunnel. This work provides an improvement by quantifying time-resolved description of shock structures over a turbine-relevant test article.

Conclusions

Femtosecond Laser Electronic Excitation Tagging (FLEET) was used to optically evaluate the complex supersonic flow over a wavy hub surface representing two-dimensional model of a bladeless turbine. The molecular nitrogen tracking employed in this experiment allowed measurements within the high gradients of velocity caused by compression and separation shocks. Uncertainties were found to be around 6.6% for a mean flow velocity of 500 m/s. Measurements of velocity components compared well to CFD simulations, but disagreed in the precise location of the separation shock. Probability density functions were adopted to evaluate the unsteadiness at different locations, which are caused because of multiple shocks, shock boundary layer interactions, and shock-shear layer interactions. Demonstration of instantaneous shear stress measurements with multi-point FLEET tagging were shown. Finally, the transient flow phenomena that occur during shut down of the turbine were quantified and overlaid with shadowgraph results.

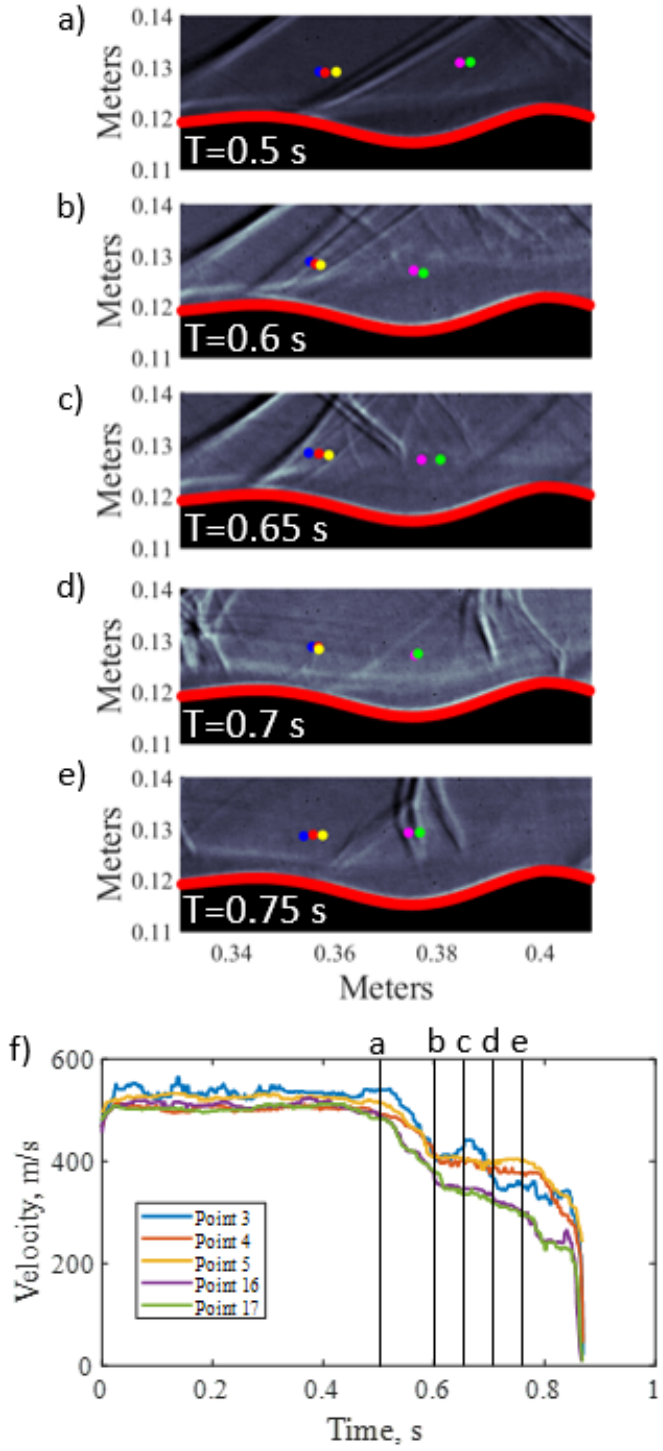

Figure 4.14. (a-e) instantaneous shadowgraph images during unstarting of the test section. (f) Velocity trace of color-coded points in the unstarting flow field from FLEET measurements.

4.3 Boeing/AFOSR Mach 6 Quiet Tunnel

The proceeding section describes the application of FLEET measurements to the Boeing/AFOSR Mach 6 Quiet Tunnel at Purdue University. An initial experiment was conducted in this facility to evaluate the precision and accuracy of velocity measurements as well as the capability of conducting useful aerodynamic measurements. This experiment represents the first application of high speed non-intrusive off-body velocity measurements in this facility. The results of the experiment are to composed into a manuscript entitled "*Evaluation of femtosecond laser electronic excitation tagging(FLEET) velocimetry in a Mach 6 quiet tunnel*" which is currently in peer-review in the AIAA Journal. The body of the manuscript is adapted into this thesis, and future prospects for the improvement of the measurement technique in this facility are presented. Before this experiment was conducted, low-pressure benchmarking was necessary to ensure that measurements would be successful.

4.3.1 Benchmarking at Low Pressure

Previous literature shows that FLEET signal is significantly reduced at low pressures [62], which is a large concern for testing at Mach 6 where the static-to-total pressure ratio (P/P_0) is 0.00063. Before test time could be scheduled in the BAM6QT, proof-of-concept experiments were performed to replicate the conditions to be experienced during actual testing. An optical vacuum cell capable of reaching pressures as low as 0.002 psi was used to perform a benchmarking study on FLEET performance in tunnel representative conditions. In the cell, a number of data acquisitions were taken at pressures replicating the range of wind tunnel stagnation pressures from 15.5-125 psi. To mimic the conditions that would be seen in the measurement region, a number of pressure ratios were considered. The first is the isentropic $P_1/P_0 = 0.00063$ at $\gamma = 1.4$ and Mach $= 6$. As the flow comes over the 5 half$-$angle cone tip it produces a conical shock with a static-to-static pressure ratio $P_2/P_1 = 1.642$. The static temperature of the flow in the wind tunnel reaches 53K based on isentropic expansion, while the experiments conducted in the cell were at room temperature. Following the ideal gas law, to correct for number density, a pressure ratio $P_{cell}/P_2 = 5.6$ was also employed. To create the conditions to be tested in the vacuum cell, these pressure ratios were multiplied

together to give $P_{cell}/P_0 = 0.00579$. The range of pressures test in the cell was 0.096−0.774 psi. To set the pressure, the cell was evacuated with the vacuum pump and then filled back up to the desired pressure with pure nitrogen from a gas cylinder. This process was repeated five times to ensure that all oxygen and other contaminants were removed. The pressure was monitored with a high accuracy GE Druck Unik 5000 pressure transducer with a range of 0-14.7 psia and an accuracy of 0.04% of full scale.

As described previously for the proposed experiment, the same optical layout was used. A Photron SA-z coupled to a Lambert HiCatt intensifier and an 85 mm focal length lens was used to capture images of the FLEET signal. The camera was framed at 1 kHz with a resolution of 1024x1024 pixels. To recreate the signal decay at 1 MHz and 200 kHz acquisition rates, 50 images were taken at delays of 0, 1, 2, 3, 4, 5, 10, 15, 20 and 25 μs after the laser pulse. The Solstice:Ace femtosecond laser was continuously pulsed at a 1 kHz repetition rate with an energy of 1.7 millijoules per pulse. The laser beam was focused with a 250 mm achromatic doublet lens system. The 1.75" thick Corning 7979 window to be used for laser delivery into the BAM6QT was also placed into the beam path. The window is detrimental to FLEET for two reasons: chirp of the laser beam, and supercontinuum generation. The first effect, chirp, is a dispersion of the laser beam as it travels through a medium. Since the femtosecond laser has a large spectral bandwidth (∼40 nm FWHM), the longer wavelengths travel faster than the shorter wavelengths. This causes an effective lengthening of the laser pulse which leads to a decrease in peak power of the laser. The second effect, supercontinuum generation, occurs when laser light is converted to incoherent broadband light in a medium. This occurs when the peak irradiance of the beam surpasses the threshold for self-phase modulation [129]. Depending on the magnitude of this effect, all signal can be lost and the window can be destroyed. To combat this, the laser diameter is increased by a factor of three with a beam-expanding achromatic telescope. This ensures that the irradiance is never high enough to induce supercontinuum generation. Three views of the proof-of-concept experiment are shown in Figure 4.15.

Baseline settings for the imaging system across all of the simulated tunnel pressures. Intensifier gate was set to 500 nanoseconds, and gain was set to 60%. This represents conservative settings for wind tunnel data acquisition. If higher signal levels become necessary,

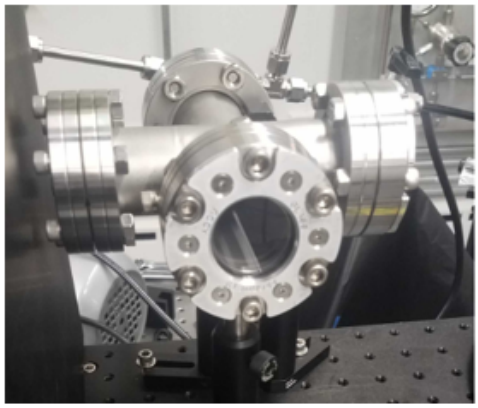

Vacuum Cell

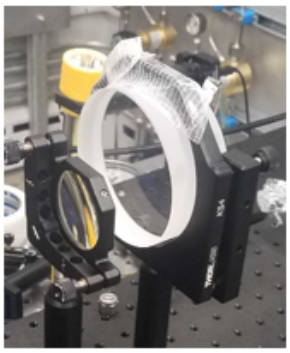

Window and focusing lens

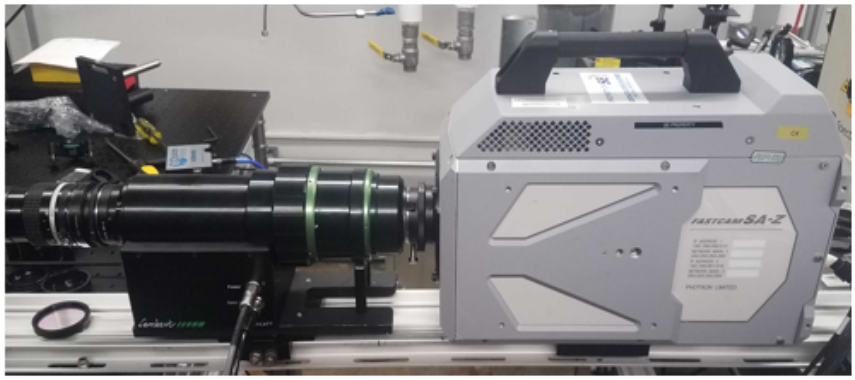

Camera and Intensifier

Figure 4.15. Schematic of the proof-of-concept experiment showing the vacuum cell, wind tunnel wind and focusing lens, and the integrated imaging system.

higher gains can be used. Once data were collected at all test pressures and post-processed, three factors were considered to assess quality. Signal lifetime, FLEET spot quality, and signal-to-noise ratio (SNR) all show favorable results to indicate that data collection in the BAM6QT can be successful. Shown in Figure 4.16 is a display of the raw FLEET signal at delays up to 10 μs after the laser pulse. This gives a representation of how the signal performs over time. To gather accurate velocity measurements, the processing code must be able to calculate the centroid of each spot reliably. For this to be possible, the spot must be bright enough above the background noise, and fit relatively well to a defined shape for centroid finding algorithms. As Figure 4.16 elucidates, the signal in these acquisitions can be seen prominently above the noise and is a continuous quasi-Gaussian shape which can be tracked by the post processing algorithm well for up to 10 μs after the laser pulse. At 1 MHz repetition rate this allows for 10 velocity measurements to be made for each laser pulse. At 200 kHz, 2 velocity measurements can be made.

Figure 4.17 shows the intensity in pixel counts vs time for all tested pressures. As can be seen, the signal decays quickly after T_0, however it is still high enough to be picked up by the image processing code. Since the image processing code creates an analytic two-dimensional Gaussian function to represent each image, spot quality can be assessed with a direct comparison of the raw data to this model. The correlation coefficient, R^2 is used as an indicator for spot quality, and ranges from a value of 1 for a perfect fit, to 0 for completely uncorrelated data. Figure 4.18 displays the correlation coefficient values for all the data acquired. For delays up to 5 μs, the correlation is above 0.75 for all data. After this time, the coefficient stays above 0.6, which is still a favorable fit. This metric promises that centroids can be found accurately, a key factor in obtaining low-uncertainty velocity measurements.

The signal-to-noise ratio (SNR) is defined as the ratio of average signal level to the standard deviations of intensity for the background noise. Based on thresholding, the image processing algorithm can completely ignore the noise in the data so long as it is sufficiently lower than the signal. If SNR is greater than 50, noise can be automatically filtered from the data by a pre-processing routine. With lower SNR, user validation of the background subtraction threshold must be performed. Velocity measurements are still valid down to

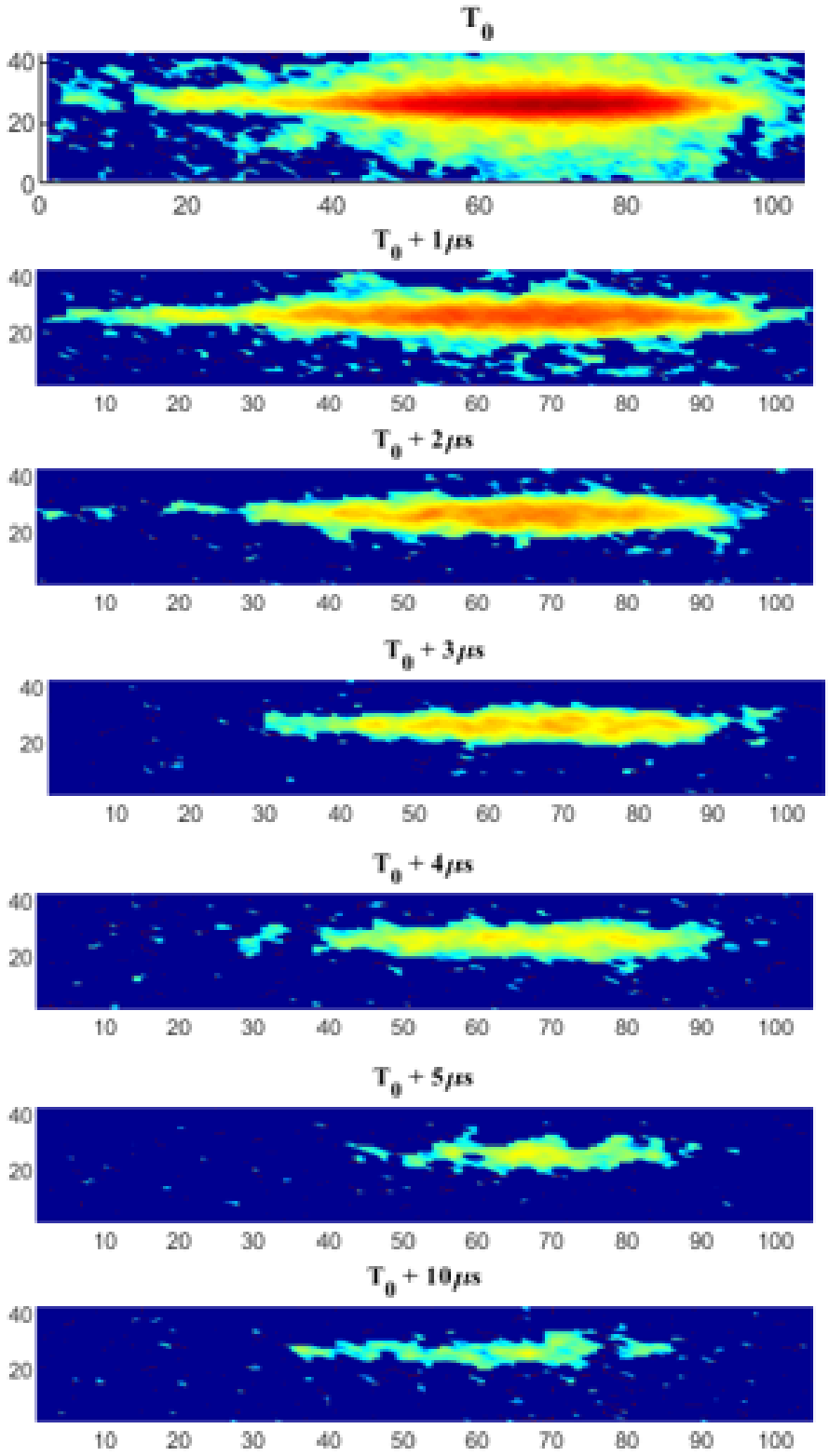

Figure 4.16. Instantaneous FLEET signal at all time delays from laser pulse T_0

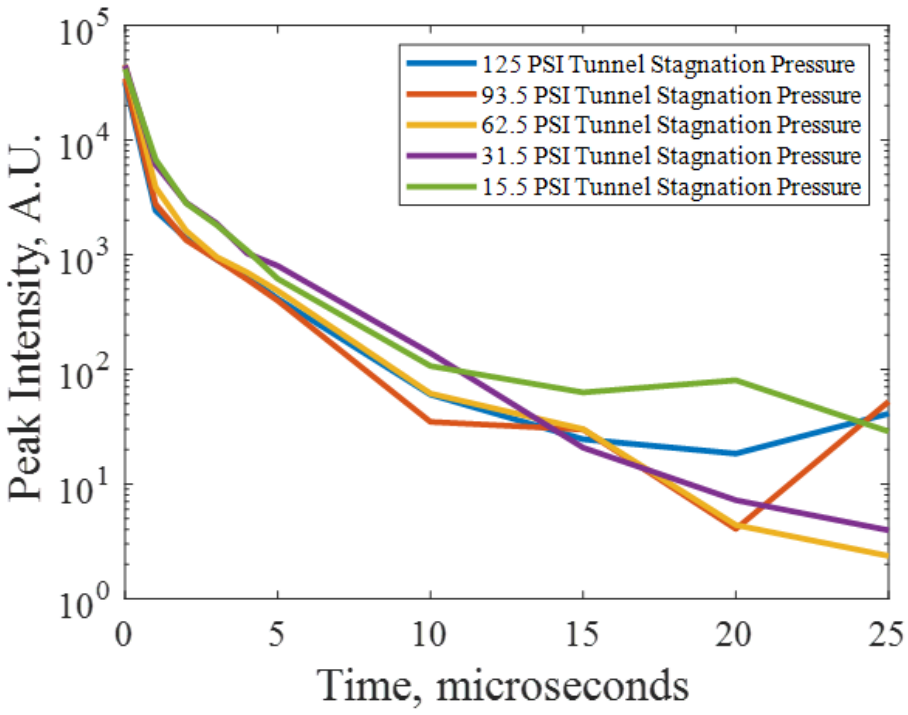

Figure 4.17. Signal Intensity vs. Time for all pressures and time delays

SNR >3 with proper processing. Figure 4.19 shows the SNR time history across all tested conditions.

In previous experiments, [47] the signal lifetime of FLEET has generally been shown to be <50 μs, with SNR greater than 50-100. The reason for the decrease in lifetime (and decreased SNR at longer time delays) in the simulated experiment is an extra window at the wall of the vacuum cell. This window resides near the focal point of the laser beam, and absorbs a large percentage of the laser energy. Since this window will not be in the beam path for the proposed quiet tunnel experiment, it is likely that signal intensity and lifetime will increase significantly, allowing even higher quality data to be collected. Nevertheless, this proof-of-concept experiment shows that FLEET can perform well for velocity measurement at the low pressure conditions present in the BAM6QT.

4.3.2 *Femtosecond laser tagging for boundary layer velocity measurements in the Boeing/AFOSR Mach-6 Quiet Tunnel*

Purdue University, West Lafayette, IN, 47907

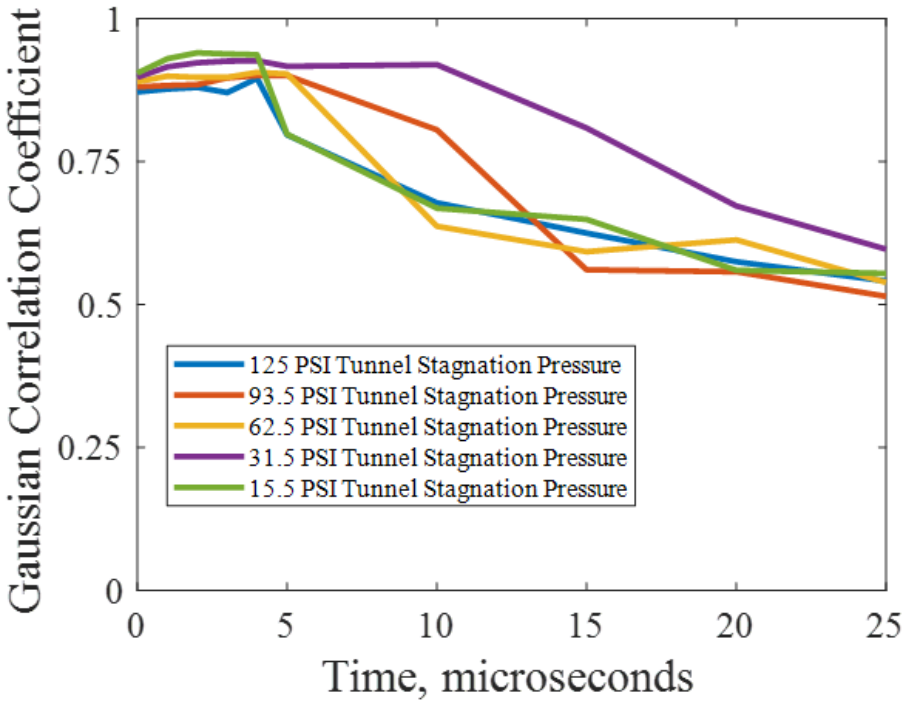

Figure 4.18. Gaussian Correlation Coefficient vs Time for all pressures and time delays

Sandia National Laboratories, Albuquerque, NM, 87185

Introduction

Experiments to demonstrate and evaluate the use of femtosecond laser electronic excitation tagging (FLEET) velocimetry [47], [48] in the Boeing/AFOSR Mach 6 Quiet Tunnel (BAM6QT) [133] are described. Reliable optical diagnostic implementation in hypersonic ground test facilities can prove difficult due to high-speeds and low optical access. In the case of a quiet wind tunnel, it is necessary to maintain a highly polished nozzle that prohibits the use of particle-based velocimetry methods. FLEET is well suited for this environment since it can be employed in pure air or nitrogen flows without seeding and requires only small windows to deliver a laser and view the motion of tagged molecules with a high-speed camera. Recent works have demonstrated initial measurements in hypersonic facilities such as AEDC Tunnel 9 [116] and the Sandia Hypersonic Wind Tunnel [71]. Other recent experiments have applied FLEET for measurements in various high-speed wind tunnels [13], [27], [70]. The BAM6QT is a quiet flow facility with low levels of freestream noise. FLEET is

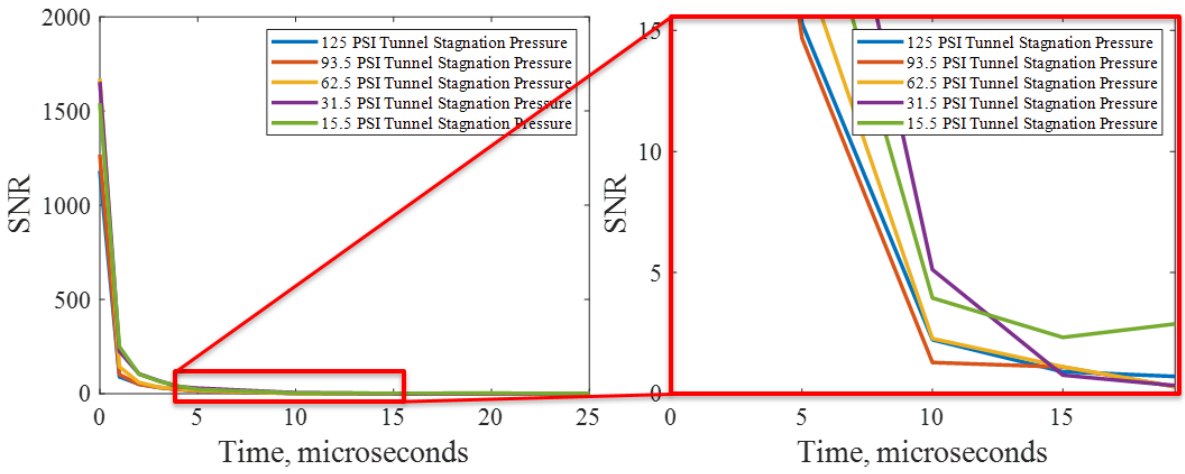

Figure 4.19. Signal to Noise Ratio vs Time for all pressures and time delays

demonstrated for measurements of freestream velocities and the boundary layer velocity profile over an axisymmetric test article during operation at Mach 6. The data capture detailed flow characteristics and are in good agreement with computed velocity profiles. Strategies for molecular tracking are evaluated, and the precision of the technique based on various post-processing methods is discussed.

Experiment and Data Processing

Optical Arrangement

The basic mechanism of FLEET relies on photodissociation of N_2 molecules using a high peak intensity femtosecond (fs) laser that is focused to a point or a line, followed by visible emission of long-lived fluorescence upon recombination. The "tagged" molecules in the flow are tracked with a high-speed camera, and the spatially calibrated images are used to extract the displacement per unit time for velocity measurements. Since native molecules are tracked rather than particles, this approach avoids bias errors due to particle inertia and challenges in seeding near solid boundaries. Hence, FLEET and other molecular tagging methods are promising approaches in hypersonic flow regimes where sharp velocity gradients can exist across shocks or within boundary lasers.

The optical arrangement used in this experiment is shown in Figure 4.20. The 800 nm fs laser (Spectra Physics, Solstice) is sent through a beam expander to avoid white light generation and damaging the optical window. It is then aligned onto a vertical traverse system to allow translation of the measurement location in the flow. On the traverse, the beam passes through an f = +300 mm achromatic focusing lens and is sent into the test section with a mirror to generate the FLEET signal within the focal volume. The laser pulse energy is 1.4 mJ/pulse over a 160 fs pulse duration, as measured inside the test section. Through a separate bottom window, a high-speed camera (Photron, Fastcam SA-Z) coupled to a high-speed intensifier (Lambert, HiCatt, GaAsP Enhanced Red Phosphor) records the images from a perpendicular orientation. The laser photodissociates N_2 at 1 kHz, and the subsequent motion during recombination is imaged at a camera frame rate of 250 kHz. FLEET has been shown to produce higher signal-to-noise ratios in pure nitrogen rather than

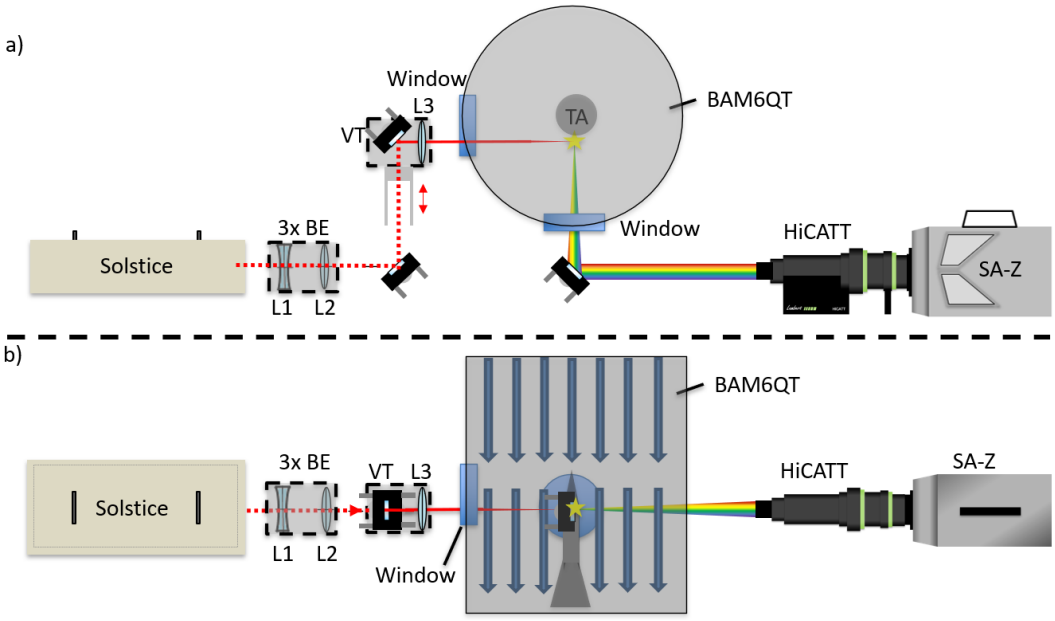

Figure 4.20. Optical arrangement for FLEET velocimetry in the Boeing/AFOSR Mach 6 Quiet Tunnel from (a) end and (b) top views. TA: test article, BAM6QT: Boeing/AFOSR Mach-6 Quiet Tunnel, BE: beam expander, VT: vertical traverse, L1: f = -100 mm achromat lens, L2: f = +300 mm achromat lens, L3: f = +300 mm achromatlens, PE: periscope.

air [62], so the driver tube of the BAM6QT is evacuated and filled to the desired stagnation pressure from nitrogen cylinders before each test run.

Data Processing

Several steps are needed to convert the raw images into velocity measurements, with select processes highlighted in Figure 4.21. In Figure 4.21(a) the raw data from a measurement outside of the test article boundary layer can be seen. An advantage of using images from a perpendicular camera view is that the FLEET signal appears as a short line rather than a point. While measuring lines limits the data collection to one component of velocity, it gives the option of binning the signal to reduce spatial noise and increase precision. In 4.21(b), this vertical binning is shown, reducing the image information to a one-dimensional intensity profile. By performing this binning, the velocity measurement becomes spatially averaged along the length of the line, which in this case is about 10 mm. To obtain a spatially resolved velocity profile, the line can be broken into smaller sub-bins. The peaks in the signal

intensity are first found using a simple peak finding algorithm, and then interpolated with a quadratic function over a 2 pixel local radius to achieve sub-pixel resolution for the spot location. This result is shown in Figure 4.21(c). In (a), the shape and intensity distribution of the tagged spot becomes highly degraded over the successive observations. Without this vertical binning and peak finding, the images from time delays greater than 12 μs would not have sufficient signal-to-noise ratio to be processed accurately. By assuming that the velocity does not change through the duration of the observation, a linear regression can be applied to the displacements to create one velocity measurement. This has the effect of further decreasing uncertainty of individual spot displacements. The regression result is shown in Figure 4.21(d). A correlation coefficient >0.999 in this data gives strong evidence that the negligible acceleration assumption is valid. For measurement points inside the boundary layer, the usable data is limited to 2-4 displacement observations due to decreased signal lifetime. Through the peak finding and curve-fitting steps, spatial and temporal calibrations are introduced so displacement in pixels/observation can be reported as velocity in m/s.

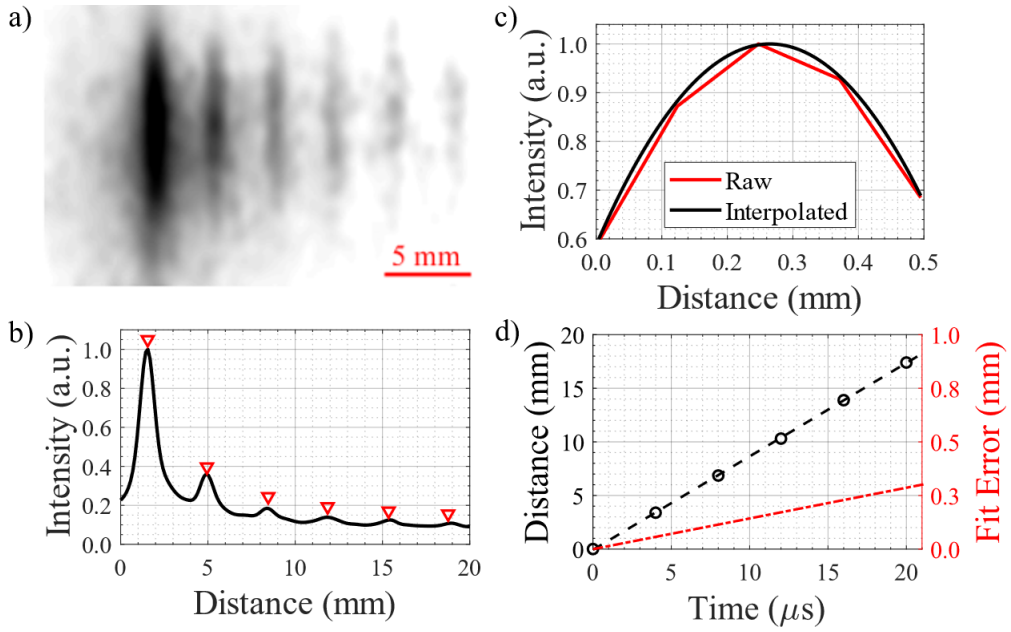

Figure 4.21. (a) Raw multi-exposure image of FLEET signal acquired in the perpendicular camera view. (b) Vertically-binned intensity profile with peaks highlighted by red triangles. (c) Snapshot of local quadratic interpolation of peaks for sub-pixel resolution. (d) Linear curve fit of sequential displacements with R^2>0.999 showing negligible velocity change over the interrogation length.

Results

Precision and Accuracy

As a baseline for the precision and accuracy of the measurement, the freestream velocity behavior is first evaluated. The result is plotted in Figure 4.22. Before 0.5 s, the flow is not fully established in the wind tunnel. Up until about 0.2 s, the flow velocity is insufficient to acquire any data. After this, there is a rapid acceleration of the flow as the test section becomes started. There is a sharp and temporary dip in the tunnel velocity, possibly due to a reflected wave traveling in the tunnel. By 0.5 s, the flow has become fully established. From this time until the end of data acquisition, the flow is at Mach 6, and the velocity change is due to the gradual decrease in total temperature of the flow due to expansion of the gas in the driver tube of the facility. Based on the pressure and temperature traces of the facility, an estimated freestream velocity magnitude can be computed. From Chynoweth [134], the uncertainty in Mach number is 0.1 due to difficulty measuring the state variables P_0 and T_0. This uncertainty band is added to the theoretical calculation of the freestream velocity in Figure 4.22. Since the velocity decreases during the tunnel run, precision is computed as the standard deviation of all samples with respect to a 400 sample moving mean of the velocity measurement. The precision in this case is 6.53 m/s, or 0.76% with respect to the mean velocity value of 856 m/s. While this is comparable to previous FLEET works [21], the actual velocity fluctuations in the BAM6QT are estimated to be less than 0.1% based on the pressure in fluctuations reported in [133]. As such, the precision for this technique is not sufficient to track the slightest freestream fluctuations, but is sufficient to capture the transition to turbulent conditions. The FLEET measurement agrees within 1.5% of the theoretical tunnel freestream velocity of the facility, which has a possible uncertainty of a similar magnitude due to the measurements of state variables required. The accuracy of FLEET measurements in this experiment are potentially better than 1.5%; however, no directly comparable data are available to provide a more accurate assessment.

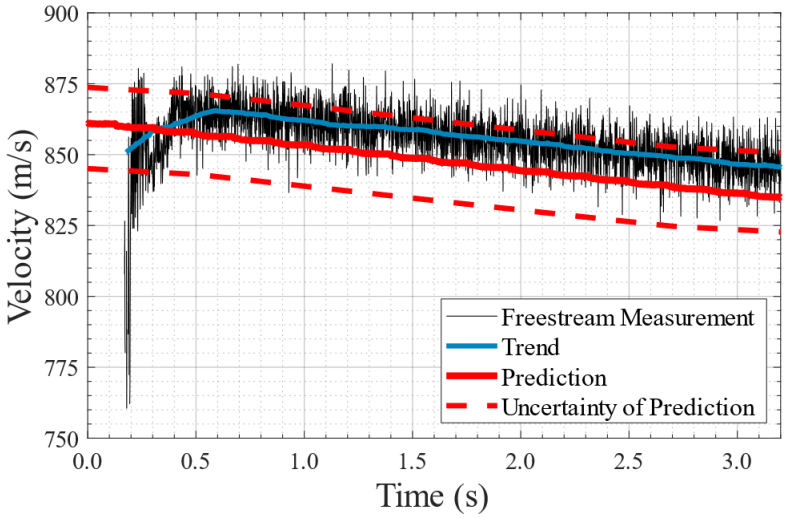

Figure 4.22. Comparison of freestream FLEET velocity measurement and predicted velocity from tunnel instrumentation.

Boundary Layer Traverse

Over a series of 10 wind tunnel runs, a statistical boundary layer velocity reconstruction was created by traversing the interrogation point of the laser towards the test article in small increments. For each of these traverse points, velocities are calculated for each instantaneous image (3200 samples). The tunnel stagnation conditions vary slightly between tunnel runs, so data points must be registered by Reynolds number. To do this, velocity during portions of time (200 ms) of relatively constant Reynolds number ($\pm 5{*}10^3$/m) are averaged. These velocity values through the boundary layer traverse are normalized by the freestream velocity value at the corresponding Reynolds number measured with FLEET outside of the boundary layer. For comparison to these results, a CFD simulation at the nominal test conditions (U_∞=860 m/s, P_0=2.28 Bar, T_0=420 K) was performed with the implementation of the DPLR [135] solver contained in the STABL-2D software package. The comparison is shown in Figure 4.23 and normalized by freestream velocity and boundary layer thickness (δ=3.5 mm).

The calibrated traverse stage gives a high precision measurement of the relative location of each measurement point in the boundary layer. However, there is a uniform bias error in the location of all traverse points because the absolute location of the test article is not

known with high precision. This bias error is accounted for in the plot by minimizing the total error in location with respect to the CFD prediction. The uncertainty in boundary layer location is defined by the FWHM diameter of the FLEET measurement line limiting spatial resolution, while the uncertainty in the non-dimensional velocity is based on the range of data across all Reynolds numbers. Figure 4.23 shows remarkable agreement between experiment and simulation, demonstrating that FLEET can accurately resolve small spatial gradients in this hypersonic environment. The proximity to the test article was limited so as to not risk potential damage to the model surface from the high-power laser in these initial measurements.

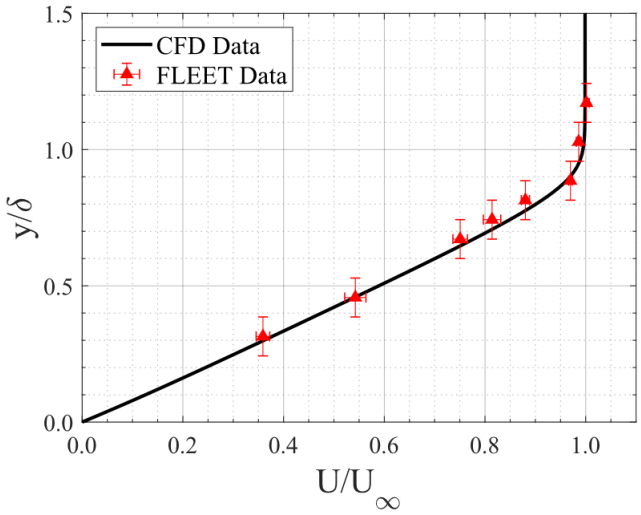

Figure 4.23. Boundary layer traverse measurements overlaid on CFD prediction.

Instantaneous Boundary Layer Profile

The signal appears as a short line between 8-15 mm in length depending on where the measurement is taken with respect to the test article. To create an instantaneously resolved boundary layer profile, the laser is aligned such that the distance from the test article varies along the tagged line. Velocity calculation is performed as previously described, but intensity profiles are created from 10 pixel bins rather than the entire length of the signal. This is similar to what is described in [13] in order to measure a velocity profile along the line. This velocity profile can be seen from the raw data in Figure 4.24(a) with velocity vector

overlays. The right portion of the line lies further into the boundary layer and thus has a lower velocity than the left portion of the line. Figure 4.24(b) shows a plot of the velocity measurement as a function of location in the test article boundary layer with an overlay of the CFD simulation. Again, there is strong agreement showing that FLEET can be used to make instantaneous spatially resolved boundary layer measurements in this facility.

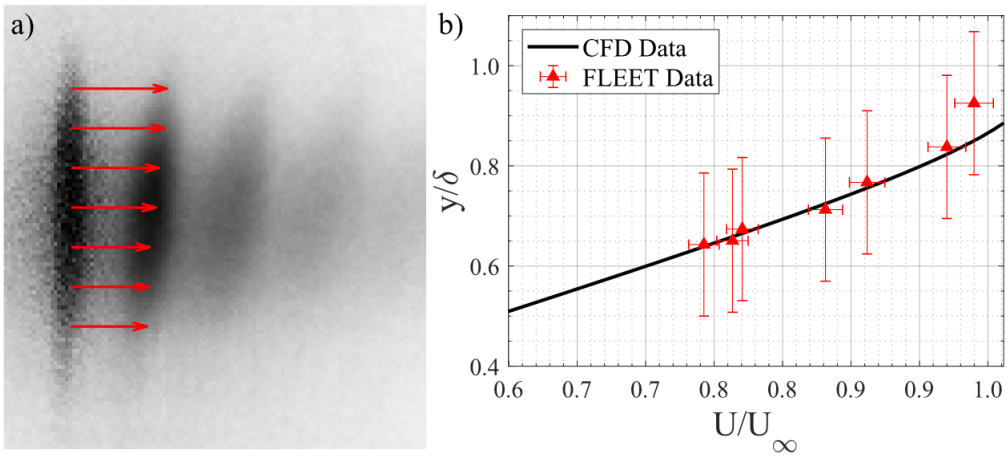

Figure 4.24. (a) Raw data image with velocity vectors showing changing magnitude over the length of the tagged line. (b) Trend of velocity against distance from test article overlaid on a CFD prediction.

Flow Unsteadiness

While the 1 kHz measurement system is not sensitive enough in precision or frequency resolution to measure inherent boundary layer instabilities, the time traces of the boundary layer traverse points show low-frequency unsteadiness. The time trace of one of these traverse points (y/δ=0.8) is shown in Figure 4.25(a). To highlight the trend, a 50 sample median filter is applied. Clear cyclic undulations can be seen in this time trace, especially in the first half of the tunnel run. To give context to this time-trace, the measured stagnation pressure of the tunnel is also plotted in 4.25(a). Time zero in this plot corresponds to the onset of quiet flow in the tunnel, 0.5 s into the test duration. Stepped decreases in the pressure trace coincide with the troughs in the velocity graph. These decreases in the pressure occur due to reflection of the expansion wave in the driver tube of the facility, with a cycle time of around 200 ms. A Fast-Fourier Transform (FFT) is performed on both signals to extract

the spectral content. A spike can be observed at 5.5 Hz in each FFT plot in Figure 4.25(b), giving strong evidence that the oscillations in the velocity trace are directly related to the stepped nature of the pressure history.

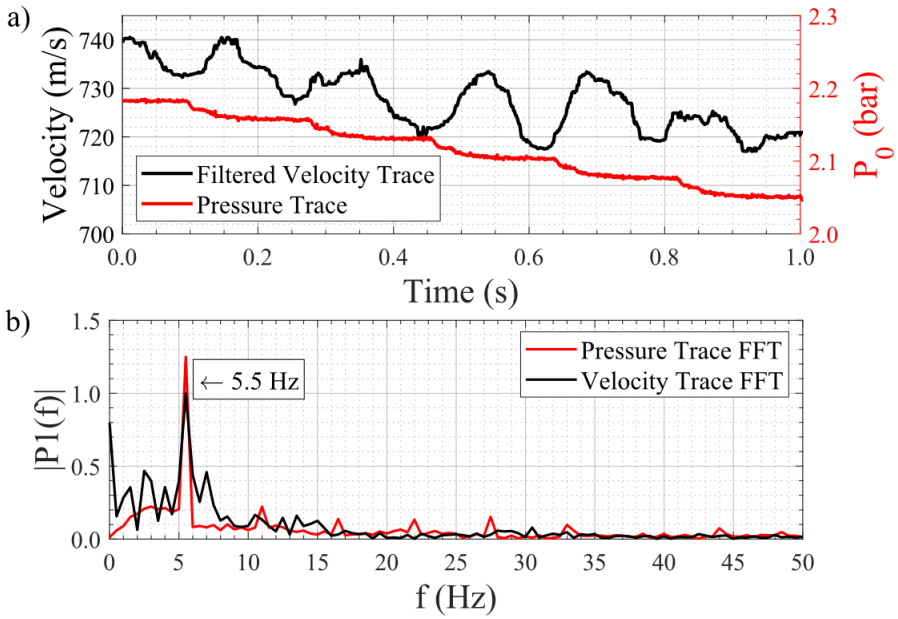

Figure 4.25. (a) Simultaneous time-traces of FLEET velocity measurements at y/δ=0.8 (50 sample moving mean filter) and tunnel stagnation pressure measurement. (b) Overlay of power spectra for both signals showing correlation of velocity to periodic drops in tunnel stagnation pressure.

Conclusions and Future Work

A first demonstration of FLEET for boundary layer velocimetry in the Boeing-AFOSR Mach-6 Quiet Tunnel has been conducted. Preliminary results show a precision of 0.75% and an accuracy better than 1.5%. Other results that were shown include a statistical boundary layer traverse which shows strong agreement to CFD estimation, demonstration of instantaneous boundary layer profiles along a line, and capturing of low-frequency dynamics in the boundary layer of the test article. Future improvements to the technique will focus on improving the single-shot precision and spatial resolution. A proposed advance for this measurement is generating excitation with a third harmonic femtosecond laser to produce increased signal, longer lifetime, and smaller focused spots, which has been described in [19].

For additional benefit in signal levels, trace amounts of argon may be added to enhance the FLEET emission mechanism, as demonstrated in [52], [53]. The final proposed alteration for the experiment is to increase camera magnification to reduce surface fitting error, as shown in [55]. With these improvements, further enhancements in the precision and spatial resolution of FLEET measurements in the Boeing/AFOSR Mach-6 Quiet Tunnel are anticipated.

4.3.3 Optimization of Measurement Technique for Quiet Hypersonic Flow

The overall focus of the BAM6QT is to study laminar to turbulent boundary layer transition in a clean hypersonic environment. The previously applied methods of achieving this have been high frequency surface sensors for heat flux and pressure, or infrared imaging for surface temperature [136]. Some off-body techniques have been recently applied to measure density fluctuations [137]. To fully complement and enhance capability for measuring boundary layer transition, FLEET must be demonstrated to capture minute fluctuations in the magnitude of velocity over small spatial differences. To achieve this practicality, a few things must be prioritized. Among these are single-shot precision, spatial resolution, and reduction in uncertainty of the measurement location.

Enhanced Precision

Under quiet flow conditions in the BAM6QT, the pressure fluctuations $p/p_0 < 0.05\%$. This represents a velocity fluctuation magnitude of $\pm$ 0.2 m/s or 0.025%. To capture turbulent intensity inlet boundary conditions for CFD analysis, FLEET must be sensitive enough in precision to measure this minute level of flow fluctuation. This would represent a 30X improvement in precision, which is likely out of reach. However, in order to evaluate and locate boundary layer transition, precision must be enhanced in near-wall measurements as well. From the technical note in the preceding section, data quality is known to diminish in the vicinity of the wall. Thus, this represents a difficulty in capturing the relevant flow physics of interest.

Naturally, it becomes desirable to improve the single-shot precision of FLEET applied in the BAM6QT to the maximum attainable value. The first method of improving the precision

is to increase the imaging magnification. By imaging the FLEET spot onto a digital sensor, the signal is discretized over a finite number of pixels. FLEET signal is generally regarded to follow a Gaussian profile [27], although more complex surface fitting such as pseudo-Voight profiles have been examined [20]. To find the accurate sub-pixel centroid location of the profile, least-squares fitting schemes are applied to achieve the analytic formula for the surface fit. A minimum of 3 discrete data points (pixels) are necessary to create a one-dimensional Gaussian least-squares fit. However, the error in actual centroid location from this curve fit can be considerable with this few number of bins [138]. Typical FLEET images capture the signal over a range from 5-30 pixels depending on the magnification. At 5 pixels, the centroid estimation error can be as great as 0.5 pixels. At 30 pixels, this uncertainty can decrease below 0.1 pixels. Thus, if the FLEET spot is a constant size, increased imaging magnification will discretize the spot over more sensor pixels, resulting in decreased surface fitting error.

In the same work describing error in Gaussian fits [138], background noise and peak signal amplitude also play a large role in determining the accuracy of centroid finding. To improve this with respect to FLEET measurement, the ultimate signal intensity and lifetime must be maximized. Unfortunately, at low pressures, the signal lifetime of FLEET decreases drastically. Recent efforts [71] have shown the FLEET emission lifetime can be improved by excitation with 267 nm lasers at low pressures. With increased emission lifetime, the SNR will be larger at increased imaging delays. With higher SNR the centroid finding uncertainty will be decreased. Argon enhancement has been shown to influence and extend the recombination processes of nitrogen which lead to optical emission [139]. While this has not been studied at low pressures, it represents a second avenue for increasing the signal and lifetime of FLEET emission in the BAM6QT. Both excitation by 267 nm laser and enhancement by argon doping will be investigated in the BAM6QT in hopes of greatly improving signal lifetimes and thus decreasing centroid finding error.

Improved Spatial Resolution

In the first experiment, the spatial resolution was around 1 mm with respect to the boundary layer height, due to the large size of the tagged volume. For test articles such

as the cone-cylinder-flare that were used, typical boundary layer thickness is 4-5 mm. This dictates that FLEET can only capture the boundary layer in a few discrete intervals. Inside of these intervals there is a significant spatial velocity gradient. The velocity difference across the top and bottom portions of the tagged FLEET molecules can be up to 200 m/s. This can be seen in Figure 4.23 in the y/δ uncertainty of the measurements. This limits the applicability of FLEET to capture spatial fluctuations on this scale. A second factor of spatial resolution is the streamwise component. In the time-of-flight arrangement which is the basis of all molecular tagging velocimetry schemes, the spatial resolution in the flow direction is a function of how far the molecules travel throughout the imaging time. This can be as long as 5 - 10 mm with multi-framing of the FLEET signal. In certain flows, it can be shown that the flow acceleration is negligible over this distance, but that is not always a valid assumption. Minimizing the framing time, as described in [19], [20] is necessary in hypersonic facilities.

The spatial resolution in the boundary layer is a product of two factors: molecular diffusion of the dissociated nitrogen, and the minimum beam waist of the focused laser. Molecular diffusion occurs because the laser creates a local over-concentration of dissociated nitrogen atoms. This high concentration wants to expand outward to push the system toward equilibrium. The problem of molecular diffusion is enhanced at low pressure such as in the quiet tunnel, where there is less resistance to the tagged spot expanding. To combat this problem, it is desirable to image the FLEET signal as fast as possible, before the spot has had time to expand significantly. As mentioned before, it is already desirable to minimized the total acquisition time in hypersonic flow to improve the spatial resolution in the streamwise direction.

The beam waist of the laser determines the focused spot where FLEET dissociation happens. This is a function of the quality of the laser, the accuracy of alignment, the lenses used, and the wavelength of the laser. The beam waist equation 4.9, as described previously, is restated here. This formula describes in a simple relation the influence of all laser parameters on controlling the focused size of the laser.

$$w_0 = m^2 \frac{2\lambda F}{\pi D} \tag{4.9}$$

The simplest parameter, m^2, or beam quality, has a large impact on the beam waist. This is a factor of how well the laser system is constructed. Commercial laser systems such as the one used previously can have m^2 values <1.1. Burst-mode systems such as what was used in 3 can have m^2 from 3.5-10+. Modulating the m^2 in this manner has a direct linear relation with the minimum beam waist that can be achieved with the laser. For a constant laser energy, increasing the beam waist has an inverse-square law relation with the maximum irradiance which directly impacts the amount of signal that can be produced for the measurement. Often times the m^2 can not be improved greatly in commercial laser systems, although poor alignment and choice of focusing lenses and mirrors can dramatically increase the m^2 value along the beam path. Thus, it is desirable to chose proper focusing optics and prioritize proper alignment techniques to create the smallest possible beam waist for a given system.

In the denominator of the beam waist equation, the D represents the input beam diameter. If this can be increased, the beam waist will decrease. In the previous application of the experiment, the beam diameter was tripled using a 3:1 telescope. By performing this beam expansion, it is expected to decrease the beam waist by a factor of 3. Unfortunately this may not always be the case, as using expansion optics can negatively affect the m^2 value of the beam, by introducing aberrations.

The last two factors to influence the beam waist are λ and F. F is the focal length of the optical system. Minimizing this will minimize the beam waist, but with space constraints this can not often be changed drastically. However, the wavelength, λ, can be modulated. By using harmonic crystals, the fundamental wavelength of the laser (800 nm) can be adjusted to 400 nm or 267 nm by frequency doubling or tripling. Thus, by decreasing the wavelength the effective spatial resolution can be improved. This has already been described in [71] to decrease the linewidth of the tagged FLEET volume. For future experiments in the BAM6QT, excitation with a wavelength of 267 nm will be prioritized to decrease the beam waist and improve spatial resolution.

Reduction in Spatial Uncertainty

The last avenue for short-term improvement of FLEET in the BAM6QT is the reduction in spatial uncertainty of measurements. The first two improvements deal with improving the capability and precision of the measurement itself. If the measurement has extreme precision in magnitude, but its location is unknown, it will not be a useful measurement. Fine detail must be known about where a velocity measurement was taken with respect to the surface of the test article top make useful inferences about the behavior of the boundary layer. This problem becomes complicated in the environment of the BAM6QT because geometry varies in three dimensions. Special care must be taken in setup and calibration of the imaging and laser systems to ensure that the measurement location can be evaluated with 0.1 mm accuracy.

In the first experiment, the imaging system was calibrated with a two-dimensional dot-target plate located at the centerline of the wind tunnel. This method gives information on the streamwise and spanwise location of the laser measurement with respect to the wind tunnel. This is generally regarded as a reliable calibration method. With proper alignment of the camera, paying attention to maintaining the imaging axis perpendicular to the calibration plate, low spatial uncertainty can be obtained in the imaging plane. However, this method does not give information on the depth of the measurement in the transverse direction of the wind tunnel. If the laser focal volume is not precisely located at the centerline of the tunnel where the camera is calibrated, a large spatial uncertainty is introduced. This was not accounted for in the original measurement, and the laser focus was off from the tunnel centerline by 4 mm. To correct for this in future works, a physical beam target will be placed in the test section at the tunnel centerline to ensure that the laser focus in the correct location. This is necessary to full calibrate the imaging system with respect to the wind tunnel.

While the previously described steps have proven reliable to calibrate the imaging system to a know reference location (wind tunnel centerline) in three dimensions, the location of interest is the test article. Unfortunately, the test article cannot be considered immediately as a reliable reference location. The mounting of the test article is nominally located on the

wind tunnel centerline, but due to cantilevered mounting, sagging of the article is possible. Other positional errors in the location of the test article surface are possible such as tolerance errors in the machining, and random vibration during testing. To account for static bias error in the position of the test article, back-lit imaging is necessary during the camera calibration process to determine the absolute location of the test article surface in the imaging field of view. A stated previously, with small boundary thickness on the order of 4-5 mm dictates the desired positional uncertainty of the test article surface and measurement location should be on the order of 0.1 mm. Sagging of the test article due to cantilevered mass on the sting mount is well capable of inducing deformations greater than this value, and thus must be accounted for.

An even larger concern in positional uncertainty is the dynamic motion of the test article. While the tunnel is in operation, aerodynamic forces can act on the model and cause motion. This motion can either by quasi-steady with the tunnel transient, or include random vibration. To determine this, backlit imaging with the calibrated high speed FLEET camera can be used. A time-trace of the test article with known reference points can be analyzed for the duration of the wind tunnel test. If the motion is quasi-steady, the location of the test article will be expected to vary in a predictable manner during the test operation, without the influence of random vibration. If this is the case, this can be reliably accounted for in the measurement location calculation by taking note of the time in which measurements are taken. If there is a considerable amount of random vibration in the test article location, this can be detrimental in the reduction in spatial uncertainty of the measurement. Essentially, whatever the existing magnitude of random vibration will set the minimum achievable spatial uncertainty in the measurement location.

4.3.4 Investigation of Third-Harmonic Excitation and Argon Enhancement

A bench-scale investigation of the effects and potential benefits of third-harmonic excitation and argon enhancement was conducted to further inform continuing BAM6QT FLEET tests. A third harmonic generation kit was purchased form EKSMA optics to convert the 800 nm fundamental laser wavelength to 267 nm. In the experimental arrangement, the conversion kit has an efficiency of 8.22%. The 1.24 mJ of 800 nm input results in 102 μJ

of 267 nm beam. The input and output beam diameter is 10 mm. The imaging system consists of a Photron Fastcam SA-z, LaVision UV-IRO, and a Cerco 45 mm camera lens, with an f number of 2. The camera is synchronized to take a burst of 10 images at 200 kHz for every laser pulse. The image resolution is 384x180 pixels and the magnification is 18.2 pixels per mm. To enable direct comparison of intensity, lifetime and spot width between all datasets, the imaging system settings are kept constant throughout the duration of the test. The intensifier gate is 3500 ns, and the gain is 63%. A custom-constructed 4-port vacuum chamber was used to maintain a constant controlled environment for testing. To set the controlled environment, a Robinair 15500 is used to pull down the cell to the desired testing pressure. Alicat mass flow controllers are used to precisely control flow rate of nitrogen and argon into the cell to maintain a specified gas composition by volume, and to continuously recycle cell contents. A Druck DPI 611 pressure calibrator is used to monitor pressure in the cell.

With an f = +150 mm UVFS focusing lens, both the 800 nm and 267 beams can be focused into the calibration cell, flip-mirror mounts are used to create separate beam paths for the input 800 nm beam and the 267 nm beam so that the experiment can evaluate both wavelengths of excitation with full energy. The calibration cell utilized 5 mm thick UVFS windows to allow laser excitation and signal to transmit into and out of the measurement volume. Gas cell pressures from 4000-1600 Pa are tested with argon concentration of 0-5% by volume, with exctiation at 800 nm and 267 nm.

The first result to be analyzed is the effect of pressure on spot width and lifetime for each excitation wavelength. The desire for utilizing 267 nm excitation, especially at low pressures, is to increase the signal lifetime as well as decrease the spot width. Both of these effects are previously mentioned in [19] and verified here. In Figure 4.26 a), the signal lifetime is shown for varying pressure with both excitation wavelengths. This lifetime is reported as the exponential decay time constant, τ, which refers to the time it takes for initial signal to decay to 1/e times the original intensity. Immediately, the improvement in lifetime of signal for the 267 nm excitation is apparent. For all pressures, the lifetime is greater than 50% better for third harmonic excitation as compared to fundamental wavelength excitation. Even more remarkable, is the trend against pressure for both wavelengths. For the 800

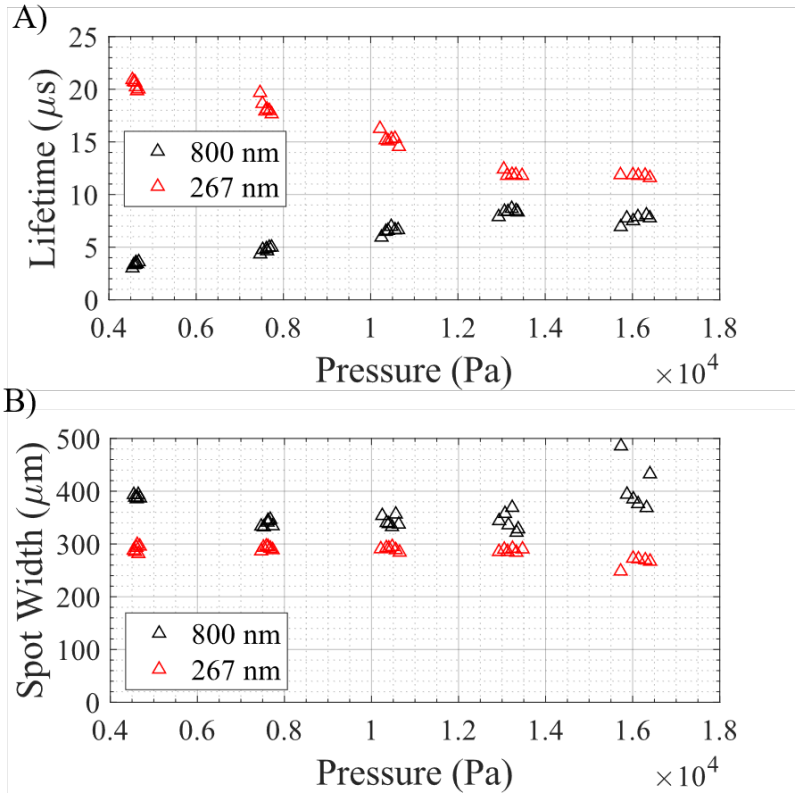

Figure 4.26. A) Lifetime vs pressure for 800 nm and 267 nm FLEET excitation. B) Spot size vs pressure for 800 nm an 267 nm excitation.

nm excitation, the signal lifetime decreases with decreasing pressure. On the contrary, the 267 nm excitation shows increasing lifetime for decreasing pressure. At the lowest pressure tested, the 267 nm excitation shows a 4x improvement over the fundamental. As shown previously, the decrease in lifetime at decreased pressures for FLEET is severely detrimental for measurement accuracy and tracking of flow acceleration. For framing at 250 kHz, which is generally standard for FLEET measurements, the 800 nm lifetime allows for 3-5 images of the signal. With extended lifetimes available due to 267 nm excitation, the number of images could be increased to 12-20, which greatly extends the amount of streamwise tracking available in hypersonic environments. Already, with just the initial result, 267 nm shows a large benefit toward application at low pressures over 800 nm.

Figure 4.26 b) shows the spot width of signal at all tested pressures for both excitation wavelengths. The spot width is calculated as the FWHM of the Gaussian least-squares function used to fit the data. With decreased laser wavelength, ignoring changes in beam quality or input beam diameter, one would expect a factor of 3 reduction in beam waist between 800 nm and 267 nm. In reality, conversion to third harmonic can alter the beam quality and adversely affect the beam waist size. Focal shift due to the bandwidth of the laser beam is also a cause of this effect. Nonetheless, from Fig. 4.26 b), there is a clear reduction in FLEET spot size with 267 nm. The maximum improvement is around 25%. With a decreased beam waist, the spatial resolution of the velocity measurement is improved, and smaller flow features and spatial gradients can be measured. This is especially important for the BAM6QT implementation where the boundary layer thickness is on the order of several millimeters, and the most number of discretizations in measurement location is desired.

For low-pressure environments, Figures 4.26 a) and b) already prove that 267 nm is a marked improvement over fundamental harmonic excitation. Continuing into the evaluation, the effect of doping the flow with small percent of argon is investigated. Zhang [53] already studies the effect of doping nitrogen with argon at atmospheric pressure. The femtosecond-laser excitation is capable of pumping metastable argon excited states which in turn promote the nitrogen first and second positive recombination mechanisms over time which increases the lifetime and signal intensity. This improvement has not been studied at low pressure, or with 267 nm excitation. For the work of Zhang [53], argon concentrations up to 100% are

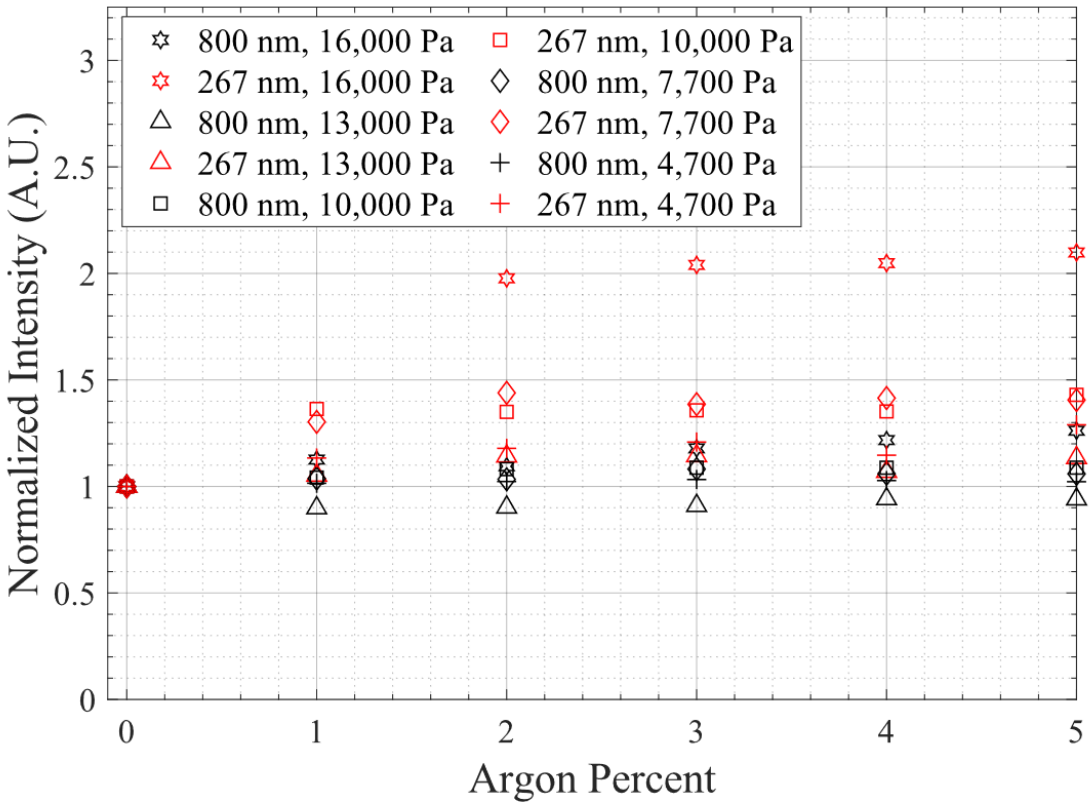

Figure 4.27. FLEET signal intensity vs percent argon at different pressures with 800 nm and 267 nm excitation. Data normalized by zero argon percent signal intensity

investigated. For the practicality of the BAM6QT studies, only low percent argon is allowable, due to the mis-match in isentropic expansion coefficient between nitrogen and argon. With an overly large argon concentration, the gas-flow properties and tunnel operation will be drastically impacted.

The first parameter to consider for the argon enhancement study is ultimate signal amplitude. This is directly related to SNR of the measurement, which in FLEET [20] has an inverse relationship to uncertainty. With a maximization of SNR, the highest precision can be achieved. Figure 4.27 shows the results of normalized signal intensity with respect to increasing argon percentage at all the tested pressures. The intensity is normalized by the peak signal intensity of the 0% argon percentage case at all pressures, so any value above 1 represents an increase in signal intensity, and any value below 1 is a decrease in signal intensity over the baseline. It is immediately apparent that argon, in any concentration, delivers an increase in peak signal intensity for 267 nm excitation. The most remarkable improvement occurs at 16000 Pa, where the relative improvement exceeds 100%. For all other pressures, the improvement is near 50% or less with 267 nm excitation. While this may not seem like a large improvement, it can have a considerable impact on the uncertainty of the technique, especially in low-pressures where SNR levels may approach unusable levels. Surprisingly, the excitation with 800 nm shows minimal or non-apparent improvement with argon doping at these decreased pressure levels.

The last parameter to be evaluated is the signal lifetime variation with increasing levels of argon. Figure 4.28 shows this result plotted against all tested conditions. Surprisingly here, while there was a considerable increase in signal intensity with argon doping, the signal lifetime appears to be completely un-correlated. Nevertheless, the benefit of argon doping is apparently from the peak signal amplitude improvement.

4.3.5 Implementation of Fundamental Molecular Tagging Advancements

The physical implementation of all fundamental advancements described in this thesis would take a considerable amount of resources and additional effort to accomplish. The overall goal of this research is to make significant progress in showing the feasibility of improving the fundamental data output quality of molecular tagging methods in terms of

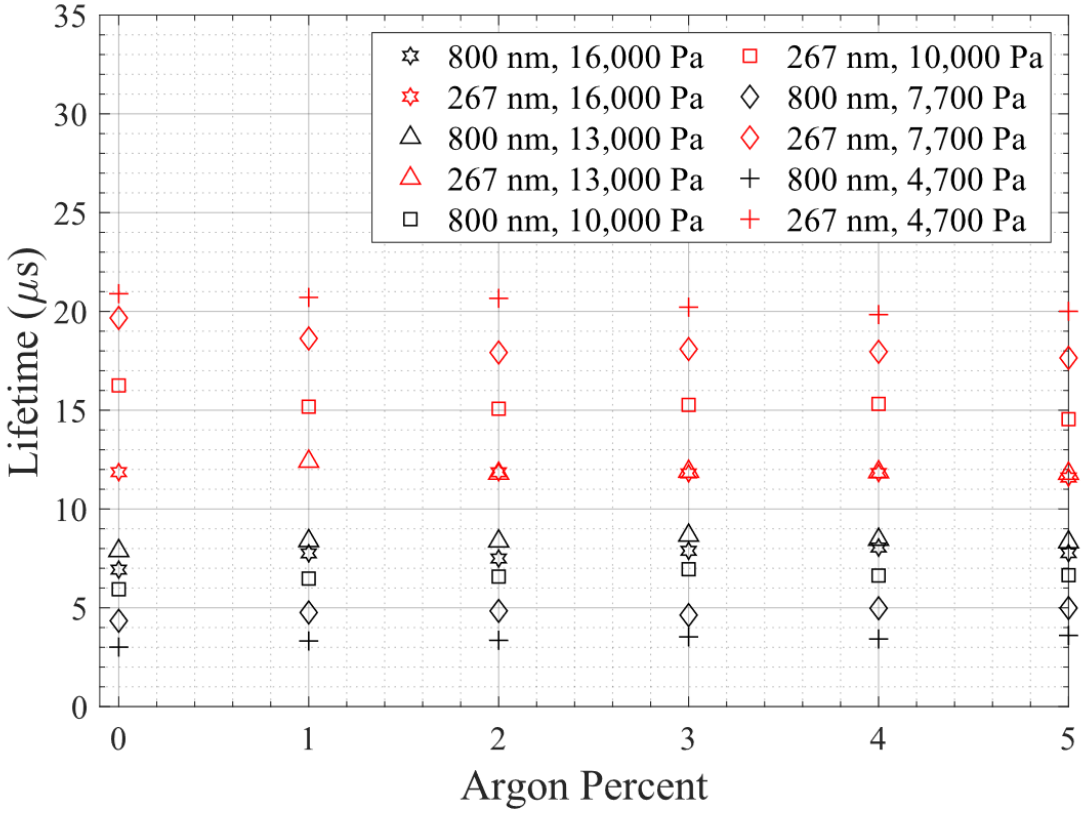

Figure 4.28. FLEET signal decay lifetime vs percent argon at different pressures with 800 nm and 267 nm excitation

precision, implementation, and aerodynamic results with respect to frequency resolution and spatial measurement extent. These baseline advances have been evaluated to show an increased measurement quality for when they are capable of being implemented into higher-speed and more advanced facilities such as the BAM6QT.

Multiple Spot Tracking for Extreme Precision

Two of the measurements conducted originally during the first test campaign that were not incorporated into the original publication were the study of signal variation with varying tunnel stagnation pressure, and laser excitation energy. With some initial surprise, the signal did not seem to improve significantly with increased tunnel stagnation pressure, although this is supported by previous literature at very low pressures [48]. The excitation energy study suggested that the minimum usable laser energy for measurements in the BAM6QT is around 750 μJ/pulse.

With the lower-power femtosecond laser used in this initial experiment, the maximum pulse energy available is around 2.5 mJ. In an ideal situation, a diffractive optical element could be used to produce 3 individual excitation points in the BAM6QT using this laser. However, if the higher-energy capable femtosecond laser used in 2 (6-7 mJ), the beam could be split to produce 8 simultaneous measurement points.

If the previous advancement in spatial extent were implemented into the BAM6QT, instantaneous spatial correlation of velocity in the boundary layer could be achieved. This could give insight into phenomena such as the unsteadiness observed with relation to the stagnation pressure fluctuations in the tunnel. Additionally, by putting the measurement points in close proximity and using spatial averaging, the precision of velocimetry could be greatly enhanced. Since ultimate precision is a clear goal of the measurements in this facility, spatial averaging may be necessary as a path forward. With first or second-level spatial averaging, the precision can instantaneously be improved by $60-70\%$. With respect the measurements made previously, this could be used to achieve an improvement of the precision level from 0.75% to 0.225%. Improvements in the optical and data processing arrangements to allow this, in combination with the other previously described methods in

precision improvement may allow for the capturing of instantaneous small scale fluctuations in this quiet flow facility.

High Frequency Measurements

As previously noted, the lower pulse energy limit for measurements in the BAM6QT is 750 μJ per pulse. While this is not currently capable with any burst-mode femtosecond laser, the technology is rapidly maturing closer to this point. In the semi-near term, if this pulse energy becomes available at repetition rates between 100 kHz-1 MHz, high-frequency resolution FLEET can be applied in this facility. This would enable for more in-depth study of boundary layer transition due to second-mode instabilities. By using high repetition rate FLEET and sweeping along the test article axis in the boundary layer, any increase in fluctuation intensity at high frequencies can be captured and studied to understand onset and growth of these flow mechanisms.

5. SUMMARY OF ADVANCEMENTS AND CONCLUSION

This thesis includes 3 chapters which detail major advancements in velocity measurement with molecular tagging methods as listed below:

1. Advances in the spatial extent of FLEET
2. Extension of molecular tagging capabilities
3. Aerodynamic application in ground test facilities

5.1 Demonstrated Advancements

5.1.1 Advances in the spatial extent of FLEET

The desire to improve the spatial extent of FLEET stems from the need to measure parameters such as spatial coherence scales, vorticity, and shear stress. In order to achieve this, optical arrangements to create gridded FLEET excitation were conceived and evaluated. The simplest method considered was to use conventional beamsplitting optics to create multiple beam paths. This method is described in Chapter 4 as part of the bladeless turbine test campaign. The downfall of this method is its complexity and spatial constraint. To achieve more than 3 points with this arrangement would be prohibitively expensive and time consuming to implement. For desirable separation of the measurement points, optics must be placed in extremely close proximity which limits the practicality of the technique. Improving on this technique was the microlens arrangement, as described in Chapter 2. This method was capable of measuring 3x3 grids, but was not flexible in stand-off distance, number of spots, or grid separation. Additionally, due to the Gaussian intensity distribution of the beam traveling through a spatial array of lenses, the SNR uniformity of across the extent of the tagged grid was much less than acceptable. Nonetheless, this method gave sufficient data to begin developing processing codes capable of handling gridded FLEET results.

The final method for improving the spatial extent of FLEET is to use diffractive optical element (holographic) beam splitters. These optics allow for design and control of the number of grid points, the grid separation, and adjustment of the measurement standoff distance. In this work, a DOE beamsplitter was used to make 4x4 grid-FLEET measurements in free-stream and near-obstacle flow fields. Measurement precision equals that of previously demonstrated single-point measurements. The grid-FLEET data allows for instantaneous calculation of spatial velocity gradients which can be used to measure shear stress and vorticity. This arrangement is now being considered for implementation to high-speed ground test facilities for spatially-resolved FLEET measurements at hypersonic velocities.

With gridded data, processing must be approached differently. Special considerations and advanced methods for processing these data sets are discussed. Included in this are methods for improved outlier detection based on excitation spot quality and shape, adaptive velocity measurement calculation based on smooth flow along a streamline, and multi-spot precision enhancements. Through adaptive velocity calculation, assumptions are made regarding the spatio-temporal behavior of the flow including smoothness in velocity and acceleration to represent real physical characteristics. These assumptions can smooth random fluctuations in uncertainty due to centroid finding, but may negate the ability to measure small-scale turbulent deviations. For ultra-high precision measurements, multi-point correlation processing was invoked. This method was considered as a similarity to PIV processing methods, where one velocity measurement is constructed from the displacements of multiple particles in the same vicinity. By grouping multiple FLEET spots for one measurement, the random uncertainty in any one displacement is smoothed out by the ensemble, and the overall precision is increased in a trade-off with spatial resolution.

5.1.2 Extension of molecular tagging capabilities

Increased Repetition Rate

In the work of this thesis, FLEET measurements were demonstrated at a repetition rate of 1 MHz. This represents an improvements of three orders of magnitude above the previously possible 1 kHz measurement via commercial laser systems. Typical boundary layer

disturbances in hypersonic flows can range from 50−500 kHz [87], so this repetition rate is necessary to capture the spectral content of the flow. The two underlying factors in achieving this improvement in temporal resolution are the understanding of lower signal threshold of FLEET, and the advancement in burst-mode femtosecond laser technology. While laser development is outside the scope of this thesis, the advancements in understanding of FLEET informs the research in this area to the specific needs of the measurement method. A supersonic slot-jet device was constructed in order to create high flow velocities in a small form factor with high optical access. Using this jet, a lower pulse energy threshold was determined by repeatedly decreasing excitation energy with a commercial 1 kHz laser system. When the lower energy threshold was determined, efforts were put forth to produce this energy with the fs burst-mode laser at repetition rates from 100 kHz−1 MHz.

Demonstration experiments were performed showing capability of 200 kHz time-resolved measurements in air and pure nitrogen, with precision to match previous works at lower repetition rates. Single-shot data were collected with 1 MHz laser excitation, but the available imaging system was not sufficient to capture time-resolved measurements. At 200 kHz and 1 MHz excitations, it was shown that instantaneous measurements along the streamwise extent of the flow are possible because previously tagged tracer packets continue to fluoresce as they follow the flow and new excitation points are created. Future improvements of the laser platform are underway, which promise to eventually give the capability of performing 100 kHz−1 MHz measurements with longer stand-off distances, at low pressures in practical large scale test sections, and in multiple-point configurations.

Extension to Reacting Environments

The work by DeLuca [62] shows FLEET lifetimes to be less than 1 μs in flames, which precludes its useful application to reacting test sections. While this signal was usable in a minimal amount, current camera technology is not fast enough to make full use of lifetimes this short. Femtosecond laser activation and sensing of hydroxyl (FLASH) was developed to produce longer-lived tracers in reacting environments. In combusting environments, the fs laser creates tracers out of dissociated water molecules instead of nitrogen. Since the OH radicals do not exhibit long-lived fluorescence, their location must be 'read' by a secondary

PLIF laser sheet in order to be imaged by a camera. Initial development and characterization of this measurement technique was conducted at various conditions of write-read laser delays, equivalence ratios, and excitation energies in a hydrogen-air Hencken burner, to assess SNR and tracer lifetimes for measurement optimization. This experiment showed that the method was possible in high-speed and unsteady flame environments.

Multiple timing and operation schemes were identified for the FLASH method and their individual merits and downfalls were considered. Ultimately, two versions of the technique were attempted in the exhaust of the THOR RDE. Both timing methods (10 Hz and 1 MHz) resulted in sufficient SNR to track the FLASH signal in the combustion chamber exhaust. The implementation of the 10 Hz timing system proved unreliable due to laser drift and facility vibration as expected, but was used as a simplified arrangement to demonstrate sufficient SNR of the method. The 1 MHz timing strategy proved more reliable and resulted in the initial characterization of the RDE exit flow with respect to the ability to couple a turbine for energy extraction.

5.1.3 Aerodynamic application in ground test facilities

Bladeless Turbine

To demonstrate the capability of FLEET to provide useful aerodynamic measurements in practical environments, multiple test campaigns were conducted in supersonic and hypersonic test facilities. The first of these was the supersonic bladeless turbine test campaign. The measurement was demonstrated on the test article with air flow before the facility was upgraded to flow pure nitrogen. Steady and unsteady two-component velocities were made in the flow field through oblique shocks, recompression regions and shear layers. These results were able to correctly measure the magnitude and location of all relevant flow features, and agreed well with CFD predictions. By using beamsplitters, three simultaneous velocity measurements could be made in close proximity. While this method of multi-point FLEET was determined to be overly complex, it showed that instantaneous shear stress measurements at the edge of a shear layer could be obtained. Lastly, transient measurements of unstarting in the test section showed evidence of normal shocks propagating over the test

article and returning the flow to the subsonic regime. Acquiring this measurement is important for calibration CFD methods because these complex transient supersonic phenomena are traditionally difficult to recreate in reduced-order modeling environments.

Boeing-AFOSR Mach 6 Quiet Tunnel

The second applied test campaign was conducted in the Boeing-AFOSR Mach 6 Quiet Tunnel. Here, an emphasis was placed on measurement with extreme precision in the boundary layer of a cone-cylinder-flare test article. Through careful alignment, data collection and processing, a precision of 0.33% was achieved in the highest quality measurements, with less than 1% disagreement to theoretical velocity magnitude. Using a calibrated traverse stage, a 4 mm extent of the model boundary layer was studied. The results of this traverse agreed remarkably well with CFD simulations at the experimental conditions. Lastly, periodic unsteadiness was measured in select regions of the boundary layer. The frequency of this unsteadiness was directly related to pressure wave cycling in the driver tube of the wind tunnel. As a follow-on to this test campaign, recommendations for precision and accuracy improvement were laid out. In order for FLEET to prove most useful, these performance drivers must be driven to the absolute minimum. The spatial resolution of presently demonstrated measurements in the BAM6QT was 1 mm. This is remarkably large with respect to the velocity gradients in the model boundary layer. By reducing the measurement volume, large improvements to the data quality can be obtained. This notion is demonstrated in a low pressure vacuum chamber through the use of 267 nm laser excitation rather than the fundamental 800 nm. Other methods of improving the precision include using third harmonic excitation [71] to gain higher signal levels and lifetimes. Higher camera magnification as shown in [55] can decrease the absolute uncertainty in pixel centroids with respect to the overall displacement. Slight argon enhancement [53] can also improve signal magnitude and lifetime. Lastly, positional uncertainty of measurements can be greatly reduced. It is necessary to know the mean and unsteady location of the model and the excitation point in the tunnel with less than 0.1 mm certainty in order to register the measurement point accurately with respect to the test article surface. By performing the original test campaign

and evaluation of FLEET in the BAM6QT, all of these necessary technique improvements have been identified.

5.2 Conclusion

Through the work of this thesis, both fundamental and applied advances to molecular tagging velocimetry were achieved. In the introduction, the need for high-fidelity, low uncertainty velocity measurements in harsh and high-speed environments were identified in order to support hypersonic aerospace systems simulation and development. After a review of the previous molecular tagging research, a clear lack in the spatial extent, frequency resolution, usable flow environment, and practical applications was identified. Through the research presented in here, large steps of improvement are shown in each of these areas. After the work that has been conducted here, molecular tagging velocimetry is now shown as a powerful tool for measurement in high-speed and harsh-environment flow facilities, and poses a large benefit over alternative velocity measurement techniques.

REFERENCES

[1] S. F. Rafano Carná and R. Bevilacqua, "High fidelity model for the atmospheric re-entry of CubeSats equipped with the Drag De-Orbit Device," *Acta Astronautica*, vol. 156, pp. 134–156, Mar. 2019, ISSN: 00945765. DOI: 10.1016/j.actaastro.2018.05.049.

[2] T. Rivell, "Notes on Earth Atmospheric Entry for Mars Sample Return Missions," Tech. Rep., 2006. [Online]. Available: http://www.sti.nasa.gov.

[3] D. G. Fletcher, "Fundamentals of Hypersonic Flow - Aerothermodynamics," *RTO AVT Lecture Series*, pp. 10–14, 2004.

[4] J.-P. Junc-Laplace, "Design , Fabrication and Characterization of a New Wind Tunnel Facility – Linear Cascade with a Wake Simulator," pp. 1–122, 2011. [Online]. Available: https://digitalcommons.lsu.edu/gradschool_theses.

[5] A. Welsh, "Low Turbulence Wind Tunnel Design and Wind Turbine Wake Characterization Recommended Citation," Tech. Rep., 2013. [Online]. Available: https://dc.uwm.edu/etd/180.

[6] F. Giardino and J. Rocha, "Design and characterization of a high-speed subsonic aeroacoustic wind tunnel," *Journal of Aircraft*, vol. 56, no. 1, pp. 108–120, Dec. 2019, ISSN: 15333868. DOI: 10.2514/1.C035113. [Online]. Available: https://arc.aiaa.org/doi/abs/10.2514/1.C035113.

[7] I. Azzawi, X. Mao, and A. Jaworski, "Design, fabrication and characterization of low speed open-jet wind tunnel," *undefined*, 2016.

[8] A. Wagner, E. Schülein, R. Petervari, K. Hannemann, S. R. Ali, A. Cerminara, and N. D. Sandham, "Combined free-stream disturbance measurements and receptivity studies in hypersonic wind tunnels by means of a slender wedge probe and direct numerical simulation," *Journal of Fluid Mechanics*, vol. 842, pp. 495–531, May 2018, ISSN: 14697645. DOI: 10.1017/jfm.2018.132. [Online]. Available: https://doi.org/10.1017/jfm.2018.132.

[9] D. Borgmann, S. Hosseinverdi, J. C. Little, and H. F. Fasel, "Investigation of low-speed boundary-layer instability and transition using experiments, theory and DNS," American Institute of Aeronautics and Astronautics (AIAA), Jun. 2020. DOI: 10.2514/6.2020-2948. [Online]. Available: https://arc.aiaa.org/doi/abs/10.2514/6.2020-2948.

[10] L. Duan, M. M. Choudhari, A. Chou, F. Munoz, R. Radespiel, T. Schilden, W. Schröder, E. C. Marineau, K. M. Casper, R. S. Chaudhry, G. V. Candler, K. A. Gray, and S. P. Schneider, "Characterization of Freestream Disturbances in Conventional Hypersonic Wind Tunnels," *Journal of Spacecraft and Rockets*, vol. 56, no. 2, pp. 357–368, Mar. 2019, ISSN: 0022-4650. DOI: 10.2514/1.A34290. [Online]. Available: https://arc.aiaa.org/doi/10.2514/1.A34290.

[11] C. Zhang, L. Duan, and M. M. Choudhari, "Direct numerical simulation database for supersonic and hypersonic turbulent boundary layers," *AIAA Journal*, vol. 56, no. 11, pp. 4297–4311, Sep. 2018, ISSN: 00011452. DOI: 10.2514/1.J057296. [Online]. Available: www.aiaa.org/randp..

[12] J. Tank, G. Jacobs, and G. Spedding, "Detailed comparison between DNS and wind tunnel experiment for an airfoil at Re = 20,000 with a view towards control," *APS*, A17.002, 2017. [Online]. Available: https://ui.adsabs.harvard.edu/abs/2017APS..DFDA17002T/abstract.

[13] D. Reese, P. M. Danehy, E. L. Walker, M. B. Rivers, and W. K. Goad, "FLEET Velocimetry in the Common Research Model's Wing Wake," in *AIAA Scitech 2020 Forum*, Reston, Virginia: American Institute of Aeronautics and Astronautics, Jan. 2020, ISBN: 978-1-62410-595-1. DOI: 10.2514/6.2020-1276. [Online]. Available: https://arc.aiaa.org/doi/10.2514/6.2020-1276.

[14] S. P. Schneider, "Development of Hypersonic Quiet Tunnels," 2008. DOI: 10.2514/1.34489. [Online]. Available: http://arc.aiaa.org.

[15] V. Athmanathan, J. M. Fisher, Z. Ayers, D. G. Cuadrado, V. Andreoli, J. Braun, T. Meyer, G. Paniagua, C. A. Fugger, and S. Roy, "Turbine-integrated High-pressure Optical RDE (THOR) for injection and detonation dynamics assessment," American Institute of Aeronautics and Astronautics (AIAA), Aug. 2019. DOI: 10.2514/6.2019-4041.

[16] J. P. Bonnet, D. Grésillon, and J. P. Taran, "Nonintrusive measurements for high-speed, supersonic, and hypersonic flows," *Annual Review of Fluid Mechanics*, vol. 30, no. 1, pp. 231–273, Jan. 1998, ISSN: 00664189. DOI: 10.1146/annurev.fluid.30.1.231. [Online]. Available: http://www.annualreviews.org/doi/10.1146/annurev.fluid.30.1.231.

[17] S. Beresh, S. Kearney, J. Wagner, D. Guildenbecher, J. Henfling, R. Spillers, B. Pruett, N. Jiang, M. Slipchenko, J. Mance, and S. Roy, "Pulse-burst PIV in a high-speed wind tunnel," *Measurement Science and Technology*, vol. 26, no. 9, p. 095 305, Sep. 2015, ISSN: 13616501. DOI: 10.1088/0957-0233/26/9/095305. [Online]. Available: https://iopscience.iop.org/article/10.1088/0957-0233/26/9/095305%20https://iopscience.iop.org/article/10.1088/0957-0233/26/9/095305/meta.

[18] K. M. Casper, S. J. Beresh, J. F. Henfling, R. W. Spillers, B. O. Pruett, and S. P. Schneider, "Hypersonic wind-tunnel measurements of boundary-layer transition on a slender cone," *AIAA Journal*, vol. 54, no. 4, pp. 1250–1263, Jan. 2016, ISSN: 00011452. DOI: 10.2514/1.J054033. [Online]. Available: https://arc.aiaa.org/doi/abs/10.2514/1.J054033.

[19] Y. Zhang, D. R. Richardson, S. J. Beresh, K. M. Casper, M. Soehnel, R. Spillers, T. Grasser, and P. Farias, "Tailoring FLEET for Cold Hypersonic Flows," American Institute of Aeronautics and Astronautics (AIAA), Jan. 2020. DOI: 10.2514/6.2020-1020.

[20] L. E. Dogariu, A. Dogariu, R. B. Miles, M. S. Smith, and E. C. Marineau, "Non-intrusive hypersonic freestream and turbulent boundary-layer velocity measurements in aedc tunnel 9 using fleet," in *AIAA Aerospace Sciences Meeting, 2018*, American Institute of Aeronautics and Astronautics Inc, AIAA, 2018, ISBN: 9781624105241. DOI: 10.2514/6.2018-1769.

[21] R. A. Burns, P. M. Danehy, B. R. Halls, and N. Jiang, "Femtosecond laser electronic excitation tagging velocimetry in a transonic, cryogenic wind tunnel," in *AIAA Journal*, vol. 55, American Institute of Aeronautics and Astronautics Inc., Dec. 2017, pp. 680–685. DOI: 10.2514/1.J055325.

[22] M. A. André, R. A. Burns, P. M. Danehy, S. R. Cadell, B. G. Woods, and P. M. Bardet, "Development and Application of Molecular Tagging Velocimetry for Gas Flows in Thermal Hydraulics," *Nuclear Technology*, vol. 205, no. 1-2, pp. 262–271, Jan. 2019, ISSN: 0029-5450. DOI: 10.1080/00295450.2018.1516954. [Online]. Available: https://www.tandfonline.com/doi/full/10.1080/00295450.2018.1516954.

[23] C. S. Winski, P. M. Danehy, A. N. Watkins, P. Shea, J. Meeroff, K. T. Lowe, and H. Houlden, "Space Launch System Booster Separation Supersonic Powered Testing with Surface and Off-body Measurements," American Institute of Aeronautics and Astronautics (AIAA), Jun. 2019. DOI: 10.2514/6.2019-3505. [Online]. Available: https://arc.aiaa.org/doi/abs/10.2514/6.2019-3505.

[24] A. Boutier, W. J. Yanta, and G. Smeets, "Velocity Measurements in Hypersonic Flows: A Review," in *New Trends in Instrumentation for Hypersonic Research*, Springer Netherlands, 1993, pp. 593–602. DOI: 10.1007/978-94-011-1828-6{_}53. [Online]. Available: https://link.springer.com/chapter/10.1007/978-94-011-1828-6_53.

[25] G. Alfonsi, *Reynolds-averaged Navier-Stokes equations for turbulence modeling*, Jul. 2009. DOI: 10.1115/1.3124648.

[26] D. Favier, "The Role of Wind Tunnel Experiments in CFD Validation," in *Encyclopedia of Aerospace Engineering*, Chichester, UK: John Wiley & Sons, Ltd, Sep. 2010. DOI: 10.1002/9780470686652.eae034. [Online]. Available: http://doi.wiley.com/10.1002/9780470686652.eae034.

[27] J. Fisher, J. Braun, T. R. Meyer, and G. Paniagua, "Application of femtosecond laser electronic excitation tagging (FLEET) velocimetry in a bladeless turbine," *Measurement Science and Technology*, Jan. 2020, ISSN: 0957-0233. DOI: 10.1088/1361-6501/AB7062.

[28] I. Grant, G. McCutcheon, A. H. McColgan, and D. Hurst, "Optical-velocimetry, wake measurements of lift and induced drag on a wing," *Optics and Lasers in Engineering*, vol. 44, no. 3-4, pp. 282–303, Mar. 2006, ISSN: 01438166. DOI: 10.1016/j.optlaseng.2005.04.002.

[29] B. Hoeveler, A. Bauknecht, C. Christian Wolf, and F. Janser, "Wind-Tunnel Study of a Wing-Embedded Lifting Fan Remaining Open in Cruise Flight," *Journal of Aircraft*, vol. 57, no. 4, pp. 558–568, Jul. 2020, ISSN: 1533-3868. DOI: 10.2514/1.C035422. [Online]. Available: https://arc.aiaa.org/doi/10.2514/1.C035422.

[30] M. Azzazy and R. M. Hall, "Optical boundary-layer transition detection in a transonic wind tunnel," *AIAA Journal*, vol. 27, no. 4, pp. 405–410, May 1989, ISSN: 00011452. DOI: 10.2514/3.10127. [Online]. Available: http://arc.aiaa.org.

[31] S. C. Matt, W. Hou, and D. Josset, "Optical sensing of laminar to turbulent transition and boundary layer turbulence (Conference Presentation)," in *Ocean Sensing and Monitoring XI*, W. ". Hou and R. A. Arnone, Eds., vol. 11014, SPIE, May 2019, p. 15, ISBN: 9781510626935. DOI: 10.1117/12.2521321. [Online]. Available: https://www.spiedigitallibrary.org/conference-proceedings-of-spie/11014/2521321/Optical-sensing-of-laminar-to-turbulent-transition-and-boundary-layer/10.1117/12.2521321.full.

[32] T. Liu, "Pressure- and Temperature-Sensitive Paints," in *Encyclopedia of Aerospace Engineering*, Chichester, UK: John Wiley & Sons, Ltd, Dec. 2011. DOI: 10.1002/9780470686652.eae076. [Online]. Available: http://doi.wiley.com/10.1002/9780470686652.eae076.

[33] E. L. Lash, C. S. Combs, P. A. Kreth, and J. D. Schmisseur, "Study of the dynamics of transitional shock wave-boundary layer interactions using optical diagnostics," in *47th AIAA Fluid Dynamics Conference, 2017*, American Institute of Aeronautics and Astronautics Inc, AIAA, 2017, ISBN: 9781624105005. DOI: 10.2514/6.2017-3123. [Online]. Available: http://arc.aiaa.org.

[34] B. Vasudevan, S. P. Srikanth, H. D. Shashidhar, and G. Jagadeesh, "Surface pressure and heat transfer measurements the unsteady separated hypersonic flow field over double cones," Tech. Rep.

[35] K. M. Casper, S. J. Beresh, J. F. Henfling, R. W. Spillers, B. O. M. Pruett, and S. P. Schneider, "Hypersonic Wind-Tunnel Measurements of Boundary-Layer Transition on a Slender Cone," *AIAA Journal*, vol. 54, no. 4, pp. 1250–1263, Apr. 2016, ISSN: 0001-1452. DOI: 10.2514/1.J054033. [Online]. Available: http://arc.aiaa.org/doi/10.2514/1.J054033.

[36] J. A. BARTZ and R. J. VIDAL, "Surface measurements on sharp flat plates and wedges in low-density hypersonic flow.," *AIAA Journal*, vol. 7, no. 6, pp. 1099–1109, Jun. 1969, ISSN: 0001-1452. DOI: 10.2514/3.5281.

[37] J. M. Simmons, "Measurement techniques in high-enthalpy hypersonic facilities," *Experimental Thermal and Fluid Science*, vol. 10, no. 4, pp. 454–469, 1995, ISSN: 08941777. DOI: 10.1016/0894-1777(94)00066-H.

[38] *Schlieren imaging of hypersonic boundary-layer instabilities - Cavitar Ltd.* [Online]. Available: https://www.cavitar.com/library/measurements-of-hypersonic-boundary-layer-instabilities-using-a-pulsed-laser-schlieren-technique/.

[39] O. J. Williams and A. J. Smits, "Application of PIV to the Measurement of Hypersonic Turbulence," Tech. Rep., 2012, pp. 9–12.

[40] M. Casper, S. Stephan, J. Windte, P. Scholz, R. Radespiel, S. Scharnowski, and C. J. Kähler, "Hypersonic PIV in a ludwieg tube wind tunnel at mach 5.9," in *28th AIAA Aerodynamic Measurement Technology, Ground Testing, and Flight Testing Conference 2012*, 2012, ISBN: 9781624101892. DOI: 10.2514/6.2012-3197.

[41] O. J. Williams, D. Sahoo, M. L. Baumgartner, and A. J. Smits, "Experiments on the structure and scaling of hypersonic turbulent boundary layers," *Journal of Fluid Mechanics*, vol. 834, pp. 237–270, Jan. 2018, ISSN: 14697645. DOI: 10.1017/jfm.2017.712.

[42] R. R. Miles, J. N. Forkey, and W. R. Lempert, "Filtered rayleigh scattering measurements in supersonic/hypersonic facilities," in *AIAA/ASME/SAE/ASEE 28th Joint Propulsion Conference and Exhibit, 1992*, 1992. DOI: 10.2514/6.1992-3894.

[43] N. Jiang, M. Webster, W. R. Lempert, J. D. Miller, T. R. Meyer, and P. M. Danehy, "MHz-Rate NO PLIF imaging in a Mach 10 hypersonic wind tunnel," in *48th AIAA Aerospace Sciences Meeting Including the New Horizons Forum and Aerospace Exposition*, 2010, ISBN: 9781600867392. DOI: 10.2514/6.2010-1407.

[44] P. M. Danehy, C. B. Ivey, J. A. Inman, B. F. Bathel, S. B. Jones, A. C. McCrea, N. Jiang, M. Webster, W. Lempert, J. Miller, and T. Meyer, "High-speed PLIF imaging of hypersonic transition over discrete cylindrical roughness," in *48th AIAA Aerospace Sciences Meeting Including the New Horizons Forum and Aerospace Exposition*, 2010, ISBN: 9781600867392. DOI: 10.2514/6.2010-703.

[45] R. Sánchez-González, R. Srinivasan, R. D. W. Bowersox, and S. W. North, "Simultaneous velocity and temperature measurements in gaseous flow fields using the VENOM technique," *Optics Letters*, vol. 36, no. 2, p. 196, Jan. 2011, ISSN: 0146-9592. DOI: 10.1364/ol.36.000196.

[46] M. A. Mustafa and N. J. Parziale, " Simplified read schemes for krypton tagging velocimetry in N 2 and air," *Optics Letters*, vol. 43, no. 12, p. 2909, Jun. 2018, ISSN: 0146-9592. DOI: 10.1364/ol.43.002909.

[47] J. B. Michael, M. R. Edwards, A. Dogariu, and R. B. Miles, "Femtosecond laser electronic excitation tagging for quantitative velocity imaging in air," *Applied Optics*, vol. 50, no. 26, pp. 5158–5162, Sep. 2011, ISSN: 15394522. DOI: 10.1364/AO.50.005158.

[48] R. Miles, "Femtosecond Laser Electronic Excitation Tagging (FLEET) for Imaging Flow Structure in Unseeded Hot or Cold Air or Nitrogen," in *51st AIAA Aerospace Sciences Meeting including the New Horizons Forum and Aerospace Exposition*, Reston, Virigina: American Institute of Aeronautics and Astronautics, Jan. 2013, ISBN: 978-1-62410-181-6. DOI: 10.2514/6.2013-340. [Online]. Available: http://arc.aiaa.org/doi/10.2514/6.2013-340.

[49] M. R. Edwards, A. Dogariu, and R. B. Miles, "Simultaneous temperature and velocity measurement in unseeded air flows with FLEET," in *51st AIAA Aerospace Sciences Meeting including the New Horizons Forum and Aerospace Exposition 2013*, American Institute of Aeronautics and Astronautics Inc., 2013, ISBN: 9781624101816. DOI: 10.2514/6.2013-43. [Online]. Available: https://arc.aiaa.org/doi/abs/10.2514/6.2013-43.

[50] N. D. Calvert, A. Dogariu, M. R. Edwards, and R. B. Miles, "Density scaling and calibration of FLEET temperature measurements," in *31st AIAA Aerodynamic Measurement Technology and Ground Testing Conference*, American Institute of Aeronautics and Astronautics Inc, AIAA, Jan. 2015, ISBN: 9781624103643. DOI: 10.2514/6.2015-2564. [Online]. Available: https://collaborate.princeton.edu/en/publications/density-scaling-and-calibration-of-fleet-temperature-measurements-2.

[51] B. R. Halls, N. Jiang, J. R. Gord, P. M. Danehy, and S. Roy, "Mixture-fraction measurements with femtosecond-laser electronic-excitation tagging.," *Applied optics*, vol. 56, no. 11, E94–E98, Apr. 2017, ISSN: 1539-4522. DOI: 10.1364/AO.56.000E94. [Online]. Available: http://www.ncbi.nlm.nih.gov/pubmed/28414346.

[52] N. D. Calvert, Y. Zhang, and R. B. Miles, "Characterizing FLEET for aerodynamic measurements in various gas mixtures and non-air environments," in *32nd AIAA Aerodynamic Measurement Technology and Ground Testing Conference*, American Institute of Aeronautics and Astronautics Inc, AIAA, 2016, pp. 1–16, ISBN: 9781624104381. DOI: 10.2514/6.2016-3206.

[53] Y. Zhang, N. Calvert, M. N. Shneider, and R. B. Miles, "Enhancement of FLEET in Argon Gas Mixtures," in *32nd AIAA Aerodynamic Measurement Technology and Ground Testing Conference*, Reston, Virginia: American Institute of Aeronautics and Astronautics, Jun. 2016, ISBN: 978-1-62410-438-1. DOI: 10.2514/6.2016-3249. [Online]. Available: http://arc.aiaa.org/doi/10.2514/6.2016-3249.

[54] M. R. Edwards, C. M. Limbach, R. B. Miles, and A. A. Tropina, "Limitations on high-spatial-resolution measurements of turbulence using femtosecond laser tagging," in *53rd AIAA Aerospace Sciences Meeting*, American Institute of Aeronautics and Astronautics Inc, AIAA, 2015, ISBN: 9781624103438. DOI: 10.2514/6.2015-1219.

[55] C. J. Peters, P. M. Danehy, B. F. Bathel, N. Jiang, N. Calvert, and R. B. Miles, "Precision of FLEET Velocimetry using High-Speed CMOS Camera Systems," in *31st AIAA Aerodynamic Measurement Technology and Ground Testing Conference*, Reston, Virginia: American Institute of Aeronautics and Astronautics, Jun. 2015, ISBN: 978-1-62410-364-3. DOI: 10.2514/6.2015-2565. [Online]. Available: http://arc.aiaa.org/doi/10.2514/6.2015-2565.

[56] C. M. Limbach and R. B. Miles, "Rayleigh scattering measurements of heating and gas perturbations accompanying femtosecond laser tagging," in *AIAA Journal*, vol. 55, American Institute of Aeronautics and Astronautics Inc., Aug. 2017, pp. 112–120. DOI: 10.2514/1.J054772.

[57] M. R. New-Tolley, M. N. Shneider, and R. B. Miles, "Modeling of the FLEET filament interaction with a nonuniform gas flow," in *AIAA SciTech Forum - 55th AIAA Aerospace Sciences Meeting*, American Institute of Aeronautics and Astronautics Inc., 2017, ISBN: 9781624104473. DOI: 10.2514/6.2017-0257.

[58] N. D. Calvert, A. Dogariu, and R. B. Miles, "2-D velocity and vorticity measurements with FLEET," in *AIAA AVIATION 2014 - 30th AIAA Aerodynamic Measurement Technology and Ground Testing Conference*, American Institute of Aeronautics and Astronautics Inc., Jan. 2014, ISBN: 9781624102875. DOI: 10.2514/6.2014-2229. [Online]. Available: https://collaborate.princeton.edu/en/publications/2-d-velocity-and-vorticity-measurements-with-fleet-2.

[59] P. M. Danehy, B. F. Bathel, N. D. Calvert, A. Dogariu, and R. B. Miles, "Three Component Velocity and Acceleration Measurement Using FLEET," in *30th AIAA Aerodynamic Measurement Technology and Ground Testing Conference*, Reston, Virginia: American Institute of Aeronautics and Astronautics, Jun. 2014, ISBN: 978-1-62410-287-5. DOI: 10.2514/6.2014-2228. [Online]. Available: http://arc.aiaa.org/doi/10.2514/6.2014-2228.

[60] N. D. Calvert, A. Dogariu, and R. B. Miles, "FLEET boundary layer velocity profile measurements," in *44th AIAA Plasmadynamics and Lasers Conference*, 2013. DOI: 10.2514/6.2013-2762.

[61] Y. Zhang and R. B. Miles, "Shear layer measurements along curved surfaces using the fleet method," in *AIAA Aerospace Sciences Meeting, 2018*, American Institute of Aeronautics and Astronautics Inc, AIAA, 2018, ISBN: 9781624105241. DOI: 10.2514/6.2018-1768. [Online]. Available: https://arc.aiaa.org/doi/abs/10.2514/6.2018-1768.

[62] N. J. DeLuca, R. B. Miles, W. D. Kulatilaka, N. Jiang, and J. R. Gord, "Femtosecond Laser Electronic Excitation Tagging (FLEET) Fundamental Pulse Energy and Spectral Response (FLEET) Fundamental Pulse Energy and Spectral," in *30th AIAA Aerodynamic Measurement Technology and Ground Testing Conference*, 2014. DOI: 10.2514/6.2014-2227.

[63] D. Zhang, B. Li, Q. Gao, and Z. Li, "Applicability of Femtosecond Laser Electronic Excitation Tagging in Combustion Flow Field Velocity Measurements," *Applied Spectroscopy*, vol. 72, no. 12, pp. 1807–1813, Dec. 2018, ISSN: 19433530. DOI: 10.1177/0003702818788857. [Online]. Available: http://journals.sagepub.com/doi/10.1177/0003702818788857.

[64] N. Jiang, B. R. Halls, H. U. Stauffer, S. Roy, P. M. Danehy, and J. R. Gord, "Selective two-photon absorptive resonance femtosecond-laser electronic-excitation tagging (STARFLEET) velocimetry in flow and combustion diagnostics," in *32nd AIAA Aerodynamic Measurement Technology and Ground Testing Conference*, American Institute of Aeronautics and Astronautics Inc, AIAA, 2016, pp. 1–7, ISBN: 9781624104381. DOI: 10.2514/6.2016-3250.

[65] N. Jiang, J. G. Mance, M. N. Slipchenko, J. J. Felver, H. U. Stauffer, T. Yi, P. M. Danehy, and S. Roy, "Seedless velocimetry at 100 kHz with picosecond-laser electronic-excitation tagging," *Optics Letters*, vol. 42, no. 2, p. 239, Jan. 2017, ISSN: 0146-9592. DOI: 10.1364/ol.42.000239.

[66] J. M. Fisher, M. E. Smyser, M. N. Slipchenko, S. Roy, and T. R. Meyer, "Burst-mode femtosecond laser electronic excitation tagging for kHz–MHz seedless velocimetry," *Optics Letters*, vol. 45, no. 2, p. 335, Jan. 2020, ISSN: 0146-9592. DOI: 10.1364/ol.380109.

[67] Y. Zhang, G. Marshall, S. Beresh, D. Richardson, and K. Casper, "Multi-line FLEET using interference masks," *Optics Letters*, vol. 45, no. 14, pp. 3949–3952, Jun. 2020, ISSN: 0146-9592. DOI: 10.1364/ol.392779. [Online]. Available: https://www.osapublishing.org/viewmedia.cfm?uri=ol-45-14-3949&seq=0&html=true%20https://www.osapublishing.org/abstract.cfm?uri=ol-45-14-3949%20https://www.osapublishing.org/ol/abstract.cfm?uri=ol-45-14-3949.

[68] C. J. Peters, R. B. Miles, R. A. Burns, B. F. Bathel, G. S. Jones, and P. M. Danehy, "Femtosecond laser tagging characterization of a sweeping jet actuator operating in the compressible regime," in *32nd AIAA Aerodynamic Measurement Technology and Ground Testing Conference*, American Institute of Aeronautics and Astronautics Inc, AIAA, 2016, pp. 1–22, ISBN: 9781624104381. DOI: 10.2514/6.2016-3248. [Online]. Available: https://arc.aiaa.org/doi/abs/10.2514/6.2016-3248.

[69] R. A. Burns and P. M. Danehy, "FLEET velocimetry measurements on a transonic airfoil," in *AIAA SciTech Forum - 55th AIAA Aerospace Sciences Meeting*, American Institute of Aeronautics and Astronautics Inc., 2017, ISBN: 9781624104473. DOI: 10.2514/6.2017-0026.

[70] R. A. Burns and P. M. Danehy, "Unseeded velocity measurements around a transonic airfoil using femtosecond laser tagging," *AIAA Journal*, vol. 55, no. 12, pp. 4142–4154, Oct. 2017, ISSN: 00011452. DOI: 10.2514/1.J056154.

[71] Y. Zhang, D. R. Richardson, S. J. Beresh, K. M. Casper, M. Soehnel, J. Henfling, and R. Spillers, "Hypersonic wake measurements behind a slender cone using FLEET velocimetry," American Institute of Aeronautics and Astronautics (AIAA), Jun. 2019. DOI: 10.2514/6.2019-3381.

[72] D. K. Lauriola, M. Gomez, T. R. Meyer, S. F. Son, M. N. Slipchenko, and S. Roy, "High-speed particle image velocimetry and particle tracking methods in reactive and non-reactive flows," in *AIAA Scitech 2019 Forum*, American Institute of Aeronautics and Astronautics Inc, AIAA, 2019, ISBN: 9781624105784. DOI: 10.2514/6.2019-1605.

[73] S. J. Beresh, J. F. Henfling, R. W. Spillers, and S. M. Spitzer, "'Postage-stamp PIV': Small velocity fields at 400 kHz for turbulence spectra measurements," *Measurement Science and Technology*, vol. 29, no. 3, Feb. 2018, ISSN: 13616501. DOI: 10.1088/1361-6501/aa9f79.

[74] M. E. Smyser, M. N. Slipchenko, T. R. Meyer, A. W. Caswell, and S. Roy, "Burst-mode laser architecture for the generation of high-peak-power MHz-rate femtosecond pulses," *OSA Continuum*, vol. 2, no. 12, p. 3490, Dec. 2019, ISSN: 2578-7519. DOI: 10.1364/OSAC.2.003490. [Online]. Available: https://www.osapublishing.org/abstract.cfm?URI=osac-2-12-3490.

[75] N. J. DeLuca, R. B. Miles, N. Jiang, W. D. Kulatilaka, A. K. Patnaik, and J. R. Gord, "FLEET velocimetry for combustion and flow diagnostics," *Applied Optics*, vol. 56, no. 31, p. 8632, Nov. 2017, ISSN: 1559-128X. DOI: 10.1364/ao.56.008632.

[76] L. R. Boedeker, "Velocity measurement by H_2O photolysis and laser-induced fluorescence of OH," *Optics Letters*, vol. 14, no. 10, p. 473, May 1989, ISSN: 0146-9592. DOI: 10.1364/ol.14.000473.

[77] F. Lozano, J. Saavedra, J. Fisher, G. Paniagua, A. Martinez-Cava, and E. Valero, "Experimental approach to characterize base region Coanda flow topology induced by pulsating blowing," 2019. DOI: 10.13009/EUCASS2019-762.

[78] H. Hu and M. M. Koochesfahani, "Molecular tagging velocimetry and thermometry and its application to the wake of a heated circular cylinder," in *Measurement Science and Technology*, vol. 17, Institute of Physics Publishing, Jun. 2006, pp. 1269–1281. DOI: 10.1088/0957-0233/17/6/S06.

[79] R. A. Burns and P. M. Danehy, "Unseeded Velocity Measurements Around a Transonic Airfoil Using Femtosecond Laser Tagging," 2017. DOI: 10.2514/1.J056154. [Online]. Available: www.aiaa.org/randp..

[80] N. D. Calvert, A. Dogariu, and R. B. Miles, "2-D velocity and vorticity measurements with FLEET," in *AIAA AVIATION 2014 - 30th AIAA Aerodynamic Measurement Technology and Ground Testing Conference*, American Institute of Aeronautics and Astronautics Inc., 2014, ISBN: 9781624102875. DOI: 10.2514/6.2014-2229.

[81] N. R. Grady, T. Friedlander, R. W. Pitz, C. D. Carter, and K.-Y. Hsu, "Hydroxyl Tagging Velocimetry in a Supersonic Flow over a Piloted Cavity," 2010. DOI: 10.2514/6.2010-1405. [Online]. Available: http://arc.aiaa.org.

[82] C. M. Limbach and R. B. Miles, "Rayleigh scattering measurements of heating and gas perturbations accompanying femtosecond laser tagging," in *AIAA Journal*, vol. 55, American Institute of Aeronautics and Astronautics Inc., 2017, pp. 112–120. DOI: 10.2514/1.J054772.

[83] R. Burns, P. M. Danehy, S. B. Jones, B. R. Halls, and N. Jiang, "Application of FLEET Velocimetry in the NASA Langley 0.3-Meter Transonic Cryogenic Tunnel," American Institute of Aeronautics and Astronautics (AIAA), Jun. 2015. DOI: 10.2514/6.2015-2566.

[84] R. Burns, P. M. Danehy, S. B. Jones, B. R. Halls, and N. Jiang, "Application of FLEET Velocimetry in the NASA Langley 0.3-Meter Transonic Cryogenic Tunnel," American Institute of Aeronautics and Astronautics (AIAA), Jun. 2015. DOI: 10.2514/6.2015-2566.

[85] M. M. Koochesfahani and D. G. Nocera, "Molecular Tagging Velocimetry," in *Handbook of Experimental Fluid Dynamics*, J. Foss, C. Tropea, and A. Yarin, Eds., Springer-Verlag, 2007, ch. 5.4, pp. 362–471. [Online]. Available: https://www.egr.msu.edu/tmual/MTV.html.

[86] Q. Tang, Y. Zhu, X. Chen, and C. Lee, "Development of second-mode instability in a Mach 6 flat plate boundary layer with two-dimensional roughness," *Physics of Fluids*, vol. 27, no. 6, 2015, ISSN: 10897666. DOI: 10.1063/1.4922389.

[87] F. Li, M. Choudhari, C.-L. Chang, and J. White, "Secondary Instability of Second Mode Disturbances in Hypersonic Boundary Layers," Tech. Rep. [Online]. Available: https://ntrs.nasa.gov/search.jsp?R=20120010339.

[88] C. Zhang, "Experimental observation of the second-mode waves using PIV technique," *Journal of Visualization*, vol. 21, no. 6, pp. 915–919, Dec. 2018, ISSN: 18758975. DOI: 10.1007/s12650-018-0501-7.

[89] A. Rose, *Vision: human and electronic.* Plenum Press, 1973, p. 197, ISBN: 9781468420395.

[90] B. Brock, R. Harris Haynes, B. S. Thurow, G. Lyons, and N. E. Murray, "An examination of MHz rate PIV in a heated supersonic jet," in *52nd Aerospace Sciences Meeting*, American Institute of Aeronautics and Astronautics Inc., 2014, ISBN: 9781624102561. DOI: 10.2514/6.2014-1102.

[91] P. M. Danehy, S. O'Byrne, A. F. P. Houwing, J. S. Fox, and D. R. Smith, "Flow-tagging velocimetry for hypersonic flows using fluorescence of nitric oxide," *AIAA Journal*, vol. 41, no. 2, pp. 263–271, 2003, ISSN: 00011452. DOI: 10.2514/2.1939.

[92] R. Miles, C. Cohen, J. Connors, P. Howard, S. Huang, E. Markovitz, and G. Russell, "Velocity measurements by vibrational tagging and fluorescent probing of oxygen," *Optics Letters*, vol. 12, no. 11, p. 861, Nov. 1987, ISSN: 0146-9592. DOI: 10.1364/ol.12.000861.

[93] J. N. Forkey, N. D. Finkelstein, W. R. Lempert, and R. B. Miles, "Demonstration and characterization of filtered Rayleigh scattering for planar velocity measurements," *AIAA Journal*, vol. 34, no. 3, pp. 442–448, Mar. 1996, ISSN: 0001-1452. DOI: 10.2514/3.13087. [Online]. Available: http://arc.aiaa.org/doi/10.2514/3.13087.

[94] N. M. Sijtsema, N. J. Dam, R. J. Klein-Douwel, and J. J. Ter Meulen, "Air photolysis and recombination tracking: A new molecular tagging velocimetry scheme," *AIAA Journal*, vol. 40, no. 6, pp. 1061–1064, 2002, ISSN: 00011452. DOI: 10.2514/2.1788.

[95] R. A. Burns, P. M. Danehy, B. R. Halls, and N. Jiang, "Femtosecond Laser Electronic Excitation Tagging Velocimetry in a Transonic, Cryogenic Wind Tunnel," 2016. DOI: 10.2514/1.J055325. [Online]. Available: www.aiaa.org/randp..

[96] S. Roy, J. D. Miller, M. N. Slipchenko, P. S. Hsu, J. G. Mance, T. R. Meyer, and J. R. Gord, "100-ps-pulse-duration, 100-J burst-mode laser for kHz–MHz flow diagnostics," *Optics Letters*, vol. 39, no. 22, p. 6462, Nov. 2014, ISSN: 0146-9592. DOI: 10.1364/ol.39.006462.

[97] H. Corell and T. Mikael, *Applications of ocean transport modelling*. 2012, pp. 1–40, ISBN: 9789174474961.

[98] L. D. Huebner, K. E. Rock, R. T. Voland, and A. R. Wieting, "Calibration of the langley 8-foot high temperature tunnel for hypersonic airbreathing propulsion testing," in *Advanced Measurement and Ground Testing Conference*, American Institute of Aeronautics and Astronautics Inc, AIAA, 1996. DOI: 10.2514/6.1996-2197.

[99] A. Balter-Peterson, F. Nichols, B. Mifsud, and W. Love, "Arc jet testing in NASA Ames research center thermophysics facilities," in *4th Symposium on Multidisciplinary Analysis and Optimization, 1992*, American Institute of Aeronautics and Astronautics Inc, AIAA, 1992. DOI: 10.2514/6.1992-5041.

[100] Q. Liu, D. Baccarella, W. Landsberg, A. Veeraragavan, and T. Lee, "Cavity flameholding in an optical axisymmetric scramjet in Mach 4.5 flows," *Proceedings of the Combustion Institute*, vol. 37, no. 3, pp. 3733–3740, 2019, ISSN: 15407489. DOI: 10.1016/j.proci.2018.08.037.

[101] R. W. Pitz, J. A. Wehrmeyer, L. A. Ribarov, D. A. Oguss, F. Batliwala, P. A. Debarber, S. Deusch, and P. E. Dimotakis, "Unseeded molecular flow tagging in cold and hot flows using ozone and hydroxyl tagging velocimetry," *Measurement Science and Technology*, vol. 11, no. 9, pp. 1259–1271, 2000, ISSN: 09570233. DOI: 10.1088/0957-0233/11/9/303.

[102] J. A. Wehrmeyer, L. A. Ribarov, D. A. Oguss, and R. W. Pitz, "Flame flow tagging velocimetry with 193-nm H_2O photodissociation," *Applied Optics*, vol. 38, no. 33, p. 6912, Nov. 1999, ISSN: 0003-6935. DOI: 10.1364/ao.38.006912.

[103] A. N. Perkins, M. Ramsey, D. J. Strickland, R. W. Pitz, J. A. Wehrmeyer, and A. Alexander, "Dual-pulse hydroxyl tagging velocimetry (HTV) in jet engine exhausts," in *45th AIAA/ASME/SAE/ASEE Joint Propulsion Conference and Exhibit*, 2009, ISBN: 9781563479762. DOI: 10.2514/6.2009-5108. [Online]. Available: http://arc.aiaa.org.

[104] N. Jiang, W. R. Lempert, G. L. Switzer, T. R. Meyer, and J. R. Gord, "Narrow-linewidth megahertz-repetition-rate optical parametric oscillator for high-speed flow and combustion diagnostics," *Applied Optics*, vol. 47, no. 1, pp. 64–71, Jan. 2008, ISSN: 15394522. DOI: 10.1364/AO.47.000064.

[105] M. Raffel, C. E. Willert, S. T. Wereley, J. Kompenhans, S. Willert, S. T. Wereley, and J. Kompenhans, *Particle Image Velocimetry: A Practical Guide*. Springer, 2007, vol. 2nd, p. 448, ISBN: 9783540723073. DOI: 10.1097/JTO.0b013e3182370e69. [Online]. Available: http://dx.doi.org/10.1007/978-3-540-72308-0.

[106] Z. Wang, T. Kamimoto, and Y. Deguchi, "Industrial Applications of Tunable Diode Laser Absorption Spectroscopy," in *Temperature Sensing*, InTech, Jul. 2018. DOI: 10.5772/intechopen.77027.

[107] A. Alexander, J. Wehrmeyer, W. Runge, B. Blandford, A. V. Anilkumar, and R. Pitz, "Nonintrusive measurement of gas turbine exhaust velocity using hydroxyl tagging velocimetry," in *26th AIAA Aerodynamic Measurement Technology and Ground Testing Conference*, Seattle, Washington, 2008, ISBN: 9781563479427. DOI: 10.2514/6.2008-3709.

[108] J. Ye, D. Shi, W. Song, G. Li, Z. Zhang, and Z. Hu, "Investigation of turbulence flow characteristics in a dual-mode scramjet combustor using hydroxyl tagging velocimetry," *Acta Astronautica*, vol. 157, pp. 276–281, Apr. 2019, ISSN: 00945765. DOI: 10.1016/j.actaastro.2018.12.040.

[109] J. Ye, G. Li, J. Shao, Z. Hu, X. Zhao, and W. Song, "Application of the hydroxyl tagging velocimetry to direct-connect supersonic combustor experiment," in *Fourth International Symposium on Laser Interaction with Matter*, Y. Ding, G. Feng, D. H. H. Hoffmann, J. Cao, and Y. Lu, Eds., vol. 10173, SPIE, May 2017, p. 1 017 314. DOI: 10.1117/12.2268256. [Online]. Available: http://proceedings.spiedigitallibrary.org/proceeding.aspx?doi=10.1117/12.2268256.

[110] M. C. Ramsey, T. C. Folk, A. N. Perkins, R. W. Pitz, and T. P. Jenkins, "Assessment of the application of hydroxyl tagging velocimetry to rocket engine exhausts," in *45th AIAA/ASME/SAE/ASEE Joint Propulsion Conference and Exhibit*, 2009, ISBN: 9781563479762.

[111] L. A. Ribarov, S. Hu, J. A. Wehrmeyer, and R. W. Pitz, "Hydroxyl tagging velocimetry method optimization: Signal intensity and spectroscopy," in *Applied Optics*, vol. 44, OSA - The Optical Society, Nov. 2005, pp. 6616–6626. DOI: 10.1364/AO.44.006616.

[112] L. A. Ribarov, J. A. Wehrmeyer, R. W. Pitz, and R. A. Yetter, "Hydroxyl tagging velocimetry (HTV) in experimental air flows," *Applied Physics B: Lasers and Optics*, vol. 74, no. 2, pp. 175–183, Feb. 2002, ISSN: 09462171. DOI: 10.1007/s003400100777.

[113] M. D. Lahr, R. W. Pitz, Z. W. Douglas, and C. D. Carter, "Hydroxyl tagging velocimetry in cavity-piloted mach 2 combustor," in *Collection of Technical Papers - 44th AIAA Aerospace Sciences Meeting*, vol. 1, 2006, pp. 492–506, ISBN: 1563478072. DOI: 10.2514/6.2006-40.

[114] N. Grady and R. W. Pitz, "Vibrationally excited hydroxyl tagging velocimetry," *Applied Optics*, vol. 53, no. 31, p. 7182, Nov. 2014, ISSN: 0003-6935. DOI: 10.1364/ao.53.007182.

[115] J. Shao, J.-f. YE, S. WANG, G.-h. LI, B.-l. FANG, Z.-r. ZHANG, Z.-y. HU, and J.-Y. LI, "2D HTV image processing in the complex combustion field," in *Fifth International Symposium on Laser Interaction with Matter*, Y. Zhao, Ed., vol. 11046, SPIE, Mar. 2019, p. 47, ISBN: 9781510627581. DOI: 10.1117/12.2523356. [Online]. Available: https://www.spiedigitallibrary.org/conference-proceedings-of-spie/11046/2523356/2D-HTV-image-processing-in-the-complex-combustion-field/10.1117/12.2523356.full.

[116] L. E. Dogariu, A. Dogariu, R. B. Miles, M. S. Smith, and E. C. Marineau, "Femtosecond Laser Electronic Excitation Tagging Velocimetry in a Large-Scale Hypersonic Facility," *AIAA Journal*, vol. 57, no. 11, pp. 4725–4737, Nov. 2019, ISSN: 0001-1452. DOI: 10.2514/1.j057759.

[117] J. A. Wehrmeyer, L. A. Ribarov, D. A. Oguss, F. Batliwala, R. W. Pitz, and P. A. Debarber, "Flow tagging velocimetry for low and high temperature flowfields," in *37th Aerospace Sciences Meeting and Exhibit*, 1999. DOI: 10.2514/6.1999-646. [Online]. Available: http://arc.aiaa.org.

[118] R. A. Burns, C. J. Peters, and P. M. Danehy, "Unseeded velocimetry in nitrogen for high-pressure, cryogenic wind tunnels, part I: Femtosecond-laser tagging," *Measurement Science and Technology*, vol. 29, no. 11, Oct. 2018, ISSN: 13616501. DOI: 10.1088/1361-6501/aade1b.

[119] M. E. Smyser, M. N. Slipchenko, T. R. Meyer, A. W. Caswell, and S. Roy, "Burst-mode laser architecture for the generation of high-peak-power MHz-rate femtosecond pulses," *OSA Continuum*, vol. 2, no. 12, p. 3490, Dec. 2019, ISSN: 2578-7519. DOI: 10.1364/osac.2.003490.

[120] B. R. Halls, N. Jiang, J. R. Gord, P. M. Danehy, and S. Roy, "Mixture-fraction measurements with femtosecond-laser electronic-excitation tagging," *Applied Optics*, vol. 56, no. 11, E94, Apr. 2017, ISSN: 0003-6935. DOI: 10.1364/ao.56.000e94. [Online]. Available: https://www.osapublishing.org/viewmedia.cfm?uri=ao-56-11-E94&seq=0&html=true%20https://www.osapublishing.org/abstract.cfm?uri=ao-56-11-E94%20https://www.osapublishing.org/ao/abstract.cfm?uri=ao-56-11-E94.

[121] J. Braun, G. Paniagua, J. Sousa, and B. H. Saracoglu, "Design and Experimental Assessment of Bladeless Turbines for Axial Inlet Supersonic Flows," in *Proceedings of the ASME Turbo Expo*, 2019.

[122] N. F. DA COSTA VINHA, G. PANIAGUA, J. F. LOPES DE SOUSA, and B. H. SARACOGLU, "AXIAL FLUID MACHINE AND METHOD FOR POWER EXTRACTION," May 2015.

[123] G. Tedeschi, H. Gouin, and M. Elena, "Motion of tracer particles in supersonic flows," *Experiments in Fluids*, vol. 26, no. 4, pp. 288–296, 1999, ISSN: 07234864. DOI: 10.1007/s003480050291.

[124] P. J. Thomas, "On the influence of the Basset history force on the motion of a particle through a fluid," *Physics of Fluids A*, vol. 4, no. 9, pp. 2090–2093, 1992, ISSN: 08998213. DOI: 10.1063/1.858379.

[125] V. M. Boiko, V. I. Zapryagaev, A. A. Pivovarov, and S. V. Poplavski, "Correction of PIV data for reconstruction of the gas velocity in a supersonic underexpanded jet," *Combustion, Explosion and Shock Waves*, vol. 51, no. 5, pp. 587–596, Sep. 2015, ISSN: 15738345. DOI: 10.1134/S001050821505010X.

[126] B. J. Petrosky, P. Maisto, K. Todd Lowe, M. A. André, P. M. Bardet, P. I. Tiemsin, C. J. Wohl, and P. M. Danehy, "Particle image velocimetry applications using fluorescent dye-doped particles," in *53rd AIAA Aerospace Sciences Meeting*, American Institute of Aeronautics and Astronautics Inc, AIAA, 2015, ISBN: 9781624103438. DOI: 10.2514/6.2015-1223.

[127] J. M. Fisher, M. Smyser, T. R. Meyer, M. N. Slipchenko, A. W. Caswell, J. R. Gord, and S. Roy, "Burst-mode 100 khz – 1 mhz fleet velocimetry in supersonic and hypersonic flows," in *AIAA Scitech 2019 Forum*, American Institute of Aeronautics and Astronautics Inc, AIAA, 2019, ISBN: 9781624105784. DOI: 10.2514/6.2019-1822.

[128] G. Paniagua, D. Cuadrado, J. Saavedra, V. Andreoli, T. Meyer, J. P. Solano, R. Herrero, S. Meyer, and D. Lawrence, "Design of the Purdue Experimental Turbine Aerothermal Laboratory for Optical and Surface Aerothermal Measurements," *Journal of Engineering for Gas Turbines and Power*, vol. 141, no. 1, Jan. 2019, ISSN: 15288919. DOI: 10.1115/1.4040683.

[129] R. Paschotta, "Supercontinuum Generation," in *Encyclopedia of Laser Physics and Technology*, 2008.

[130] S. Chakravarthy, O. Peroomian, U. Goldberg, and S. Palaniswamy, "The CFD++ computational fluid dynamics software suite," in *SAE Technical Papers*, SAE International, 1998. DOI: 10.4271/985564.

[131] J. Braun, G. Paniagua, F. Falempin, and B. Le Naour, "Design and Experimental Assessment of Bladeless Turbines for Axial Inlet Supersonic Flows," *Journal of Engineering for Gas Turbines and Power*, vol. 138, no. 2, pp. 1–15, 2019, ISSN: 0742-4795. DOI: 10.1115/1.4045359. [Online]. Available: https://asmedigitalcollection.asme.org/solarenergyengineering/article/doi/10.1115/1.4032243/379589/Optical-Analysis-of-a-Two-Stage-XX-Simultaneous%20https://asmedigitalcollection.asme.org/gasturbinespower/article/doi/10.1115/1.4045359/1066208/Design-and-Exp.

[132] J. Saavedra and G. Paniagua, "Transient Performance of Separated Flows: Experimental Characterization of Flow Detachment Dynamics," ASME International, Jun. 2019. DOI: 10.1115/gt2019-91020.

[133] S. P. Schneider, "Development of hypersonic quiet tunnels," *Journal of Spacecraft and Rockets*, vol. 45, no. 4, pp. 641–664, Jul. 2008, ISSN: 00224650. DOI: 10.2514/1.34489.

[134] B. C. Chynoweth, "Measurements of Transition Dominated by the Second-Mode Instability at Mach 6," Tech. Rep., Jan. 2016. [Online]. Available: https://docs.lib.purdue.edu/dissertations/AAI10745569.

[135] M. J. Wright, G. V. Candler, and D. Bose, "Data-Parallel Line Relaxation Method for the Navier-Stokes Equations," *AIAA JOURNAL*, vol. 36, no. 9, 1998. DOI: 10.2514/2.586. [Online]. Available: http://arc.aiaa.org.

[136] B. C. Chynoweth, J. B. Edelman, K. A. Gray, G. R. McKiernan, and S. P. Schneider, "Measurements in the boeing/AFOSR mach-6 quiet tunnel on hypersonic boundary-layer transition," in *47th AIAA Fluid Dynamics Conference, 2017*, American Institute of Aeronautics and Astronautics Inc, AIAA, 2017, ISBN: 9781624105005. DOI: 10.2514/6.2017-3632.

[137] E. K. Benitez, J. S. Jewell, and S. P. Schneider, "Focused Laser Differential Interferometry for Hypersonic Flow Instability Measurements with Contoured Tunnel Windows," American Institute of Aeronautics and Astronautics (AIAA), Jan. 2020. DOI: 10.2514/6.2020-1282.

[138] H. P. Garnir, Y. Baudinet-Robinet, and P. D. Dumont, "Error in the determination of Gaussian peak centroids," *Nuclear Inst. and Methods in Physics Research, B*, vol. 28, no. 1, pp. 146–153, 1987, ISSN: 0168583X. DOI: 10.1016/0168-583X(87)90051-6.

[139] Y. Zhang and R. B. Miles, "Femtosecond laser tagging for velocimetry in argon and nitrogen gas mixtures," *Optics Letters*, vol. 43, no. 3, p. 551, Feb. 2018, ISSN: 0146-9592. DOI: 10.1364/ol.43.000551.